Durham E-Theses

Uncertainty analysis of depth predictions from seismic reflection data using Bayesian statistics

MICHELIOUDAKIS, DIMITRIOS

How to cite:

MICHELIOUDAKIS, DIMITRIOS (2018) *Uncertainty analysis of depth predictions from seismic reflection data using Bayesian statistics*, Durham theses, Durham University. Available at Durham E-Theses Online: http://etheses.dur.ac.uk/12878/

Use policy

The full-text may be used and/or reproduced, and given to third parties in any format or medium, without prior permission or charge, for personal research or study, educational, or not-for-profit purposes provided that:

- a full bibliographic reference is made to the original source
- a link is made to the metadata record in Durham E-Theses
- the full-text is not changed in any way

The full-text must not be sold in any format or medium without the formal permission of the copyright holders.

Please consult the full Durham E-Theses policy for further details.

Academic Support Office, Durham University, University Office, Old Elvet, Durham DH1 3HP
e-mail: e-theses.admin@dur.ac.uk Tel: +44 0191 334 6107
http://etheses.dur.ac.uk

Uncertainty analysis of depth predictions from seismic reflection data using Bayesian statistics

Dimitrios Georgiou Michelioudakis

Department of Earth Sciences

Durham University

A thesis submitted for the degree of

Doctor of Philosophy

June 2018

Copyright © Dimitrios Georgiou Michelioudakis, 2018

The copyright of this thesis rests with the author. No quotation from it should be published without the author's prior written consent and information derived from it should be acknowledged.

Software used:

This Thesis was written in LaTeX. The seismic reflection data processing was performed using *GLOBE Claritas*^{TM}. *PGS Nucleus* modelling package was used to compute theoretical source signature. Statistical analysis was performed in *Matlab Mathworks.* Figures and graphs were plotted using *Seismic Unix* (Stockwell, 1999; Stockwell, 2011) and *Matlab Mathworks.* Petrophysical analysis and well-seismic tie using 2D profiles and available wireline logs was performed in *RokDoc*^{TM}. *Inkscape* was used for image editing and image conversion.

Abstract

Velocity model building is a critical step in seismic reflection data processing. An optimum velocity field can lead to well focused images in time or depth domains. Taking into account the noisy and band limited nature of the seismic data, the computed velocity field can be considered as our best estimate of a set of possible velocity fields. Hence, all the calculated depths and the images produced are just our best approximation of the true subsurface.

This study examines the quantification of uncertainty of the depths to drilling targets from two dimensional (2D) seismic reflection data using Bayesian statistics. The approach was tested in Mentelle Basin (south west of Australia), aiming to make depths predictions for stratigraphic targets of interest related with the International Ocean Discovery Program (IODP), leg 369.

For the purposes of the project, Geoscience Australia 2D seismic profiles were reprocessed. In order to achieve robust predictions, the seismic reflection processing sequence was focused on improving the temporal resolution of the data by using deterministic deghosting filters in pre-stack and post-stack domains. The filters, combined with isotropic/anisotropic pre-stack time and depth migration algorithms, produced very good results in terms of seismic resolution and focusing of subsurface features. The application of the deghosting filters was the critical step for the subsequent probabilistic depth estimation of drilling targets.

The best estimate of the velocity field along with the migrated seismic data were used as input to the Bayesian algorithm. The analysis, performed in one seismic profile intersecting the site location MBAS-4A, produced robust depth predictions for lithological boundaries of interest compared to the observed depths as reported in the IODP expedition. The significance of the result is more pronounced taking into account the complete lack of independent velocity information.

Petrophysical information collected from the expedition was used to perform well-seismic tie, mapping the lithological boundaries with the reflectivity in the seismic profile. A very good match between observed and modelled traces was achieved and a new interpretation of the Mentelle Basin lithological boundaries in seismic image was provided. Velocity information from sonic logs was also implemented to perform anisotropic pre-stack depth migration. The migrated image successfully mapped the subsurface targets to their correct depth location while preserving the focus of the image.

The pre-drilling depth estimation of subsurface targets using Bayesian statistics can be considered as a great example of successfully quantifying the uncertainty in depths and effectively merging seismic reflection data processing with statistical analysis. The derived well-seismic tie in MBAS-4A will be a valuable tool towards a more complete regional interpretation of the Mentelle Basin.

Declaration

I hereby, declare that this thesis is my own work and that to the best of my knowledge and belief it contains no material previously published or written by any other person except where due reference is made in the text of the thesis.

Dimitrios Georgiou Michelioudakis
June 2018

Δῶς μοι πᾶ στῶ καὶ τὰν γᾶν κινάσω
Give me the place to stand, and I shall move the earth
Archimedes of Syracuse (287 BC - 212 BC)

Acknowledgements

First and foremost, I would like to thank my primary supervisor and, in reality, my scientific mentor during this PhD project, Prof. Richard Hobbs. Undeniably, this project wouldn't have been possible without your encouragement, guidance and mainly patience to answer all my, sometimes unreasonable, questions. Frankly, I could not have imagined having a better advisor for my PhD.

Many thanks go to my second supervisor, Camila Caiado, who introduce me to the complicated but particularly interesting world of Bayesian statistics, provide me her statistical algorithm and helped with the statistical analysis of the project. My sincere thanks goes also to Prof. Christine Peirce for her valuable suggestions concerning the study.

A huge thanks to the postgraduate community of the department for facilitating the difficult process of balancing the studies with social life. In particular, I would like to single out the 'Geophysics Bay' for the regular coffee breaks and stimulating conversations. Special thanks to my Greek postgraduate friends for bringing the 'Greek wind' in the department.

Last but not least, I am immensely grateful to my family: my parents and brother for spiritually and practically supporting me throughout my PhD studies and my life in general. I wouldn't be here without them.

Contents

List of Figures

List of Tables

Acronyms and Abbreviations

1D	1 - Dimensional
2D	2 - Dimensional
3D	3 - Dimensional
AVO	Amplitude Variation with Offset
BHM	Bayesian History Matching
BRAINS	Bayesian Regression Analysis in Seismology
CDP	Common Depth - Point
CMP	Common Mid - Point
CIG	Common Image Gather
DSDP	Deep Sea Drilling Project
$\boldsymbol{f-k}$	Frequency - Wavenumber
$\boldsymbol{f-x}$	Frequency - Offset
GA	Geoscience Australia
GP	Gaussian Process
IODP	International Ocean Discovery Program
MB	Mentelle Basin
NMO	Normal Move - Out
NMSE	Normalised Mean Square Error
NP	Naturaliste Plateau
OAE	Oceanic Anoxic Event
preSTM	pre-stack Time Migration
preSDM	pre-stack Depth Migration
PGS	Petroleum Geo Services
PEP	Predictability
SB	Seabed
SRME	Surface Related Multiple Elimination
SU	Seismic Unix (Stockwell, 1999; Stockwell, 2011)

$\boldsymbol{S/N}$	Signal to Noise Ratio	
TWT	Two - Way Time	
VCS	Vertical Cable Seismic	
VSP	Vertical Seismic Profile	
$\boldsymbol{\delta}$	Delta Parameter	Greek symbols
$\boldsymbol{\epsilon}$	Epsilon Parameter	
$\boldsymbol{\varepsilon}$	Model discrepancy	
$\boldsymbol{Z/z}$	Depth (m or Km)	
$\boldsymbol{\eta}$	Eta parameter	
$\boldsymbol{\rho}$	Density (gr/m^3)	
$\boldsymbol{k}$	Wavenumber (m^1)	
$\boldsymbol{k_x}$	Wavenumber in x dimension (m^1)	
$\boldsymbol{k_y}$	Wavenumber in y dimension (m^1)	
$\boldsymbol{k_z}$	Wavenumber in z dimension (m^1)	
$\boldsymbol{\omega}$	Angular Frequency (rad/s)	
$\boldsymbol{\mathcal{A}_{ij}}$	Amplitude of traces in CMP	English/Latin symbols
$\boldsymbol{AI}$	Acoustic Impedance $((\mathrm{gr} \cdot \mathrm{m})/(\mathrm{cm}^3 \cdot \mathrm{s}))$	
$\boldsymbol{A_{i_{source}}}$	Amplitude components for source's inverse filter	
$\boldsymbol{A_{i_{rec.}}}$	Amplitude components for receiver's inverse filter	
$\boldsymbol{c}$	Sea water velocity (m/s)	
$\boldsymbol{dt}$	Sampling interval (ms or s)	
$\boldsymbol{\Delta T_0}$	Zero Offset Two-Way Time increment (ms or s)	
$\boldsymbol{\Delta V_{rms}}$	Root Mean Square Velocity increment (m/s or Km/s)	
$\boldsymbol{\Delta V_{int.}}$	Interval Velocity increment (m/s or Km/s)	
$\boldsymbol{\Delta z}$	Depth increment (m or Km)	
$\boldsymbol{e}$	Recording Error	
$\boldsymbol{f_{center}}$	Center frequency of the deghosting filters (Hz)	
$\boldsymbol{G}$	Ghost function	
$\boldsymbol{h_s}$	Distance - Offset from scatterer to source (m)	
$\boldsymbol{h_r}$	Distance - Offset from scatterer to receiver (m)	
$\boldsymbol{T/\mathcal{T}/t}$	Recorded Traveltime (ms or s)	
$\boldsymbol{T_0}$	Zero Offset Two-Way Time (ms or s)	
$\boldsymbol{R}$	Reflectivity	
$\boldsymbol{\mathcal{R}}$	Receiver position	
$\boldsymbol{R_{flat}}$	Reflectivity - Flat sea surface approximation	

$\boldsymbol{R_{stat.}}$	Reflectivity (pre-stack) - Rough sea surface approximation
$\boldsymbol{R'_{stat.}}$	Reflectivity (post-stack) - Rough sea surface approximation
$\boldsymbol{s}$	Slowness (s/m)
$\boldsymbol{\mathcal{S}}$	Source Position
$\boldsymbol{Sc}$	Semblance
$\boldsymbol{V_p}$	Primary wave Velocity (m/s or Km/s)
$\boldsymbol{V_{p0}}$	Primary wave Average Velocity (vertical direction) (m/s or Km/s)
$\boldsymbol{V_s}$	Secondary wave Velocity (m/s or Km/s)
$\boldsymbol{V_{inst.}}$	Instantaneous Velocity (m/s or Km/s)
$\boldsymbol{V_{int.}}$	Interval Velocity (m/s or Km/s)
$\boldsymbol{V_{rms}}$	Root Mean Square Velocity (m/s or Km/s)
$\boldsymbol{x}$	Offset between source-receiver (m or Km)
$\boldsymbol{x_c}$	CMP position along a seismic profile (m or Km)

Chapter 1

Introduction

1.1 International Ocean Discovery Program - Leg 369

Deciphering the time relationships and mechanisms that link the climate conditions between tropics and polar regions is of great importance for reconstructing paleoclimatic changes. By inferring the paleoclimatic conditions we can potentially improve our predictions for the future. To achieve this goal, it is essential to collect stratigraphic records from strategic locations around the globe such as the high latitude ocean. In this context, past periods with high average global temperature, such as the Initial Eocene Thermal Maximum and the Cretaceous Hothouse, attracted the scientific community over recent years, providing very interesting insights into the mechanisms of natural short term change in climate, ocean conditions and biogeochemical cycling.

The International Ocean Discovery Program (IODP), proposal 760, was proposed by a consortium of scientists, aiming to answer a number of questions focused on the high latitude regions. The selected locations, off south west Australia, the Naturaliste Plateau (NP) and Mentelle Basin (MB) were considered ideal for the purpose, having been spot-cored by the earlier fore-runner of IODP, the Deep Sea Drilling Project (DSDP), and proven to have Cretaceous aged sediments.

By sampling the stratigraphic units of NP-MB, the aim was to reconstruct the paleoclimatic regime of high latitude climates and simultaneously obtain valuable information about the paleoceanographic and tectonic history of the region, aspects that were critically missing within the paleotemperature and palaeoceanographic community. Key question to be addressed were the details of rise and collapse of the Cretaceous Hothouse period, details that would improve our understanding about the mechanics of climate change, possibly linking the phenomenon with volcanic events and provide paleoclimatologists with new data to better constrain their models.

More specifically this IODP project could provide answers for the following key questions (Hobbs et al., 2017):

1. rise and collapse of Cretaceous Hothouse: Finding the causes of warming, peak of the event and subsequent cooling;
2. Oceanic Anoxic Events (OAEs): Roles of productivity and ocean circulation;
3. Godwana breakup: Position of the MB and neighbouring area against Antartica;
4. Cenozoic paleoceanography: Change in paleoceanographic conditions after opening of Tasman Passages;
5. basement composition and depositional history: Occurrence of volcanic phases in SW Australia and nature of sub - basalt basement terrain.

In a broad sense, results from the IODP project could give an insight on how the Earth's climate and oceans respond to elevated levels of atmospheric CO2 concentration.The region of MB is poorly sampled as the only lithostratigraphic information available is provided by the DSDP borehole (Davies et al., 1974). In order to acquire samples from the region, six drilling locations were planned,three primary (MBAS-4, MBAS-8 and MBAS-9) and three secondary sites (MBAS-3, MBAS-5 and MBAS 6) (Figure 1.1). Of these locations four sites were cored with varying degrees of success (Hobbs et al., 2017). Two of the sites (MBAS-4 - IODP site U1513 and MBAS-8 - IODP site U1514) were also wireline logged (Fig. 1.1).

1.2 Geological Setting of Naturaliste Plateau - Mentelle Basin

The western and southern margins of Australia are defined as the two arms of a triple junction that formed during the final stages of Gondwana breakup (Powell et al., 1988; Royer and Coffin, 1992; Direen et al., 2007). A significant geological feature of that region is Naturaliste Plateau (NP) which is a large submarine plateau extending from Western Australia into the Indian Ocean (Fig. 1.2). Having a rectilinear shape, NP spans an area of approximately 90,000 km^2 with water depths between 2000 and 5000 m (Petkovic, 1975a; Petkovic, 1975b; Jongsma and Petkovic, 1977; Borissova, 2002).

Naturaliste Plateau is surrounded by two different continent-ocean transition zones (COT), with the northern being 30 to 90 km wide and the southern up to 250 km wide (Borissova, 2002). These two transition zones are formed due to separate breakup events. The northern is originated from the breakup between India and Australia-Antarctica during the Valanginian - Hauterivian periods (Gibbons et al, 2012), whereas the southern zone was formed later due to the breakup between

Australia and Antartica (Direen et al., 2011). Although the affinity of Naturaliste Plateau isn't totally defined, taking into consideration the results from geochemical analysis of dredged material (Halpin et al., 2008; Beslier et al., 2004), borehole cores (Ford, 1975) and geophysical studies (Petkovic, 1975b; Jongsma and Petkovic, 1977; Borissova, 2002; Direen et al., 2007) it is now believed that the Naturaliste Plateau basement has a continental origin. In particular, a crystalline continental crust covered by volcanic rocks and related intrusives dated as contemporary with the break-up of Australia and India (Crawford et al. 2006; Direen et al., 2007).

At the east of Naturaliste Plateau lies the Mentelle Basin (MB) (Figs. 1.1, 1.2). It is a sparsely explored, sedimentary basin, between the Naturaliste Plateau and the southern part of the Western Australian Shelf. Seismic images based on early seismic surveys showed that Mentelle Basin is elliptical in shape, with minor and major axes 200 km east-west and 220 km north-south respectively. Its main depocenter is believed to contain sediments from Cretaceous to Holocene producing an interval of more than 3 s Two-Way Time (TWT) on the seismic image (Borissova, 2002; Bradshaw et al., 2003). These sediments are possibly underlain by older sediments from an earlier rifting event.

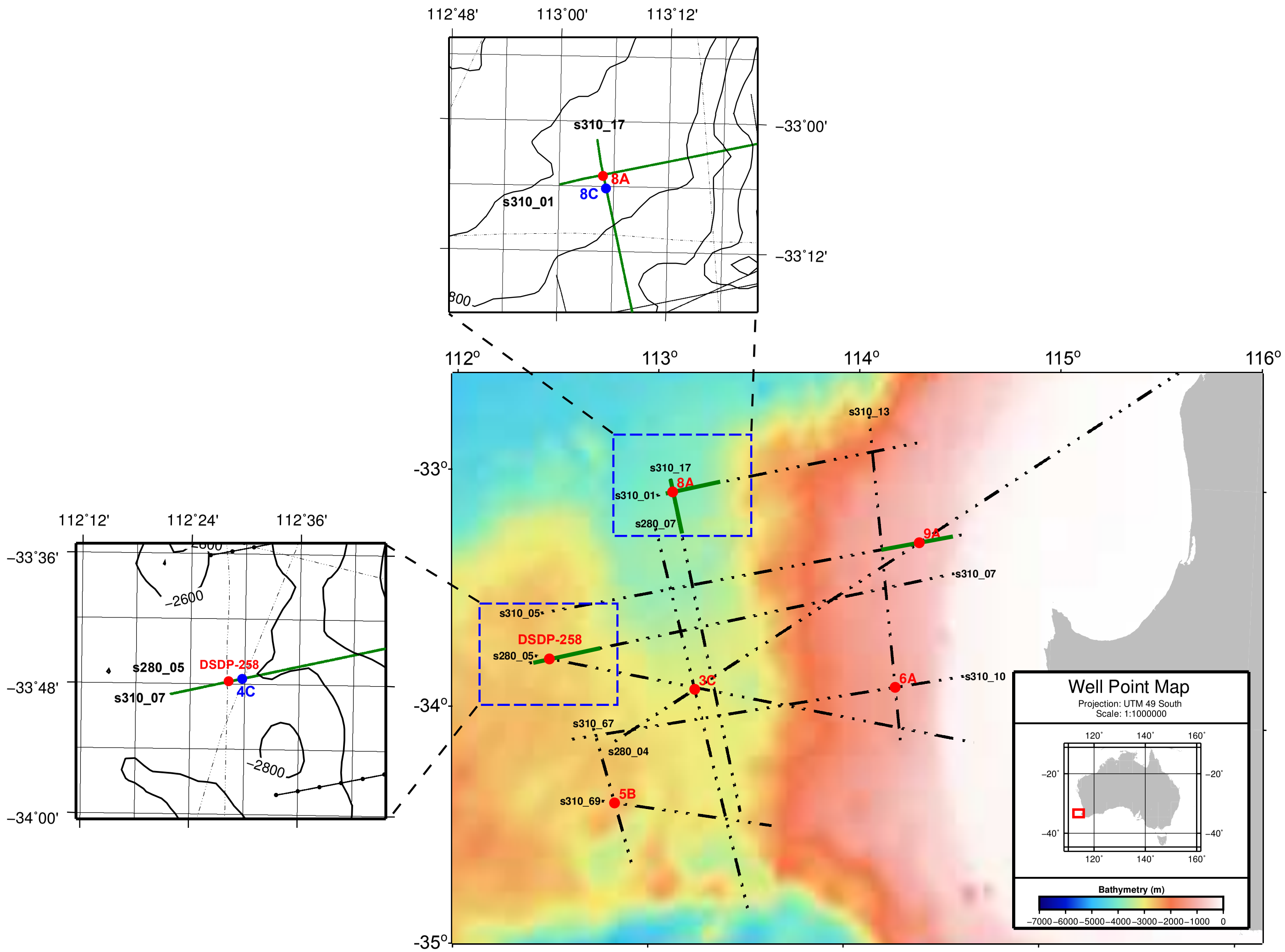

Figure 1.1: Bathymetric map of Mentelle Basin. The positions of 2D seismic lines (dashed black lines) and initially proposed well locations (red circles) are shown. Green solid lines represent the seismic segments presented in this Thesis. Blue circles in the insets show the actual drilled positions after re-evaluation of the initial targets (Wells 4C, 8C respectively). DSDP - 258 is the 1973 drilled core as reported in Davies et al., 1974.

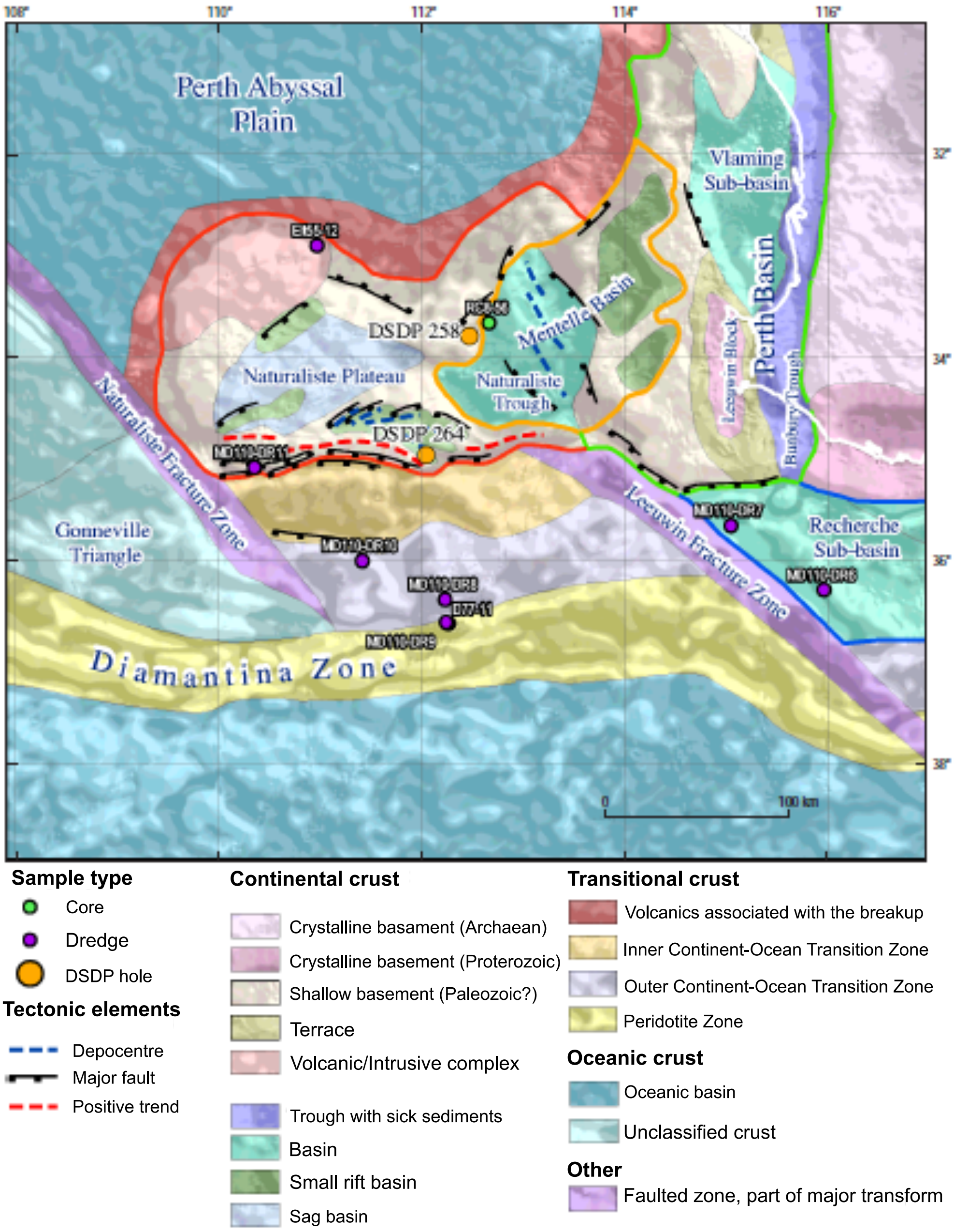

Figure 1.2: Tectonic setting of Naturaliste plateau and Mentelle Basin (modified from Borissova, 2002).

1.3 Stratigraphy of Mentelle Basin

The stratigraphic features of MB are not delineated, with the only lithological information provided by borehole DSDP-258. Figure 1.3 shows the details of the penetrated sequences during the DSDP drilling, tied to a pre-stack time migration (preSTM) profile (details of processing are described in Chapter 2). Specifically, in Davies et al., 1974 the following lithological sequences were reported:

- vertical hatching - cyan colour: 114 m of Miocene deep - water carbonate oozes;
- horizontal hatching - blue colour: 171 m of Paleogene limestones and chalks with chert bands;
- wavy hatching - brown colour: 229 m of Cretaceous black shales;
- stipples - yellow colour: 11 m of Lower Cretaceous glauconitic sands.

It has to be noted that in Figure 1.3 the borehole tied to the preSTM image reflectivities, serves as a pictorial example and does not represent a precise well-seismic tie for that region. As we will describe later, the well-seismic tie requires a complete well log information (V_p, V_s, ρ), information that wasn't acquired during the DSDP expedition.

Nevertheless, in terms of describing the structural features of MB, the results of the borehole site (DSDP-258) in conjunction with originally processed and reprocessed seismic data from Geoscience Australia (GA) S280 and S310 surveys, Shell Petrel Development Survey and Geoscience Australia Continental Margins Surveys 18 (Sargent et al, 2011), allowed the division of the stratigraphy of MB into the following seismically interpreted tectonostratigraphic megasequences (by Maloney et al, 2011):

▷ **Miocene to Quaternary megasequence:** This megasequence is characterized by thin, variable thickness, low amplitude reflections which are described as carbonate oozes;

▷ **Miocene unconformity:** Miocene unconformity shows a variable seismic character. In the vicinity of DSDP - 258 site it appears as a smooth reflector at which the underlying Late Cretaceous chalk beds terminate;

▷ **Paleogene Megasequence:** The megasequence is consisted of Oligocene and Eocene sediments that appear in seismic profiles as dipping reflectors which terminate to the overlying Miocene unconformity;

▷ **Late Cretaceous – Eocene Megasequences:** Results from borehole DSDP-258 show that below the Paleogene Megasequence, there is a thin layer of Turonian - Santonian chalk beds. Within this sequence, a high amplitude reflection can be identified, which coincides with an increase in the P – wave velocity (V_p). This is likely caused by chert beds, recovered at a depth of 220 m at DSDP-258.

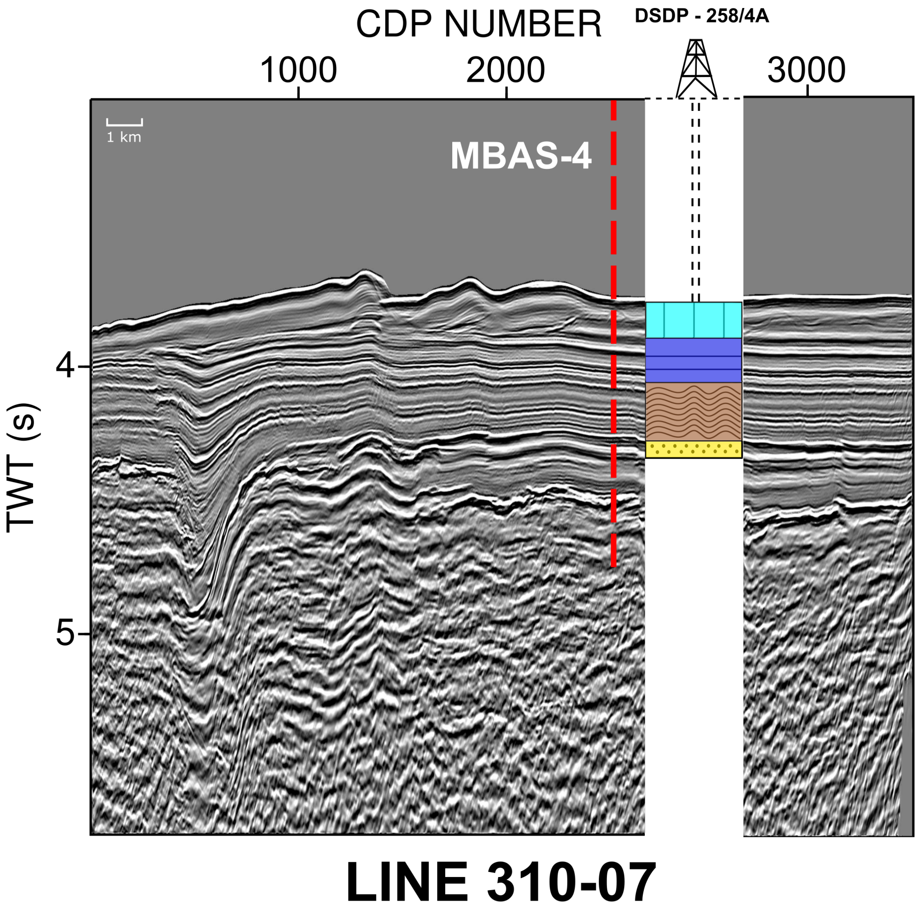

Figure 1.3: DSDP-258 borehole tied to a ghost free pre-stack time migrated (preSTM) profile S310-07. In the lithological interpretation: vertical hatching in cyan colour - Miocene carbonate oozes; horizontal hatching in blue colour - Paleogene chalks with chert bands; wavy hatching in brown colour - Cretaceous black shales; black stipples in yellow colour - Lower Cretaceous glauconitic sands. Red dashed line intersecting profile S310-07, indicates the position of the proposed site for the well MBAS-4. Note that the borehole - seismic tie is approximate as no wireline log was acquired during the DSDP drilling.

The lowermost megasequences are speculative as they have not been drilled, so the interpretation is based on knowledge from the adjacent Perth Basin.

▷ **Valanginian – Late Hauterivian breakup unconformity:** The Valanginian - Hauterivian unconformity is the easiest traceable seismic reflector in MB. It is characterized by severe lateral discontinuities - faults and it is linked to the breakup between India and Australia - Antartica (Borissova, 2002; Direen et al, 2008);

▷ **Jurassic Megasequence:** As it lies beneath the Valanginian - Late Hauterivian volcanics, the seismic resolution appears to be severely degraded, but generally it appears to be laterally discontinuous and underlies the main depocentres of the MB;

▷ **Permian Megasequence:** The last major sequence that is seismically traceable in the MB thickest depocentres is of Permian age and exhibit the same character with the Jurassic Megasequence.

1.4 Aims of Thesis

As a significant part of this study was spent before the actual drilling of the targets (IODP drilling cruise September - November 2017), the important deliverable was the prediction of depths to subsurface units using a number of 2D seismic reflection profiles.

However, a major hindrance of that effort was the absence of in - situ velocity information. DSDP-258 only reported the penetrated lithostratigraphic units with their relevant thickness, but at that time no wireline logs were acquired. Having the two - way time intervals from the seismic data and with the velocities inferred during the velocity analysis stage, we could deduce depth information. Unfortunately, we need to recognize subsurface targets in the time domain to convert to depth. Expressed differently: to unambiguously map lithological boundaries in a seismic profile, a well to seismic tie is required which can link geological interfaces in depth to reflectivities in time seismic data.

Without any prior well log information the task of estimating the depths of the subsurface targets is challenging and needs the synergy of seismic reflection data processing in both time and depth domains with a method of uncertainty estimation, which can provide a realistic prediction of the targets' depths taking into account the relevant uncertainties present in the system.

Taking into account the above, the study primary aims are summarised in the following:

- Delineate main subsurface targets in Mentelle Basin by reprocessing a number of 2D seismic reflection data (acquisition from Geoscience Australia).
- Quantifying uncertainties in velocity models from seismic reflection data and perform predictions about the depths to drilling targets associated with the IODP drilling.
- Correlating reflectivity in seismic images with lithological boundaries.

The first aim is addressed by applying deterministic deghosting filters in pre- and post-stack domains which boost the low/high frequency content of the signal. The merits of the operators are maximised when they are combined with a complete seismic processing strategy which includes designature, demultiple and pre-stack time migration (preSTM) and/or pre-stack depth migration (preSDM) algorithms. To ensure that the quality of the images fit the purposes of the project, the available 2D seismic lines were reprocessed in time and depth domains.

The second task is addressed by implementing a Bayesian algorithm (Caiado, 2012a). The algorithm effectively uses the $T_0 - V_{rms}$ picks, along with the observed amplitudes of reflection events in a Common - Mid Point (CMP) gather, as input information and outputs probabilistic estimations of all the pertinent values important in seismic exploration $(T_0, V_{rms}, V_{int.}, z)$. As the algorithm uses seismic gathers as input, the output uncertainty estimations will reflect the quality of the seismic reflection processing strategy followed. Thus, the rationale of reprocessing the 2D seismic lines is not solely related to the subsurface image results as deliverable but it is also coupled with the nature of the statistical approach used (see Chapter 2, Chapter 3 for details).

The final target of correlating seismic events, as appeared in the seismic profiles, with lithological boundaries is fulfilled by performing well-seismic tie. As the approach requires apart from seismic images, the petrophysical properties and measured depths of the drilling targets, the task was accomplished after the actual drilling of the IODP - leg 369.

1.5 2D seismic reflection data

The 2D seismic reflection data were acquired for Geoscience Australia by the CGGVeritas vessel CGG Duke, in the region of the Mentelle Basin between 20th December 2008 and 8 January 2009. A total 2572.13 km of high quality, oil industry standard, seismic data was acquired, comprising 18 lines of the Southwest Margins (SWM) (Figure 1.1).

Although for the purposes of the project, segments of 12 lines were originally reprocessed, in this Thesis a total number of four 2D seismic reflection segments are shown.

1.6 Summary of Thesis

This study is written in a logical order, emphasizing initially in the pre-drilling evaluation (seismic reflection processing and application of statistical algorithm) and eventually in the post-drilling processing (well - seismic tie).

Chapter 2 focuses on the reprocessing of Geoscience Australia (GA) 2D lines in time domain. It includes a thorough description of the processing steps applied in order to achieve a well focused time domain representation of the subsurface. From pre-stack processing to post-stack cosmetic processing, the steps are analysed and the results are critically evaluated. A detailed comparison of deghosting operators is given with the aim to improve the temporal resolution of the image. Furthermore, due to the bathymetric variability of MB, different types of noise dominated different 2D profiles. As a result, the processing steps were optimised for every line independently so as to effectively tackle the different noise components.

Most of the data consisting Chapter 2 were processed approximately 1.5 years before the actual IODP drilling, at a time when the proposed drilled locations and targets were under consideration by the IODP committee. Therefore, some of the 2D lines described in the study, are given as an example of seismic reflection processing flow and do not necessarily serve as input data for the subsequent statistical analysis and well - seismic tie.

Following the time domain processing of Chapter 2, Chapter 3 is the core of the Thesis. It focuses on the imaging of targets in depth domain and generating probabilistic estimations of variables related with seismic reflection processing. It describes the rationale of all the processing steps applied in Chapter 2 and explains the need for depth domain processing as a tool to build a more realistic velocity model and by inference achieve more constrained predictions.

The statistical techniques used are explained and most importantly their adaptation for seismic processing is provided. Through depth domain velocity model building and statistical analysis, predictions for depths to drilling targets at the site of the proposed MBAS-4 area are reported. The chapter finishes by generating random velocity fields from the retrieved statistical distribution and performing different sets of depth migration images. The relative differences arising from the different velocity fields are evaluated and effectively an example of the risk analysis technique of probabilistic imaging is given.

As a natural continuation of the seismic data preconditioning explained in Chapter 2 and the depth domain analysis with predictions in Chapter 3, Chapter 4 compares the true depths as reported after the IODP expedition with the modelled/predicted ones. To perform an unbiased comparison, the well logs were edited appropriately and synthetic traces were generated using the observed reflectivity from the well logs along with wavelet extracted directly from post-stack seismic data. The analysis is continued with the well-seismic tie and mapping of lithostratigraphic boundaries with reflectivity in seismic profile. The latter is subsequently mapped in the depth domain and a comparison of the original with the new interpretation is given.

The chapter is concluded by using the true sonic log information to perform anisotropic depth migration. This process aided to restore the original depths to drilling targets but simultaneously generate a well focused image.

In Chapter 5, advantages and disadvantages of the techniques used throughout the study are stated, focusing primarily on the stability of the deghosting operators as a tool to constrain the interpretation (Chapter 2), on the isotropic approximation of the statistical algorithm and eventually on the well - seismic tie process using deghosted data.

As a conclusion of this study, in Chapter 6 we recapitulate the main results of the project and propose future implementations that could be applied to render the combined usage of seismic processing with statistical analysis more robust.

Chapter 2

Deterministic Inverse Filters and Time Domain Processing

In this chapter a step by step description of the operators applied to the available 2D GA seismic data is given. As the lines intersect the planned well locations, they are grouped and presented in pairs with respect to their corresponding well. The reprocessing covers all the parts of an oil industry standard time processing sequence, from source deconvolution and deghosting to isotropic and anisotropic pre-stack time migration (preSTM) and post-stack processing. Testing of the parameters for each step was done to find the set of operators which produced an optimum result.

As the objective of this study is to estimate the depths to drilling targets, clarifying the subsurface interfaces is of the utmost importance. A key element to achieve this is the application of post-stack and pre-stack deterministic deghosting filters as a tool to improve the temporal resolution of the data. The resulted images are compared and their stability is tested utilizing amplitude spectra and $f - k$ plots.

Preconditioning the data through deghosting filters and preSTM is critical to achieve better statistical predictions. However, it is noted that due to the nature of the deghosting process, care must be taken so as to avoid generating illusory reflectivity (high frequency events) which will hinder the correct interpretation.

To test the validity of the operators in a range of data sets, the inverse filters are applied in three marine environments with different sea water depths, from very deep environment (MBAS-8: profiles S310-01 / S310-17, seabed at $\approx$ 5.1 s TWT), to deep water depths (MBAS-4: profile S310-07, seabed at $\approx$ 3.7 s TWT) and shallow water conditions (MBAS-9: profile S310-05, seabed at $\approx$ 1.5 s TWT).

2.1 Proposed site MBAS-4

In Table 2.1, the acquisition specifications for the reprocessed S310 Mentelle Basin (MB) profiles are given. Differences between the acquired 2D lines are related with the streamer depth (colour coded in Table 2.1).

Table 2.1: Acquisition specifications for reprocessed profiles S310.
Colour code represents lines with different streamer depths.
Profile locations shown in Fig. 1.1

Parameter	**Value (S310-07, S310-01, S310-17, S310-05)**
Source type	Tuned point-source air-gun array
Gun type	Bolt 1500LL air guns
Number of guns	29
Nominal source volume	70.3 L (4290 cu in)
Nominal source pressure	13.7 Mpa (2000 psi)
Nominal source depth	7 ±1 m
Shotpoint interval	37.5 m
Streamer type	Sercel Seal Solid
Number	1
Streamer Length	8100 m
Number of groups	648
Group length	12.5
Nominal streamer depth	10 ±1 m, 12 ±1 m, 8 ±1 m
Nominal inline offset	94
Average Water Velocity	1504 m/s
Average sea state - Swell	2 m
Recording system	Sercel SEAL v5.2
Record length	12 s
Sample interval	2 ms
Low-cut filter/ slope	2Hz analog at 6dB/Oct
High-cut filter/ slope	200Hz analog at 370 dB/Oct
Recording format	SEGD 8058 rev.1
Polarity	SEG Reverse (Impedance Increase: Through)

2.1.1 Time domain processing of line S310-07

In Table 2.2, the processing steps applied to seismic line S310-07 are given. The processing sequence involves two different flows (description in Table 2.2). Different steps are primarily associated with when the deghosting filters are applied. In the first flow, the deghosting filters are derived and applied post-stack. In the second, similar operators are applied pre-stack (shot gathers). The resulted profiles are juxtaposed and advantages/disadvantages of each flow are described.

In the following, we will give a detailed analysis of every processing step applied to the profile. To avoid repetition of the steps shared in both flows, these will be described only once.

Table 2.2: Time domain processing sequence for seismic line S310-07.

S310-07
Reformat and geometry import - CDP spacing = 6.25 m - Nominal CDP fold = 108 (**Flows 1 & 2**)
Instrument delay correction = 100 ms, Source-Receiver datuming (**Flows 1 & 2**)
Minimum phase low cut Butterworth filter 4 Hz, 18 db/octave (**Flows 1 & 2**)
Modelled designature inverse filter (shot gathers) (**Flows 1 & 2**)
Swell noise attenuation ($f-k$ domain) (**Flows 1 & 2**)
Deterministic inverse filter for source's notch compensation (shot gathers)
derived from post-stack amplitude spectrum (**Flow 2**)
Receiver's notch compensation in $f-x$ domain (shot gathers) (**Flow 2**)
Linear noise elimination ($f-k$ domain) (**Flow2**)
CMP Sorting and 2^{nd} order Velocity analysis (every 312.5 m / 50 CMPs) (**Flows 1 & 2**)
Straight ray isotropic Kirchhoff pre-stack Time Migration (preSTM) (**Flows 1 & 2**)
Spherical Divergence Correction (**Flows 1 & 2**)
Outer Trace Mute and Stack (**Flows 1 & 2**)
Deterministic inverse filters for source's & receiver's notch compensation
derived from observed average notches as appeared in the post-stack amplitude spectrum (**Flow 1**)
Time variant zero phase Butterworth filter (**Flows 1 & 2)**
(defined by low cut - low pass - highpass - high cut (Hz)) (**Flows 1 & 2)**:
10-20-100-125 at seabed (sb),
10-20-100-125 at sb + 0.3 s,
8-15-100,120 at sb + 0.6 s,
5-10-90-110 at sb + 0.9 s,
3-8-50-70 at sb + 2.5 s
Frequency - distance ($f-x$) deconvolution for random noise attenuation (**Flows 1 & 2)**
Phase Inverse Q compensation = 200 (**Flows 1 & 2)**
Cosmetic sea noise mute (**Flows 1 & 2)**

2.1.1.1 Source Deconvolution

The initial operator applied to the data set was an inverse filter that aims to shape the source signature along with its bubble pulse coda. De-signature process ideally compresses the source function to a spike and simultaneously zero phases the data. The filter was modelled using the *Nucleus* source modelling package [Petroleum Geo Services (PGS)] which takes into account the acquisition parameters, the volume and type of air - guns and the physical parameters of the water (sound speed and temperature) during the seismic acquisition. The modelled signature didn't include any source's or receiver's ghost. It was convolved in the pre-stack (shot) domain as the periodicity of the bubble pulse is close to constant from shot to shot (Sargent et al., 2011). Note that the approach of modelling the far field signature using *Nucleus* was mainly chosen due to the unavailability of the actual recorded far-field signature during the acquisition from GA. Furthermore, the operator is fast to built and its application is straightforward. However, a modelled signature cannot perfectly replicate the reality (acquisition conditions), an effect which can potentially lead to incomplete debubbling or zero phasing. The latter can be unambiguously evaluated during the process of well-seismic tie.

In Fig. 2.1 the modelled source function with its inverse filter are shown (Figs. 2.1a, 2.1b). The latter is produced by matching the modelled signature with a band - limited spike. Figs.

2.1c and 2.1d show the effect of the filter prior and after applying the de-signature operator to an unprocessed shot gather. The high peak to bubble ratio of the source was such that the source signature has minimal bubble pulse coda amplitude. As a result, de-signature filter only produced subtle differences located mainly at the earliest of arrivals.

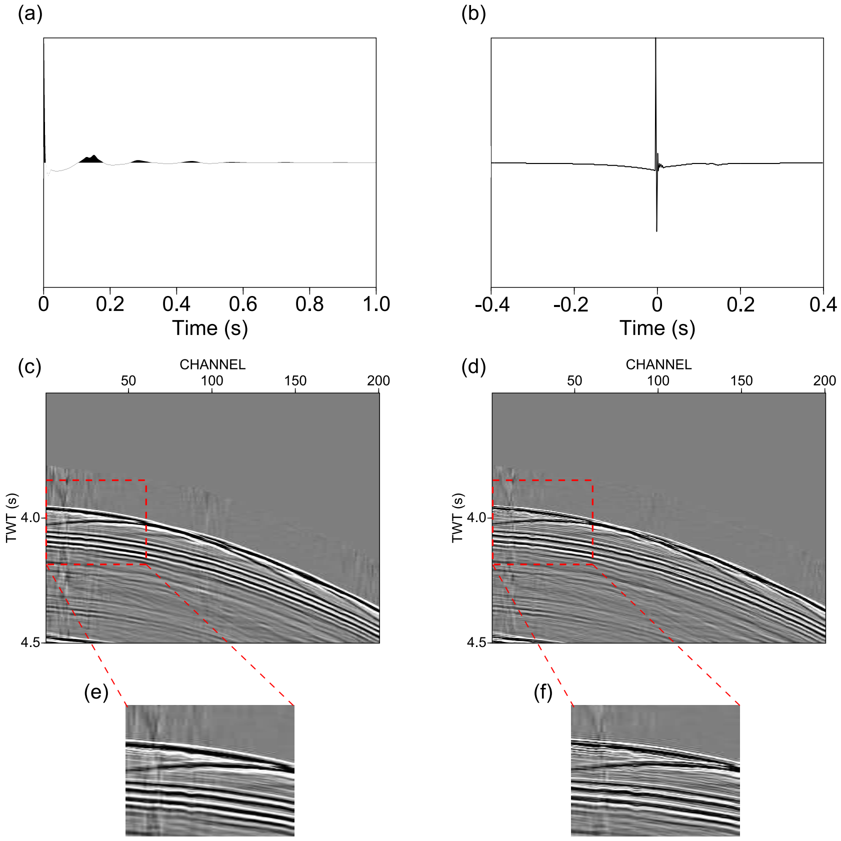

Figure 2.1: Eliminating the source signature. (a) The source signature for lines of seismic survey S310 as modelled using the *Nucleus* package (no source's or receiver's ghosts modelled); (b) The inverse of the source signature after matching the signature in (a) with a band-limited spike; (c) An unprocessed shot gather; (d) Same as in (c) after convolving with the filter in (b); (e) and (f) show the zoomed versions of the nearest channels of (c) and (d) respectively.

2.1.1.2 Swell Noise attenuation

Swell noise is a sea waves' induced noise, typically recorded during marine seismic acquisition (as discussed in Elboth et al., 2009). In seismic gathers, swell noise is manifested as low frequency / high amplitude events that mask the continuity of reflection arrivals (Figure 2.2a). In cases where this source of noise is not optimally eliminated, it can degrade the image's quality. In 2.2b, the remnant swell noise locally contaminates the stack image (red arrows), especially at later times. The image is unmigrated and was generated using a velocity field which will later be used for pre-stack time migration (preSTM). Swell noise is more evident at later times / deeper structures due to the poor signal / noise ratio (S/N), locally obscuring the structures continuity.

Typically, swell noise can be attenuated using wavelet transforms (Miao and Cheadle, 1998) or in $f-x$ domain using noise detection algorithms and statistical methods (Elboth et al., 2008; Schonewille et al., 2008; Bekara and Van der Baan, 2010). Due its low frequency nature, swell noise is located adjacent to the wavenumber axis (K) in the $f-k$ spectrum. As a result, a targeted dip filter in $f-k$ space can successfully eliminate the noise, leaving the primary signal intact.

An example of the swell noise elimination is presented in Fig. 2.3, where the noisy shot gather in Fig. 2.3a is cleaned by using a targeted dip filter that eliminates dips larger than 20 ms / trace (Fig. 2.3b). Although generic, the filter attenuates most of the noise and safely leaves the primary events unaffected (Fig. 2.3c). Figs. 2.3a - 2.3c are presented after AGC application, thus the noise difference shown in Fig. 2.3cis relative and not absolute. In regions where the contamination is more pronounced, a low frequency shadow appears. The latter can be largely suppressed with the synergy of preSTM, stacking and post-stack time variant filtering.

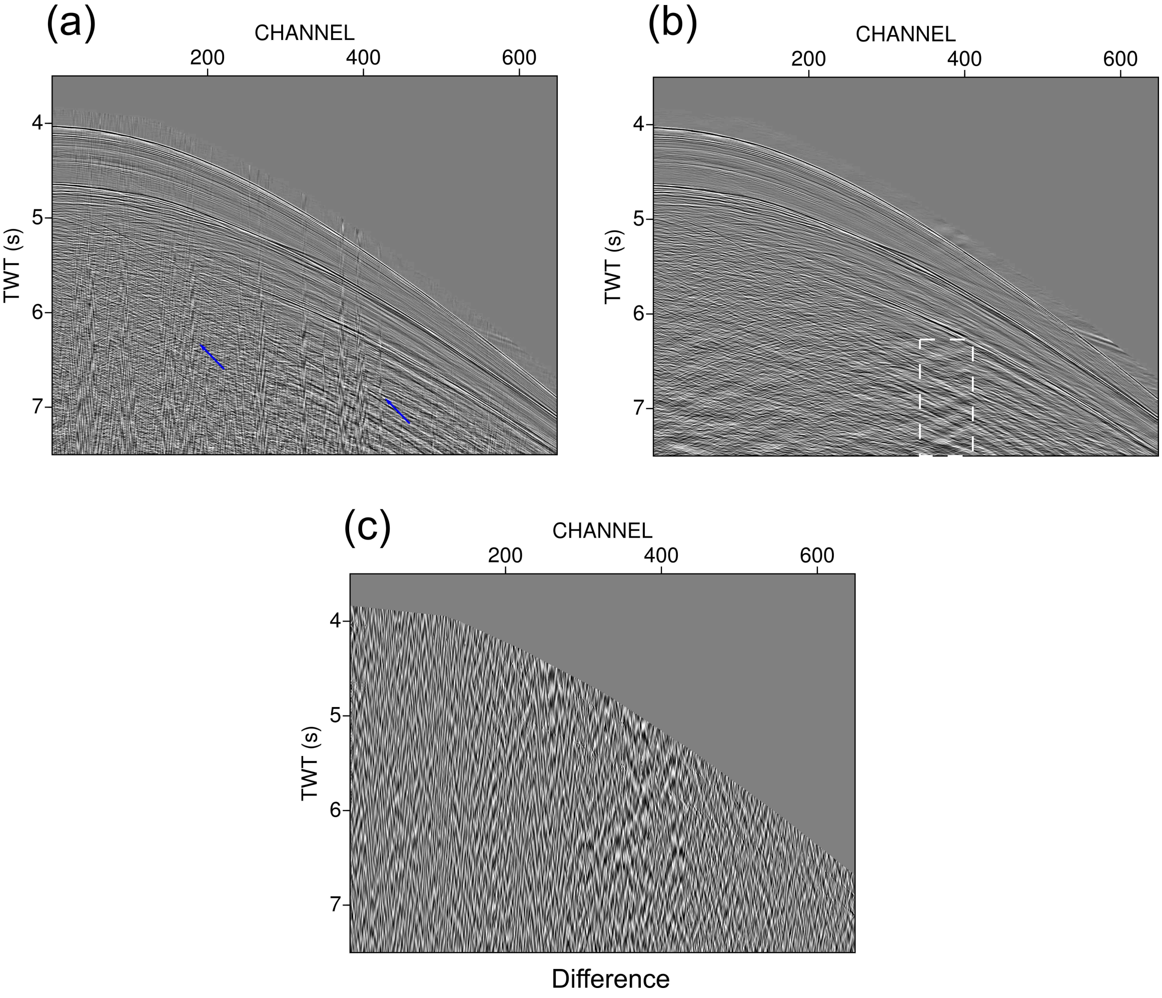

Figure 2.2: Swell noise attenuation in $f-k$ domain. (a)Input shot gather after low cut filter application; (b) Same shot after dip filtering in $f-k$ domain. Swell noise is mostly attenuated, but in the regions where it was more pronounced (poor S/N), a low frequency remnant noise is still evident (white dashed box). The latter can be suppressed by time migration process, stacking and time-variant filtering. Both panels have muted sea noise and AGC applied; (c) Difference between signals of panels (a), (b).

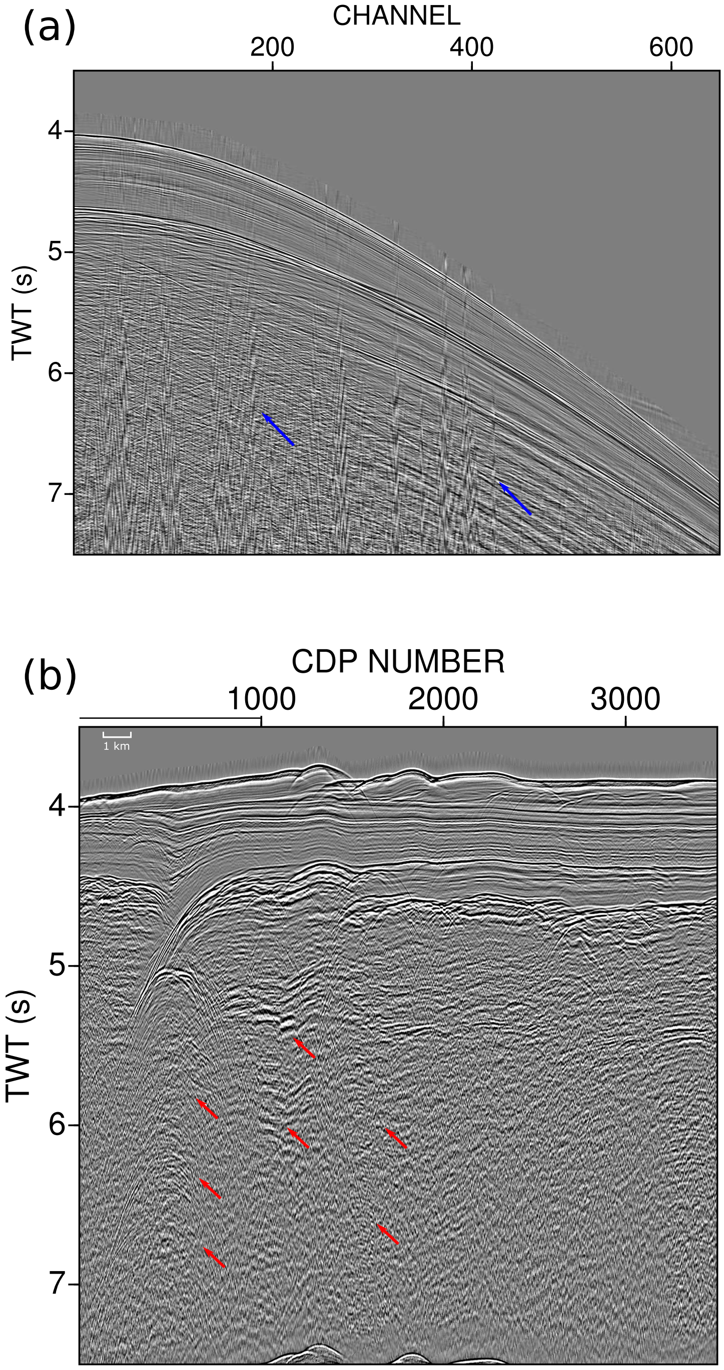

Figure 2.3: Swell noise and its effect on stack domain. (a) Example of shot gather with severe swell noise content. Note how the noise stripes are superimposed on the signal (blue arrows indicate some regions with swell noise content); (b) Unmigrated stack profile without any swell noise attenuation. Possible deeper structures are contaminated by noise (red arrows).

2.1.1.3 Velocity analysis & pre-stack Time migration

As the primary target of this research project is to quantify the uncertainties in velocity models for depth prediction, we need to constrain the inferred velocity values as well as possible. The latter can be achieved, by eliminating the dip effect of the stacking velocities and reposition the data to their correct subsurface location in the pre-stack domain. For this reason, we chose to perform pre-stack time migration to our data set aiming to achieve the best focusing of reflection events in the final image.

For the process of preSTM, multiple techniques and algorithms exist (for a full description of available techniques see Bancroft, 2007). As $Claritas^{TM}$ performs preSTM in constant offset planes, we sorted the shot gathers to that domain (applications of preSTM in common-offset planes in Sullivan and Cohen, 1987; Deregowski, 1990; Kim and Krebs, 1993). During preSTM, energy from every trace in a CMP gather is spread in traces of neighbouring gathers along a constant offset plane. The algorithm used for migration is based on Kirchhoff principles. Kirchhoff migration sums the energy along diffraction curves and places the amplitude of the summation at a predefined scatter point location. The diffraction's shape is defined by either V_{rms} values for time migration or via raytracing techniques using the $V_{int.}$ field for depth migration. The governing equation for calculating the diffraction shape for time migration purposes is given by the Double Square Root equation

$$T = \left(\frac{T_0^2}{4} + \frac{h_s^2}{V_{rms}^2}\right)^{\frac{1}{2}} + \left(\frac{T_0^2}{4} + \frac{h_r^2}{V_{rms}^2}\right)^{\frac{1}{2}} \tag{2.1}$$

where T, two - way traveltime, V_{rms}, Root Mean Square velocity, T_0, zero offset two - way time, h_s and h_r offsets from the location of the migrated trace to the location of the source and receiver respectively. Note again, that for time migration the summation principle is based on the V_{rms} value at the position of the scatter point, meaning that all the calculated times (T) associated with the diffraction curve, for all the available offsets, are derived from one local V_{rms} value.

The process of preSTM is performed iteratively and includes sorting to common offset planes, preSTM using the initial V_{rms} field inferred during the velocity analysis stage, sorting back to CMP domain for inverse NMO correction and refinement of the V_{rms} velocity field. The refinement process is critical for the correct building of the V_{rms} field until the target reflection events appear to be flat in the resultant Common Image Gathers (CIGs). For our data set we initially performed multiple passes of 2^{nd} order (isotropic) NMO correction.

In Figure 2.4, we present an example of 3 unmigrated and time migrated gathers along the profile, generated using different V_{rms} fields. The gathers presented are muted in their far offset to avoid NMO stretch effects. The presence of basalts in our area ($\approx$ 4.5 s TWT) eliminates most of the high frequency content of the seismic waves later than this time. As a result, the velocity model building process didn't include any intra or sub basalt picks and we assumed a constant $V_{rms} = 1850\ m/s$ below this interface. Note the gradual improvement of the flatness of the gathers after applying a more precise velocity field and also the focusing of the traces in the gathers before and after preSTM (panels 2.4a, 2.4b, 2.4c).

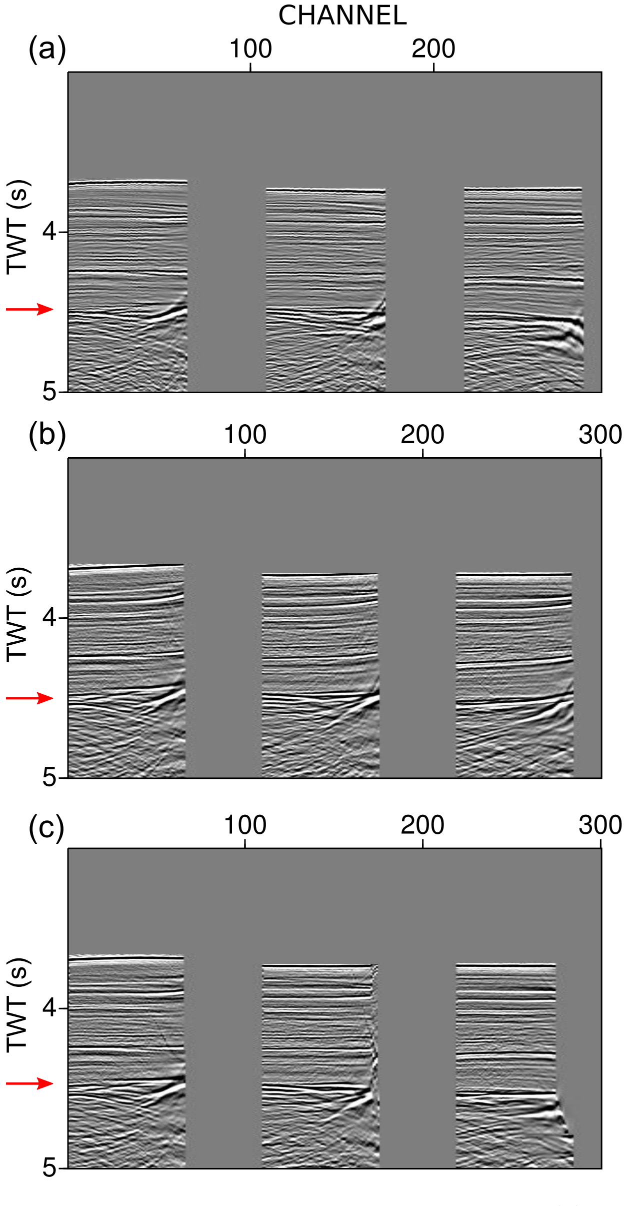

Figure 2.4: Comparison of gathers in different iterations of preSTM. (a) 3 CMPs before preSTM; (b) Same gathers as in (a) but after preSTM and using a different velocity field from (a). The migration partially repositioned the data as they are more focused than in (a) especially in later TWTs. However, the gathers appear overmigrated and will not lead to sharp reflections after stacking; (c) PreSTM gathers same as in (a) after using a more robust velocity field. Note the nearly flat arrivals which after stacking will result into a focused subsurface image. Red arrows indicate top basalt arrivals. All panels are shown with AGC, outer trace mute and sea noise mute.

2.1.1.4 Deterministic inverse filters in the post-stack domain

A different type of noise, recorded during marine seismic reflection data acquisition consists of a localised decrease of the amplitude spectrum, resulting from the destructive interference between upgoing (primary signal) and downgoing signal, after reflection at the sea water - air boundary. This local decrease (notch), hinders the recording of a full broadband amplitude spectrum and compromises the resolution of the final subsurface image. Due to the presence of notches over discrete frequency bands, one related with source (source notch) and the other with receivers (receivers' notch), the usable frequencies are further restricted to a narrower frequency band. These effects can be corrected during a seismic reflection processing flow, a process that is called deghosting.

In a given spectrum, the position of the notches is a function of the source and receiver depth below the sea surface, therefore if their location is known then the position of the notches can be deterministically predicted. In theory, if the reflectivity surface generating the downgoing wave (sea water - air boundary), was nearly flat ($R \approx -0.9$), the notch would be located in a narrow frequency band making its healing more straightforward, by applying an inverse filter at the expected notch frequency. However, the flat surface approximation is simplistic as in most cases the sea surface is rough, resulting in a downgoing wavefield with both coherent and incoherent scattering characteristics (Asgedom et al., 2017). The combination of these effects result in an amplitude spectrum with notches that are not located in their expected frequency position, but appear as a wider decrease of the amplitude spectrum covering a range of frequencies. These misshapen notches can be healed by applying an inverse filter which matches the resulted shape of the notches as appeared in the post-stack average amplitude spectrum.

In general, the deghosting methods can be either acquisition based (Tenghamn et al., 2007), which includes recording of both pressure waves and the vertical component of the particle velocity or processing based techniques (Amundsen, 1993; Katibe, 1999; Amundsen et al., 2016). Complex acquisition systems have been developed to acquire a full broadband spectrum, providing a signal rich both in low and high frequencies (Soubaras and Dowle, 2010; Amundsen et al., 2017).

A robust method to suppress notches that span over a wider frequency band, as appear in the post-stack spectrum, can be achieved by applying deterministic inverse filters having amplitudes which follow a statistical distribution function of negative reflection coefficients that mimic the effect of depth variation caused by a rough sea - surface (for a complete description of this approach see Sargent et al., 2011). The approximation is performed using a Gaussian distribution, with a mean value μ and standard deviation σ being chosen to tailor the shape of the frequency spectrum to that of the observed source / receiver notches. In this way, the previously localised inverse filter (flat sea surface) is spread into a wider range of frequencies to model the scattering effects of the downward recorded wave. In practice, the filters are constructed as the inverse of a time series $(1, 0, ..., r_{-n} ..., r_0, ..., r_n)$, where the time delay of r_0 is found by the inverse of the observed local mimima of the post-stack amplitude spectrum. The amplitudes r_{-n}, r_n are following a Gaussian distribution of negative reflection coefficients (Sargent et al., 2011).

A schematic representation of the application of deterministic filters, for profile S310 - 07, is presented in Figure 2.5. Based on the acquisition information for the source and receivers depths (Table 2.1), several tests were performed using different amplitude ranges and sampling intervals. A stable inverse filter for source notch was calculated with amplitude values of: -0.05, -0.1, -0.15, -0.3, -0.15, -0.1, -0.05 sampled every 0.5 ms (Appendix Table D.3), with central frequency of 105 Hz (Figure 2.5b). The filter was resampled to 2 ms to match the seismic data sampling rate and finally matched with a spike to generate the inverse filter appropriate for application in our stacked data set. Note that the sampling interval is important, so as to efficiently tailor the width of the operator with the average observed shape of the notch. Similarly, a deterministic filter for receiver's notch was constructed using amplitude values of: -0.05, -0.1, -0.15, -0.18, -0.15, -0.1, -0.05 sampled every 0.5 ms (Appendix Table D.3), with central frequency of 74 Hz (Figure 2.5c). To compensate for the energy lost by scattering effect into the incoherent wavefield, the source's and receiver inverse filter coefficients don't add to -1. In this way we avoid a disproportional heal of receiver's notch with respect to the source's notch, an effect that could boost noise in notch frequency and generate illusory reflectivity. The latter approach is totally data dependent and in our example produced stabilized results.

The preSTM stacked profile in panel 2.5a is convolved in time domain with the aforementioned deterministic inverse ghost filters (2.5b, 2.5c), targeting the source and receiver's notch respectively. The output profile in 2.5d has improved the resolution of the reflection events without significantly boosting any high frequency noise content of the signal. The profile is shown after application of a zero phase low cut filter (4 Hz – 18db/octave), thus the result is mainly different only in the mid-high frequency band compared to the input data. Panels 2.5e - 2.5h show the amplitude spectrum from panels 2.5a - 2.5d. In the frequency domain, the convolution operator $*$ is substituted by a scalar multiplication $\times$. The decrease of the spectral amplitude values in panel 2.5e (uncorrected image), after $\approx 70Hz$ is directly related with the presence of source and receiver notch at $\approx 107Hz$ and $\approx 75Hz$ respectively (acquisition parameters, Table 2.1). However, the amplitude spectrum doesn't show any localised notches but instead their detrimental effect is spread over a wide range of frequencies. Hence the need for a tailored inverse filter to efficiently shape the spectrum. The resulting shaped amplitude spectrum after applying the deghosting filters is plotted in 2.5h. Note how the post-stack deterministic filters have effectively boosted the misshaped spectrum in 2.5e, both in mid and in higher frequencies retrieving information that was originally only partially resolved.

Although effective, the application of deterministic filters have the risk of generating strong reverberate noise that could be easily mistaken as real signal (Sargent et al., 2011). Therefore, after notch elimination, a careful comparison between original and deghosted profiles needs to be performed in order to avoid interpreting boosted noise as real reflectivity (see section 5.1).

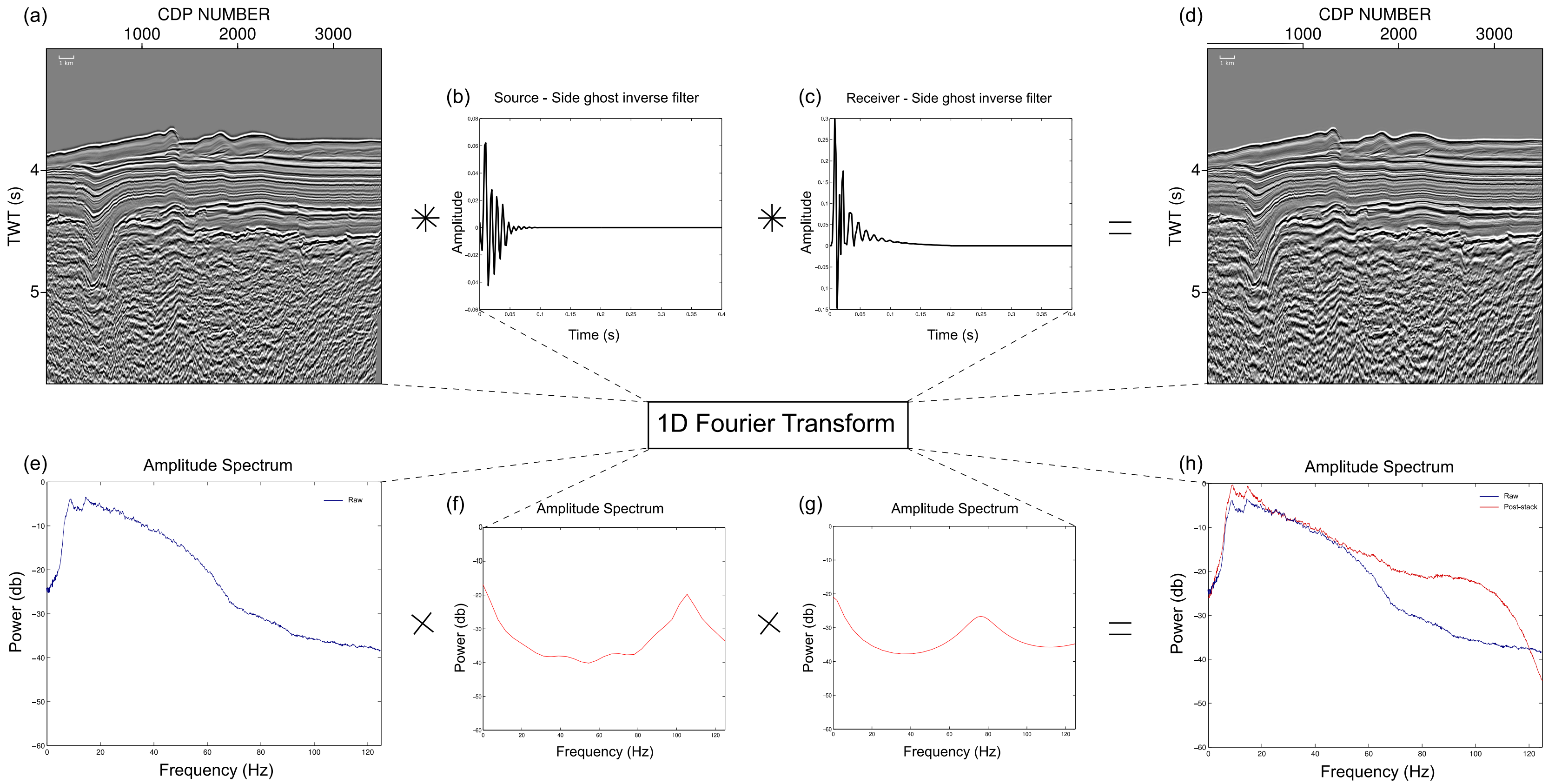

Figure 2.5: post-stack deterministic deghosting process. In (a) the preSTM stacked profile includes ghost effects. The image is convolved in time domain with two independent deterministic filters, (b) and (c), for source and receiver deghosting respectively and produce the deghosted profile in (d). Note that in (d) the image is shown after low cut filter application. In (e)-(h) the amplitude spectra of the images/filters are shown. The convolution process ($*$) in time domain is converted into scalar multiplication ($\times$) in frequency domain after 1D Fourier transform.

2.1.1.5 Time variant filtering and random noise elimination

The presence of the basalt sequence in our area of interest effectively separates the image features of the profile S310-07 into two discrete regions. One high frequency / high reflectivity region above the basalts and one lower frequency / poor reflectivity below them. This means that a generic time invariant filter would fail to delineate correctly both the high and the lower resolution events of the profile. Thus, a time-variant filter (Table 2.2) was applied tailored to optimise the signal spectrum with time.

Simultaneously to the application of time - variant filter, tests where performed to eliminate the random noise content from the final profile. Although not significant in the post - basalt section due to high S/N ratio, random noise elimination can aid to locally clarify shallow, especially, targets and improve the continuity of the reflection events. Techniques such as $f-x$ deconvolution (Canales, 1984) and structural semblance smoothing (Milkereit and Spencer, 1989) were tested for their efficiency and eventually $f-x$ deconvolution was used (filter length = 15 traces, traces of filter per filter selection = 30).

2.1.1.6 Inverse Q

The last processing step applied to the profile was used to compensate for the absorption and dispersion effects during seismic wave propagation which effectively alter the amplitude and phase of the seismic signal. This wave attenuation is described by the dimensionless factor Q (Kjartansson, 1979) where large values indicate less effect of the medium during wave propagation and small values the inverse. A compensation by inverse Q filtering the data was performed using the approach of Wang (2002). Multiple values of Q parameter, and different combinations of compensating both the amplitude and phase of the profile were tested, but the value of $Q = 200$ with phase only correction was eventually applied. Note that the Q factor values cannot be reliably calculated from surface seismic data but a better quantification can be achieved through Vertical Seismic Profile (VSP) data (Wang, 2004) or laboratory measurements, though this introduces issues of how to scale the laboratory frequencies to seismic frequencies.

2.1.1.7 Pre-stack source's & receiver's side deghosting (shot gathers)

As described in section 2.2.1.4 the ghost arrivals can be suppressed in the post-stack domain by creating deterministic inverse filters tailored to match the observed notches, as determined from the average post-stack spectrum. If the original goal of the processing scientist is to deliver a well focused image with optimum resolution (as a function of data quality), this flow can be judged sufficient to create an adequate image. Nonetheless, the flow deghosts only the zero offset approximation of the data and as a result does not contain explicit information for the multiple offset representation of the signal in the pre-stack domain. Contrary to the post-stack data deghosting process, a pre-stack variable offset deghosting filter is also a function of the angle of incidence both for source and receiver ghost arrivals. If applied correctly, deghosting in the pre-stack domain has the following advantages with respect to filtering in the post-stack domain:

- the deghosted CMP gathers can lead to more constrained semblance picks and by inference more robust velocity models, as the velocity analysis using a semblance spectrum is also a function of the temporal frequency of the transformed gathers (Jones, 2010);
- the deghosted CMP gathers can be used for preSDM purposes to obtain an image in depth domain with good spatial resolution and focusing;
- the deghosted CMP gathers can result in more constrained Amplitude Variation with Offset (AVO).

In general, the offset dependent deghosting can involve plane wave decomposition of the signal by transforming into different domains, such as $f - k$ or $f - x$, deconvolving the upgoing from the downgoing signal by a deghosting operator and finally transforming the signal back to t-x domain (Verschuur et al, 1992; Amundsen, 1993; Katibe, 1999). In our case, for the receiver's side ghosts, we used an algorithm in $Claritas^{TM}$ which performs deghosting in the $f - x$ domain and can compensate for variable depth streamer. By using as input the average streamer depth (or information for the recorded streamer depths on a shot basis) and the range of incident angles of the plane waves we can perform a shot by shot directional deghosting.

The approach of receiver deghosting in $f-x$ domain has a number of advantages compared to modelling and applying the operator in $f-k$ domain. Deghosting in $f-k$ domain requires tapering of near and far channels to eliminate edge effects. This means that the notch compensation for these angles/offsets will be incomplete. Furthermore, filtering of the signal in $f - k$ domain into plane-wave incidence angles can lead to potential loss of primary information. To avoid these effects the deghosting is performed in $f - x$ domain. In reality, monochromatic multichannel operators are calculated in plane-wave domain with the range of the plane-wave incident angles (dip range) solved being controlled by the processor. Note that when an average streamer depth is used as input, the deghosting process cannot fully compensate for the possible variability of the streamer depth during the acquisition, which will lead to an incomplete healing of the receiver's notch. During the acquisition of Geoscience Australia seismic data, only the average streamer depth was recorded in the Observer's Log. Therefore, the average streamer depth of 10 m was chosen combined with angles between 0°-90°, which model only a shot with an off end signal.

In order to perform a complete pre-stack notch compensation, a source deghost filter is required. To a first approximation, we can assume that the sea surface is flat and set the reflection coefficient $R_{flat} \approx -0.9$. For our data set, this approach gave suboptimum results (section 2.2.1.9), disproportionally correcting the source notch and decreasing the overall power of the spectrum. Therefore, we opt to apply the same deterministic inverse filter as it was extracted in the post-stack domain. Although this filter is not angle dependent (it was derived using the zero-offset, post-stack assumption), it does incorporate the average variability of the source notch. After application in the shot domain, it produced the most robust results among all the sets of filters tested, having a center frequency (f_{center}) located at the expected source's notch location (section 2.2.1.9).

The above description can be expressed in mathematical terms using ghost functions. A ghost function (G_s, G_r for source and receiver respectively) incorporates the effects of sea surface (shape, scattering), propagation direction of seismic waves and source/receiver depths (Asgedom et al., 2017). For a complete mathematical description of ghost functions see Amundsen, 1993. In frequency - wavenumber ($f-k$) domain, a ghost function can be expressed as

$$G(k_x, k_y, \omega, z) = 1 + R \exp(-2ik_z z) \tag{2.2}$$

where k_z, k_x, wavenumber components in horizontal dimensions, z source or receiver depth, $k_z = \sqrt{k^2 - k_x^2 - k_y^2}$ with $k = \frac{\omega}{c}$, ω angular frequency, c water layer velocity and R the sea surface reflection coefficient. Note that the true ghost function can be exactly estimated when the total wavefield (pressure) and the upgoing wavefield are known, with the latter being derived by the measurement of vertical particle velocity information (Fokkema and van den Berg, 1993). However, for conventional marine acquisition, the total ghost function cannot be derived and we approximate the ghost function by tuning the sea water reflectivity (R), having as a prior information the depths, z, of the receivers. In the simplest case, the sea surface can be considered flat with values $0 \leq R_{flat} \leq -0.9$. As this approximation is frequency and angle invariant, it cannot predict the ghost when significant sea-surface variation is present. The model can be generalised by approximating the sea water reflection coefficient with a Gaussian distribution (Sargent et al., (2011)) assuming that the sea wave height follows a Gaussian distribution (Thorsos, 1988), with equation 2.2 taking the form (equation 2.3)

$$G(k_x, k_y, \omega, z) = 1 + R_{stat}(k_x, k_y, \omega) \exp(-2ik_z z) \tag{2.3}$$

where the reflection coefficient R_{stat} is angle and frequency dependent. This expression represents the pre-stack variable offset ghost function. Following the same notation, if we want to construct an expression suitable to represent the post-stack deterministic deghost filter as described in Sargent et al., (2011), we can reduce equation 2.3 to the following expression (equation 2.4)

$$G(\omega, z) = 1 + R'_{stat}(\omega)\exp(-2ik_z z) \tag{2.4}$$

where R'_{stat} represents the post-stack statistical approximation case. Note that in equation 2.4 the reflection coefficient is only frequency dependent following the zero-offset post-stack assumption. Thus, the operator can compensate for variations in the sea water height surface and for source or receiver geometries that are inadequately determined (Sargent et al., 2011). Note that due to the mechanics of modelling the ghost function with the described statistical approach its phase response at the 90° emerging angle is not stabilized.

Mathematically, equation 2.4 cannot be robustly applied in the pre-stack domain as it doesn't incorporate any angle information. Nevertheless, a stable inverse filter derived post-stack can be applied pre-stack if the angle variability with respect to the offset (angle) is limited. This assumption can be considered valid for deep marine environments as in the profile S310-07. Practically, this means that the filter will be stable for near to mid offsets but its robustness is questionable for the far offset traces and shallow targets (early TWT). So, for 2^{nd} order velocity analysis with isotropic velocity model building, where an outer trace mute is also applied, application of deterministic inverse filter may result in a stable final image with well shaped amplitude spectrum.

In cases where all the available offsets are required (anisotropic velocity model building for time or depth migration), this type of deghosting filter could lead to suboptimum results and possibly high frequency noise in the final image. The latter is partially mitigated by the stacking process which improves the signal to noise ratio proportionally to the number of traces used ($S/N \propto \sqrt{N_{traces}}$), suppressing the non-coherent high frequency noise.

It is pertinent to note, that this trade off between pre-stack deghosting and final output stability is of critical importance where we opt to use the time domain deghosted gathers for pre-stack depth migration (preSDM) applications. In this case, we require deghosted shot gathers that will be migrated, with an optimised $V_{int.}$ field, into well focused and high resolution Common Image Gathers (CIG) (for examples of depth migration with pre-stack deghost filters applications see Chapter 3).

The application of the deterministic filters to the stacked depth migrated CIG's isn't straightforward. As the deghosting filter is in time we need first to scale the depth axis in time domain using a depth to time conversion. This raises a number of issues. The Kirchhoff depth migration process performs mapping of time domain to depth domain, by summing the signal along asymmetric diffraction curves constructed using traveltime maps calculated from ray-tracing techniques. The frequency content of a final preSDM image and its respective amplitude spectrum, incorporates a set of effects that are fundamentally different from time domain imaging such as offset-dependent stretch of wavelet, sensitivity to velocity differences within the layers in the velocity model and resampling of the data (Jones and Fruehn, 2003). The combined effect of these factors plus the depth to time domain mapping of the image, alter the post-stack amplitude spectrum and effectively distort the shape of the expected source/receiver notches. As the deterministic filters are primarily constructed to match the observed amplitude spectrum of post-stack time domain data, any alteration of its shape will analogously affect the output image, producing suboptimum results. Hence the option to pursue the design of post-stack deghosting filters for the PreSDM image was not taken in favour of the simpler route of applying the filters prior to preSDM whilst the data was still in the time domain, which proved to be a more robust approach.

In Figure 2.6, we present an example of the combined effect of receiver notch compensation with application of deterministic inverse deghosting filter for source notch in the pre-stack domain. Figures 2.6a - 2.6c demonstrate the result before and after processing in the shot domain. The operators are combined with noise attenuation in $f-k$ domain to eliminate the strong swell noise (red arrows in 2.6a). Note particularly the linear events in 2.6b, generated as a by - product of the receiver's notch compensation (blue arrows). These linear events were eliminated using a dip filter in $f-k$ domain. Nevertheless, in regions where the signal to noise ratio (S/N) is poor, particularly in near offsets and later TWT, there still remained some residual swell noise which was not completely eliminated (green arrows in 2.6c).

Furthermore, in Figs. 2.6d - 2.6f we present the $f-k$ spectra of 2.6a - 2.6c respectively. Note the progressive compensation of mid to high frequency events after applying the deghosting filters and the targeted elimination of linear noise after applying dip filters. An interesting characteristic that is evident in $f-k$ spectra is the angle dependent lower power band in the notch region associated with the receiver depth (black arrows in Figs. 2.6e, 2.6f), which implies an incomplete healing of this notch due to insufficient depth information. Thus, the inability of the algorithm to track sea water variations is mapped in the $f-k$ spectra as a relevant decrease of the power of the signal. Although this indicates a suboptimum receiver's notch compensation, the combined use of the deghosting filters in the pre-stack domain, produced robust results in terms of retrieving high resolution events, as we will show in the following sections. However, it is expected that having a more detailed depth information on a shot by shot basis, would result in a more complete recovery of the seismic signal.

The shape of the resulted $f-k$ spectra also demonstrate the applicability of deterministic inverse filter for source notch elimination in the pre-stack domain. The apparent stability of the filter in this example, provides a tool for efficient pre-stack ghost compensation, a result which aids cases where the deghosted gathers are part of a pre-stack depth migration (preSDM) loop.

A final by-product of applying pre-stack receiver's notch compensation in our data set, was the elimination of the diffraction events that were locally evident in low (S/N) areas. In Figure 2.7 we present an example of that result, were the diffraction signal is suppressed after deghosting, due to modelling only the off end signal of the data.

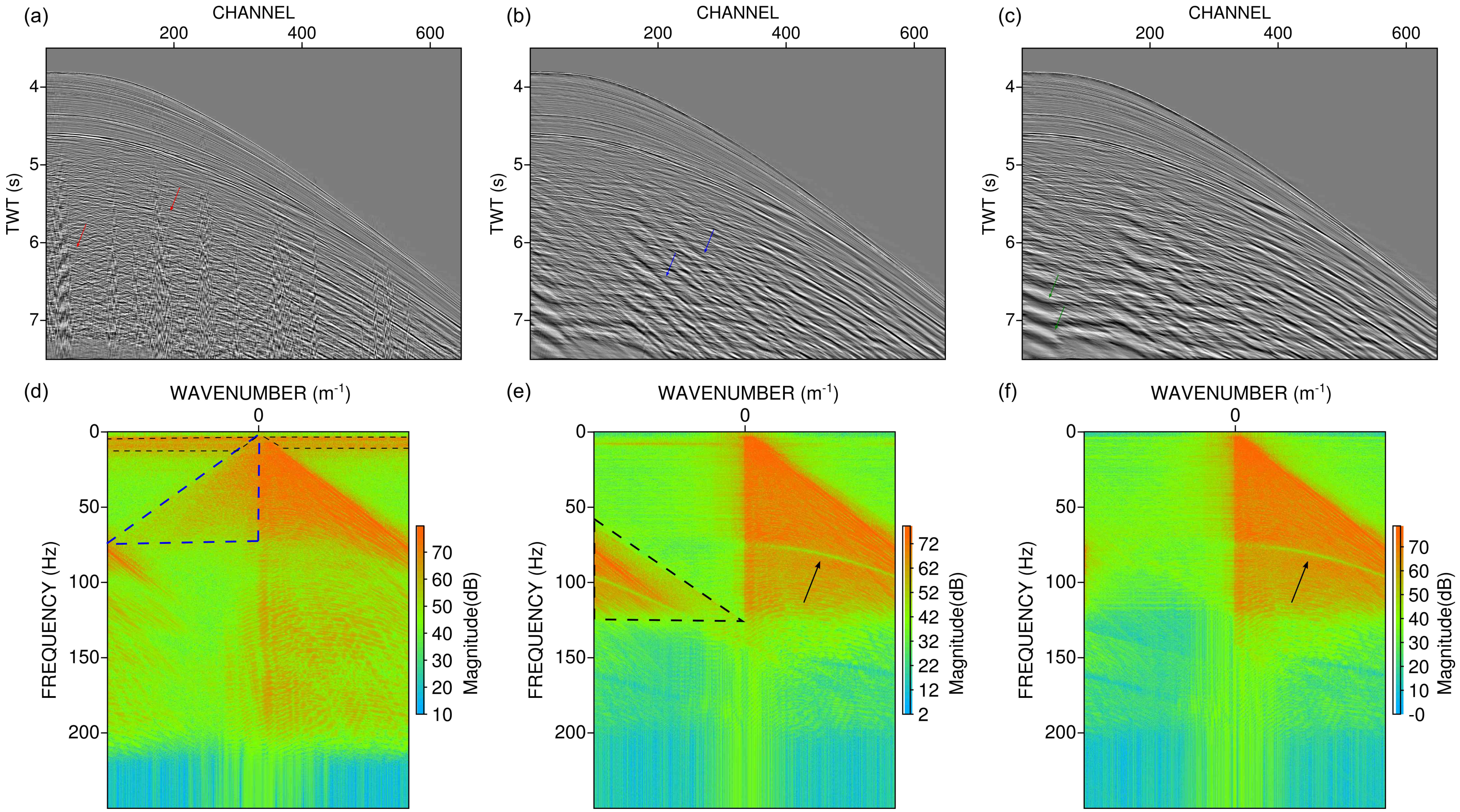

Figure 2.6: Example of a shot gather before and after notch compensation. (a) Gather without swell noise elimination and notch compensation (red arrows show the swell noise content); (b) Same as (a) but after deghost filters application and swell noise using $f-k$ filtering. Note that due to the receiver deghosting operator, apparent linear events incise the gather (blue arrows); (c) Gather after linear event elimination using an $f-k$ filter. For later TWT and near offsets, due to poor S/N the swell noise is unsuccessfully eliminated (green arrows, TWT after 6.5 s); In (d), (e), (f) the $f-k$ spectra of panels (a), (b) and (c) respectively. The obvious decrease in the power of the signal close to expected receiver notch (black arrow) implies an incomplete notch compensation due to insufficient depth information.

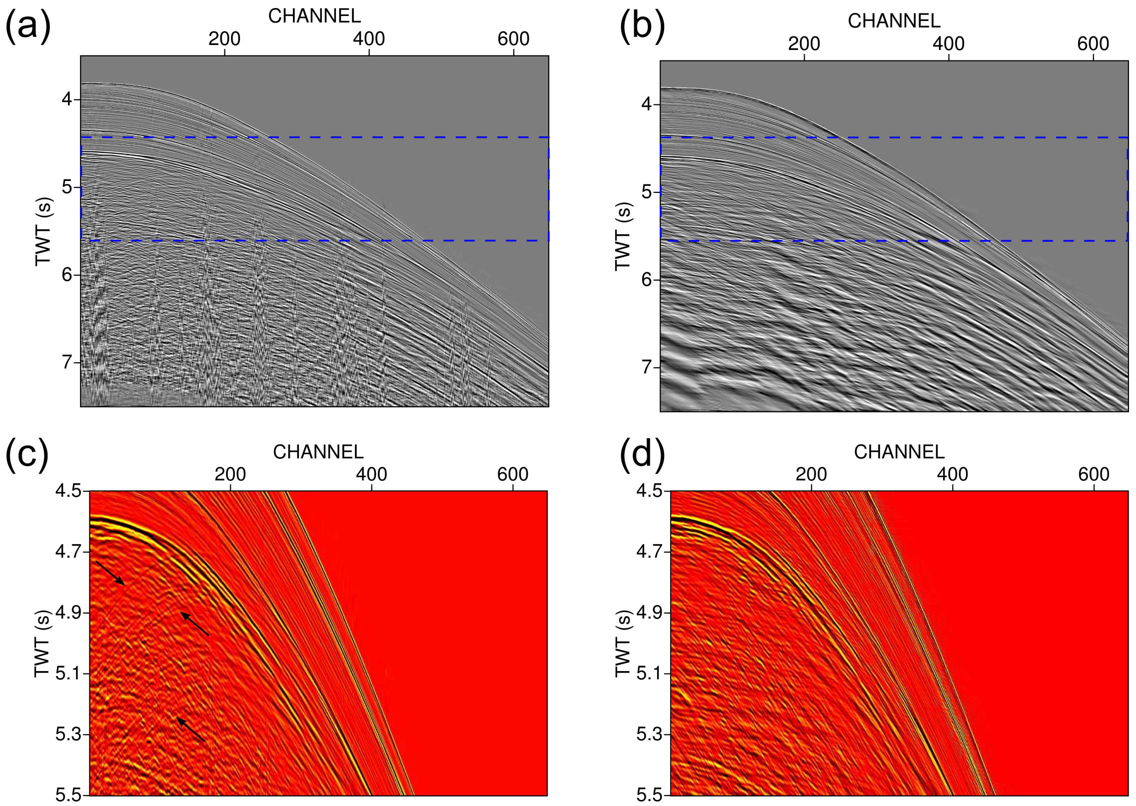

Figure 2.7: Comparison of same shot with and without receiver and source ghosts compensation and $f-k$ filtering. (a) A shot gather before the inverse filter application; (b) Same as in (a) after applying deghosting operators and $f-k$ filtering; (c) A spatially compressed view of the blue rectangle from (a), with the latter being presented in a different color palette to emphasize signal differences. Note the diffractions below the basalt reflection (≈ 4.6 s TWT), that locally interfere with the signal; (d) Same as in (c) after the inverse filters' application. The diffraction noise is visually eliminated due to modelling only the signal which corresponds to dips between 0 and 1 (right side reflections).

2.1.1.8 Comparison of two processing flows

The two approaches of processing seismic reflection data, discussed above, are based primarily on the deghosting filters applied either in pre-stack or in post-stack domain. Each flow, yielded different results in terms of amplitude spectrum shape and image resolution, which can become more apparent in different domains. In the following paragraphs, we will give a number of examples for the most pronounced differences as seen in shot, CMP and stack domains and critically evaluate the effectiveness of the filters.

2.1.1.9 Shot Domain

As the application of pre-stack deghost filters was performed on the shot gathers, comparison of these gathers with different combination of filters can reveal important characteristics of the deghosting process and the effects that this could have on the amplitude spectra of the signal. In Fig. 2.8 we present one shot gather, before (Fig. 2.8a-i) and after the application of 3 different sets of pre-stack filters (Figs. 2.8a-ii, 2.8a-iii, 2.8a-iv). In Fig. 2.8a-ii, the shot has been corrected only for receiver's ghost, whereas in Figs. 2.8a-iii and 2.8a-iv a source's deghosting filter was also applied. Fig. 2.8a-iii was compensated using a modelled source ghost filter incorporated (convolved) originally with the source designature filter as described in section 2.2.1.1 using *Nucleus* package. In Fig. 2.8a-iv, the source ghost was shaped using the deterministic inverse filter estimated post-stack (section 2.2.1.4). Their corresponding amplitude spectra are plotted in Fig. 2.8b with the expected receiver's and source's notches in green and brown arrows respectively.

It is critical to understand at this point, that the shapes of the amplitude spectra as appeared in the shot domain will constructively interfere during the stacking process and produce an average post-stack spectrum with the smooth version of the characteristics evident in the pre-stack domain. In other words, notches or picks in the shot domain amplitude spectra, will become their smooth counterparts post-stack. The amount of difference between the pre- and post-stack amplitude spectra is a function of the variability of notches' position along the profile which is directly linked to the amount of swell (weather conditions) during the acquisition of the data.

In our example, the source and receiver's deghosting, using different sets of filters, produced interesting results. More precisely, from the comparison of amplitude spectra it is evident that the combination of the receiver's notch compensation in conjuction with the deterministic source inverse filter (Fig. 2.8a-iv, green color) gave a boosted amplitude spectrum, that clarifies the shallowest parts of the signal. On the contrary, the combined use of receiver's notch compensation with the modelled source inverse filter, produced a nearly flat spectrum until ≈ 75 Hz but for higher frequencies, the spectrum appears uneven, with a low amplitude region until 100 Hz and boosted region beyond that limit. The latter result indicates that the harmonic waves of 100 Hz - 115 Hz will be disproportionally boosted in every shot gather resulting in a high frequency 'ringing' effect in the parts of the signal with good S/N ratio. Simultaneously, the uneven compensation between the range 75 Hz - 100 Hz, creates a smeared appearance of the reflection arrivals, an effect that leads to less sharp events in the final seismic profile. Note that the 'ringing' is attributed to the application of an inverse operator with a sharp phase change at the notch positions, changes that are different from the expected phase of the true ghost function (Asgedom et al., 2017).

An interesting effect of receiver's notch compensation combined with deterministic source inverse filter is evident in the mid to high frequencies of its spectrum (green curve, green box). Although the filters results in a signal compensation, the amplitude spectrum curve shows a decrease at ≈ 80 Hz and then becomes again flat at a different amplitude level until the highest frequencies of the spectrum. The position of that decrease coincides with the expected receiver notch position (green arrow). This indicates that the notch isn't totally eliminated and a better combination of filters could potentially produce better results.

As we will show later (section 2.2.1.11), this incomplete notch compensation generates a remnant notch in the stack profile, compromising a limited frequency window of the signal. However, for delineating the subsurface targets of interest, this spectrum is considered optimum, taking into account both the results using other filters and the approximate solution based on the poorly constrained receiver's depth information. Still, it is evident that the source's inverse filter derived from the post-stack average spectrum produces the most robust results in terms of amplitude shaping and stability of the signal.

As we mentioned above, the stability of deterministically derived filters like these, is a function of the notch variability along the profile and must be tailored accordingly to every data set. In reality, it is unclear if a similar type of approach could work in data sets with more variable notches, as in that case their inverse filters derived post stack may not be representative of the variable notches within the shot gathers and the application could result either in serious 'ringing' effects or decrease of the amplitude level at mid - range frequencies.

The results from the processing of this profile, demonstrate a robust example of the applicability of the deterministically derived post stack filters in the pre-stack domain, an approach that partially departs from that of Sargent et al., (2011), where deterministic deghost filters were tested only post-stack. Our approach can be considered as a tool to improve resolution in data sets with notches that are not perfectly localised (need of a bell - shaped inverse filter), but simultaneously have a level of variability that allows stabilized results in the pre-stack domain.

2.1.1.10 CMP Domain & Velocity analysis

The pre-stack source and receiver ghost compensations have dual benefits on the CMP and by inference semblance spectrum domains used for velocity analysis. In Fig. 2.9 a CMP gather is presented before (Fig. 2.9a) and after (Fig. 2.9c) the application of deghosting filters with their semblance spectra shown, at Figs. 2.9b, 2.9d, respectively. The gather is plotted after the designature step and without swell - noise attenuation. Firstly, as the boost of the higher frequencies is translated into sharper and more well defined reflections, the shallower part of the gather (seabed until 4.2 s TWT), produces well defined maxima in the semblance space and as a result in more constrained $t_0 - V_{rms}$ picked pairs (compare the black dashed trends in Figs. 2.9b and 2.9d). The latter process, can lead to a more precise velocity model building and robust results in the shallowest parts of the profile. Secondly, the use of deghosting filters can boost the lower and mid band frequency content (for comparison of amplitude spectra see Fig. 2.8b). This effect can result in a increase of the semblance value in regions where, originally, the values were significantly lower (red dashed circles in Fig. 2.9d). Although, below our region of interest, the amplitude increase of the lower frequency content could locally provide more reliable picked velocities and aid in intra - basalt / sub - basalt imaging.

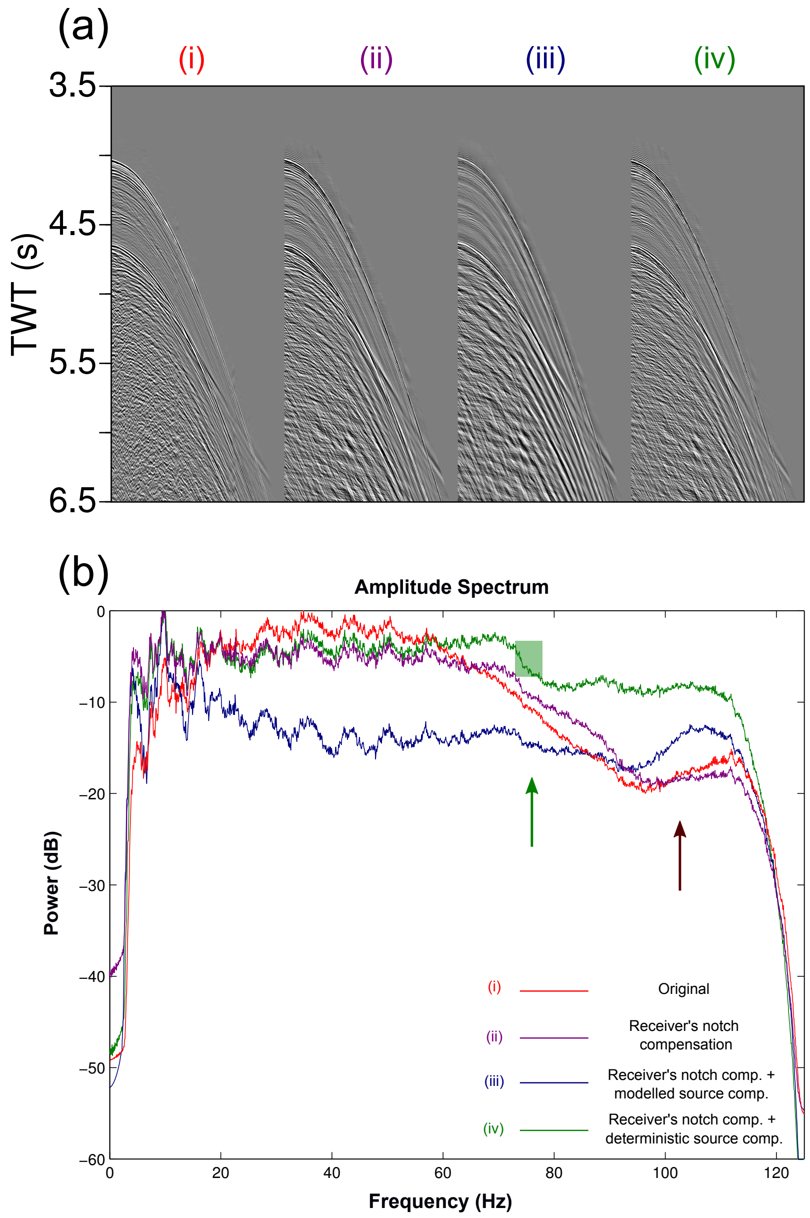

Figure 2.8: Application of different inverse filters in shot domain. (a) (i) a shot gather without any ghost compensation; (ii), with receiver's only notch compensation; (iii) with receiver's notch compensation and modelled source compensation; (iv) with receiver's plus deterministic source ghosts compensation; (b) The corresponding amplitude spectra from the set of shots of (a). The colors are the same with each shot annotation in (a). The most pronounced amplitude compensation is generated after shaping the spectrum with the combination of deterministic source and automatic receiver deghosting (case (iv), green curve). However, due to imprecise depth information, the receiver's notch is not perfectly eliminated, introducing an amplitude decrease (green area), which after constructively stacking the signal will result to an apparent remnant notch.

Although out of the scope of this example, it is worth noting that the improved definition of the reflection events after ghost compensation, can result in better localised events in the Radon space. Indeed, in Fig. 2.10 we test this claim with the same CMP gather as in Fig. 2.9. The gathers in Figs. 2.10a and 2.10c are transformed in the Radon space (panels 2.10b, 2.10d), with parameters $P_{min} = -100$ (minimum moveout in ms), $P_{max} = 500$ (maximum moveout in ms), at 6.5 Km offset and $dp = 5$ (moveout increment in ms). Although subtle, the local maxima / minima in the radon space (2.10d) are more localized and less smeared than those from 2.10c, an effect that could be important during the demultiple process using the Parabolic Radon Transform, providing a a more robust separation between primary and multiple in the transformed domain.

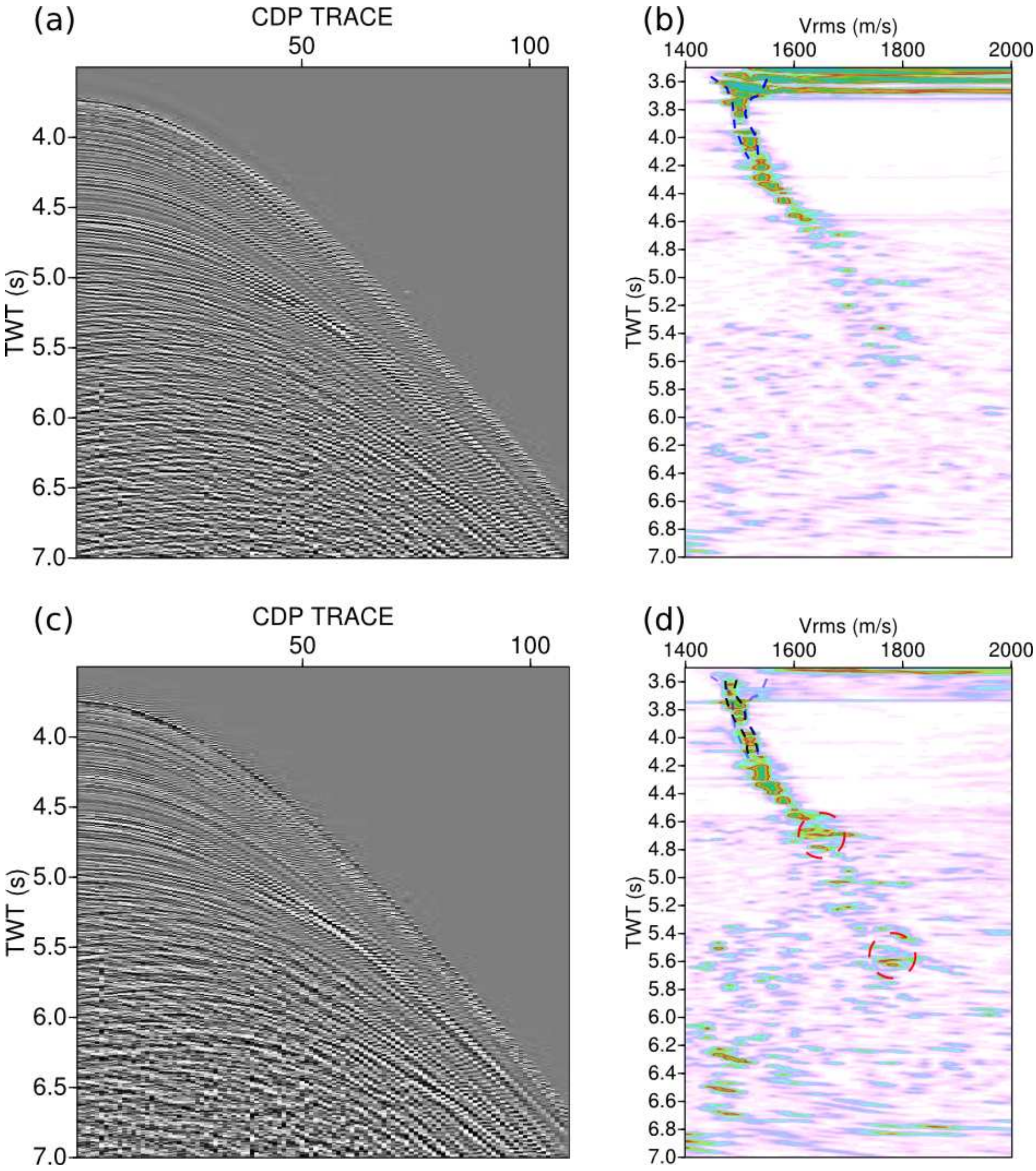

Figure 2.9: Effect of pre-stack deghosting on the velocity analysis using semblance. (a) a CMP gather, after source's de-signature; (b) Semblance spectrum derived from panel (a). The blue dashed trends show the range of possible values for $T_0 - V_{rms}$ picks (shallow arrivals) based purely on the semblance values; (c) Same as in (a), but with compensation for source and receiver notches; (d) Semblance spectrum derived from panel (c). The improved resolution of the signal is mapped onto sharper semblance values, especially in the shallowest areas (TWT $\leq$ 4.2 s - black dashed trends comparison in (b) and (d)). This can lead to a better constrained $T_0 - V_{rms}$ pairs. The pre-stack inverse filters also result in improved low frequency content that allows more confident picking of the velocity model at later time (relative value increase at $\approx$ 4.7 s, $\approx$ 5.6 s (red dashed circles in (d)).

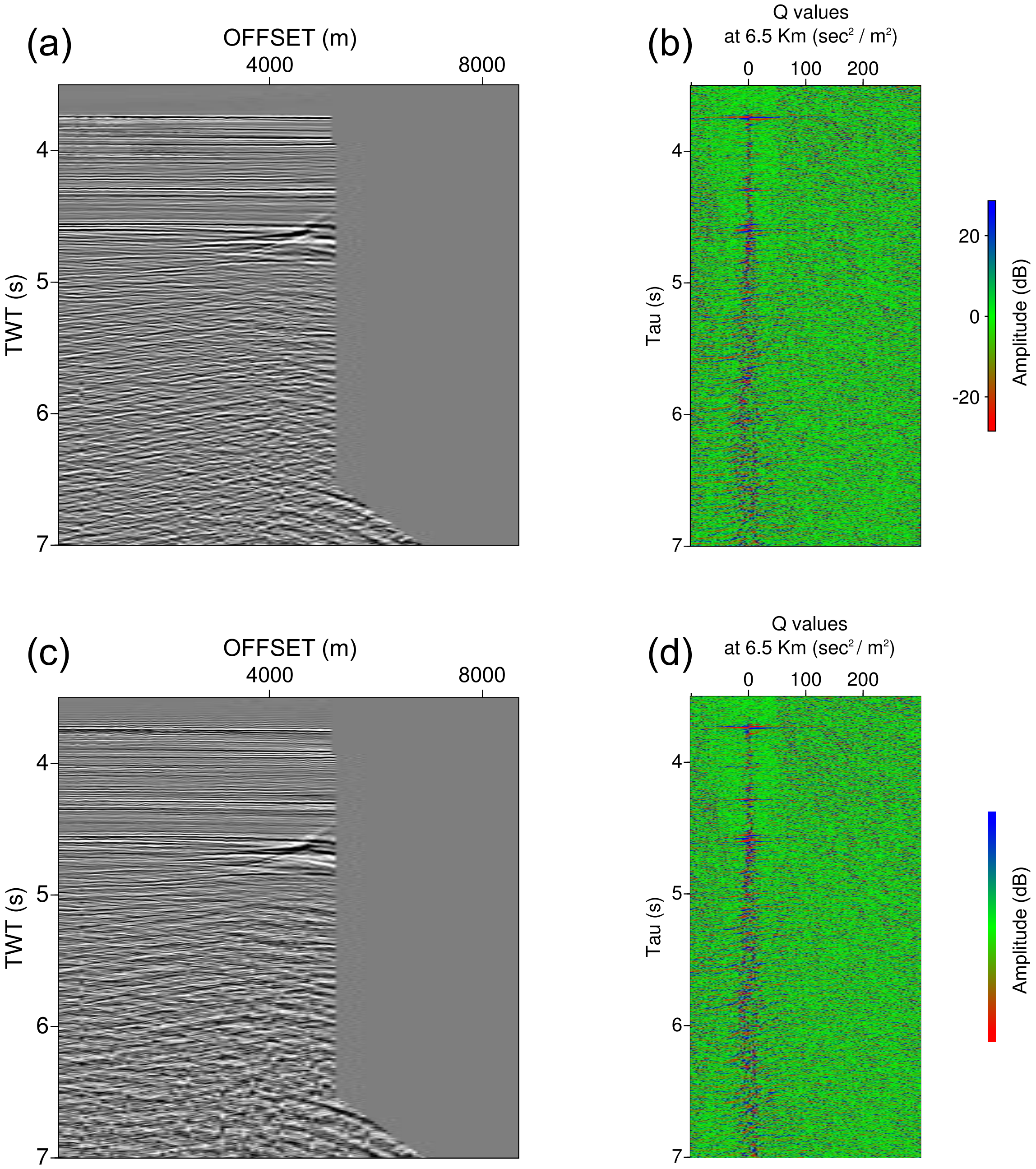

Figure 2.10: Effect of pre-stack deghosting in Radon space. (a) CMP gather same as in Fig. 2.9a but after NMO correction and outer trace mute; (b) Parabolic Radon transform of gather in (a); (c) Same as in Fig. 2.9c; (d) Same as in (b), using input data from (c). The improved resolution of the gather is mapped onto more constrained and less smeared local maxima/minima values, especially for the region associated with sub - basalt reflectivity (> 4.6 s TWT). This can potentially aid to an easier separation between primary and multiple signals.

2.1.1.11 Stack domain

The improved resolution achieved after using the pre-stack filters is apparent in the post-stack domain. Figure 2.11 compares the preSTM image before the application of the deghosting filters (2.11a) with the deghosted, from pre-stack domain, profile (2.11c). The improvement in temporal resolution is evident in the zoom Figs. 2.11b, 2.11d, which show the differences in the shallow sedimentary sequence where the local decrease of the wavelet period leads to sharper imaging of seismic boundaries (overlaid white CDP trace in 2.11d). A notable difference is the event at $\approx 4.03s$ TWT (dark arrows and yellow boxes in 2.11c, 2.11d), which can be tracked across the whole image.

An extra comparison test for the validity of pre-stack operators is shown in Fig. 2.12. Fig. 2.12a plots the processed profile S310-07 after pre-stack notch compensation. The two zoomed Figs. 2.12b and 2.12c show the region close to the proposed location for processing flows 2 and 1 respectively (Table 2.2). Some differences are apparent both in shallow and in deeper sedimentary sequences (red arrows and red curly bracket in Fig. 2.12c).

The retrieved temporal resolution shown in the images is also mapped in their relevant amplitude spectra as shown in Fig. 2.12d. The raw preSTM profile amplitude spectrum (blue colour) is corrected after application of the post-stack inverse filters (red curve) but further improved after compensation in the pre-stack domain (green curve). In accordance with results from Figure 2.8b, the green curve includes a partially healed notch, due to incomplete receiver depth information. However, both post-stack and pre-stack compensations appear to have successfully imaged the shallow sedimentary sequences which was the objective of the exercise.

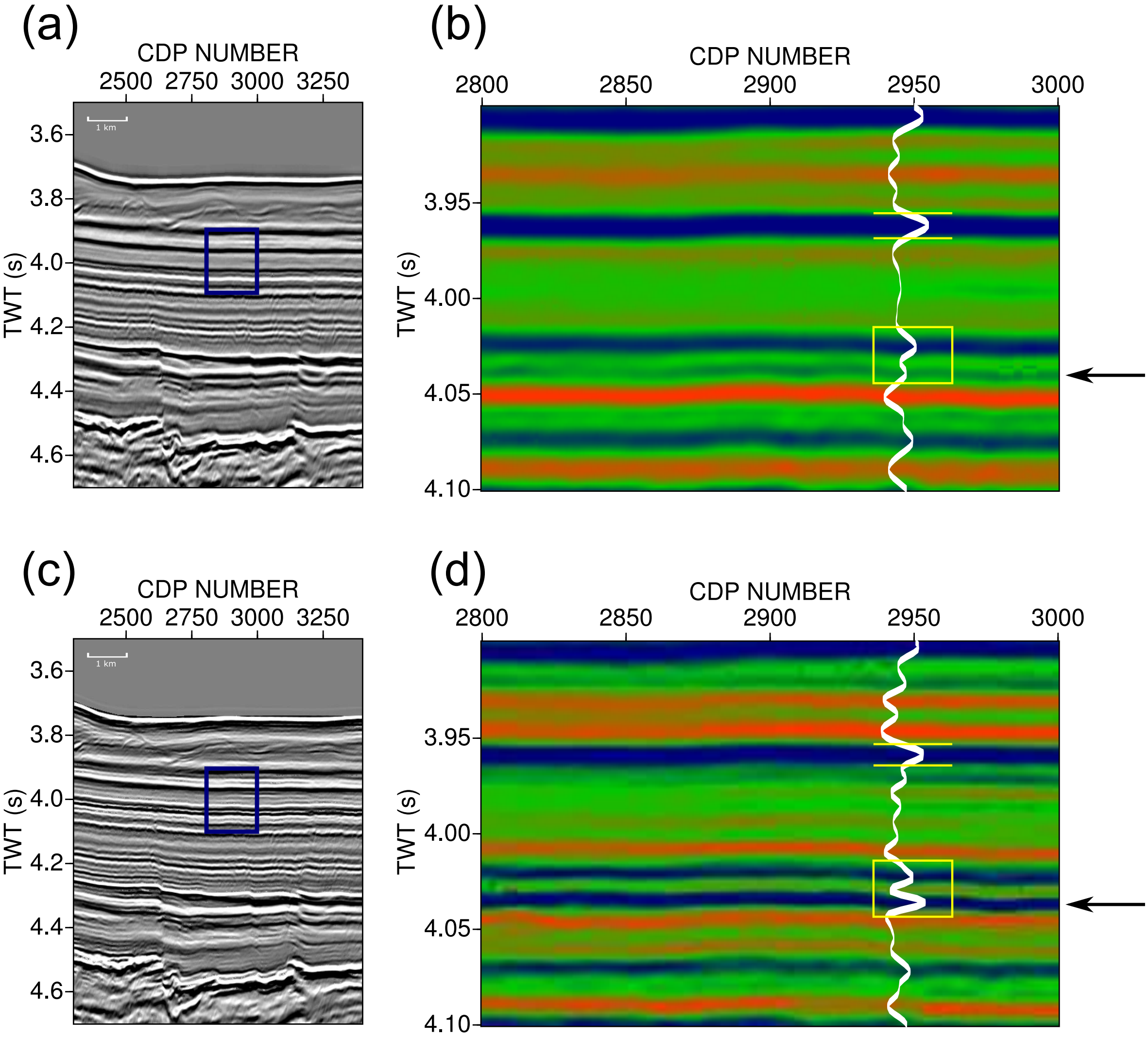

Figure 2.11: Comparison of preSTM images with ghosts and after ghost suppression in the pre-stack domain. (a) Segment of the preSTM profile; (b) A horizontally exaggerated version of the blue box in (a). The superimposed white curve represents the seismic trace extracted from CDP number 2950 (with a higher gain). Though the focusing of the events is considered optimum, the resolution is compromised by the source and receiver notches; (c) Same segment as in (a) but with notch compensation in the pre-stack domain; (d) Zoomed version of blue box in (c) with CDP trace 2950 superimposed. Note the retrieved events compared to (b), with the most pronounced differences manifested as a local decrease of the wavelet period (regions between two yellow lines in (b),(d)) and boost of the amplitude in regions where were originally poorly resolved (black arrows and yellow box in (b),(d) respectively).

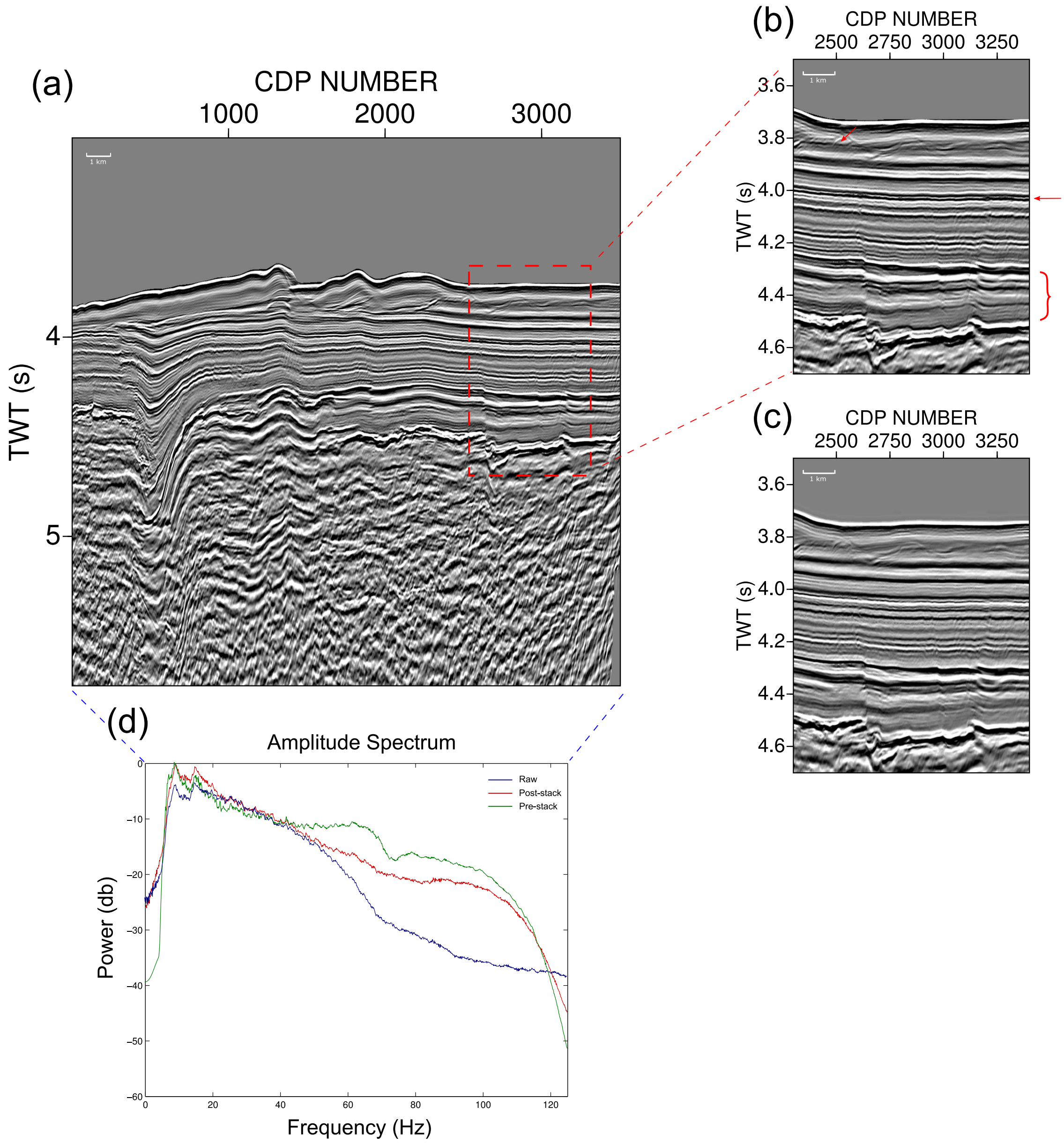

Figure 2.12: Comparison of preSTM images with application of pre- and post-stack deghosting filters. (a) preSTM profile with ghost compensation in the pre-stack domain; (b) A zoomed panel of (a) from the region close to proposed site location; (c) Same as in (b) extracted from the preSTM profile using post-stack deterministic filters. Some differences between (b) and (c) are apparent in the shallowest parts (red arrows) and in the deeper sedimentary sequences (red curly bracket); (d) The post-stack amplitude spectra of the profiles without any ghost compensation (blue curve), with post-stack compensation (red) and with compensation in the pre-stack domain (green). The green curve contains a remnant notch due to incomplete ghost compensation (green shaded box), but the overall amplitude spectrum is comparable to the post-stack application of filters.

2.1.1.12 Anisotropic preSTM

The previous processing flows are aimed to produce focused final images (time domain) using a geologically plausible velocity model. These two goals were achieved by applying a modelled source designature filter combined with deterministic inverse filters applied pre- or post-stack and constraining the velocity field through an iterative isotropic preSTM loop. The latter process yielded nearly flat CIGs that were then stacked to produce a final subsurface image. The isotropic time migration was the tool to reposition the data to their original subsurface location and it was chosen for the following reasons:

- practical time constraints of the project. Building and testing an anisotropic velocity model for each profile would result in a considerable delay of the delivery of final stack images;
- the statistical algorithm used in this project isn't coded to provide uncertainty estimations for anisotropic parameters (η, ϵ, δ);
- Constraining the anisotropic parameters in a statistical model is not straightforward without an independent information from well logs.

The last reason is probably the most understated of all three. As all the processing of seismic data is performed in a pre-drilling period, without any available information concerning the true velocity of the media and incomplete data about depths to drilling targets, following an anisotropic approach in time domain poses serious issues about the validity of the velocity estimations. In cases where the final velocity model serves only as a tool to deliver the most focused subsurface image, the 4th order NMO correction using η parameter may be the optimum path to follow. If the anisotropic approach in time domain is to be used for anisotropic pre-stack depth migration (preSDM) with the inclusion of Thomsen's ϵ and δ parameters (Thomsen, 1986), then some constraint on these parameters is required which ultimately requires well-logs.

Well log information enables calibration of the subsurface targets. Firstly, it provides a high frequency representation of the true velocity of the medium (instantaneous velocity, $V_{instant.}$) which can be transformed into its lower frequency surface seismic counterpart, $V_{int.}$, for migration. Secondly, the ratio between isotropically retrieved depths and depth information of the geological boundaries from well logs can be used as an estimation of δ, a parameter that cannot be physically calculated from surface seismic data. Therefore, it is clear that without incorporating independent data from well logs into our processing sequence, the estimation of anisotropic parameters is imprecise and could lead to serious pitfalls in terms of velocity estimation (for a detailed description of the pitfalls associated with the anisotropic parameters and statistical model see section 5.3).

Taking into consideration the above limitations, an anisotropic preSTM was performed in this profile, aiming to primarily depict the difference in the stacking power of anisotropic approach but does not imply an improved precision of the velocity model retrieved. For the following figures, the anisotropic results were generated using $\eta = 0.04$. In Figure 2.13 we show the comparison between isotropic/anisotropic migration results combined with either pre- or post-stack deterministic filters, in the region adjacent to the proposed site location. The anisotropic profiles in 2.13d-2.13f appear more focused and sharp, and provide the best resolved images of the sedimentary sequence. A significant difference between the isotropic and anisotropic images is the delineation of the thin horizon at around 4.0 s TWT. In 2.13a, this horizon was practically unresolved hindering the interpretation of this event, but after the application of inverse filters (panels 2.13b, 2.13c) and especially using an anisotropic algorithm for preSTM in 2.13d-2.13f the stacking power was greatly improved rendering the event completely resolved. Note that the 4^{th} NMO correction in the CMP gathers was combined with an outer trace mute that is different compared to the isotropic case, in order to accommodate a larger number of active traces, but still minimising the post - critical reflected content of the signal.

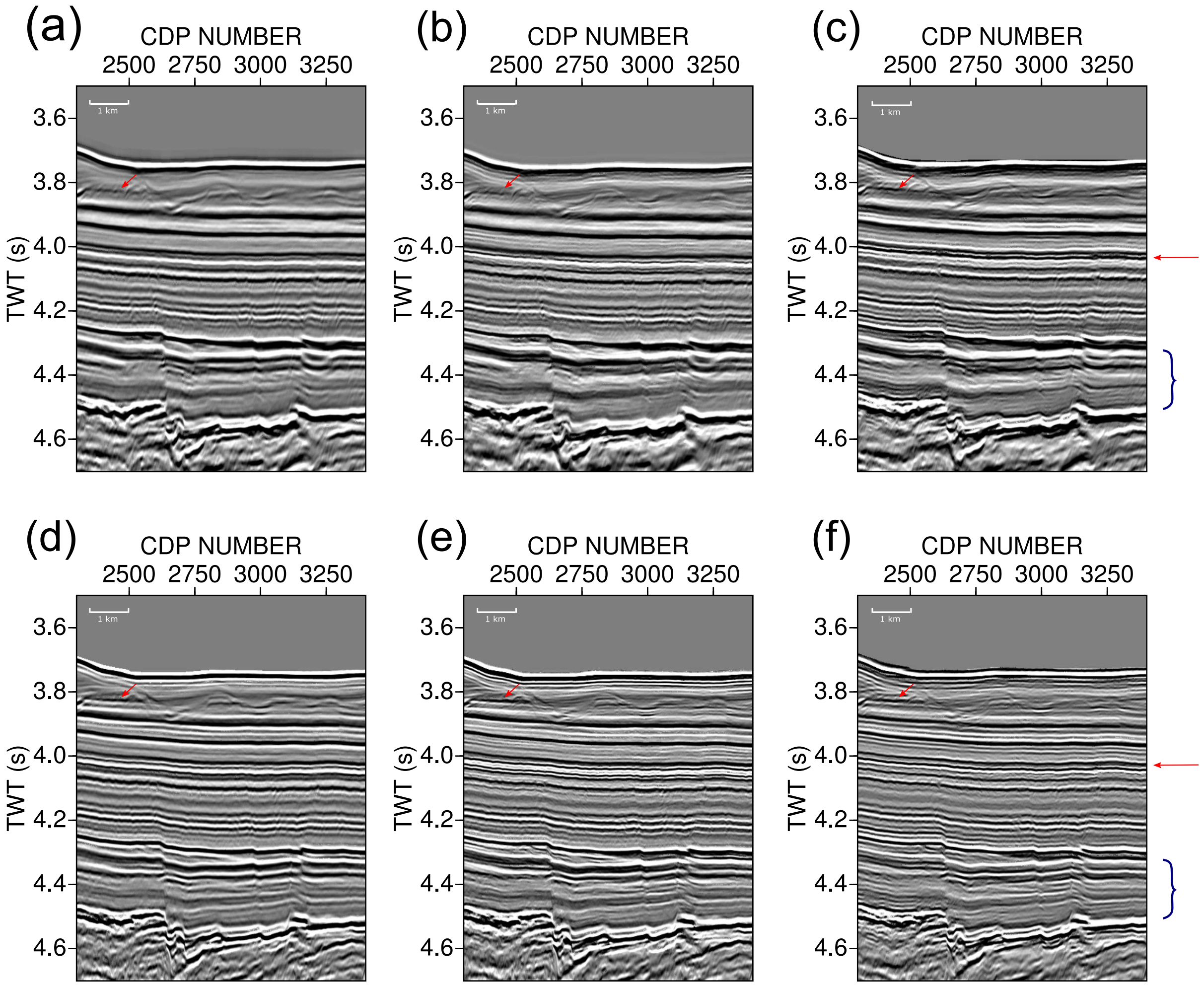

Figure 2.13: Synoptical results from all possible processing flows. (a) Isotropic preSTM image including ghosts; (b) Same as in (a) with post-stack deghosting; (c) Same as in (a) with pre-stack deghosting; (d) Anisotropic preSTM image including ghosts; (e) Same as in (d) with post-stack deghosting; (f) Same as in (d) with pre-stack deghosting. With arrows and curly brackets some differences are shown. Notable difference can be considered the thin horizon at around 4.0 s TWT (red horizontal arrow), which originally in (a) is nearly unresolved and progressively from (b) to (f) is completely delineated.

2.2 Proposed site MBAS-8

The processing sequence of lines intersecting site MBAS-8 (Figure 1.1), S310-01 and S310-17 respectively, includes the same steps as in section 2.1 (Tables D.1, D.2, Appendix D). Therefore in the following, only the final images of profile S310-01 generated from each processing flow will be shown. For results of profile S310-17 see Appendix E.

2.2.1 Time domain processing of line S310-01

In Fig. 2.14, we present the resulted preSTM images following the processing flow 1 (Table D.2). Fig. 2.14a shows the result without any ghost compensation whereas Fig. 2.14b shows the same preSTM image after the application of deterministic post-stack inverse filters. The streamer depth during the acquisition of line S310-01 was deeper than the depth for line S310-07 (Nominal streamer depth = 12 m, Table 2.1), therefore the receiver's ghost inverse filter was tailored to eliminate its produced notch. The deghosting filters applied to the data set are the following (Appendix Table D.3)

- source's side filter: $A_{source} = -0.7$ centered at a frequency $f_{center} = 94Hz$;
- receiver's side filter: $A_{rec.} = -0.05, -0.08, -0., 1-0.2, -0.1, -0.08, -0.05$ centered at frequency $f_{center} = 64Hz$.

In the zoomed panels 2.14c - 2.14f, several channels features from the shallowest part of the line and top basalts - intra/sub basalts areas are presented, with the deghosted result showing retrieved high resolution events with a simultaneous increase of the power in the low frequency band, mapped in the image as better continuation of intra/sub basalt events. Similarly, in Fig. 2.15 a comparison between results from processing flows 1 and 2 (Table D.2) is depicted, with the produced images being comparable, where the pre-stack deghosting result appears more stable at the early TWTs whereas the post-stack deterministic filter result appears richer in low frequency content due to the tailored notch compensation.

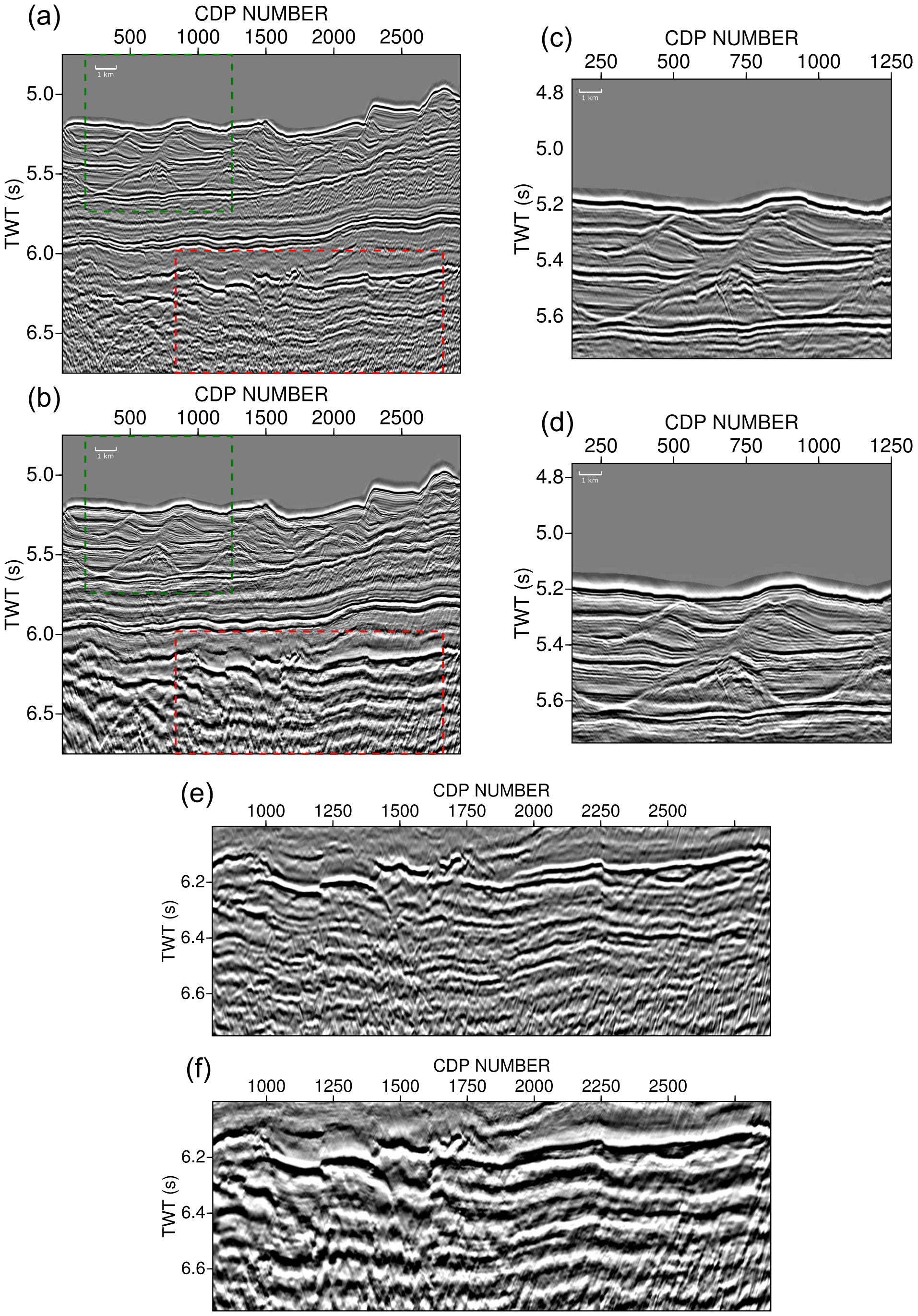

Figure 2.14: Comparison of seismic profiles before and after post-stack deghosting. (a) preSTM result including ghost arrivals; (b) Same as (a) but with amplitude shaping in the post-stack domain; (c) Zoomed version of the complex shallow channel system from profile (a). The window is defined by the green dashed box in (a); (d) Same version as in (c) taken from profile (b); (e) Zoomed version of the basalts - intra/sub basalts region taken from profile (a). The window is defined by the red dashed box in (a); (f) Same version as in (e) taken from profile (b). Note again the dual effect of the deghosting operators, with the simultaneous retrieve of high resolution shallow events and compensation of lower frequency intra / sub basalts events.

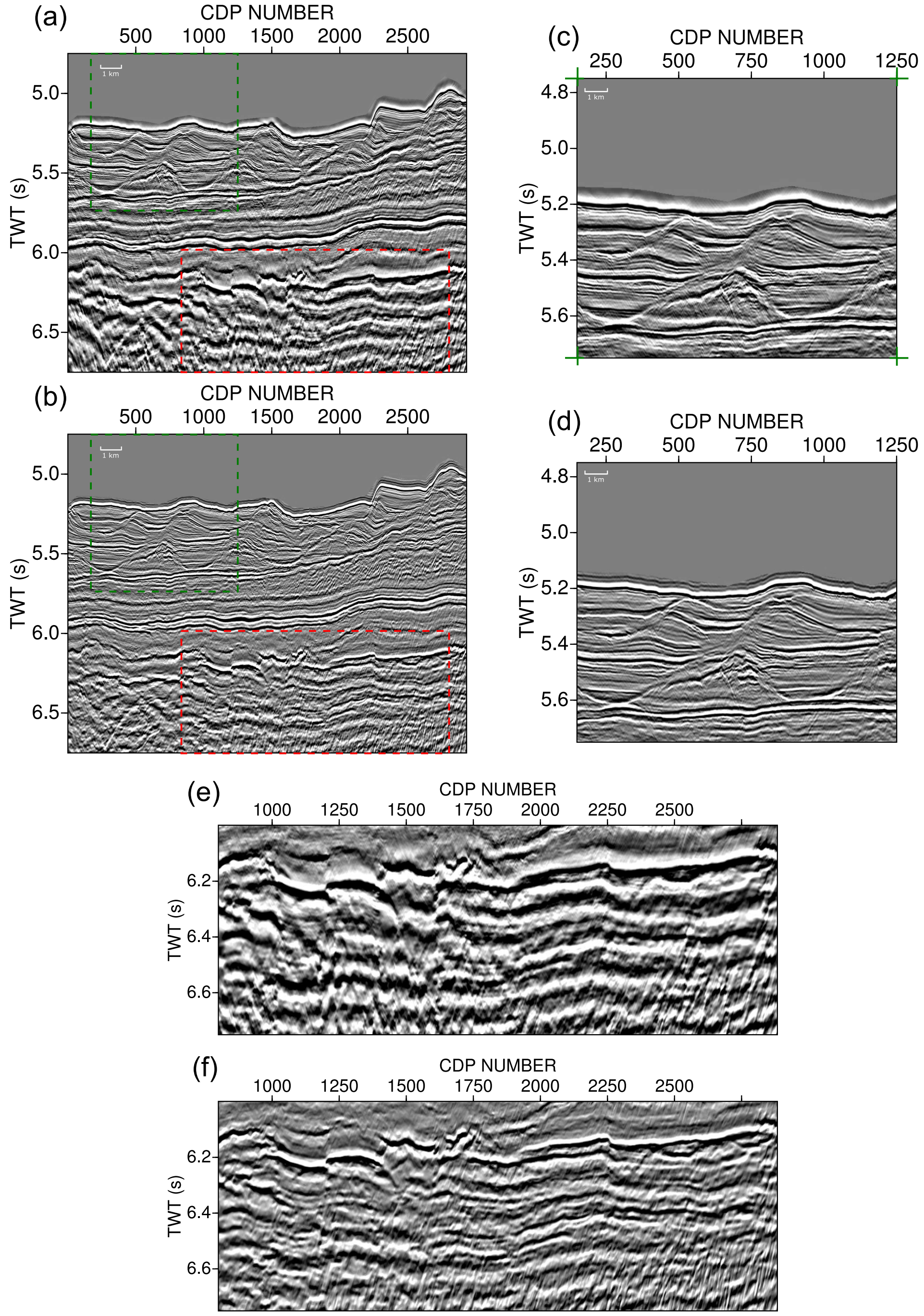

Figure 2.15: Comparison of seismic profiles after pre-stack / post-stack deghosting. (a) preSTM result after post-stack deghosting; (b) Same as (a) but with amplitude shaping in the pre-stack domain; (c) Zoomed version of the complex shallow channel system from profile (a). The window is defined by the green dashed box in (a); (d) Same version as in (c) taken from profile (b); (e) Zoomed version of the basalts - intra/sub basalts region taken from profile (a). The window is defined by the red dashed box in (a); (f) Same version as in (e) taken from profile (b). Differences are apparent due to better low frequency compensation using the post-stack deterministic filters.

Furthermore, in Figure 2.16 we present an example of anisotropic migration before and after deghosting in the post-stack domain. Differences between panels 2.16a and 2.16b are located in both shallow and deeper structures mapping the broadband nature of the compensation. The most notable difference is depicted in the zoomed panels (blue dashed rectangles area), where an originally poorly resolved event is retrieved due to low frequency boost. Note that, as in profiles S310-07/S310-17, the use of anisotropic migration serves both as a stacking/focusing tool and a velocity model building tool. In panel 2.16c, we show a comparative diagram of the amplitude spectra extracted from the stacked profiles, for all combinations of isotropic/anisotropic migration and pre/post stack deghosting. The curves are colour coded for every combination. Note the progressive healing of the receiver notch for same migration algorithm and different type of filters (brown, green, blue curves for isotropic case, orange, yellow, red for anisotropic case). Similar to previously described profiles, in the pre-stack compensation case, a remnant receiver notch is still evident as the algorithm cannot track the local variability of the streamer depth in a shot by shot basis without an explicit information of the exact receivers depths. On the contrary, for isotropic case the application of the post-stack deterministic filters successfully shaped the source/receiver notches (green curve), as they compensate for the average variability of the streamer depth.

The diagram also depicts the increased S/N due to the extra number of available traces in an image gather for stack, with all the curves related to anisotropic migration showing a considerably boosted amplitude spectrum. Note how the partially healed notch after pre-stack deghosting (blue curve) can be transformed into a nearly healed notch in the anisotropic case (red curve). In a similar manner, the curves extracted from post-stack deghosted profiles (green for isotropic, yellow for anisotropic case) show an extra compensation localised in the frequency bands of the two notches. Based purely on the spectra shape, the post-stack notch compensation combined with an anisotropic preSTM (yellow curve) healed the receiver notch and generated, compared to alternative options, the flattest amplitude spectrum.

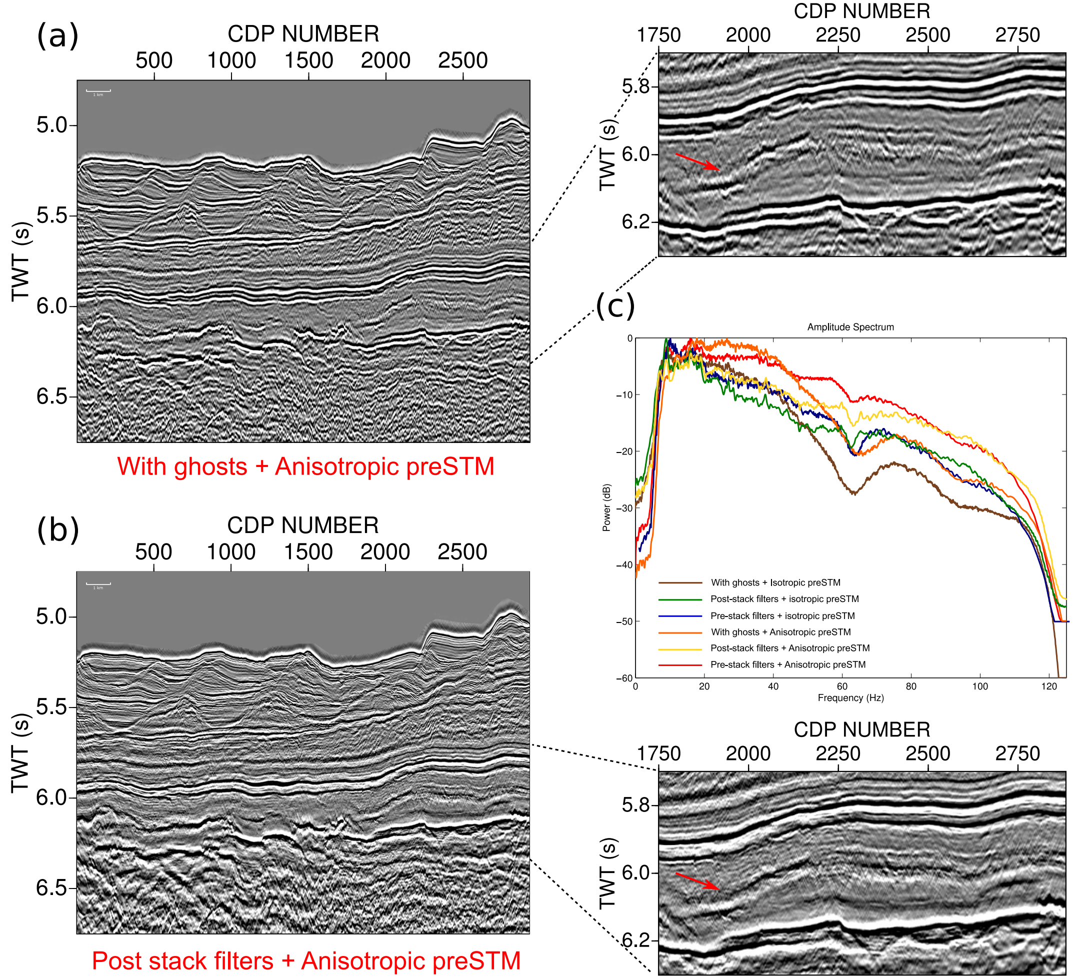

Figure 2.16: Anisotropic preSTM and notch compensation. (a) Anisotropic preSTM including ghost arrivals; (b) Anisotropic preSTM with notch compensation post-stack. The result can be considered optimum for a time domain representation of the subsurface, with the extra frequency content delineating the shallow channels features and the anisotropic algorithm providing extra focusing to the events; (c) Comparative diagram showing amplitude spectra extracted from the profiles for all combinations of isotropic/anisotropic migration and pre/post stack deghosting. Note the difference in notch compensation between different migrations and between isotropic/anisotropic pre-stack curves. The combination of anisotropic migration with post-stack deghosting produced the best shaped amplitude spectrum with nearly healed receiver notch. The zoomed panels (blue dashed rectangles) show the considerable difference in the resolution after applying the filters. Notably, the retrieved low frequency event right above the top basalts reflection (red arrows).

2.2.2 Ambiguity of deghosting operators

The previous examples and results of the application of deghosting operators in post-stack domain, demonstrate that the images have a higher resolution compared to their raw (ghost arrivals included) counterparts, which provides better constraints on the interpreted horizons of interest. However, in the case of acquisition during rough sea surface conditions, which result in a wider observed ghost notches, the uniqueness of the deghosting filters is in question, as a number of slightly different operators can produce a stable image with equally well retrieved high resolution events. The ambiguity of the operators is depicted in the following example.

In Fig 2.17 a number of zoomed panels from the shallow channel features of profile S310-01 are presented. Each panel has been deghosted using a different set of deghosting filters. All five filters used ($f_a - f_e$) have center frequencies (f_{center}) similar with the operators described in section 2.2.1, and are modelled using the following parameters:

(a) $f_a : A_{1_{rec.}} = -0.7$, $A_{1_{source}} = -0.4$ (Fig. 2.17a);

(b) $f_b : A_{2_{rec.}} = -0.7$, $A_{2_{source}} = -0.7$ (Fig. 2.17b);

(c) $f_c : A_{3_{rec.}} = -0.7$, $A_{3_{source}} = -0.9$ (Fig. 2.17c);

(d) $f_d : A_{4_{rec.}} = -0.05, -0.08, -0.1, -0.2, -0.1, -0.08, -0.05,,$ $A_{4_{source}} = -0.8$ (Fig. 2.17d);

(e) $f_e : A_{5_{rec.}} = -0.05, -0.08, -0.1, -0.4 - 0.1, -0.08, -0.05,,$ $A_{5_{source}} = -0.8$ (Fig. 2.17e).

The profiles in first three Figs. 2.17a-2.17c have been deghosted using the same receiver inverse filter, but a series of different source inverse filters whereas Figs. 2.17d and 2.17e have been deghosted using a rough sea surface approximation for the receiver ghost filter. Thus, a comparison can be made between different filters. The amplitude of source's side deghosting for filter f_c was set to define the limiting case for the possible amplitudes of the source's inverse filter.

The results depict the ambiguous nature of deghosting operators where images in Figs. 2.17a-2.17c show minimum differences in a level that is not directly discernible without a meticulous inspection. However, their spectra show differences in the source's expected notch with f_b producing a flatter result (red and blue curves in Fig. 2.17f, f_a and f_b respectively). Result after using f_c has a disproportionally healed source's notch (dark green curve and black arrow in Fig. 2.17f). Comparison between operators f_d, f_e indicate that f_e in Fig. 2.17e (light green curve in Fig. 2.17f) overshapes the receiver's notch, a result which boosts the relevant frequency range and generate illusory reflectivity. However, the latter effect is not directly evident especially compared to Fig. 2.17d using f_d (purple curve in Fig. 2.17f).

The ambiguous results after applying fundamentally different deghosting operators arise from the fact that the non-localised notches cannot be uniquely inverted. Where the seismic signal includes noise and/or the sea surface reflectivity is altered due to rough surface conditions, there will be a set of equally plausible filters which can produce an acceptable deghosted image. Though, the amplitude spectrum may help to discriminate the most appropriate inverse filters from the less appropriate inverse filters it cannot be used to determine the unique set of source's/receiver's deghosting operators. The combination of alternative criteria such as the autocorrelation function of the nearest traces from a number of shot gathers in the pre-stack/post-stack domains, could theoretically aid to further discriminate the plausible operators. A complete test of the available criteria for the ghost elimination problem will be provided in the Discussion section (Chapter 5).

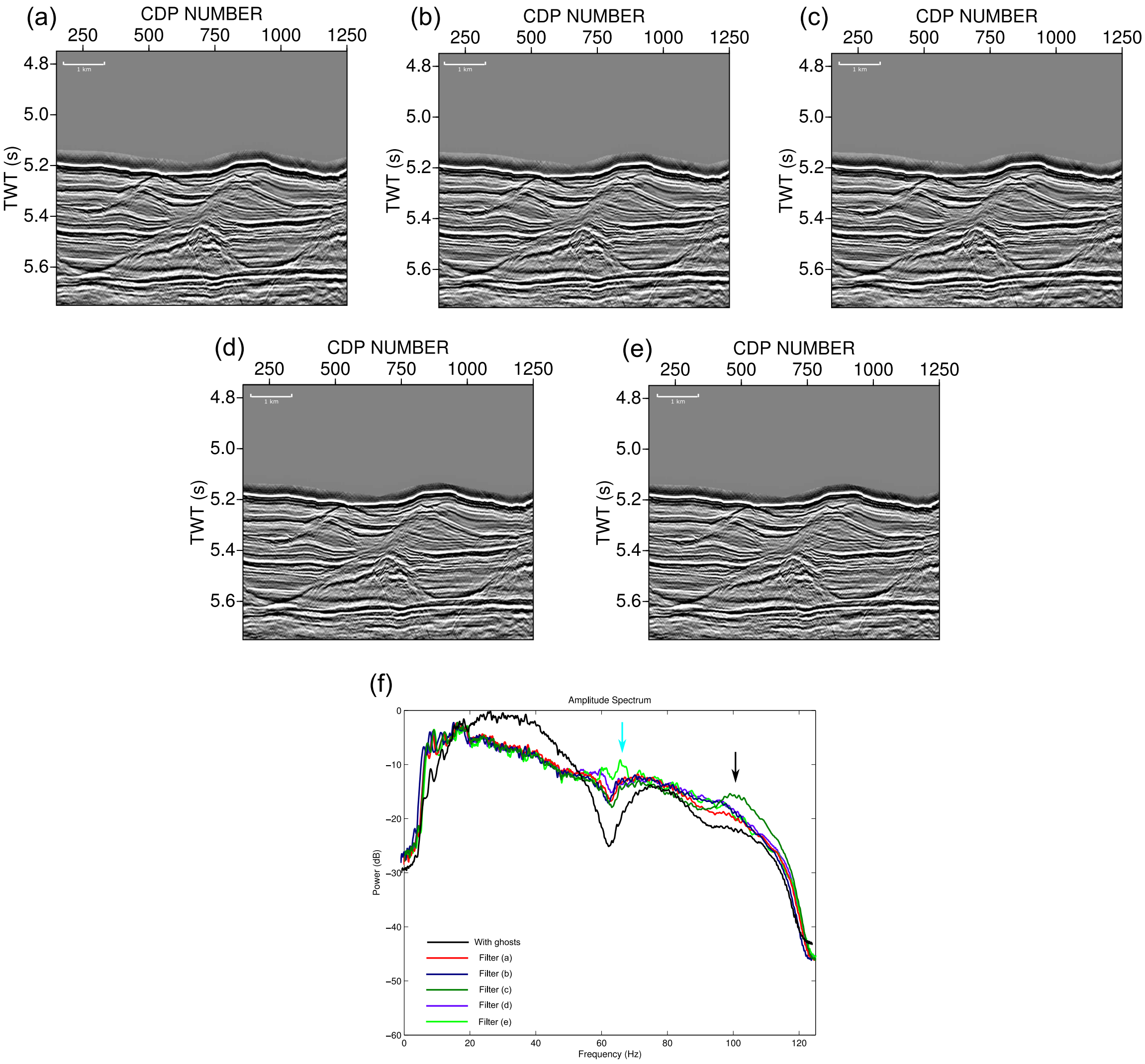

Figure 2.17: Flat vs statistical approximation in deghosting filters. (a), (b), (c) are deghosted using different sets of inverse filters (f_a-f_c) for the source's side ghost. Differences are minimal; (d), (e) show two different sets of statistical filters (f_d-f_e). Note that both images show comparable retrieved reflectivity to (a)-(c); (f) shows the relevant amplitude spectra before (black curve) and after the operators' application. Red, blue, dark green spectra show result after application of f_a-f_c ((a) - (c)), whereas purple and light green show results using f_d and f_e ((d) - (e)). Note how the misshapen source notch (local maximum of dark green curve, dark arrow) after applying f_c is not mapped into evident reverberations in (c). Similarly, the local maximum (light blue arrow) in light green curve after applying f_e is not obviously mapped in (e).

2.3 Proposed site MBAS-9

MBAS-9 is located at the continental shelf of the SW Australia, in a region where the average water depth is nearly 1 km (see bathymatry map in 1.1). The shallower environment renders the processing sequence more demanding, as in that case the surface related multiples will be superimposed over the primary signal of interest. Moreover, the direct and refraction arrivals contaminate the hyperbolic reflection events. Thus, the processing flows were tailored accordingly to eliminate these extra types of noise arrivals.

2.3.1 Time domain processing of line S310-05

As line S310-05 is acquired in a relatively shallow marine environment, all the phenomena associated with shallow marine imaging, such as surface related multiples and pronounced linear arrivals, are evident. In Figure 2.18, we present the comparison between the initial unprocessed, unmigrated, brute stack of the profile (top panel), with the final image (bottom panel) after applying processing flow 2 (Table 2.3). The original brute stack serves as an excellent example to identify all the types of noise present in our data set.

Figure 2.19a shows the brute stack along with three shots from the profile (Fig. 2.19b), which will aid understand of the different types of noise between pre- and post-stack domains. The most pronounced type of noise directly evident in the stacked domain, is the surface related multiples (1^{st}, 2^{nd} and 3^{rd} harmonics, red, orange and yellow arrows respectively), which start approximately from twice the sea bed arrival time (between 2.0 - 3.0 s TWT). Note the pronounced nature of the 1^{st} harmonic which, combined with unmigrated primary signal and poor S/N, has a detrimental effect on imaging. Also evident, the relevant weakening of the 2^{nd} and 3^{rd} multiples due to absorption effects (orange and yellow arrows respectively). This multiple signal can be also seen in the shot domain shown at the bottom panel (arrows have same color as in top panel for consistency).

Another detrimental noise is caused by the group of linear events, primarily refraction arrivals originated from the complex region below the major unconformity ($\approx$ 1.2 - 1.8 s TWT in the stack profile). As it is evident in shot domain, these arrivals are superimposed over the reflection events spanning both mid and near offsets traces (blue dashed boxes in shots SP1, SP3), but they also appear to have a laterally variant dip, as a consequence of their trajectory through the complex sedimentary sequence below the major unconformity ($\approx 1.2 - 1.8$ s TWT). The non-trivial nature of the refracted wave trains, poses a problem for their suppression in the $f - k$ domain as the arrivals would appear in a range of different dips/velocities, requiring a laterally variant dip filter approach. Hence, careful inspection of the gathers after linear events elimination is required, in order to minimise the accidental removal of the primary signal.

Table 2.3: Time domain processing sequence for seismic line S310-05.

S310-05
Reformat and geometry import - CDP spacing = 6.25 m - Nominal CDP fold = 108 **(Flows 1 & 2)**
Instrument delay correction = 100 ms, Source-Receiver datuming **(Flows 1 & 2)**
Minimum phase low cut Butterworth filter 4 Hz, 18 db/octave **(Flows 1 & 2)**
Modelled designature inverse filter (shot gathers) **(Flows 1 & 2)**
Swell noise & linear events elimination ($f-k$ domain) **(Flows 1 & 2)**
Deterministic inverse filter for source's notch compensation (shot gathers) derived from post-stack amplitude spectrum **(Flow 2)**
Receiver's notch compensation in $f-x$ domain (shot gathers) **(Flow 2)**
$f-k$ filter for linear noise elimination **(Flow 2)**
Surface Related Multiple Elimination (SRME) **(Flows 1 & 2)**
CMP Sorting and 2^{nd} order Velocity analysis (every 312.5 m / 50 CMPs) **(Flows 1 & 2)**
High resolution parabolic Radon transform **(Flows 1 & 2)**
Straight ray isotropic Kirchhoff pre-stack Time Migration (preSTM) **(Flows 1 & 2)**
Spherical Divergence Correction **(Flows 1 & 2)**
Inner/Outer trace mute and stack **(Flows 1 & 2)**
Deterministic inverse filters for source's & receiver's notch compensation derived from observed average notches as appeared in the post-stack amplitude spectrum **(Flow 1)**
Time variant zero phase Butterworth filter **(Flows 1 & 2)**: 10-20-100-125 at seabed (sb), 8-16-100-125 at sb + 0.2 s, 5-10-90,110 at sb + 0.4 s
Frequency - distance ($f-x$) deconvolution for random noise attenuation **(Flows 1 & 2)**
Phase Inverse Q compensation = 200 **(Flows 1 & 2)**
Cosmetic sea noise mute **(Flows 1 & 2)**

Finally, diffraction events also appear in the shot domain (white arrows in bottom panels). Although not as significant as the previous types of noise, out of plane diffractions will add an extra noise component to the primary signal and should be suppressed. In the following we will describe the operators applied to suppress the noise contamination.

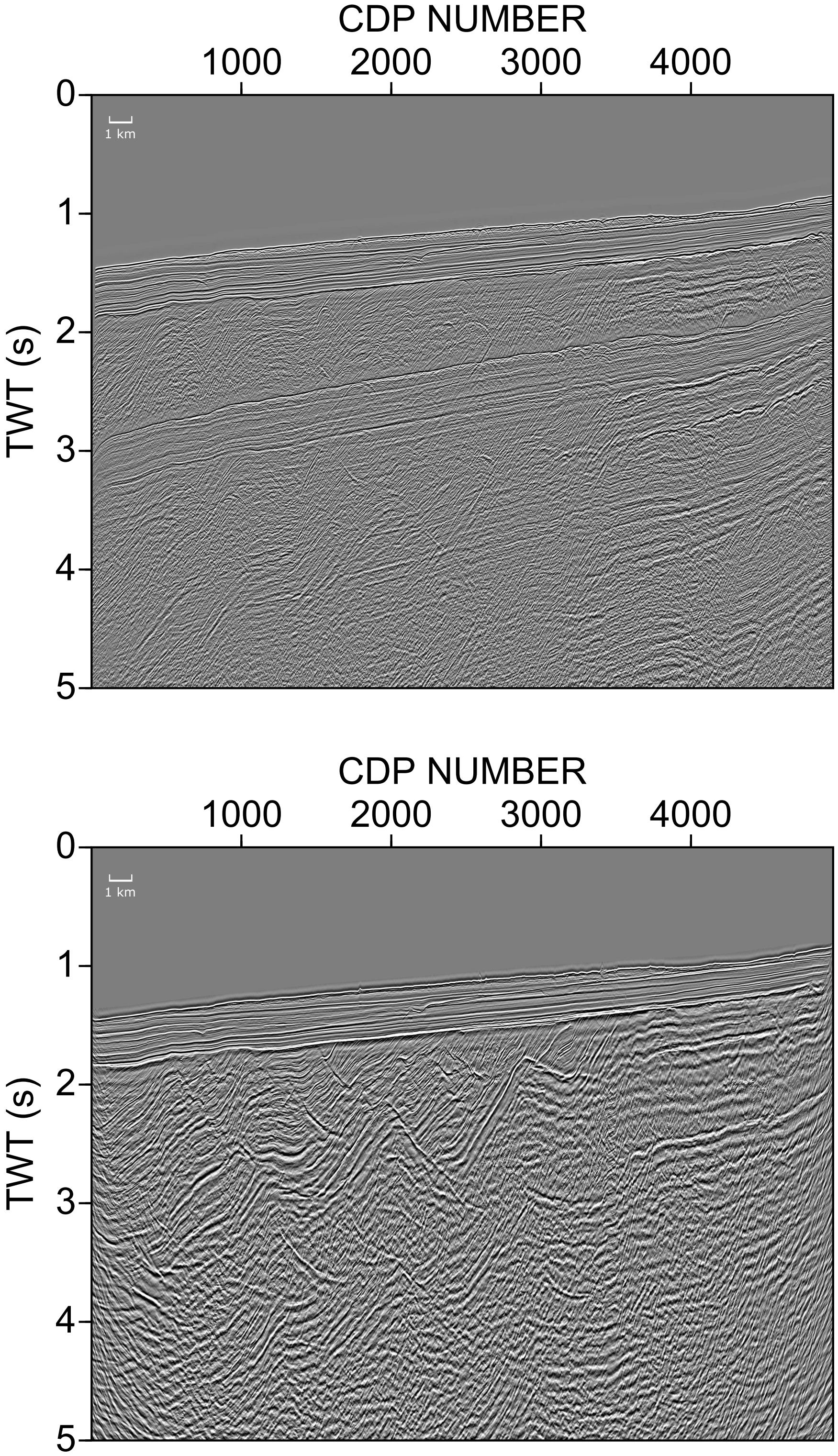

Figure 2.18: Comparison between initial and final image. Top: Brute stack. Note the multiples that contaminate structural features after 2 s TWT; Bottom: Final image after application of demultiple techniques, pre-stack ghost compensation and preSTM.

2.3.1.1 Linear noise elimination and demultiple techniques

Linear events were eliminated in the $f-k$ space using targeted dip filters in a form of polygon to cover a range of possible dips. All the polygons were formed in the $f-k$ space and the area that they cover was discarded as noise. This step was applied before applying SRME so as to avoid modelling any events that don't correspond to reflection arrivals.

The primary demultiple technique which was applied to our data set was SRME (Verschuur et al., 1992). The data driven surface related multiple elimination generates a model of the multiple content present in the signal (except from internal multiples which are not surface related), followed by adaptive subtraction of the model from our data. Note that a possible application of 1D demultiple techniques such as predictive deconvolution in time/offset $(t-x)$ domain would produce suboptimum multiple suppression as due to the long period of the multiple and the dipping seabed, the multiples appear even less periodic in $t-x$ domain. In our case, the adaptive subtraction was performed using multiple passes of two different techniques (Monk, 1993; Wang, 2003, Table 2.4). In Fig. 2.20, we present three shot gathers along the profile before (Fig. 2.20a) and after (Fig. 2.20b) applying an $f-k$ linear filter combined with SRME demultiple. Most of the linear events and a large part of the multiple content of the signal are suppressed. Zoomed panels (1), (2) and (3), from different time windows in the shot gathers show the result before and after applying the operators. The post-stack representation of this suppression is presented in Fig. 2.21. Fig. 2.21a is same as Fig. 2.18a with the zoomed interval of the 1^{st} multiple harmonic plotted in Fig. 2.21b. Figs. 2.21c and 2.21d, the result after eliminating the linear events and subtracting the multiple signal. The strong multiple content is partially suppressed but some remnant signal of the 1^{st} multiple harmonic is evident in a form of low frequency smear.

Table 2.4: Adaptive subtraction parameters.

Subtraction Method	**Parameters**
Monk	Gate = 400 ms
Wang	Gate = 200 ms, Filter Length = 8 samples
Wang	Gate = 400 ms, Filter Length = 8 samples
Wang	Gate = 600 ms, Filter Length = 8 samples
Wang	Gate = 900 ms, Filter Length = 8 samples

Although SRME demultiple worked, there is still a remnant low frequency multiple content evident in the region of the $1^{st.}$ multiple harmonic (Fig. 2.21d). Further tests could potentially improve the multiple adaptive subtraction in the lower frequency band however due to time constraints and computational resources no extra matching parameters were designed at that stage. In order to improve the suppression of the remnant noise in a computationally feasible method, we used High Resolution Parabolic Radon Transform demultiple technique (Hampson, 1986) after

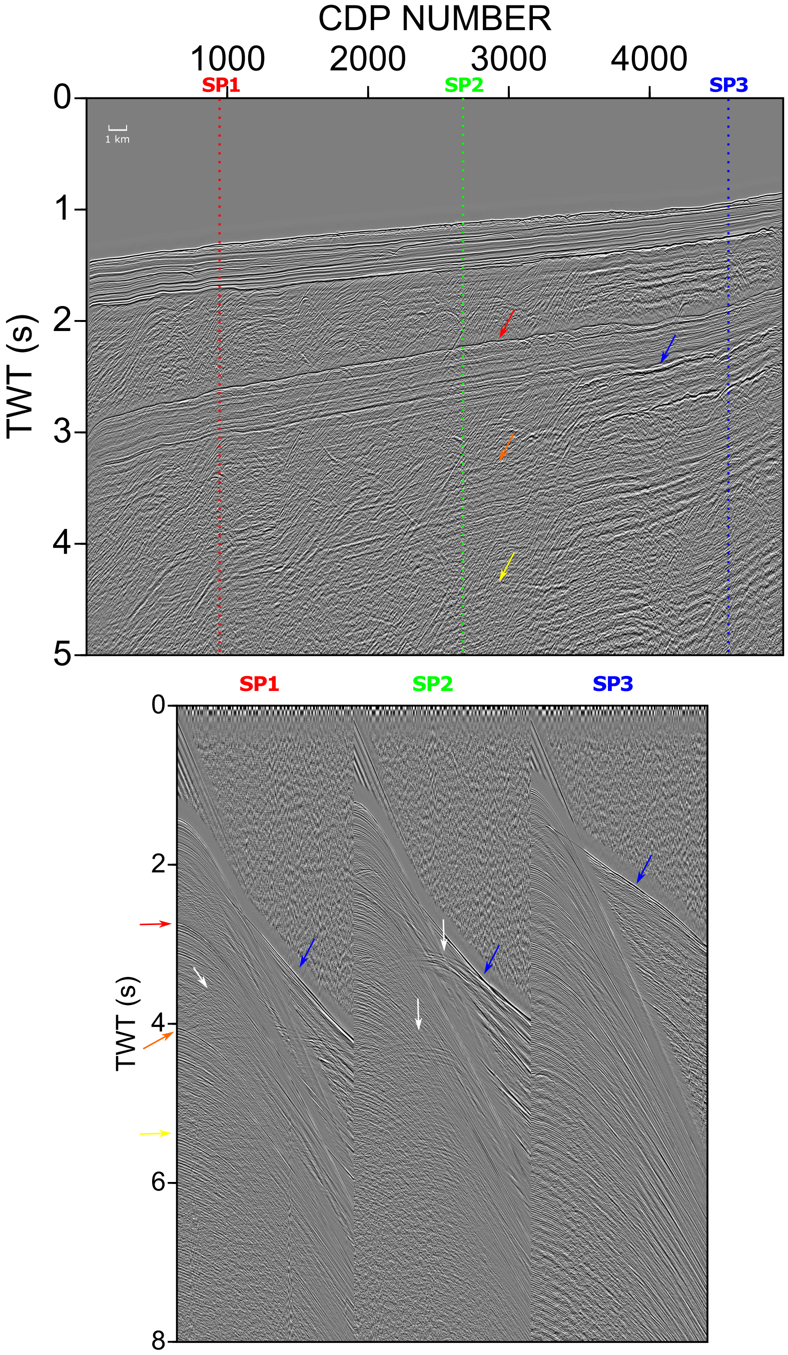

Figure 2.19: Noise content of line S310-05: The brute stack at the top (first 5 s TWT), is dominated by the 1st, 2nd and 3rd surface related multiples (red, orange, yellow arrows) and locally by a mixture of linear noise and multiples (blue arrow). For clarity, the stack is generated by a velocity field, picked only until the dipping unconformity at $\approx$ 1.5 s TWT, with the CMP gathers being muted in the far offsets. Sea noise mute, AGC and low cut filter also applied; At the bottom, three raw shot gathers from the profile are shown (first 8 s TWT). The noise features appeared in the shots are indicated with arrows under the same colors for consistency. Note especially the change of the dip of linear events along the profile, that incise the reflection events even in the near-mid offsets (blue dashed rectangles). White arrows represent diffraction events.

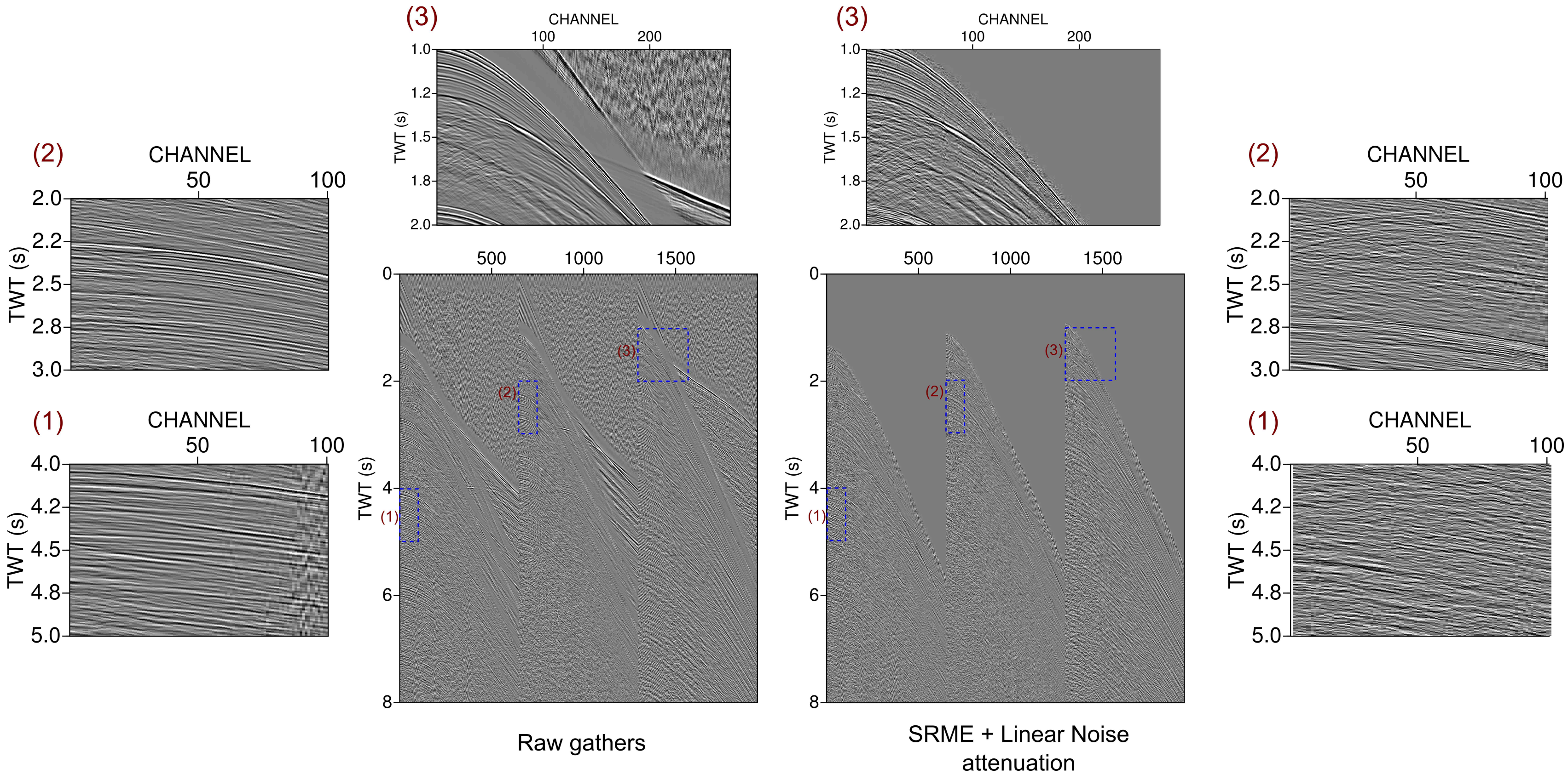

Figure 2.20: SRME and linear noise attenuation in shot domain. The shots shown are the same as in (2.19b). The zoomed panels (1), (2) and (3) indicate segments of the gathers before (left and top left) and after (right and top right) the application of SRME and $f-k$ filtering for multiple and linear noise removal respectively. In the corrected gathers, sea noise mute was also applied. Although SRME subtracted a significant part of the multiple content (pairs of panels (1)-(2)), there is a remnant multiple signal that contaminates part of the data. Filtering in the frequency - wavenumber domain ($f-k$) successfully eliminated the apparent linear events (pair of panels (3)).

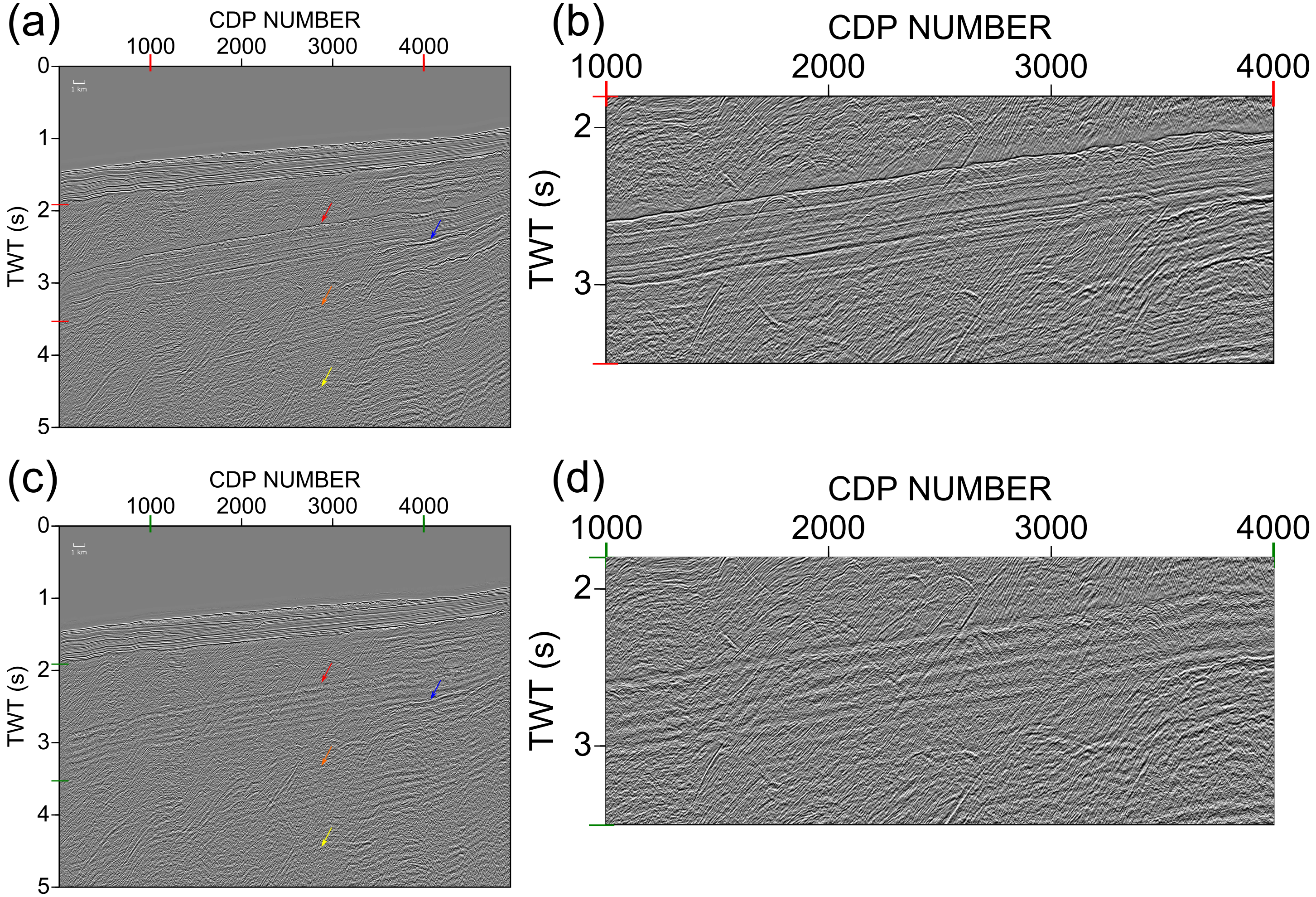

Figure 2.21: SRME demultiple and linear noise attenuation. (a) Brute stack same as in Figure (2.24a); (b) First surface related multiple without SRME elimination; (c) Brute stack after SRME and linear noise elimination in the $f - k$ domain. Note the nearly total elimination of 1^{st} surface related multiples and the successful elimination of 2^{nd} and 3^{rd} multiples (red, orange, yellow arrows), with a simultaneous improvement in the regions of interference between multiple signal and linear noise (blue arrows). The 1^{st} multiple manifests itself as a low frequency remnant noise. Outer trace mute in the CMP gathers, sea noise mute, AGC and low cut filter used to generate both profiles; (d) Same as (b) after SRME. Zoomed regions are defined by red and green dashes on the left profiles respectively.

sorting the shot gathers into CMP domain. The parameters for this processing step are given in Table 2.5). As this technique is based on the parabolic representation of the reflection events, the originally hyperbolic multiples must be converted into events with a parabolic curvature. This is accomplished by using an approximate NMO correction which overcorrects the primaries but undercorrects the multiple arrivals in the CMP domain. Thus, the Model/Noise parameters as stated in Table 2.5 represent the minimum/maximum limits of the filter after applying the approximate NMO correction. Note that the operators were also applied in a targeted time window to cover only the multiple periods and not part of the shallow sedimentary sequence. This ensures that any artefacts that may be generated during the forward / inverse radon transform would not contaminate the shallow sedimentary sequence.

The resulted profile is shown in Figure 2.22. Panels 2.22a, 2.22b plot the result after SRME (2.21c, 2.21d), whereas 2.22c, 2.22d show the final demultiple result. The noise level is further reduced without compromising the primary content of the signal. However, any remnant multiple signal will be finally suppressed below the noise level of the data following a complete processing flow, including final velocity analysis, preSTM and inner trace mute.

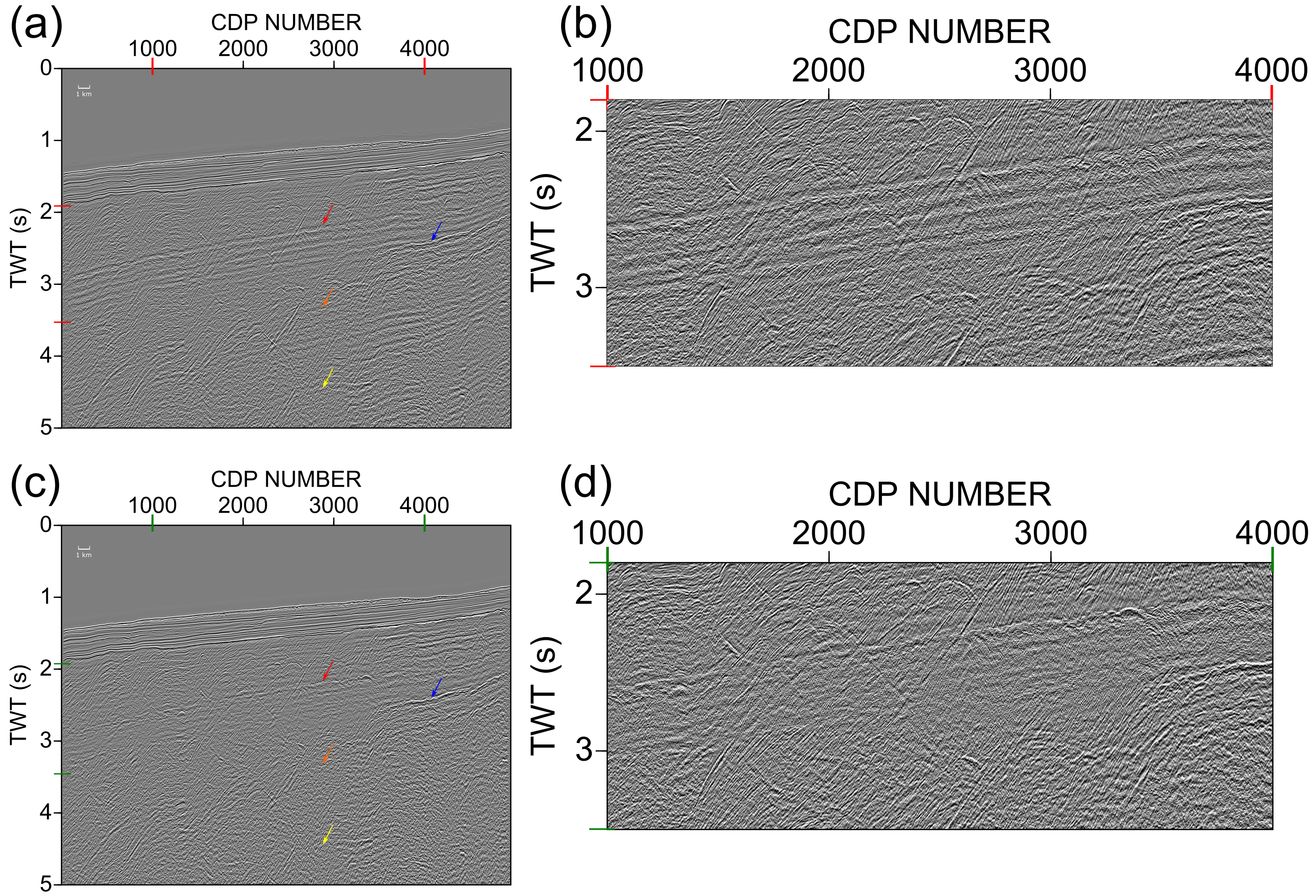

Figure 2.22: High resolution parabolic radon transform demultiple. (a) Brute stack after SRME and linear noise elimination in the $f - k$ domain, same as 2.21c; (b) First surface related multiple after SRME and linear noise elimination same as 2.21d; (c) Brute stack after SRME, linear noise elimination and high resolution parabolic radon transform. The multiple content (red, orange, yellow arrows) is practically eliminated and only few low frequency stripes are evident as a manifestation of the regions where the multiple signal existed. The latter effect will be eliminated with the synergy of detailed velocity analysis, pre-stack time migration and inner trace mute in the CDP gathers. Outer trace mute in the CDP gathers, sea noise mute, AGC and low cut filter used to generate both profiles; (d) Same as in (b) after high resolution parabolic radon transform. Zoomed regions are defined by red and green dashes on the left profiles respectively.

Table 2.5: High resolution Parabolic Radon Transform parameters.

Operator	Offset (m)	Model (ms	Noise (ms)	T_{start} (seabed, ms)	T_{end} (seabed, ms)
1	2200	-500/1000	100/200	900	1900
2	3000	-500/1000	400/650	900	1900
3	3500	-500/1000	600/850	900	1900
4	3500	-100/1100	300/700	1650	3150
5	4500	-100/1100	450/650	2400	3500

2.3.1.2 Comparison of processing flows

Deghosting the data in the pre-stack domain allowed us to assess the possible effects of the deghosting operator in the SRME demultiple process. As the technique was developed to use the upgoing wave component of the data so as to generate a multiple model (Verschuur et al., 1992), in theory the multiple elimination should be more effective after deghosting the signal. Figure 2.23 tests this hypothesis by comparing Figs. 2.23a and 2.23c, which show segments of the profile as appear after SRME without notch compensation, with the Figs. 2.23b and 2.23d which show the SRME results after deghosting in the shot domain. Due to the boost of the low frequency content by the deghosting process, the region below the unconformity appears sharper and more pronounced but there are some subtle differences between Figs. 2.23b and 2.23d that show some evidence that the deghosted data has less multiple content.

Furthermore, in Figure 2.24 we present a full comparison between preSTM images before (Figs. 2.24a, 2.24b) and after deghosting in post-stack domain (Figs. 2.24c, 2.24d, Appendix Table D.3) and pre-stack domain (Figs. 2.24e, 2.24f). Zoomed panels of the mid sedimentary sequence are shown to evaluate the effectiveness of deghosting operators. The benefit of deghosting results in better delineation of the sedimentary sequence (red arrows in Figs. 2.24a, 2.24c, 2.24e) and event resolution. However, there are no significant differences between the two deghosted images.

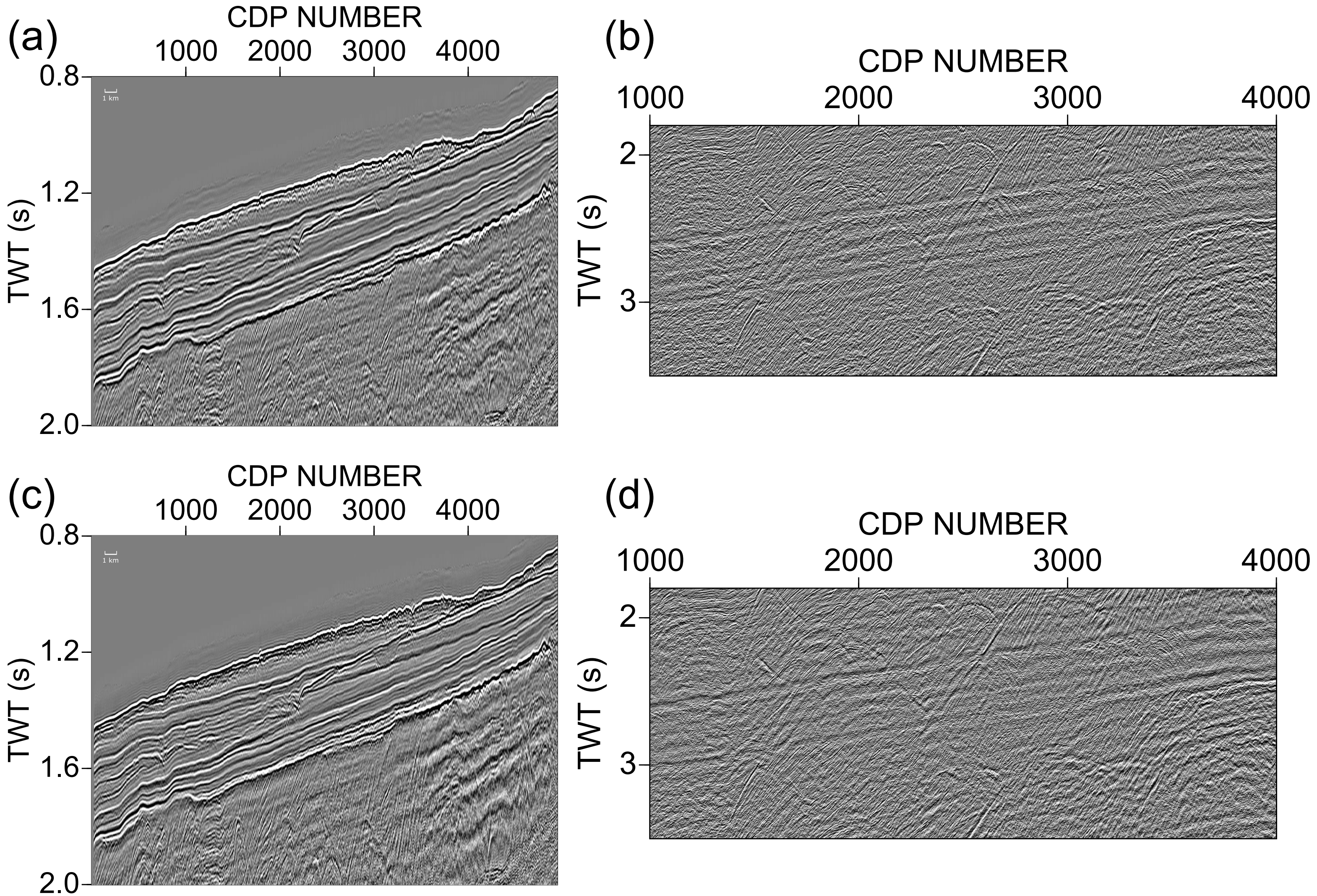

Figure 2.23: Deghosting and SRME. (a) Top sedimentary sequence as imaged after brute stack without any ghost compensation; (b) Multiple signal after SRME, same as appeared in 2.21d; (c) Same as in (a) with pre-stack notch compensation, where the reflection events are more pronounced and sharper; (d) Multiple signal after SRME in the deghosted profile. The result compared to (b) appears locally better as the SRME operator works more efficiently when the signal is consisted only from the upgoing wavefield.

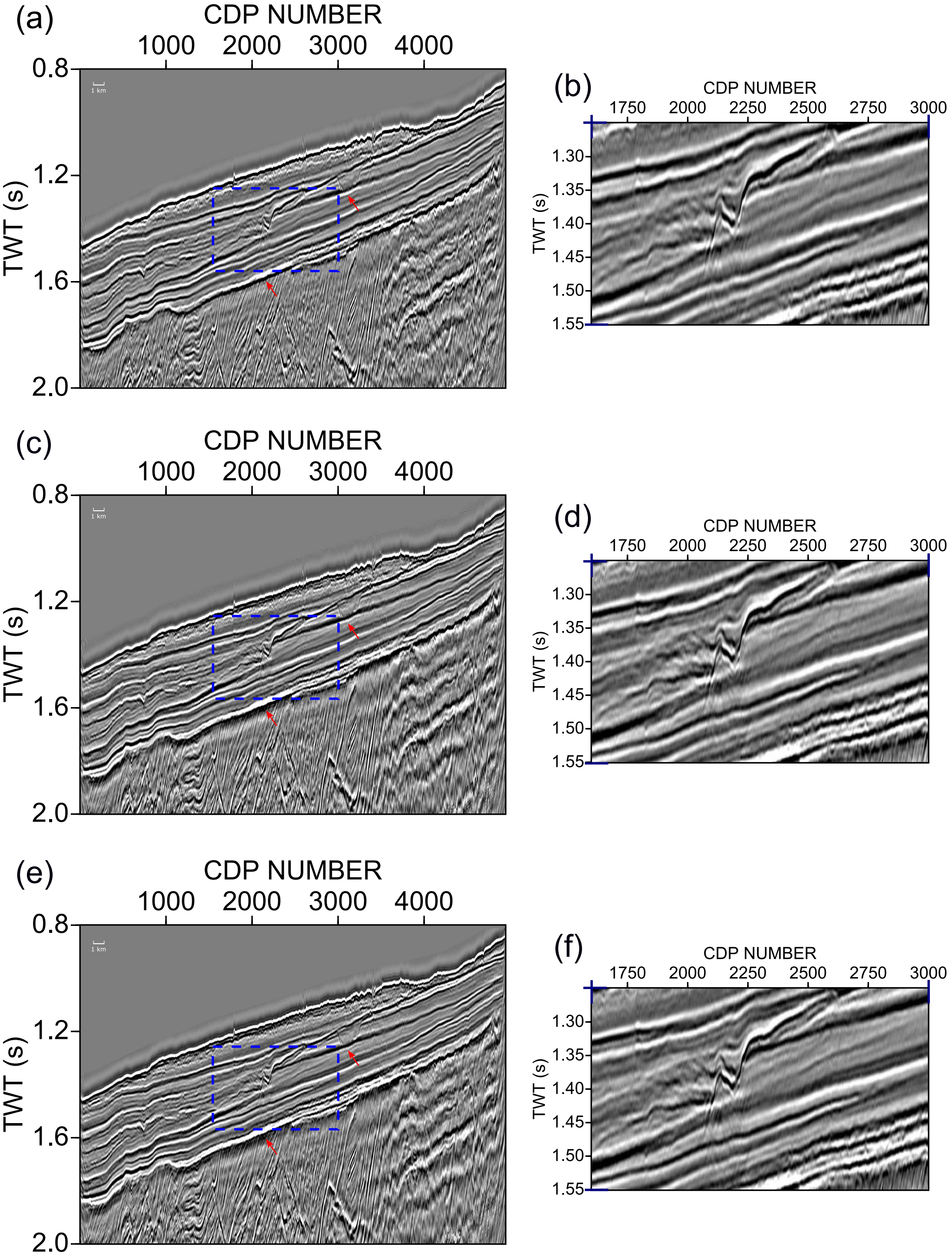

Figure 2.24: Comparison of top sedimentary sequence in preSTM results. (a) Final preSTM image without any ghost compensation; (c) Same as in (a) after post-stack deghosting; (e) Same as in (a) but with notch compensation in the pre-stack domain. With red arrows, different regions of the profile are indicated, where the gradual improvement of the resolution of the image is more pronounced; (b), (d) and (f) show a zoomed area with limits defined by the blue dashed rectangles. Note the progressive improvement of resolution before and after the filter application.

2.4 Conclusions

In this chapter, a description of the processing sequences applied in the three 2D seismic profiles was presented. The chapter focused on the implementation of deghosting operators either post-stack or pre-stack, in conjunction with the application of preSTM. Two (2) of the sites were in deep water whereas one was on the continental shelf where it was necessary to combine the deghosting and preSTM with multiple removal methods to optimally reveal the underlying primary reflectivity.

From the analysis of the results, both deghosting processing strategies gave improved temporal resolution. However, for the pre-stack case, the incomplete modelling of the receiver's notch resulted in images that were less rich in low and mid frequency content, but richer in high frequency content that resulted in an overall sharper and better resolved preSTM images.

In the following Chapter 3, we continue the seismic reflection processing in depth domain using the pre-stack deghosted gathers, with the goal to achieve a high quality preSDM image. Subsequently, the developed velocity field, refined through a depth domain velocity model building process, along with the deghosted CMP gathers will be used as input to the BRAINS algorithm. From the statistical analysis, we are going to extract probabilistic estimations about the depths of the drilling targets, which is one of the primary deliverables of this project.

Chapter 3

Bayesian uncertainty analysis for depth predictions

In Chapter 2, we used two processing flows to a number of seismic lines intersecting our proposed site locations and generated time domain representations of the subsurface for regions of Mentelle Basin. The combined use of preSTM and deghosting operators, produced well focused images with retrieved high resolution events. In this chapter we will continue our seismic data processing for specific lines, resulting in depth domain images, using pre-stack depth migration (preSDM) and produce uncertainty estimations for pertinent variables of interest (V_{rms}, T_0, $V_{int.}$ and z) using a suite of algorithms called BRAINS (from Bayesian Regression Analysis in Seismology, Caiado, 2012a; Caiado et al., 2012b). The predictions reported in the chapter along with the seismic processing strategy are published in:

Michelioudakis, D.G., Hobbs, R.W., and Caiado, C.C.S. (2018). Uncertainty analysis of depth predictions from seismic refection data using Bayesian statistics. Geophysical Journal International 213(3), 2161-2176.

3.1 Need for Uncertainty Estimation In Seismic Reflection Processing

Velocity model building is a critical step in seismic reflection processing. An optimum velocity field can generate flat common image gathers (CIGs) and well focused images in time or depth domain. Nevertheless, taking into account the noisy and band limited nature of the seismic reflection data and the ambiguity in the velocity estimation, the generated velocity field is only our best estimate of a set of possible velocity fields (Bickel, 1990; Tieman, 1994; Kosloff & Sudman, 2002). Hence, all the calculated depths and the images produced are just our best approximation of the true subsurface.

Although incorporating anisotropic parameters (Thomsen, 1986; Alkhalifah & Tsvankin, 1995; Alkhalifah, 1997) during the velocity analysis stage can assist to constrain better the depth results (Hawkins et al., 2001), the non - uniqueness of the velocity field still remains an open problem as different velocity fields can lead to nearly equally flat arrivals in the CIG (Chitu et al., 2008). The problem is compounded in the absence of any well log information, where the velocity field cannot be calibrated, rendering the final structural image only a sample among the most probable images, as an optimally focused image doesn't necessarily mean accuracy of depths (Al-Chalabi, 1994, 2014).

The aforementioned sources of uncertainty, although eventually interconnected, can be attributed to different stages of seismic data acquisition and processing. For example, the noisy and band limited nature of seismic data is linked to the inherent limitation of our acquisition systems to generate and record (in digital form) fully broadband, noise free, seismic data. Similarly, simplifying an expanding hemispherical wavefront (for constant velocity case), such as the sound wave generated from a marine seismic source, in terms of its high frequency approximation, a ray, reflects our attempt to decrease the complexity of the system explored. It is however the third type of uncertainty, ambiguity in the velocity model estimation, that although is a consequence of the two other types, is also related with the veracity of expert's judgement during velocity model building.

Conventionally, the initial estimation of the reflection two-way time (T_0) and root mean square velocity (V_{rms}) for each geological layer is based on the expert's picking of local maxima on a semblance spectrum (Neidell and Taner, 1971), computed from common - mid point (CMP) gathers. Semblance is a dimensionless measure which is calculated by the ratio of the total energy of the stack within a certain time interval to the average of the energy of the component traces in that time interval (equation 3.1)

$$Sc = \frac{\displaystyle\sum_{t}^{t+m\Delta}\left(\sum_{i=1}^{N}\mathcal{A}_{ti}\right)^2}{\displaystyle N\sum_{t}^{t+m\Delta}\sum_{i=1}^{N}(\mathcal{A}_{ti})^2} \tag{3.1}$$

where $\mathcal{A}_{ti}$ denotes the amplitude value of a trace at a time sample t. Semblance values lie in the interval [0,1], with the maximum values showing a coherent hyperbolic seismic event. As a result, strong hyperbolic seismic reflection arrivals will exhibit a large semblance value, whereas incoherent arrivals result in a small to moderate value (Sheriff and Geldart, 1995). From a statistical perspective, the maximum semblance value is analogue to minimizing the variances of the amplitudes (Caiado, 2012a).

The ambiguity associated with the velocity model building is shown schematically in Fig. 3.1. The CMP gather is NMO corrected with three slightly different velocity fields after 4.2 s TWT, but visually the reflection arrivals appear equally flat (Figs. 3.1a, 3.1b). Earlier than 4.2 s, the maxima are less ambiguous to pick and the degree of precision of each picked value is higher. However, the velocity model building for deeper structures is compromised by the depth to offset ratio defined by the acquisition geometry and the attenuated frequency and amplitude content of the signal. This velocity - depth issue, limits the sensitivity of residual moveout to velocity changes and indicates that the semblance spectrum as a tool lacks the resolution to provide us with a unique velocity model (Lines, 1993). Tomographic inversion in the migrated domain for velocity estimation is inherently non - unique (Jones, 2014) as it is trying to match the observed time values by choosing different combinations of depth (z) and slowness (s) values (Jones, 2010). Multiple realizations of the same boundary can be created, all having slightly different pairs of z, s (Figure 3.1c).

Attempts have been made to incorporate statistical information in seismic reflection data processing and perform uncertainty analysis for constraining velocities or depth results (Abrahamsen et al., 1991; Landa, 1991; Chitu et al., 2008; Lewis et al., 2015; Messud et al., 2017). Though the uncertain nature of the produced velocity field can be addressed by statistically analysing the given velocity model to quantify the uncertainty associated with each pick, this process is inherently linked with the judgement of an expert who determines which values to pick in the semblance plot. Thus, we address the problem with Bayesian methods such as Gaussian Process emulation and Bayesian History Matching (BHM), to quantify uncertainties in velocity models using a suite of algorithms called BRAINS (Caiado, 2012a; Caiado et al., 2012b).

We will apply this technique at site DSDP-258, where the borehole provided stratigraphic information (Davies et al., 1974, Fig. 1.1). Due to the poor core recovery and the lack of wireline sonic information from DSDP-258, the depth predictions of key horizons are based entirely on the velocity values inferred from surface seismic data. As the sensitivity of differential move out, during the velocity analysis stage using a semblance spectrum, is linked to the frequency content of the wavelet in pre-stack data (CMP gathers) (Chen and Schuster, 1999; Jones, 2010), we will use the preSTM deghosted gathers as input to the BRAINS algorithm aiming to achieve more constrained results. Simulaneously, these gathers will be used to perform pre-stack depth migration (preSDM) and produce an image with optimum spatial resolution and focusing, which aids to better constrain the interpretation.

The probabilistically derived velocity estimates are used to retrieve the depth information for key boundaries, tied to borehole DSDP-258 and make predictions for the depths of drilling targets for the two proposed wells at site MBAS-4, located adjacent to the borehole DSDP-258. Finally, as the probabilistic approach produces a posterior distribution of velocity values, we generate a set of velocity fields and produce different realizations of pre-stack depth migration (preSDM) images for the line segment intersecting the planned wells (Fig. 1.1).

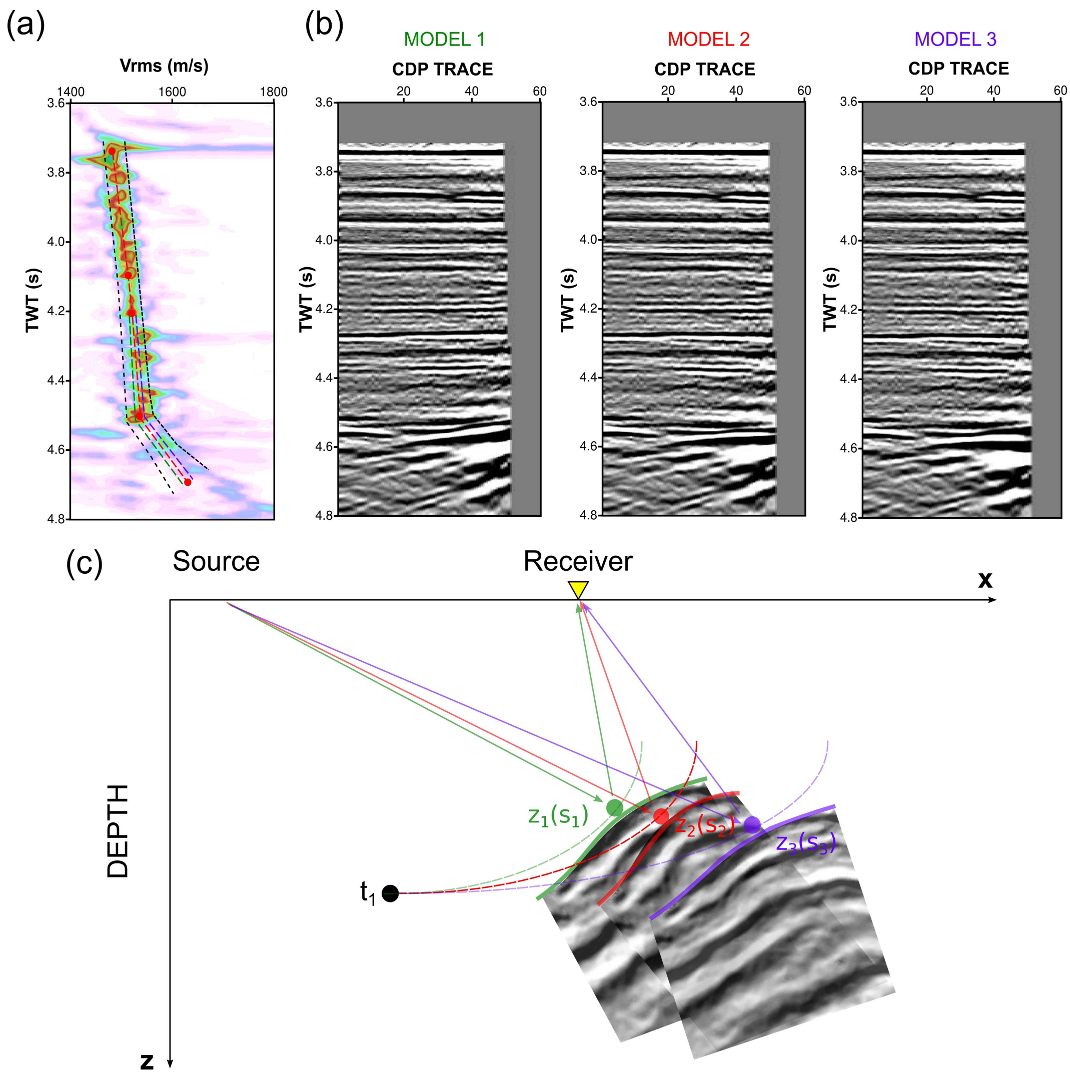

Figure 3.1: Uncertainty in velocity model building. (a) the semblance spectrum as a velocity estimation tool gives robust time-velocity picks for the shallow parts, but for later times the envelope of possible picked pairs (dashed black lines) becomes broader due to attenuation effects and poor depth to offset ratio; (b) the 3 velocity models (under colors red, purple, green), having differences only after 4.2 seconds TWT, result in equally flat gathers but can lead to different shapes and depths for the same horizons after pre-stack depth migration (preSDM); (c) tomographic inversion in the depth migration domain preserves the observed invariant time (t_1) of an arrival by using different values of thickness (z) and slowness (s). As a consequence, the mapping from time to depth can result in slightly different realizations of the same boundary. ((c) is modified from Jones, 2010, Figure 5.23).

3.2 Gaussian Process emulators for modelling seismic velocities

In the Bayesian framework, the expert's beliefs about the parameters that govern a system are represented using prior distributions, then the available data, in conjuction with a sampling model (likelihood function), are used to update our beliefs about these parameters (posterior distribution). In seismic reflection processing, we can use the observed amplitudes of reflection events in a CMP gather $\mathcal{A}_{ij}$, offsets x_j, recorded travel times T_j and picked $V_{rms} - T_0$ or derived $V_{int.} - T_0$ pairs as prior information and we aim to quantify the uncertainty of V_{rms}, T_0, $V_{int.}$ and z for the horizons of interest. BRAINS suite (Caiado, 2012a; Caiado et al., 2012b) uses a combination of Bayesian methods, such as emulation and Bayesian History Matching, to quantify these uncertainties.

Our approach is based on a discrete subsurface model (Appendix B), with a finite number i of geophysical layers and a given array of source ($\mathcal{S}_j$) - receiver ($\mathcal{R}_j$) pairs, $j = 1, ..., m$. These are symmetrically placed around a CMP, with x_j being the distance between $\mathcal{S}_j$ and $\mathcal{R}_j$. For every x_j and hyperbolic event (layer) i, we have observed amplitude values $\mathcal{A}_{ij}$ and recorded time $T_{ij}^{(r)}$. Also, for each layer we can assign a zero–offset two–way travel time T_{0_i}, its time increment ΔT_{0_i}, a root-mean-square velocity V_{rms_i} with its velocity increment ΔV_{rms_i}, an interval velocity V_{int_i} and a thickness Δz_i. Our model seeks to estimate variables $\{\Delta T_{0_i}, \Delta V_{rms_i}, V_{int_i}, \Delta z_i\}$ and their relevant uncertainties, from observed data $\{\mathcal{A}_{ij}, x_j, T_{ij}^{(r)}\}$, taking into account the prior information from picked $\{V_{rms_i}, T_{0_i}\}$ or $\{V_{int_i}, T_{0_i}\}$ pairs derived during the velocity analysis stage.

In the case of isotropic conditions and straight ray approximation, the recorded travel time of a ray to propagate from seismic source $\mathcal{S}_j$ to detector $\mathcal{R}_j$, $T_{ij}^{(r)}$, can be expressed as

$$T_{ij}^{(r)} = \sqrt{T_{0_i}^2 + \left(\frac{x_j}{V_{rms_i}}\right)^2} + \varepsilon_{ij} + e_{ij} \tag{3.2}$$

where ε_{ij} accounts for the model discrepancy due to propagating approximations and isotropic assumptions, e_{ij} corresponds to recording errors. Although recording error (e_{ij}), is present in a construction of a statistical model, as the observations are indirect and recorded with a finite accuracy, it is the model discrepancy term (ε_{ij}) that has a key role in our statistical representation. Model discrepancy integrates all the simplifications of physical laws, used to describe the model, with our incomplete knowledge about the system explored and represents our inability to build a model which depicts reality (Craig et al., 1997). Thus, by including the ε_{ij} term not only we address the potential issue of overfitting the model to the observed data (Andrianakis et al., 2015) but we also produce uncertainty estimations for the output variables of interest. As expressed in equation 3.2, ε_{ij} term represents effects related with anisotropic wave propagation (ε, δ anisotropic parameters) and ray tracing approximation.

Typically, these error terms are ignored which results in the Dix equation (Dix, 1955, eq. 3.3), where we can relate V_{rms_i} and V_{int_i} as

$$V_{int_i} = \sqrt{\frac{T_{0_i} V^2_{rms_i} - T_{0_{i-1}} V^2_{rms_{i-1}}}{T_{0_i} - T_{0_{i-1}}}} \tag{3.3}$$

and calculate the thickness Δz_i of each layer as

$$\Delta z_i = \frac{V_{int_i} \Delta T_{0_i}}{2} \tag{3.4}$$

Equations 3.3, 3.4 are based on the hyperbolic approximation of the recorded travel time. Including the error terms in eq. 3.3 allows a more robust approach, which is not restricted to hyperbolic assumptions but can express more complex models for incorporating recorded travel time from seismic rays which follow a non-normal trajectory. We use the above equations to construct a Gaussian Process (GP) model. A GP can be thought as the generalization of the univariate Gaussian probability distribution and formally is defined as "a collection of random variables with any finite number of which having a joint Gaussian distribution" (Rasmussen & Williams, 2006). They are well established models, applied in a variety of spatial and temporal problems (Ripley, 1991) including geostatistics (Matheron, 1973; Journel and Huijbregts, 1978) and Kalman filters (Ko and Fox, 2009). A GP is fully defined by its mean, $m(a)$ and covariance $k(a, a')$ functions with a, a' representing samples from the random vector.

In this chapter we will use the Gaussian Process emulators. An emulator is defined as a stochastic belief specification, which expresses probabilistic judgements for a deterministic function $f(a)$ (Craig et al., 1997; O'Hagan, 2006; Vernon et al., 2010; Caiado and Goldstein, 2015). Commonly, they are expressed in the following form (3.5)

$$f_h(a) = \sum \beta_{hj} g_{hj}(a) + u_h(a) \tag{3.5}$$

where a is input value, β_{hj} unknown scalars, $g_{hj}(a)$, known deterministic functions and $u_h(a)$ is a stochastic process, normally a GP with zero mean and a square exponential covariance function. Index h represents the output variable. As a result, in equation 3.5 we can incorporate our beliefs and the uncertainties about each variable of the system explored. Normally, it is worth constructing a regression term that best represents the function $f(a)$, so as to allow the GP term $u_h(a)$ to characterize the more complex local behaviour. By achieving that, the values of the hyperparameters governing the covariance function can become less crucial as their impact will be less pronounced on describing the system. In our statistical analysis, we use two emulators for uncertainty quantification.

Firstly, a local (1D) emulator (Appendix B.1), where we make the assumption that a set of travel times related to a given horizon in a single CMP can be approximated as a sample of a continuous function with a hyperbolic trend. If any finite set of travel times from this hyperbolic curve is believed to follow a multivariate Gaussian distribution, we can assume that the recorded travel time curve is a GP with respect to offset x with the expression taking the following form 3.6

$$\mathcal{T}_i^{(r)}(x)|\Delta T_{0_{(1,\ldots i)}}, \Delta V_{rms_{(1,\ldots,i)}} \sim \mathcal{GP}(m_{t_i}(x), k_i(x,x')) \tag{3.6}$$

or expressed in a form consistent to equation 3.2 as

$$\mathcal{T}_i^{(r)}(x) = (t_{0_i}^2 + x^2 \upsilon_{rms_i}^{-2})^{1/2} + u_i(x) \tag{3.7}$$

The first term of the right hand side of equation 3.7 represents the mean function $m_{t_i}(x)$ and the second term a stationary stochastic process with zero mean and a square exponential covariance functions $k_{t_i}(x,x')$, with the mean and covariance functions given below (equation 3.8)

$$\begin{aligned} m_{t_i}(x) &= (t_{0_i}^2 + x^2 \upsilon_{rms_i}^{-2})^{1/2} \\ k_{t_i}(x,x') &= \sigma_{n_i} + \sigma_{s_i} exp\left(-\frac{(x-x')^2}{d_i}\right) \end{aligned} \tag{3.8}$$

The terms x and x' define two random points from the offset space within a single CMP. Comparing equation 3.2 with expression 3.7 we can see that the hyperbolic trend of travel time equation is stored under the mean function $m_{t_i}(x)$ and the error terms ε_{ij}, e_{ij} are stored under the noise parameters σ_{n_i}, σ_{s_i} of the covariance function. The parameter d_i represents the length-scale of the function and defines how far the x, x' values should be to become uncorrelated. Small length scale values indicate that the function values can change quickly, whereas large values represent a smoother function. The covariance function, can be adjusted to specific applications by correctly tuning its hyperparameters (σ_{n_i}, σ_{s_i}, d_i). As our prior knowledge about their appropriate values reflects our beliefs about the system, they can be treated as constants that need to be set manually or derived from an optimization process using the training data (Rasmussen and Williams, 2006). In our case, the training data can be thought of as the set of prior $T_{0_i} - V_{rms_i}$, $T_{0_i} - V_{int_i}$ pairs picked during the velocity analysis stage. Based on the velocity analysis interval (spacing between two consecutive picked pairs), the picked values and also their variability along the picked velocity layer, we can manually calibrate accordingly, the noise, scale and length parameters of the covariance function and provide starting points for their values. Subsequently, the parameters are refined using a gradient search to find a local maximum in the likelihood and retrieve values in an area of high probability. Equations 3.6 - 3.8 can be formulated analogously for linking $\mathcal{T}_i^{(r)}$ with V_{int_i} and Δz_i, rendering the Bayesian model multidimensional.

Secondly, a 2D emulator expands the 1D uncertainty estimation into a 2D multi-gather representation by assuming that the variables ΔT_{0_i}, ΔV_{rms_i}, V_{int_i} and Δz_i, for every geophysical boundary, follow a GP over the CMP positions (x_c) along a profile (Appendix B.2). The latter, is used to constrain the inter-gather areas and produce estimates in regions where we don't have available prior pick pairs.

Note, that the GP models described above assume that the recorded travel - time values along a hyperbolic trend for every layer ($\mathcal{T}_i^{(r)}$), have been identified and stored. The process of saving travel - time information for every trace is related with the use of a tracking algorithm. Details for how the algorithm works can be found in (Caiado, 2012a; Caiado et al., 2012b).

3.3 Bayesian History Matching for model space reduction

In order to perform model calibration and reduce the parameter input space we use the approach known as Bayesian History Matching (Craig et al., 1997; Vernon et al., 2010). Bayesian History Matching (BHM) is an established method and combined with emulation techniques has been tested successfully in a variety of different scientific disciplines such as reservoir modelling (Craig et al., 1997; Cumming and Goldstein, 2009) climate modelling (Caiado and Goldstein, 2015) and galaxy formation modelling (Vernon et al., 2010). BHM should not be confused with the term History Matching widely used in the oil industry, as in the latter case, they are trying to match empirical data, such as production rates and observed pressure from well logs, with a complex model (normally called simulator) that is assumed to represent part of the subsurface (reservoir), where the parameters that govern the model don't include any uncertainty estimation. On the contrary through the process of BHM, all the possible models that can match our observed data are identified (Vernon et al., 2010). Following the same notation as in equation 3.5, in BHM, we aim to identify and iteratively discard input values, a, of the parameter space for which the evaluation of a function (emulator) $f_h(a)$ isn't likely to provide a good match to the observed data L_h. The parts of parameter space that are discarded are called implausible and the process of reducing the space is accomplished using the probabilistic criterion of implausibility $I_h(a)$ (Craig et al., 1997; Vernon et al., 2010). The general definition of Implausibility is given below.

Definition. Implausibility

For a given choice of input value a with modelled output $f_h(a)$, observation vector L_h and taking into account all the variances present in the system $Var_h(system)$, implausibility $I_h(a)$ is defined as (equation 3.9):

$$I_h^2(a) = \frac{\Big(L_h - f_h(a)\Big)^2}{Var_h(system)}. \tag{3.9}$$

Large values of $I_h(a)$ indicate that, taking into account all the uncertainties of the system (denominator of equation 3.9), it is very unlikely to obtain acceptable matches between the model outputs and the observed data at input a. However, small values of $I_h(a)$ don't necessarily mean that the input value a is correct (Vernon et al., 2010). The Implausibility measure $I_h(a)$, as expressed in equation 3.9, refers to multidimensional models (h number of output variables). A one dimensional example of the above form, taking into account all the types of uncertainties present in our system (equation 3.2) and based on the GP model as expressed in equation 3.6, can be formulated as (equation 3.10):

$$I_i^2(a) = \frac{\left(L_i - \mathbb{E}^*(T_i^{(r)}(a))\right)^2}{Var^*(T_i^{(r)}(a)) + Var(\varepsilon_i) + Var(e_i)} \tag{3.10}$$

where L_i our observed data, $\mathbb{E}^*(T_i^{(r)}(a))$, $Var^*(T_i^{(r)}(a))$ the posterior mean and posterior variance of Gaussian Process emulator and $Var(\varepsilon_i)$, $Var(e_i)$ are the variances of the modelling and observation error, respectively. Index i, represent each velocity layer. The observed data L_i, for every discrete velocity layer associated with a hyperbolic event in a CMP gather, is the local maximum value of the semblance spectrum of that hyperbolic trend calculated from the observed offset x_j, amplitude values $\mathcal{A}_{ij}$ and recorded time T_j. The non-implausible space can be reduced by applying multiple iterations of BHM. In order to identify the region of implausible input values, a cut-off limit based on Pukelsheim's 3σ rule is used (any continuous unimodal distribution at least 95% of the probability is within three sigma of the mean) (Pukelsheim, 1994). Based on that rule, input values a for which $I_h(a) > 3\sigma$ are considered implausible and are discarded. The iterative procedure is usually repeated until the difference between the regions in each wave becomes small or the posterior variance is suitably small (Andrianakis et al., 2015).

As BRAINS model is multidimensional ($T_i^{(r)}$ is linked with ΔT_{0_i}, ΔV_{rms_i}, V_{int_i} and Δz_i, referred as index h in equation 3.9), we opt to built separate implausibilities for every output h. A simple combination between the implausibility measures can be performed by taking the maximum implausibility $I_M(a) = maxI_h(a)$ which can be used to find regions of input values a with large $I_h(a)$ values. Note that the application of BHM is a fast process as it excludes the implausible space without needing to consider the full input and output space simultaneously, dissimilar to other calibration methods such as Markov Chain Monte Carlo (MCMC) or maximum likelihood methods where the calibration is performed taking into account all input / output parameters (Andrianakis et al., 2015).

3.3.1 1D example of GP and BHM

Before visualizing how Gaussian Processes and Bayesian History Matching can be adapted to the seismic reflection data world, an introductory 1D example of the statistical analysis is given below. The algorithm to generate this example was provided from the Department of Mathematical Sciences of Durham University, whereas a similar example can be also found in Andrianakis et al., 2015.

Consider the graph in the following Figure 3.2a where 6 data points are plotted. The points are generated from an underlying deterministic cosinusoidal function, $f(x) = cos(0.02\pi x)$, whose value is considered to be unknown in all but the 6 points. The first step is to fit a Gaussian Process model to the system, meaning to find a collection of most probable functions that pass from these data points and estimate, using Bayes rule, the posterior mean and covariance functions. Using the following GP model

$$\begin{gathered} m\big(f(a)\big) = 0 \\ k\big(f(a), f(a')\big) = \sigma^2 exp\left(-\frac{(a-a')^2}{d}\right) \end{gathered} \tag{3.11}$$

where $\sigma^2 = 1$ and $d = 15$, we end up with the result in Figure 3.2b (posterior mean function blue color, and 95 % credibility intervals red color). Note how the ± 2σ bounds increase away from the data points reflecting the choice of the covariance function parameters. Note also that the chosen form of the covariance structure represents our prior belief about how the underlying function behaves (for a description of different families of covariance functions and their characteristics see Rasmussen and Williams, 2006). In this example, the values of the hyperparameters σ, d were chosen manually to represent a smooth function in accordance with the parameter's input range (0 - 50). As noted previously, covariance's hyperparameters can be also derived through an optimization process using the training data.

After estimating the posterior results, the parameter space can be reduced by introducing independent empirical data. In Figure 3.3a, we incorporate the observation, $L = -0.7$ which we will be used to history match the functions. This observation is a measurement of a physical process (such as temperature, velocity, depth, etc.) with a level of uncertainty, observation error e_i in equation 3.10, ± 0.05. In 3.3b we plot the Implausibility measure (equation 3.10) which weighs the difference between observations L and the posterior mean results with respect to the uncertainties of the system. Furthermore, using Pukelsheim's 3σ rule (green line in 3.3b) the measure can be separated into implausible (red color band in 3.3a) and non - implausible regions (yellow to green color bands in 3.3a). So we can conclude by plotting $I(a)$, that values of input data a in regions between 0-17, 22-26 and 35-50 are incompatible with the requirement to match the observation $L = -0.7$.

Having separated implausible from non - implausible regions the parameter space can be further reduced by applying multiple iterations of BHM, which can be considered as a method of iterative global search (Caiado and Goldstein, 2015). This is accomplished by sampling the non - implausible space using different techniques such as Latin Hypercube design (Vernon et al., 2010), Evolutionary Monte Carlo algorithm (Williamson and Vernon, 2013), or p - variate normal distribution (Andrianakis et al., 2015). A subset of these generated samples are subsequently used to re - perform history matching. In Figs. 3.3c and 3.3d we introduce 1 and 2 new points from the non - implausible space at $x^{(7)} = 32$, $x^{(8)} = 18$, then refit the GP using these extra data points and recompute the implausibility measure. Note how after the last iteration (3.3d), the non - implausible space is further localised into constrained regions of 17-20 and 30-32.5. Further iterations can be calculated until one of the aforementioned criteria is satisfied. The same process can be followed in multidimensional examples where we want to quantify the uncertainty for more than one variable (such as in seismic data).

The method used to update information and estimate the posterior results for each iteration in the above example is Bayes linear (for a full description of this approach see Goldstein and Wooff, 2007). Briefly expressed, Bayes linear analysis uses the prior means, variances/covariances of given vectors along with observed values to update the information and estimate the adjusted means and variances/covariances. For a description of the analysis see Appendix C.

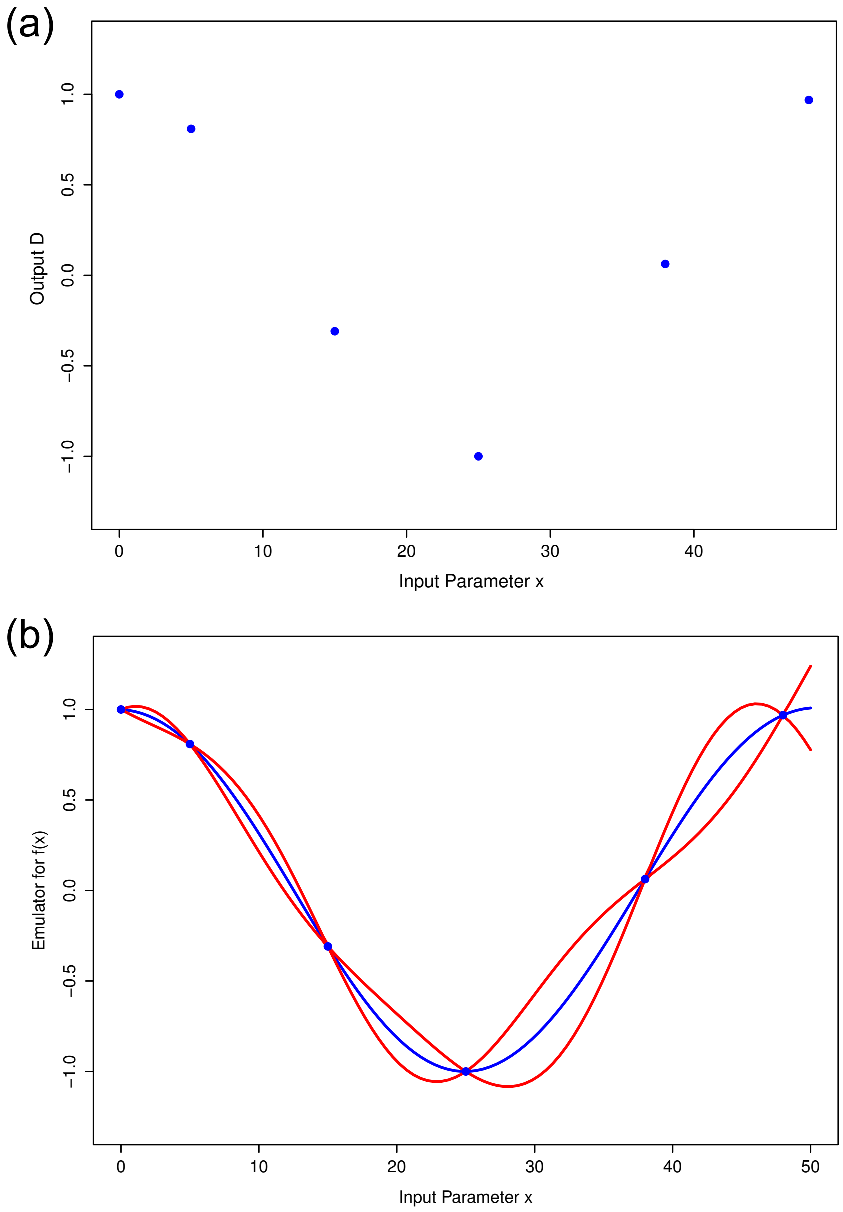

Figure 3.2: Gaussian process regression. (a) shows an underlying cosinusoidal function evaluated at 6 points. The goal is to retrieve the form of the underlying function along with a measure of uncertainty; (b) shows the retrieved functions using a GP model (see text for details) and the 6 original points from (a). The posterior mean function, blue color, $\pm\ 2\sigma$ credibility intervals (CI), red color. Note the increase of the CI away from the evaluated points reflecting our choice of GP model, mean/covariance functions and its hyperparameters.

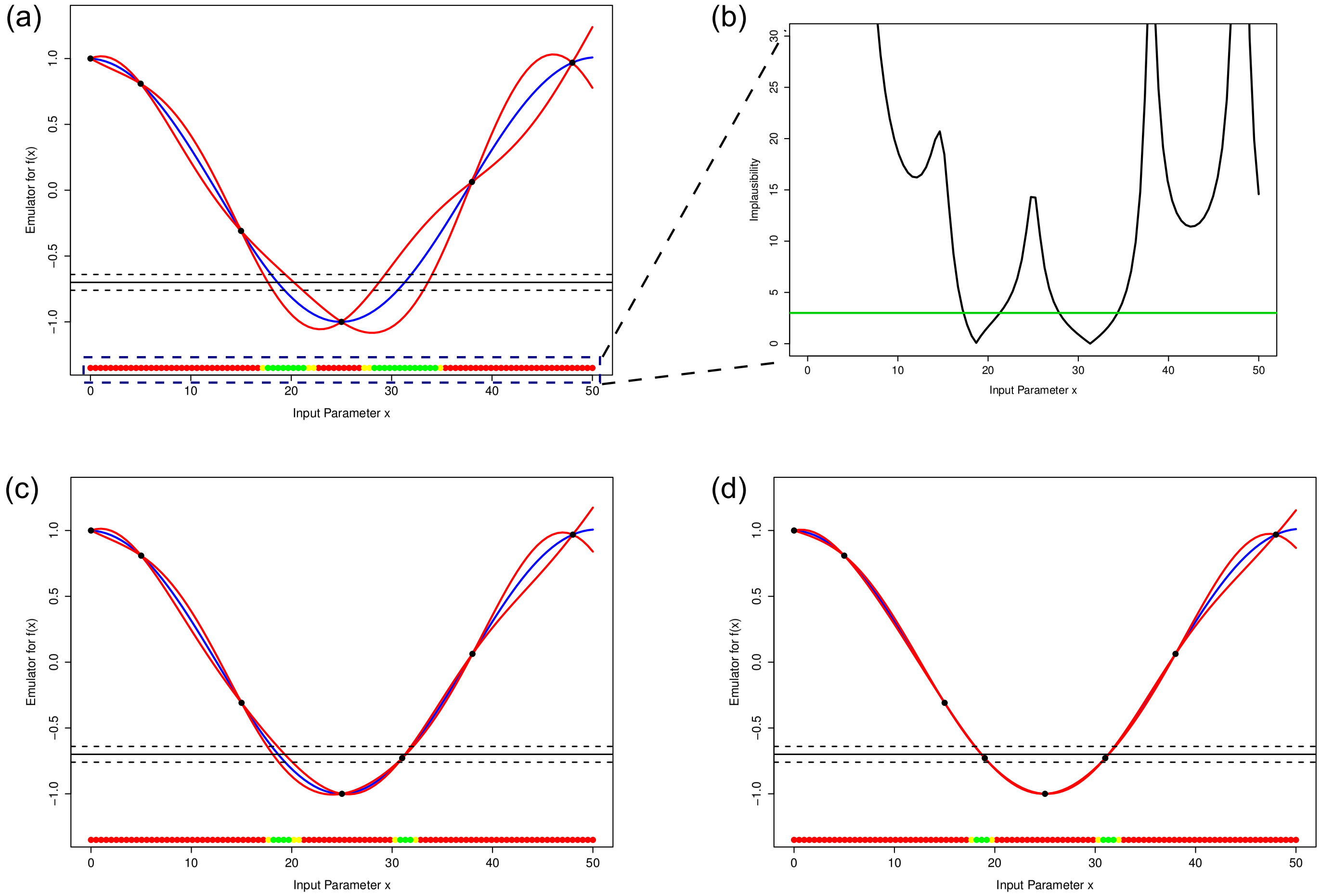

Figure 3.3: Bayesian History Matching (BHM). (a) shows the resulting GP regression as in 3.2b. We introduce an independent observation $L = -0.7$ which helps us to reduce the posterior space. Using equation 3.10 and taking into account all the uncertainties present in the system we can generate an Implausibility plot (black curve in (b)) and a cut - off criterion (green line in (b)). Thus, we can separate regions of the posterior space that are far from the observed value L, implausible space (red band at the bottom of (a)), from regions that are close to the observed value, non - implausible space (green band at the bottom of (a)). Having sequestered the non - implausible regions we can further reduce the posterior space by introducing more control points in that region, refit the GP model and recalculate the Implausibilty measure I, as shown in (c) and (d) where 1 and 2 extra points where added accordingly. Note how the non -implausible space shrinks and focuses into two distinct bands. The process terminates when stopping criteria are accomplished (see text for details).

3.3.2 GP and BHM in seismic reflection data processing

Following the discussion of the 1D example in the above section (3.3.1), the process of combining GP with Bayesian History Matching in seismic reflection processing is depicted in the following two Figs. 3.4, 3.5 for 1D (single gather) and 2D (multigather) cases respectively. Fig. 3.4 illustrates the transition between the standard semblance spectrum velocity model building to the probabilistic analysis. Consider the CMP gather in Fig. 3.4a and its mapping in semblance space in Fig. 3.4b. The process of estimating initial $T_0 - V_{rms}$ pairs for the seabed arrival at around 3.7 s TWT is related to picking the high semblance value so that our initial (prior) pick associated to this arrival (blue dot in Fig. 3.4b) is located close to the local maximum. Using the likelihood of the extended hyperbolic GP model (equations 3.6 - 3.8), along with this manually picked prior information, the posterior $T_0 - V_{rms}$ values can be estimated. Let the deduced posterior mean pair be represented by the white dot in semblance space (Fig. 3.4b), close to but possibly not at exactly the same location as the original prior pick. From the analysis, the ± 2 σ bounds are also retrieved (blue curves in 3.4a). Zoomed panel shows a number of red hyperbolic curves that lie inside the credibility intervals, where each curve is mapped to a different location in the semblance space (red dots).

Subsequently the algorithm uses the semblance spectrum as a tool to calibrate the posterior estimation and reduce the solution space. The tracked and stored amplitudes along a hyperbolic trend, are transformed into semblance space. These values contain information about the observed seismic signal, associated with the seabed arrival and are transformed into the yellow point in Fig. 3.4b. Using equation 3.10 we can now replace the semblance spectrum in 3.4b into the Implausibility spectrum in 3.4c and compared our posterior results relative to the observed signal L. The color band inside the ± 2 σ trends (blue color) indicates different level of Implausibility. In the regions where the posterior mean is far from the observed value L, the implausibility is considered large (red colour), relative to the uncertainties present in the system. This means that a pick in this region is unlikely to match the transformation of the observed seismic signal in the semblance space. On the contrary, if our pick is inside the lower implausibility regions it means that is more likely to match the observed values L.

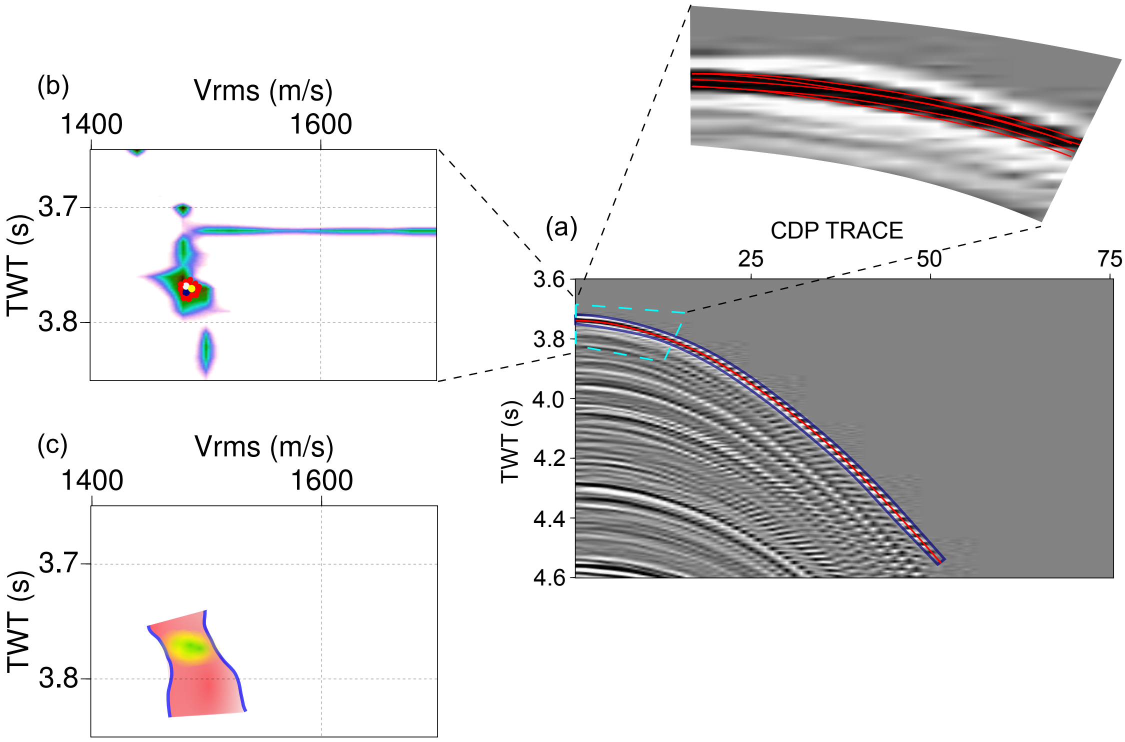

Figure 3.4: Pictorial example of 1D emulator. A CMP gather in (a) is being used for an initial semblance spectrum velocity analysis. With the aid of semblance spectrum in (b), an analyst can pick $T_0 - V_{rms}$ pairs for NMO correction and migration purposes. The pick represented by a blue dot is close to the local maximum value. Using this pick as prior information along with the GP model (equation 3.6 - 3.8), posterior results can be estimated bounded by the ± 2σ credibility intervals (blue curves in a). Posterior values transformed into semblance space shown in white dot in (b). Some of the curves that lie between the intervals are shown in zoomed panel and in semblance space (b) in red dots. Mapping the observed amplitudes of the hyperbolic trend of seabed arrival to semblance space, leads to the yellow point in (b). Using that independent information, an Implausibility panel can be generated for model calibration; In (c) blue curves indicate the ± 2σ credibility intervals, red areas represent high Implausibility measure, yellow / green low.

In a similar manner, Fig. 3.5 represents the combined use of 1D and 2D emulators. To emphasize the multidimensional nature of the GP - BHM approach this example depicts data in depth domain. The conventional semblance spectrum plots (Fig. 3.5a), for a number of CMP's along a profile, are picked to derive an initial estimate of $T_0 - V_{rms}$ pairs (red circles) associated with a number of seismic boundaries (Fig. 3.5b). The pairs don't include any uncertainty measurement and are linearly interpolated between non - adjacent CMP positions (gray dashed lines). As a result, this process leads to unique $T_0 - V_{rms}$ and $Z - V_{int.}$ volumes and unique subsurface images in time and depth domain. For the statistical approach, the $T_0 - V_{rms}$ pairs along with CMP gathers which contain the observed values L transformed in the semblance space, are used as input data to the local (1D) GP emulator to derive an estimate of the most probable functions evaluated at each picked pair. By means of calibration, we reduce the parameter space substituting the semblance spectrum by an implausibility spectrum which is calculated using equation 3.10. In Figure 3.5c, a $Z - V_{int.}$ map is presented, with the picked pairs being spatially linked with the preSDM image shown in Figure 3.5d. The coloured band inside the trend indicates different levels of implausibility. Again regions where the posterior mean is far from the observed values the implausibility is considered large (red color).

The process continues for all CMP locations where we provide prior pick information. The posterior mean and variance estimations for the picked pairs, serve as a guide to perform uncertainty analysis along the profile using the multi-gather 2D emulator (Appendix B.2) aiming to produce probabilistic estimates in the intra-CMP gathers area.

Note that the implausibility map is not restricted to the $z - V_{int.}$ space but it is calculated for any combination of T_0 or z with V_{rms} or $V_{int.}$ pairs. Each implausibility pair has different credibility bounds, locally (in every CMP location) and also laterally (along CMP locations), incorporating the different level of uncertainty in each picked pairs and spatial positions. Also, the regions between the prior information picks in each map are bounded by the posterior $\pm\ 2\sigma$ curves (blue dashed curves), with the posterior mean function curve (solid black curve) intersecting regions of lowest implausibility. The inter-layer representation of uncertainty can be achieved by interpolating the posterior results.

The final output of this process is a set of uncertainty quantification for all T_0, V_{rms}, V_{int} and Z parameters for each horizon of interest (Figure 3.5d). Hence, a by-product of the technique is that by quantifying the uncertainty of $V_{int.}$ values, we can generate a set of velocity fields bounded by the $\pm 2\sigma$ curves and produce different realizations of preSDM images. This analysis could be critical in regions with complex geology or for data rich in low frequency content and noise level, where a sole realization of imaged structures may not be sufficient for the assessment of risk at potential drill sites.

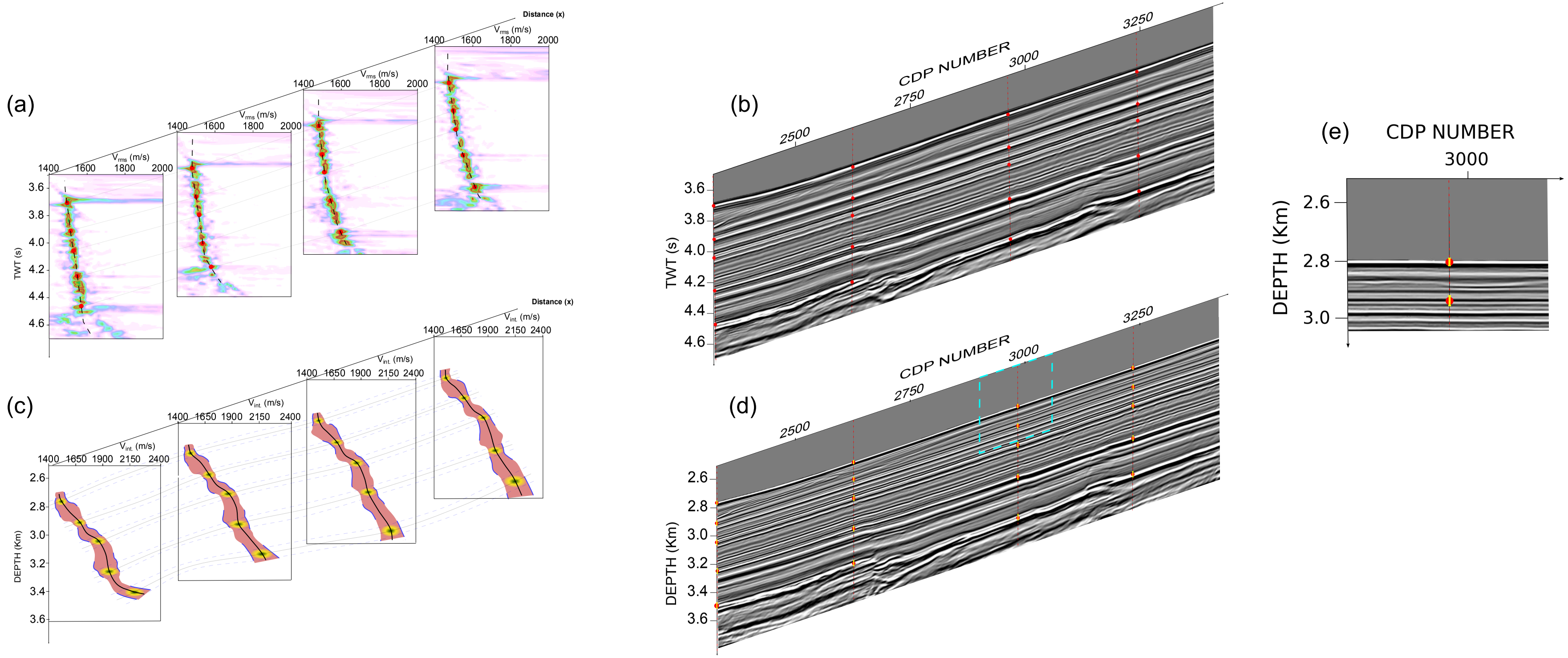

Figure 3.5: Schematic representation of the application of Gaussian Process and Bayesian History Matching (BHM) in seismic reflection data. (a) a number of semblance spectrum plots associated with CMP positions along a preSTM profile shown in (b). The T_0 - V_{rms} pairs, at semblance maxima (red circles), can be picked to follow seismic boundaries. Between analysis locations, the T_0 - V_{rms} pairs are linearly interpolated (dashed gray lines) but don't incorporate any uncertainty estimation; (c) Using GP and BHM, the semblance spectrum can be substituted by an implausibility map. Trends represent the implausibility map for z - $V_{int.}$ pairs, the latter being spatially linked with the preSDM profile in (d). Green regions, at prior picks, indicate low implausibility levels (most probable pairs) and red and yellow higher levels of implausibility. The user defined picks, both in depth and velocity domain, are bounded by the $\pm\, 2\sigma$ posterior uncertainty curves (blue dashed curves) with the posterior mean function (black solid curves) passing through the regions of lowest implausibility. The probabilistic approach gives an uncertainty estimation for each layer along a profile in positions where we don't provide prior information to define a depth velocity volume (black solid curves along layers, posterior mean function - blue dashed curves along layers, posterior $\pm\, 2\sigma$). The yellow bars on the preSDM image (d) represent the depth uncertainty from our analysis; (e) shows a zoomed version of the cyan dashed rectangle from (d).

3.4 Need for seismic data preconditioning

As mentioned in the above sections, BRAINS algorithm along with BHM uses the following information as input:

- Observed offsets, amplitude values and recorded time for reflection events in CMP gathers transformed into semblance space, $L = [\mathcal{A}_{ij}, x_j, T_{ij}^{(r)}]$.
- Prior information in a form of time - velocity picks ($T_0 - V_{rms}$ / $T_0 - V_{int.}$).

In practice we found that we required the seismic data to have the optimum temporal resolution, which for the data presented here is through deghosting, and good constraints on the values of T_0 values and both V_{rms} and $V_{int.}$ values, in order to achieve well constrained uncertainty estimations for the variables of interest for target horizons.

The first requirement is satisfied following flow 2, as described in detail in Chapter 2. CMP gathers after deghosting are expected to have more focused semblance spectra (see Figure 2.9) as the temporal resolution of the events should be increased. This can lead to an easier picking process and better map of probable hyperbolic trends from the GP emulators (Figure 3.4, 3.5).

Although not directly evident, the second requirement is critical to ensure that BRAINS predictions can be mapped into focused images not only in time but also in depth domain. Initially, the process of velocity model building, was taking place solely in time domain following a preSTM loop (picking in CMP domain, preSTM using Kirchhoff integral migration, picking residual move-out to update the velocity field, preSTM). This approach was chosen to produce quick images and T_0 - V_{rms} estimations as the velocity model building in depth domain (picking in CMP, preSDM, picking residual move-out in CIGs for velocity update, preSDM), even for isotropic case, is time consuming and computationally expensive (preSDM algorithm takes nearly 10 times longer to run compared to preSTM). However, it is known that the 1D representation of the velocity model used in the time migration algorithm (Hubral, 1977; Black and Brzostowski, 1994) sets a limit to the precision of the velocity model building for depth imaging (Jones, 2010, 2012). This means that although for structural interpretation purposes, a time domain representation of the subsurface is in some cases sufficient (Yilmaz, 2017), the process of estimating physical parameters such as velocities and depths and with their relevant uncertainties from surface seismic is more naturally associated with a depth domain processing sequence.

We opted to use the final version of the preSTM velocity field, output from the analysis in Chapter 2, as a starting model to perform isotropic Kirchhoff pre-stack depth migration (preSDM) on the deghosted CMP gathers. As our proposed site location for MBAS-4 lies in an area with a relatively simple geological structure (Fig. 1.2), we chose to run subsequent passes of vertical update (Deregowski, 1990) to refine our input velocity field until acceptably flat CIG gathers were produced. The preSDM algorithm was run in a half aperture of 4 Km and with a dip limit of 65°. The resulted depth migrated images gathers are stretched back to time using the smoothed version of the final velocity field for filtering and cosmetic final residual moveout correction (RMO) and converted back to depth domain for stacking. This additional editing of velocity field better constrains the prior information for input to the Bayesian model and simultaneously assures that the velocity model is suitable to preSDM applications.

Even in an environment with subhorizontal layers and relatively simple subsurface structure like our area of interest, the preSTM and preSDM profiles show some structural differences, with the latter showing local sharpening of the faulted zones close to well locations (Figure 3.6a, 3.6b). Furthermore, the deghosting procedure in the shot domain has produced a profile in depth domain with optimum spatial resolution and focusing. Thus, the application of pre-stack inverse filters serves as an amplitude shaping tool for products in both time and depthdomains, in contrast with implementing deterministic post-stack inverse filters (Sargent et al., 2011), only be applied to preSTM data in time domain.

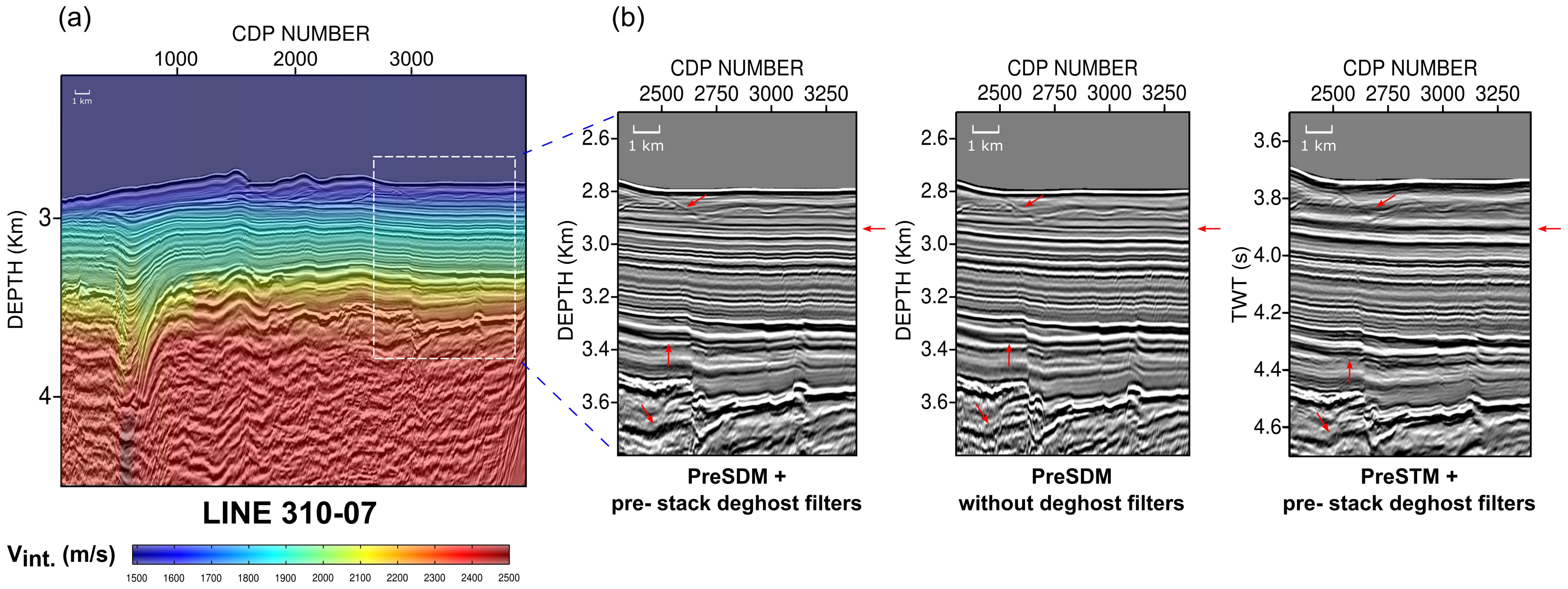

Figure 3.6: Comparison of preSTM and preSDM images. (a) PreSDM image generated using the final version (prior) $V_{int.}$ velocity field as input to migration algorithm (superimposed); (b) preSDM/preSTM images with and without prestack amplitude shaping. Red arrows indicate the most pronounced structural and spatial/temporal differences, in the shallowest and deeper parts of the images, emerged after application of depth migration and inverse filtering in the pre-stack domain. Although the geological structure is relatively simple, the image differences are locally considerable indicating the need for optimum elimination of ghost notches and velocity refinement through an iterative preSDM loop to better constrain the prior velocity information.

3.5 Depth predictions

Using the final version of the $T_0 - V_{rms}$, $T_0 - V_{int.}$ pairs as prior information for BRAINS along with the deghosted preSTM image gathers and performing BHM to reduce the parameter space, we calculate the posterior distribution of T_0, V_{rms}, V_{int} and z for each CMP value and make uncertainty estimations for the variables of interest. A comparison between the images produced using the prior and posterior mean V_{int} fields is given in Figure 3.7. The preSDM profiles don't indicate any major structural differences as the models used are nearly identical. This is a direct consequence of the Gaussian Process model and the prior picks, as the mean function in equation 3.6 encodes the hyperbolic approximation that underpins the velocity analysis process. This approximation is also used to define the moveout trajectory for the semblance spectrum calculation at the CMP positions along a profile. So it is no surprise that the closer the prior $T_0 - V_{rms}$ or $T_0 - V_{int.}$ picks are to the local maxima semblance value, the less difference will be observed between prior and posterior mean models and by inference the depth images.

However, some subtle differences can be resolved after subtracting the posterior mean preSDM image (3.7b) from its prior equivalent (3.7a), resulting in a structural difference plot (3.7c, 3.7d). The images' dissimilar features are now emphasized, indicating regions of differential depth shift. As the migration algorithm repositions the time signal to the depth domain in a top-down basis, the cumulative differences in the velocity field with respect to depth get larger and map to more pronounced depth image shifts as the depth increases. Note that as the velocity fields show only minor differences, this effect generates a vertical structural stretch with no resolvable lateral structural changes.

In terms of depths predictions, although we used an isotropic approximation of preSDM, the tie with the DSDP-258 borehole information is acceptable with a misfit of approximately 4 % (21 m) at the glauconitic sandstones level (Figs. 3.8a, 3.8b). The large misfit at the bottom shales level is attributed to the indistinct reflectivity boundary between limestones and shales (Figs. 3.8a, 3.8b), that was not within the recovered core at DSDP-258. Note, however, that the estimated depths from DSDP-258 are consistent with the ± 2σ credibility intervals. This result reassures us that our posterior mean velocity field is a good representation of the local velocity field and, by inference, can be used to make predictions about the depths to horizons in the potential drill sites.

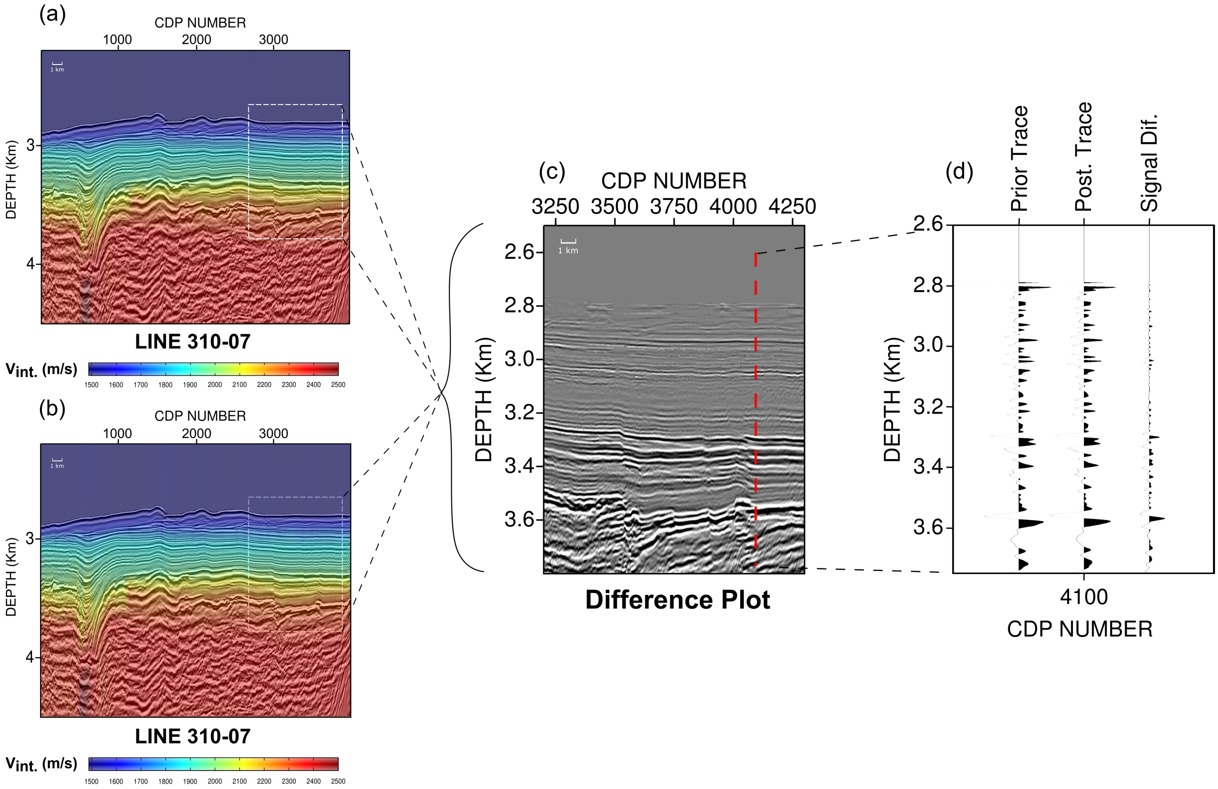

Figure 3.7: Comparison betweeen prior and posterior mean preSDM images. (a) Image generated using the prior V_{int} velocity field (superimposed); (b) Image using the posterior mean V_{int} velocity field (superimposed); (c) The velocity fields and images don't present any significant differences, therefore possible structural changes can become apparent after using a structural difference plot, which is the result of subtracting the posterior mean image (b) from prior image (a). The image features' changes are more pronounced in the deeper parts of the profile as a direct consequence of top-down reposition of the signal; (d) Example of signal difference extracted from a depth window of CDP number 4100 (red dashed line in (c)), as calculated by subtracting the prior from the posterior signal.

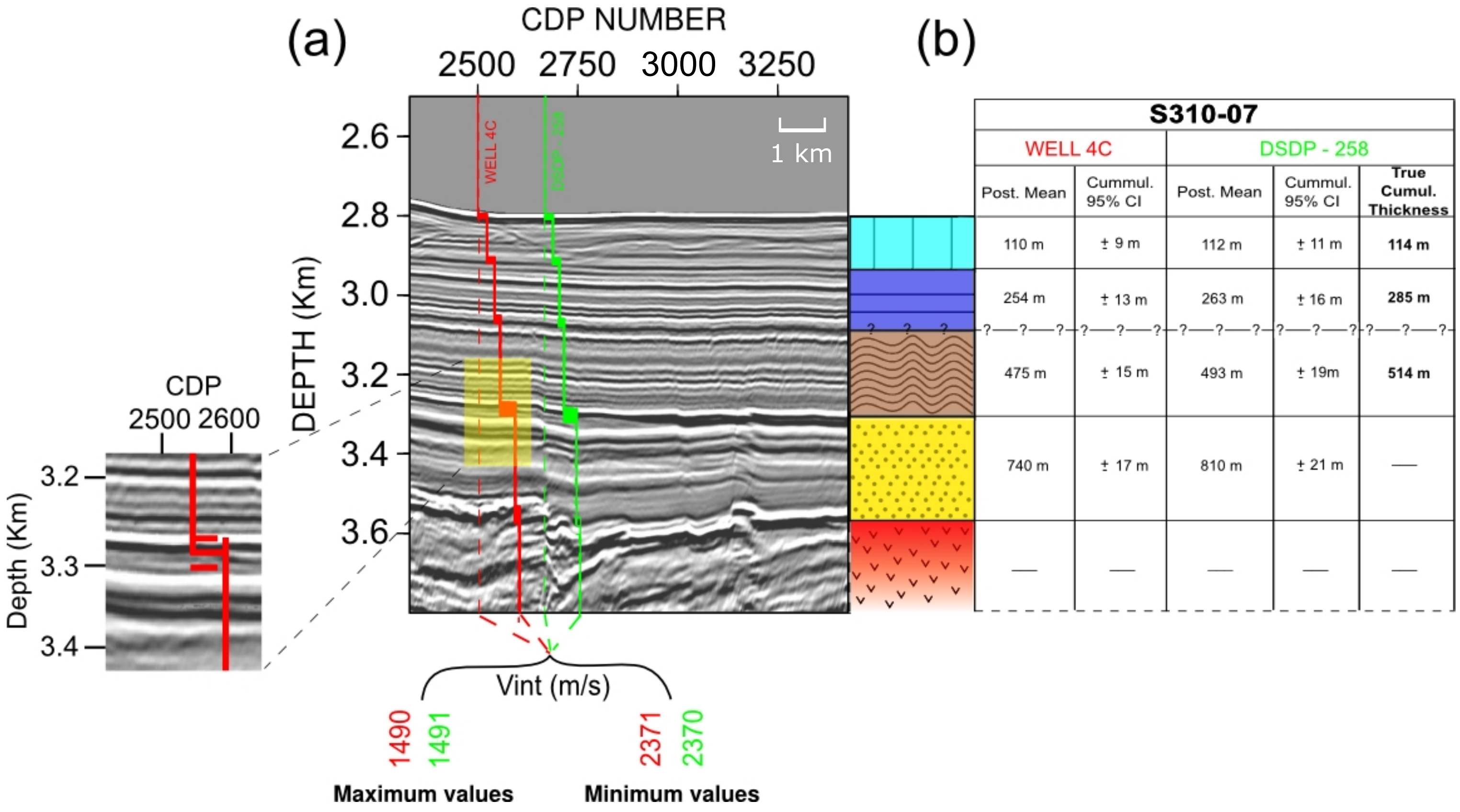

S310-07				
WELL 4C		DSDP - 258		
Post. Mean	Cummul. 95% CI	Post. Mean	Cummul. 95% CI	True Cumul. Thickness
110 m	± 9 m	112 m	± 11 m	**114 m**
254 m	± 13 m	263 m	± 16 m	**285 m**
475 m	± 15 m	493 m	± 19m	**514 m**
740 m	± 17 m	810 m	± 21 m	—
—	—	—	—	—

Figure 3.8: Posterior depth results. (a) PreSDM image for S310-07 profile. Dashed vertical lines represent the wells' locations, with the posterior range of interval velocity/depth values for each layer superimposed as filled coloured regions (red, green colours for Well 4C/MBAS-4 and DSDP-258 respectively). Zoomed panel shows the region associated with the yellow rectangle as an example of the posterior mean and $\pm 2\sigma$ trends for top glauconitic sandstones (red solid trend in zoom represent posterior mean values, dashed lines in zoom the $\pm 2\sigma$ intervals respectively); (b) The predictions for the cumulative thickness of drilling targets for each well location, associated with the lithological interpretation from Fig. 1.2.

3.6 Towards probabilistic imaging

One of the most important aspects associated with the probabilistic quantification of V_{int}, T_0 , z values though the process of GP and BHM is the capability to generate random samples by sampling from their posterior distribution (using the posterior mean and variance estimates). Subsequently, these sampled sets for a number of layers can be used to produce a new sets of preSDM images. Thus, multiple realizations of the horizons of interest can be mapped in depth domain and all can be directly compared with the prior mean and posterior mean depth images. In a similar manner, any randomly generated image can be subtracted from either prior/posterior mean images to produce the structural difference maps as shown in Figure 3.7c.

The above discussion leads to the concept of probabilistic imaging, where uncertainty estimations are mapped into depth images for a more complete geophysical characterization of the subsurface. Some of the most recent examples of this approach can be found in Chitu et al., 2008; Lewis et al., 2015; Messud et al., 2017; Hilburn et al., 2017; Protasov et al., 2017. The significance of the non-unique representation of the sub-surface is critical in areas where strong lateral velocity variations are present, especially in salt body areas where incomplete or suboptimum imaging is driven by the inefficiency to produce a robust velocity field which uniquely represents the geobody. Indeed, in some of these areas, where specialized acquisition techniques and migration algorithms are being currently used (Wide-Azimuth (WAZ) or Coil acquisition combined with Reverse-Time Migration (RTM)), the problem is not the illumination of the target but the velocity field which leads to erroneous results (Shen et al., 2018).

The, sometimes, impossible task of building a suitable velocity field can be alternatively addressed by generating a set of most probable realizations of specific boundaries (such as a salt-sediments interface or the base of a basaltic sequence) driven by randomly generated velocity models as produced from the statistical analysis of the 'best guess' velocity field (where the term 'best guess' defines the final velocity field as input to a probabilistic estimation algorithm). In our case the algorithm can produce uncertainty estimations using 'best guess' models which follow the layered approximation of the velocity field, built though a vertical update loop or using a layered model tomographic inversion.

As a proof of context for probabilistic imaging, in figure 3.9, we present a number of structural difference plots, produced by subtracting each resulted preSDM image realization, derived using a probabilistic velocity field, from the posterior mean image. The plots display a number of probable depth and shape positions for geological boundaries of interest, in accordance with the differences between the sampled velocity fields and the posterior mean velocity field (Figures 3.9a, 3.9c ± 2σ end members for posterior black shales velocity, 3.9d, 3.9e, 3.9f randomly generated values for all velocity layers, 3.9b posterior mean image). As a natural consequence of depth migration, the locations where the differences are closer to extreme values, the local image changes (localised red maxima in 3.9c, 3.9e).

The randomly generated values, bounded by the ± 2σ credibility intervals for every CMP position and every velocity layer, incorporate a confidence measure associated to each picked pair which is a combination of the observed data (amplitude values $\mathcal{A}_{ij}$, recorded travel time $T_{ij}^{(r)}$, distance x_j), and prior picks positions. Thus, the retrieved vertical pattern of blue (negative) and red (positive) regions in the normalized velocity difference plots in figure 3.9 approximate the GP 2D emulator pattern depicted in figures 3.2, 3.3, where the ± 2σ curves, along a velocity layer, show decreased uncertainty close to the prior picked CMP positions and increased away from them. These regions have a spacing of approximately 50 CMPs, which is determined by the velocity picking spacing used to generate the prior velocity model for time and depth migration (Table 2.2).

This spacing is in accordance with the assumption that the ± 2σ probabilistic representations of a horizon mapped into depth domain, is unrealistic from a geological point of view without incorporating a correlation term during the uncertainty estimation that contrains the lateral variability (Thore et al., 2002). In our data set, this correlation term is associated with the covariance function and particularly with the scale $d_i(x_c)$ in the denominator of the covariance function for the 2D GP emulator, representing how picked points in the velocity field are spatially linked along the 2D profile. By inference, it is reasonable to assume that the contribution of this factor is mapped from the velocity domain to the depth domain resulting in more plausible image realizations.

It is worth noting at this point, that the common practice in oil industry for revealing different characteristics and structural discrepancies of the probabilistic preSDM images is to perform map demigration. Map demigration is the exact opposite of map migration wherein a particular horizon is picked in preSDM image and using its associated $V_{int.}$ values, it is mapped back into time domain (Jones, 2014). Therefore, probabilistically derived $V_{int.}$ values for the same boundary can reposition the depth samples into different time domain representations (in a sense the inverse of Fig. 3.1c). Examples of estimating structural uncertainties can be found in Thore et al., 2002 and Letki et al., 2013. In our procedure, we followed an alternative approach as map demigration requires specialized algorithms which weren't available at the time of processing the data. We consider that map demigration is the optimum method to simultaneously show the possible realizations of a horizon of interest and could be readily linked to the sampling of our velocity model.

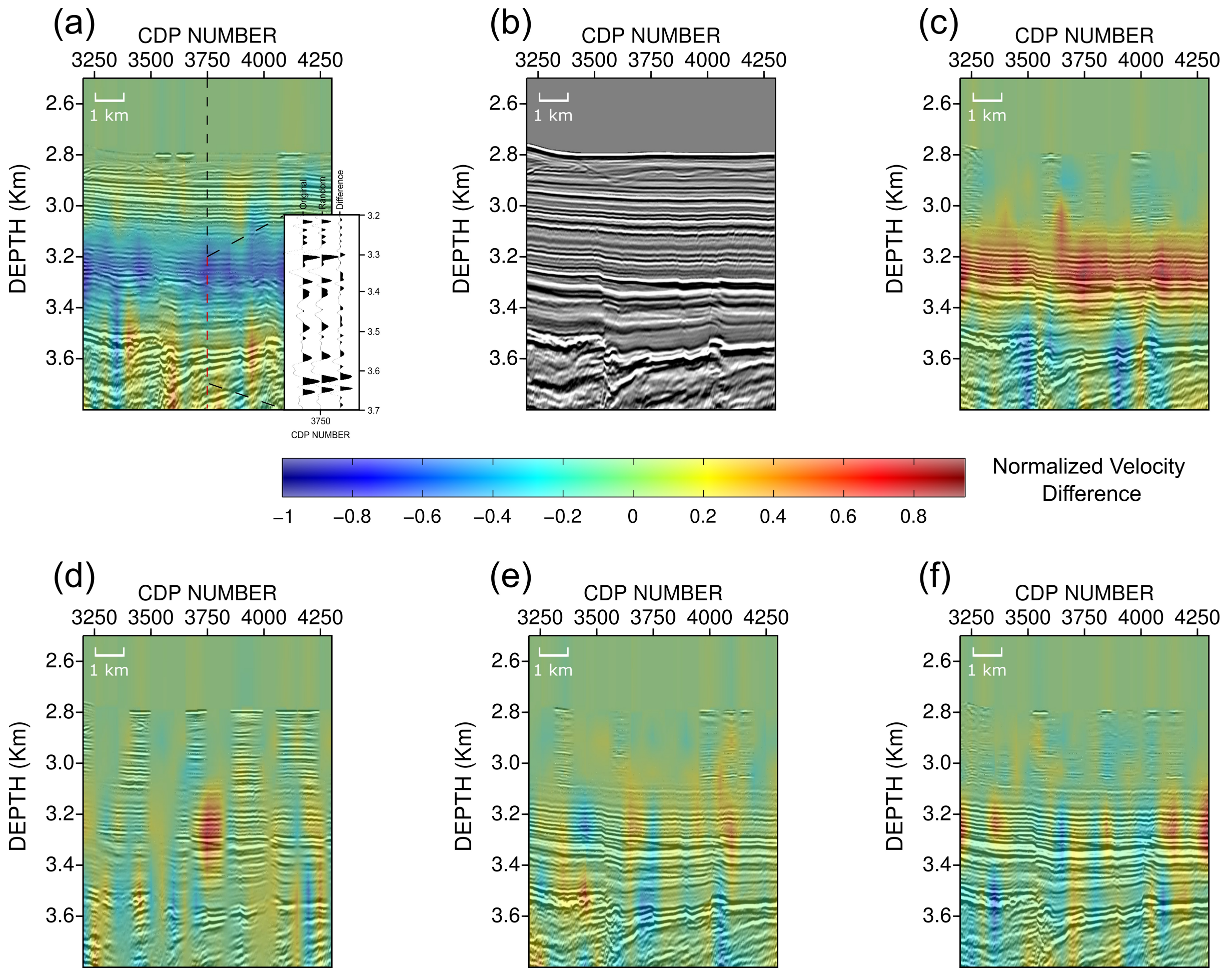

Figure 3.9: Probabilistic imaging example. (a)-(f) a number of preSDM structural difference plots, using different $V_{int.}$ fields, sampled from the posterior distribution. The superimposed coloured map represents the normalized difference between the randomly generated $V_{int.}$ velocity fields used to produce each profile and the posterior mean; (a), (c) demonstrate the $\pm\, 2\sigma$ end members for black shales velocity layer with the remaining layers pre-set to take random values from the posterior distribution. Insert on (a) shows how the difference plot is generated; (b) same as in 3.8a; (d), (e), (f) represent fields allowed to span the total $V_{int.}$ space of the posterior distribution. Note, especially, in (d), (e), (f) the pattern in the velocity difference, indicated by alternating blue / red regions congruent to the GP regression using training data picked every 50 CMPs.

3.7 Conclusion

In this chapter, we presented a method to quantify the uncertainty of depths and related values in seismic reflection data processing using seismic data from profile S310-07. Our seismic processing strategy and subsequent statistical analysis were conducted into two distinct parts. First, we aimed to improve the temporal and spatial resolution of the region close to the proposed drill sites by performing source's and receiver's notch compensation in the pre-stack domain (see Chapter 2). Subsequently, we focused on the velocity model building in the time and depth domain in order to generate well focused images and constrained prior information for input to the BRAINS model. By using Gaussian Process emulators conjointly with Bayesian History Matching (BHM), we managed to retrieve the depths of the key horizons as known from DSDP-258 borehole and make predictions about the expected depths of same horizons for the proposed drill sites.

As the probabilistic approach results in a distribution estimation for $V_{int.}$, we generated sets of new velocity models and perform preSDM to produce different image realizations. In this way, we were able to map differences in velocity models to differences in image features for our horizons of interest.

The GP emulators are deliberately parametrized to exclude explicit uncertainty estimations for anisotropic parameters (ε, δ). Instead, the anisotropic effects during seismic wave propagation are unified in the model discrepancy term (ε_{ij} or σ_{n_i}), a term which is easier to tune and with the synergy of prior information of picked $\{V_{rms},\ T_0\}$ or $\{V_{int.},\ T_0\}$ pairs, it allows constrained posterior results. The inclusion of the anisotropic terms as independent variables in our model along with their explicit uncertainty estimation, would require well log information to provide both 'true' seismic velocities and well to seismic tie to unambiguously map observed reflectivities from seismic data to lithological boundaries. Even in that case, their incorporation could pose problems concerning the robustness of their uncertainty estimations, as in time domain the terms are accessed solely through η parameter (Alkhalifah and Tsvankin, 1995; Alkhalifah, 1997), a term that is strongly coupled to the small-offset moveout velocity (V_{nmo}), that the calculation of a useful uncertainty estimation is questionable.

The statistical model described in this paper is based on the discrete layer velocity model representation and can be easily coupled with a layer-based tomographic inversion scheme. The challenge will be to incorporate an analogous model to gridded or hybrid velocity model representations (Jones et al., 2007) for complex geological structures, where the velocity regime is controlled by a combination of vertical compaction gradients and sharp velocity contrasts.

In the following Chapter 4, the predicted depths to drilling targets will be juxtaposed with respect to the true depths as extracted from the core/well logs obtained during the recent IODP expedition, leg 369. We will proceed with the well-seismic tie process using the sonic and density log information and the preSTM profile S310-07. This will enable matching the reflectivity from the seismic data to lithological interfaces to locally constrain the interpretation of MB. Moreover, by utilising a smooth version of the $V_{inst.}$ field from sonic log, an example of anisotropic preSDM will be provided. The approach will restore the drilling targets to their correct depth level, but also output an optimal focused image.

Chapter 4

Well - Seismic tie

In Chapter 3, we described an optimum processing flow in depth domain to combine seismic reflection data processing with Bayesian statistics. From the statistical analysis a set of predictions for the depths to drilling targets along with their uncertainty estimations was extracted. Using the resulting posterior distribution, random velocity fields were generated bounded by the $\pm 2\sigma$ values and produced multiple realizations of the subsurface.

In the following, the true information for the physical properties of lithological units drilled during the IODP project, leg 369 (Hobbs et al., 2017) will be used, to correlate the seismic reflectivity in preSTM profiles with impedance contrasts evaluated at the wells positions. By inference, time domain reflectivity will be mapped onto the isotropic preSDM profile and a comparison between the image with the true depths measured from well/core log analysis will be performed. Using the well-seismic tie process the seismic boundaries are matched, to an improved degree of accuracy, with geological boundaries and thereby the procedure to map time domain image to depth domain.

As the penultimate step of the project, we will use the 'instantaneous primary wave velocity information', $V_{inst.}$, as extracted from well log and rerun preSDM to test the match between the observed with the modelled depth targets. The final goal is to apply anisotropic preSDM to generate an image honouring the anisotropic effects predominately caused by the presence of a sequence of black shales. The aforementioned steps will be applied in site U1513 which was cored at the planned well location MBAS-4C.

4.1 Correlating seismic reflection data with well logs

Although the processing sequences described in Chapters 2, 3 optimally imaged the subsurface, it is only by the use of independent well log information that it is possible to unambiguously correlate geological boundaries with observed reflectivity in seismic image. With a well - seismic tie we can achieve the following (Simm and Bacon, 2014):

- zero phasing the data by comparing the synthetically derived seismic data, from well log impedance, with the surface seismic preSTM profiles;
- link the observed reflectivity in the image with lithological boundaries from the well information;
- extract a statistical wavelet representing the link between seismic data adjacent to well location and the true information from well logs (reflection series);
- offset scaling for Amplitude Variation with Offset (AVO) analysis.

The well to seismic tie procedure can be summarised by the following (White and Simm, 2003):

- use of sonic and density logs to generate the reflectivity series and impedance log. The density/sonic information must be edited and calibrated appropriately to improve the correlation result (White, 1997);
- use of seismic reflection data and observed reflectivity from well log to estimate the seismic wavelet. This includes estimating the goodness-of-fit and accuracy, its phase and delay and the best match location.

The goodness-of-fit and accuracy are calculated through the statistical measures of predictability (PEP) and normalised mean square error ($NMSE$) respectively. The PEP represents the square of the cross-correlation ($PEP \approx R^2$) between the synthetically derived signal at well location and the windowed time domain signal of a stacked CDP at or close to well location. The $NMSE$ is related to the phase error between the two signals (Simm and Bacon, 2014). A well-seismic tie is considered good for $PEP > 0.7$, $NMSE < 0.1$ (Simm and Bacon, 2014). Note that a robust analysis should include both measures as the sole usage of PEP is biased with respect to the analysis time window as it increases with decreasing time analysis length (White, 1997).

Also, the estimated wavelet has a characteristic phase and time delay (time in ms). Both variables are estimated using the phase-frequency plot after linearly fitting the data, where the intercept represents the average phase over a given frequency band and the slope the timing in ms (Simm and Bacon, 2014). As the extracted wavelet represents the impulse response of the best match filter between the zero phase modelled signal from well log information and the embedded seismic signal, the final phase/delay values corresponds to the relative phase and time shift that we must apply to the seismic data (preSTM image) to optimally match the observed with modelled data. Note that the estimation of phase and delay values from the linear fit is strongly dependent on the bandwidth of the signal used, with a broader frequency band resulting in more constrained results (White and Simm, 2003).

During the matching process, the PEP value is calculated over a specified spatial range and not around the well location. This means that the maximum PEP position around well location may not be congruent with each other. This potential mismatch on location is to address time migration issues especially in areas with dipping structures, where poor imaging or 3D effects may result in an incorrect reposition of the data. Thus, in the majority of cases the shifted maximum PEP location is located updip with respect to well area (Simm and Bacon, 2014).

A slightly more subtle effect, commonly encountered during the well-seismic tie, is related to the potential stretch or squeeze of the resulted modelled signal in trying to optimise the match and improve PEP values. Misties between synthetic and seismic data can be primarily attributed to imaging issues emanating from incorrect (or incorrectly sampled) velocity field, migration algorithm used or even 3D effects. In reality, by stretching/squeezing the seismic data a change in the interval velocity field is also performed to compensate for the local distortion applied to time domain signal to map the observed depths from the well logs. In case of dipping layers, due to ray path assumption (normal incidence rays/image rays) a substantial stretch/squeeze is accompanied by a spatial shift of the best match location from the well head (White, 1997; White, 1998).

In many cases, stretching/squeezing is the accepted practice due to the inability of the interpreter to access the pre-stack data and check the quality of CDP gathers. Where direct access to the pre-stack data is possible, the mismatch is an opportunity to recheck the robustness of the velocity field and assess the flattens of the gathers. The process of stretch/squeeze is controversial and should be only used in regions with complex subsurface targets, where time migration algorithm doesn't suffice to reposition the signal correctly or where 3D effects may be present. In all the other cases, it is preferable to revisit or even reprocess (if feasible) a small segment of the pre-stack data to improve the focusing and the reposition of subsurface targets.

4.2 Petrophysical Data - Site U1513

Site U1513 was cored at the pre-drill site Well 4C and drilled in two phases due to an initial collapse of the borehole. At this site, five holes were cored under names U1513A, U1513B, U1513C U1513D, and U1513E in neighbouring locations (maximum distance 50 m). This is recommended IODP practice to piston core the upper soft sediment to maximise recovery or for specialized analysis of recent deposits to monitor ongoing changes in climate (U1513A, B & C), before rotary coring the consolidated rock (U1513D & E). The core and the relevant petrophysical data acquired, were described and edited during the IODP expedition (Hobbs et al., 2017). From the analysis, which included: examination of smear slides and thin sections; biostratigraphy; X-ray diffraction (XRD) and X-ray fluorescence (XRF); six lithostratigraphic units are identified and reported:

- Unit I: 64.93 m thick sequence of light gray to pale yellow calcareous ooze and nannofossil ooze with sponge spicules. **Age: Pleistocene - late Miocene**;
- Unit II: 182.93 m thick sequence of white to greenish gray calcareous and nannofossil ooze/chalk and clayey nannofossil chalk with intervals of silicified limestone. **Age: Campanian-Cenomanian**;
- Unit III: 21.87 m thick sequence of alternating greenish gray, light gray, and black nannofossil rich claystone. **Age: Cenomanian**;
- Unit IV: 187.12 m thick sequence of black claystone and nannofossil-rich claystone. **Age: Cenomanian-Albian**;
- Unit V: 234.25 m thick sequence of sandstone with siltstone and silty claystone. **Age: Aptian-Valanginian**;
- Unit VI: 82.2 m thick alternation of extrusive basalt flows and breccia intruded by a diabase dike.

The available well log data were imported in the petrophysical analysis software, $RokDoc^{TM}$. Based on the thickness and the measured seabed depth at the site location, the lithostratigraphic units were assigned in depth windows (working intervals). The data are of good quality although due to time constraints, the V_p and V_s logs were not acquired over the full black claystones sequence hindering the estimation of the velocity of the medium. The logs from cored holes (U1513A to U1513E) were merged into a single plot for further processing and editing. A sub-set of the logs for the units of interest are presented in Fig. 4.1. From left to right the figure shows the caliper, gamma ray, resistivity, density logs and the incomplete V_p and V_s logs.

An accepted solution to fill the gaps in the velocity logs is to try to find an empirical relationship between the observed density values for the unit of interest with respect to the velocity logs (Gardner, G. H. F. et al., 1974). Although incomplete, the V_p and V_s logs do have some measurements at the top and bottom of the unit. As, lithostratigraphically, they are part of the same unit this empirical relationship should be representative and can potentially reproduce the missing velocity values. However, due to the number of missing points, the modelled values can only be an estimation of the subsurface and cannot exactly replicate the 'true' velocities of the medium.

Initially, a map from ρ to V_p was performed using the crossplots of their observed values (Fig. 4.2). Using the observed values of V_p and ρ at the depth window of 246 m - 455 m and fitting a linear trend on the data a numerical relationship between the two variables was established (Fig. 4.2). Subsequently, using the modelled V_p log a map into V_s space was performed. Tests were carried out to model efficiently the missing V_s values using a $V_p - V_s$ crossplot, however the results appeared to lack information and not directly comparable to the V_p trend. To produce a realistic model, an empirical approach was tested by implementing a $RokDoc^{TM}$ built-in linear relationship. The two functions used for the empirical transformation $\rho \rightarrow V_p \rightarrow V_s$ were the following:

$$\begin{aligned} V_p &= 514\rho + 830 \\ V_s &= 0.8621 V_p - 1.1724. \end{aligned} \tag{4.1}$$

The simplicity of the above equations and the linearity assumption can be justified from the uniform trend of the observed ρ log at the black claystones level. The resulted modelled V_p, V_s data in Fig. 4.3 show the optimum match with the top-bottom available data in the velocity logs and their trend appear similarly smooth with the density log. This does not unambiguously prove that the modelled velocity values are correct but it is indicative of a robust mapping between ρ and V_p, V_s. Taking into account the modelled results and due to time constraints no alternative modelling options were further tested. Although out of the scope of the well – seismic tie procedure, an interesting characteristic of the well logs is related to the Gamma ray response directly above the glauconitic sandstone level, where a high pick value is recorded. The latter may be related with a relative increase in the organic matter content at that particular depth window. However, a meticulous petrophysical analysis is needed to describe the response's origin and correlate it with other available log measurements.

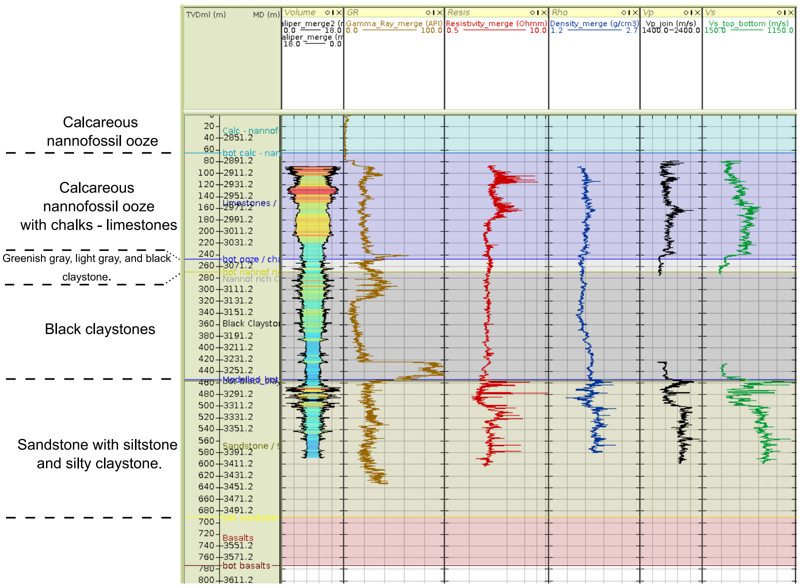

Figure 4.1: Hole U1513 log data. The following well logs are presented (left to right): Caliper log, Gamma ray log, Resistivity log, Density (ρ) log, V_p log, V_s log. The depth windows under different colors represent the main lithostratigraphic units as reported during the subsequent analysis of core logs from the same location (description of the main units where log data acquired on the left panel). Note that in the black claystones/shales interval the V_p and V_s data are incomplete.

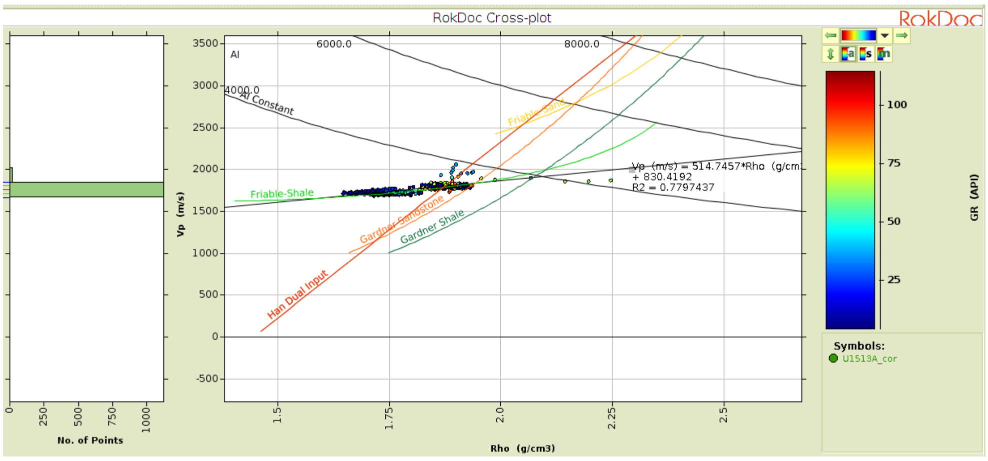

Figure 4.2: Establishing empirical relationship between ρ, V_p using crossplot. The ρ-V_p crossplot, with the linear fit describing their relationship.

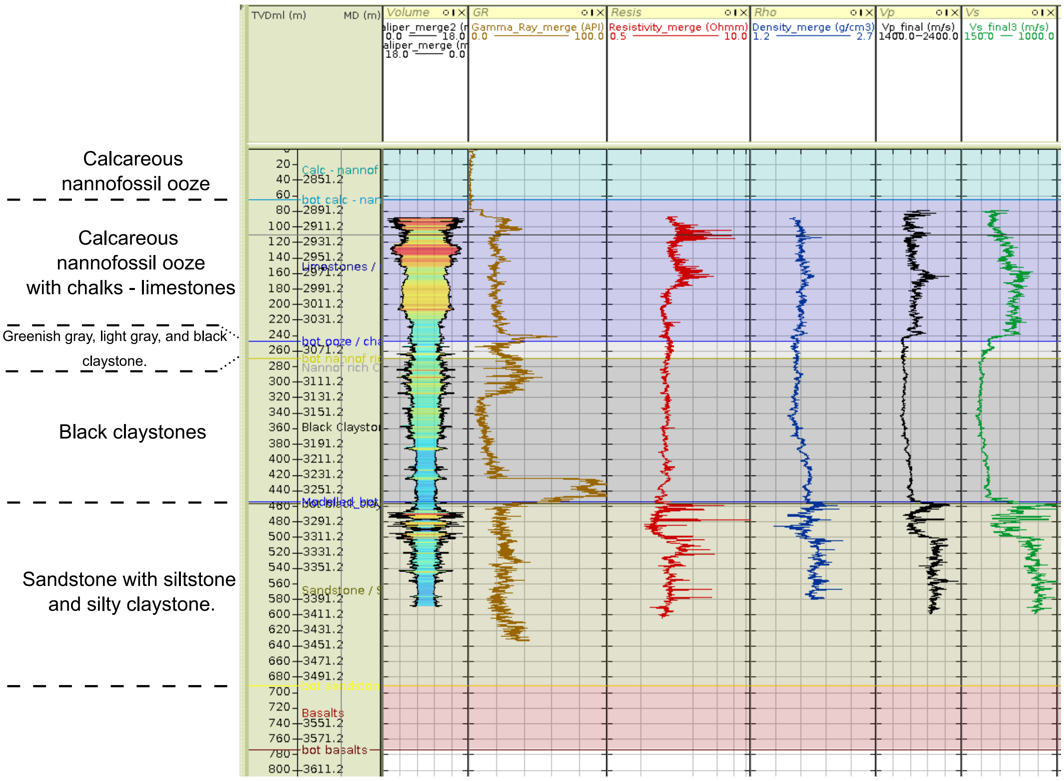

Figure 4.3: Model V_p, V_s logs for black shales unit. Using crossplots of ρ - V_p and V_p - V_s a map of the density log into velocity space can be achieved. The modelled logs at the black shales level appears to match the top/bottom true velocity trends indicating, to a first approximation, that optimum linear relationships were used (description of the main units where log data acquired on the left panel).

4.3 Well - Seismic tie

After editing the V_p - V_s logs they can be used in conjunction with the density log to generate the 'true' reflectivity of the media, which is then convolved with an idealised synthetic wavelet. This is directly compared with the surface seismic reflectivity and is used to constrain its phase and most importantly to unambiguously map reflectivity in time domain with geological boundaries in the depth domain.

Initially the process involves the creation of Acoustic Impedance (AI) log by multiplying the V_p with ρ log data. From the AI log, the reflectivity series for every sample can be calculated using the equation

$$R = \frac{AI_n - AI_{n-1}}{AI_n + AI_{n-1}} \tag{4.2}$$

The creation of reflectivity series and the subsequent tying of well information with seismic data assumes that the well logs are mapped from depth to time domain. Due to an incomplete set of checkshots/VSP data the conversion was performed using the depth-velocity measurements directly from the V_p data. There is an automatic algorithm in RokDoc to compute the velocity function assuming a constant water velocity of 1490 m/s for the water layer.

A characteristic associated with this depth to time mapping is the resampling of the time domain log data at a finer sampling interval compared to their depth domain representation. The approach, used to avoid possible aliasing effects (White and Simm, 2003), means that the resulting synthetic trace computed after convolving the reflectivity series with a wavelet, of a same sample rate, will have an equally fine sampling interval.

In order to perform a realistic comparison of the synthetic with the surface seismic signal it is common to average the reflectivity/AI in a series of blocks. An appropriate averaging method, in regions where large velocity contrasts are present, is the Backus average (Backus, 1962). The calculation is performed with respect to the moduli of the units in a given depth/time window (Simm and Bacon, 2014). In a sense, this average incorporates the effects of the velocity dispersion between sonic logs and frequency content of seismic data (White and Simm, 2003). In our data set, the ρ, V_p logs, were discretized using a depth window of 10 m.

After mapping the well data into the time domain, the well-seismic tie procedure followed. The approach uses the ‘matching technique’ (for complete description see White and Simm, 2003). The technique extracts the wavelet following a least squares approach by treating the data (reflectivity series and seismic data) as a noisy input-noisy output problem (Walden and White, 1998). The extracted wavelet represents the link between the surface seismic trace close to well location and the calculated reflectivity from well data.

The matching technique is presented pictorially in the following Figs. 4.4, 4.5, 4.6). Initially, the optimised anisotropic preSTM S310-07 profile, including ghost arrivals was imported to RokDoc (for well-seismic tie process using the deghosted preSTM anisotropic data set as input see section 5.4). In order to keep a consistent amplitude level for all the frequencies present in the time-windowed signal (Fig. 4.4), the profile was time-invariantly bandpass filtered in the band 4 - 9 - 100 - 125 Hz as opposed to the time-variant filtered described in Table 2.2. Moreover, the AGC gain was not applied and it was replaced by a post-stack divergence correction using the velocity field built for preSTM purposes.

Fig. 4.4 shows an example of well-seismic tie. The matching of reflection coefficient series to the seismic data is limited to the time window 3841-4341 ms and within a spatial range of 100 CDPs. The three sets of gathers in 4.4a indicate the best match location, the modelled traces and the observed traces close to well location (left, middle and right set respectively - the middle set shows the result after convolving the reflectivity function with the extracted wavelet). An effective wavelet length of 124 ms was extracted. The match appears to be good as both the amplitude and mainly the phase in all set of traces look reasonably similar. This is confirmed by the high PEP value in Fig. 4.4b ($PEP \approx 73$), with the best value being positioned within $\approx$ 100 m from the actual well location. The high PEP values band (red colour in 4.4b), located updip with respect to the well area, is likely to be the effect of incomplete repositioning of the data due to the 2D time migration assumption (Simm and Bacon, 2014).

The extracted wavelet in Fig. 4.4c looks reasonable consisting of two main lobes with some secondary oscillations. Its phase can be evaluated through the associated phase plot. After fitting a trend line in a frequency band, its intercept represents the extracted wavelet phase. For our data, the linear fit is performed in the band over 5 - 65 Hz, with its measured intercept being $\approx$ 60 deg. Simultaneously, the match between the modelled/seismic traces indicated a time lag of 16 ms (Fig. 4.4b), with the lag being already compensated in the figure to appreciate the tie. Before it is possible to associate the lithological units with the seismic traces, the phase and timing of the surface seismic data needs to be corrected.

The observed phase mismatch raises some questions concerning the zero phasing process as described in section 2.2.1.1. If the modelled signature was a correct replica of the theoretical far - field signature the phase mismatch should be smaller and close to zero. In cases where the modelled signature is not an optimum representation of the acquisition conditions the data are convolved with a incorrect operator which does not efficiently zero phasing them. By inference any filters applied after the designature process will further distort the observed wavelet adding extra level of uncertainty in its resulting phase. In a similar manner, any application of incorrect value for inverse Q phase will lead to a phase shift. In this example, the well-seismic tie process aided to rectify the wavelets phase giving the precision needed for the updated interpretation result.

Having quantified the phase and time error during the well-tie procedure, the relevant corrections are applied to the preSTM profile. A phase rotation of 60 ° and a time shift of 16 ms were applied to the data. After correction, the well tie with the seismic is repeated (Fig. 4.5). The format of the figure is similar as Fig. 4.4. The extracted wavelet is nearly zero phase over a large frequency band but still has some secondary oscillations. The PEP value remained similar as in Figure 4.4 with the same location of best match (Fig. 4.5b). With the improved phase and timing of the data set, the amended preSTM image has now a much less ambiguous match with respect to the reported lithostratigraphic units. The seismic trace can be directly correlated with the reflectivity time series with the sharper boundaries being easily identifiable (e.g. the blue polarity lobe for top glauconitic sandstones). Note, however, that a level of uncertainty exists due to the velocity model used for the depth to time conversion.

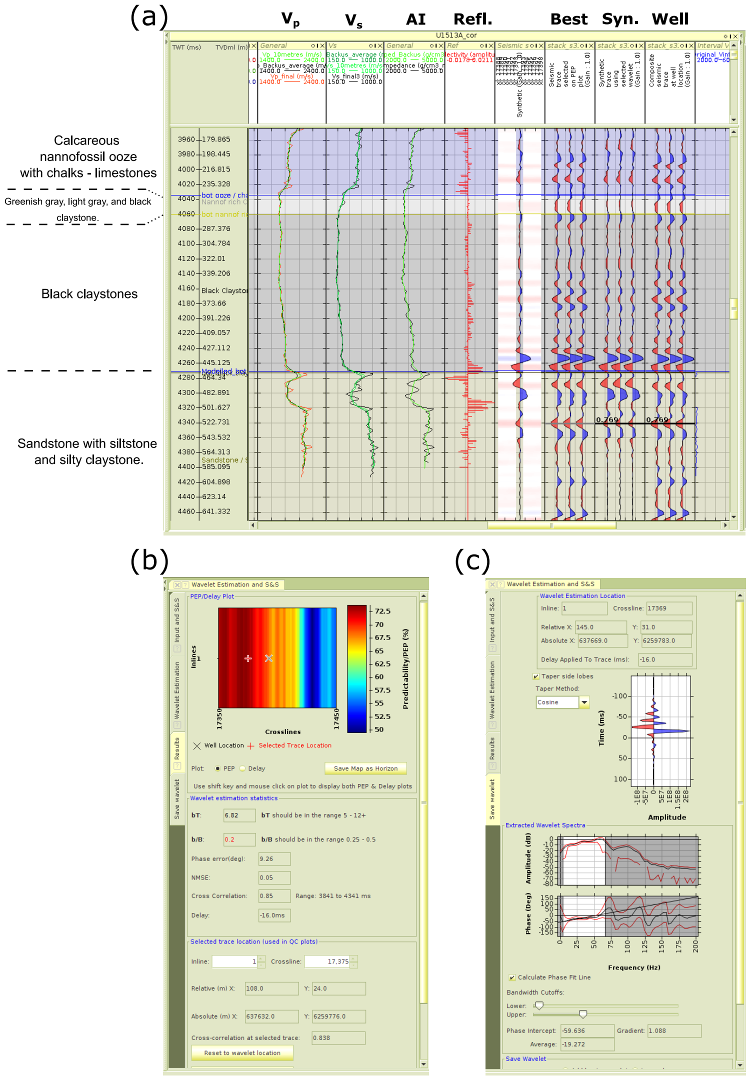

(b)

Plot: ● PEP ○ Delay

Use shift key and mouse click on plot to display both PEP & Delay plots

Wavelet estimation statistics

bT: 6.82 **bT** should be in the range 5 - 12+

b/B: 0.2 **b/B** should be in the range 0.25 - 0.5

Phase error(deg): 9.26

NMSE: 0.05

Cross Correlation: 0.85 Range: 3841 to 4341 ms

Delay: -16.0ms

Selected trace location (used in QC plots)

Inline: 1 Crossline: 17,375

Relative (m) X: 108.0 Y: 24.0

Absolute (m) X: 637632.0 Y: 6259776.0

Cross-correlation at selected trace: 0.838

(c)

Wavelet Estimation Location

Inline: 1 Crossline: 17369

Relative X: 145.0 Y: 31.0

Absolute X: 637669.0 Y: 6259783.0

Delay Applied To Trace (ms): -16.0

☑ Taper side lobes

Taper Method: Cosine

☑ Calculate Phase Fit Line

Bandwidth Cutoffs:

Phase Intercept: -59.636 Gradient: 1.088

Average: -19.272

Figure 4.4: Initial well - seismic tie. (a) shows the initial match between the synthetic and seismic signal (description of the main units where log data acquired on the left panel); (b) the *PEP* value is high ≈ 73 indicating a good match between well information and surface seismic with the best match location positioned ≈ 100 m away from the well location; (c) the extracted wavelet is not zero phase. From the phase spectrum, a calculation of the phase shift that need to apply to seismic data to appear more zero phase can be made. Linear trend for frequencies 5 - 65 Hz in (c) indicates that a phase shift of ≈ 60° (intercept of the trend) results into a nearly zero phase wavelet. Modelled and observed data have also a time delay of -16 ms. This has to be applied to the seismic profile. Modelled data shown in (a) have been time shifted to appreciate the result. Due to phase mismatch the seismic trace cannot be associated with the units boundaries. Red lines in phase/amplitude plots indicate the estimated standard errors for phase/amplitude values respectively.

A key target for the interpretation is to identify and correlate the bottom limestones /top black shales sequence. The well-seismic tie gives a reliable time value and polarity for that interface represented with the blue polarity lobe at ≈ 4037 ms TWT.

The procedure of tying surface seismic with the reflectivity series, as calculated from well logs, is stable and produces an unequivocal mapping of geological boundaries to the seismic signal. However, it is likely that this tie could improve when all the lithological units are sampled. An inspection between the modelled/recorded seismic traces demonstrates that although a phase match is achieved in the time window of interest, the amplitude values are locally discordant of each other with the main difference being located in the synthetically derived segments of V_p - V_s logs. As the statistics associated with the tying (PEP, $NMSE$), take into account both the amplitude and phase match of the signals it is more than likely that the statistical values would shift towards better values.

The quality of the tie is shown in Figure 4.6, where the synthetic trace is superimposed on top of the preSTM profile. Note how the trace matches the imaged structures. The optimum result is also driven by the frequency content of the data set. Lack of high frequency data normally hinders the process of phase estimation using a linear fit as multiple trends can equally well describe the data (White and Simm, 2003), leading to a non-uniqueness problem similar to the AVO-gradient plot (Simm et al., 2000) and velocity-depth (Lines, 1993; Al-Chalabi, 1997) ambiguities.

The tie has been performed without using stretch-squeeze during the matching process, which would artificially morph the modelled trace to match the timing/phase of the preSTM profile and thereby increase the PEP values. For example, the process could be directly applied to the low velocity zone in the glauconitic sandstones level (TWT ≈ 4300 ms), where due to the high frequency velocity oscillations a small time delay is evident. As mentioned earlier, using this process is only justified for regions with complex subsurface targets and shouldn't be applied as a panacea for discrepancies between model and reality, especially when 'reality' is synthesized using some averaged or assumed relationships.

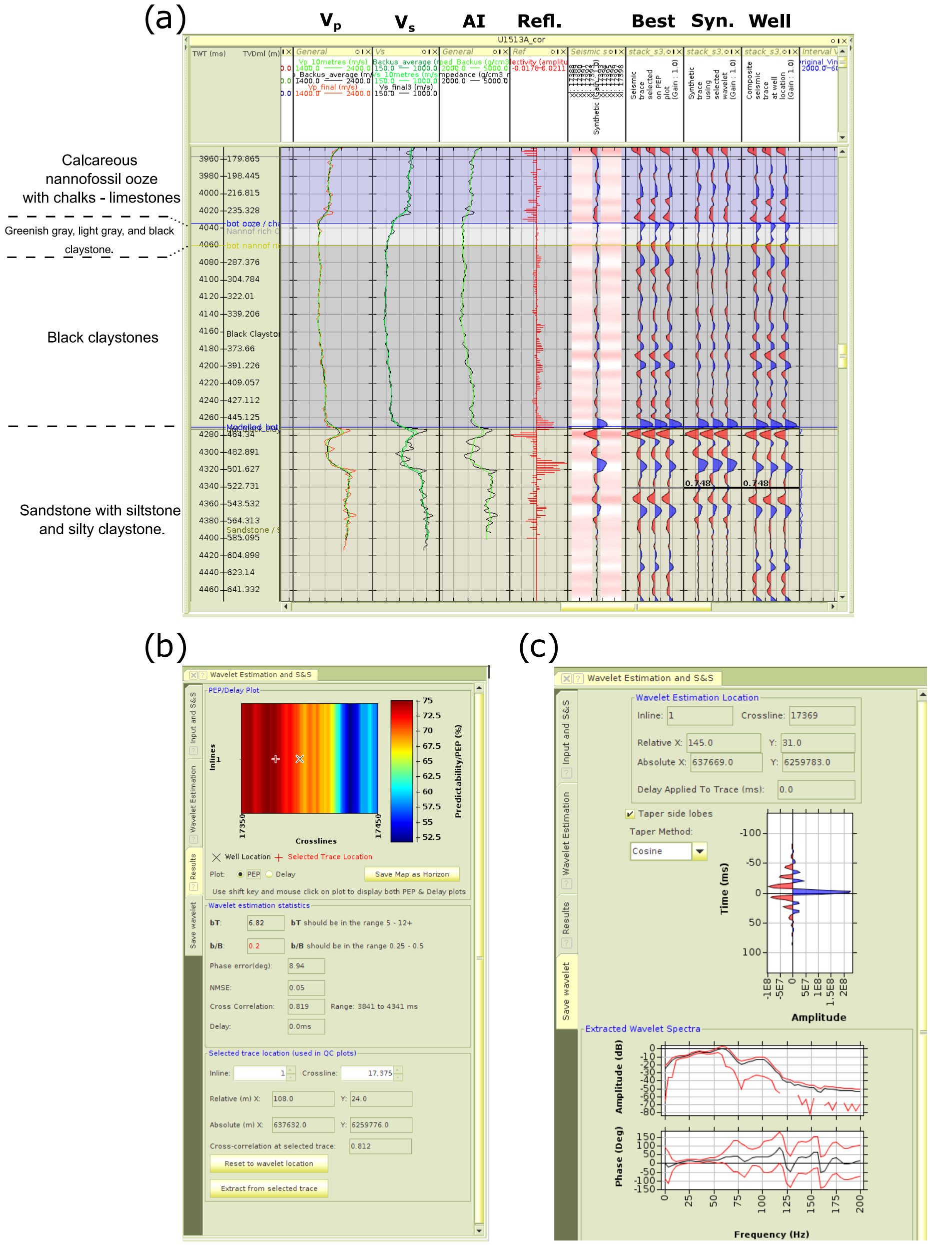

(b)

Plot: ● PEP ○ Delay

Save Map as Horizon

Use shift key and mouse click on plot to display both PEP & Delay plots

Wavelet estimation statistics

bT: 6.82 **bT** should be in the range 5 - 12+

b/B: 0.2 **b/B** should be in the range 0.25 - 0.5

Phase error(deg): 8.94

NMSE: 0.05

Cross Correlation: 0.819 Range: 3841 to 4341 ms

Delay: 0.0ms

Selected trace location (used in QC plots)

Inline: 1 Crossline: 17,375

Relative (m) X: 108.0 Y: 24.0

Absolute (m) X: 637632.0 Y: 6259776.0

Cross-correlation at selected trace: 0.812

Reset to wavelet location

Extract from selected trace

(c)

Wavelet Estimation Location

Inline: 1 Crossline: 17369

Relative X: 145.0 Y: 31.0

Absolute X: 637669.0 Y: 6259783.0

Delay Applied To Trace (ms): 0.0

☑ Taper side lobes

Taper Method: Cosine

Figure 4.5: Well - seismic tie after phase shift and delay. (a) shows the resulted tie after phase shifting the seismic data by 60 ° and time shifting by +16 ms (description of the main units where log data acquired on the left panel). Note that the matching is much more consistent with respect to the reported lithological boundaries with no observed delay or phase difference between the modelled/seismic data; (b) the *PEP* value is the same as in 4.4b, with the best match location being approximately 100 m away from the well location; (c) the extracted wavelet is now nearly zero phase for the frequency band 5 - 65 Hz, with some apparent high frequency lobes.

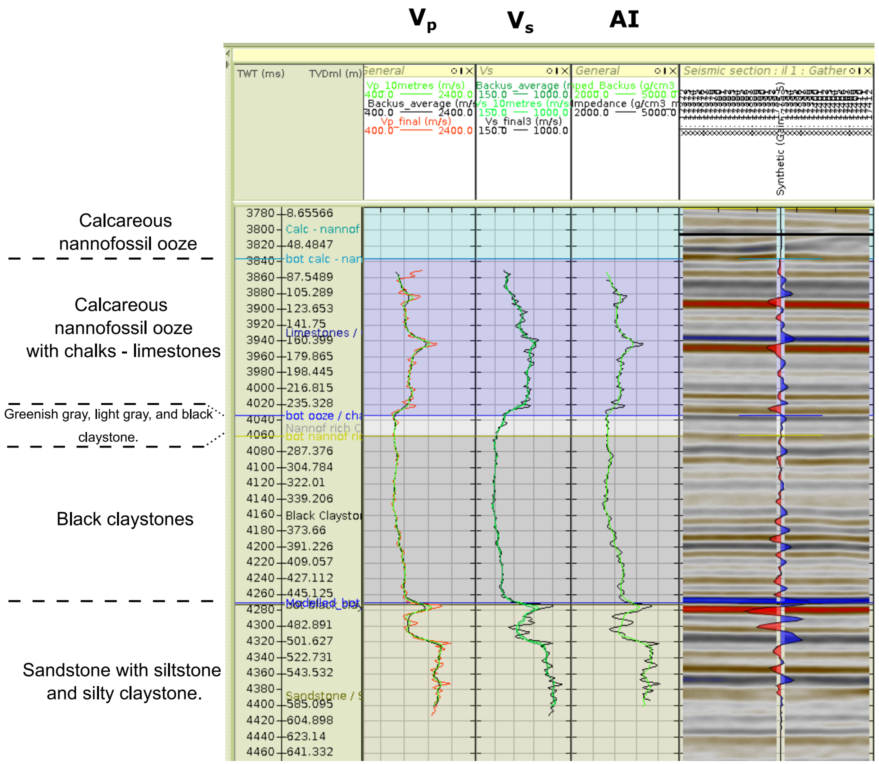

Figure 4.6: Modelled trace in preSTM profile The model trace generated from the convolution of the reflectivity series and the extracted wavelet is superimposed on top of the preSTM profile close to well location. For most of the trace length the match is reasonable with tiny discrepancies at the low velocity zone in the glauconitic sandstones unit (TWT $\approx$ 4300 ms). Note that no stretch or squeeze was performed in order to keep the matching values in a realistic level (description of the main units where log data acquired on the left panel).

4.4 Updated intepretation and true depths

After establishing the relationship between the time domain seismic data with the reflectivities from well logs and the geological units boundaries, the modelled depths to drilling targets along with their uncertainty estimations from Chapter 3 can be compared with the observed depths from Hole U1513.

Figure 4.7 shows the time domain, well - seismic tie based, correlation of the lithological boundaries to subsurface image. The preSTM profile in Fig. 4.7a is the same as used to perform the seismic tie. Fig. 4.7b is the same as in Fig. 4.6 but in order to perform a direct comparison with the seismic profiles used throughout this study the color palette is changed to grayscale. The overlaid seismic trace, closest to well location, represents the modelled trace as calculated using the extracted wavelet and the time reflectivity series (same as in 4.6). Blue/dark lobes represent positive amplitude values whereas red / white represent negative ones. Fig. 4.7c depicts the zoomed version of the green region from Fig. 4.7a and it has exactly the same scale in time/space with 4.7b. Thus, the tied boundaries in time domain can be compared with the macro scale profile in Fig. 4.7a. The lithological description is similar as in Fig. 3.8b but the thin Unit III (greenish gray to light gray - black claystone) was added. As the wireline log measurements were acquired over the depth window of $88 - 258$ m from the seabed, the first interface between Units I and II and the last between Units V and VI weren't identified.

The interfaces between the boundaries as extracted during the well-seismic tie process are depicted as dashed coloured lines. Light green line represents the transition from the limestones to light gray-black claystones whereas dark green line and brown line represent the boundaries between gray-black claystones/black claystones and black claystones/sandstones respectively. Also, in panels 4.7a, 4.7c vertical red dashed lines represent the CDP closest to well location.

A more exact representation of well-seismic tie requires a depth domain equivalent of the Fig. 4.7. Fig. 4.8, shows the picked and tied boundaries both in time and depth simultaneously. In Fig. 4.8a the anisotropic preSTM image is plotted normal to the isotropic preSDM for a direct comparison between picked pairs in time domain with their relevant map in depth domain. The preSTM profile (time values decreasing upwards) is the same used for tying the reflectors as described in section 4.3 whereas the preSDM profile is similar to Fig. 3.8a but with a phase shift for easier comparison with its time domain representation. The phase shift on the preSDM data was performed in time domain after depth to time conversion using the smooth version of the final $V_{int.}$ velocity field. In the colour coded interpretation (Fig. 4.8b), red curves represent assumed interpretation used for velocity model building in Chapter 2, Chapter 3 and for preSTM/preSDM. Green curves illustrate the interpreted horizons after well-seismic tie, whereas blue curves those boundaries based on the combination of reported core logs and preSDM image. The numbering of the boundaries follows the colour code. Fig. 4.8c shows the V_p sonic log for Hole U1513. Note that due to the isotropic approximation of the preSDM algorithm for depth imaging, the superimposed curves in the depth image (Fig. 4.8a, 4.8b) represent only the reported interfaces tied to reflectivities and not the actual depths of the drilling targets (Table in Fig. 4.8c).

The first major difference between predictions and truth is associated with the position of the calcareous nannofossil oozes-ooze chalks boundary (blue color, number 2, 4.8b). Based on the DSDP-258 report (Davies et al., 1974) the first major interface was located at ≈ 114 m depth from sea bed, representing the boundary between Miocene carbonate oozes and Paleogene limestones chalks with chert bands. Therefore, a horizon was picked in time domain, based on that prior information (red curve number 2, 4.8b). Taking into account the reflectivity log with respect to the true depth location, the depth associated with that reflectivity is at ≈ 116 m. The predicted depth at Hole U1513 (MBAS-4/Well 3C) location as inferred using the probabilistic approach and depth domain processing from Chapter 3 was 110 m ± 9 m (Fig. 3.8, Table in Fig. 4.8c, red curve number 2 in Fig. 4.8b), inside the credibility intervals indicating that the prediction was good. However, the true depth of that boundary as observed in the core log data from Hole U1513 is reported at ≈ 65 m. As the recording of most of the well log data started at ≈ 88 m, tying this boundary with seismic is ambiguous. Using the isotropic preSDM image and the core log data a plausible position could be represented by the blue curve in Fig. 4.8b.

The interface between the ooze limestones-chalks/black claystone was tied at ≈ 248 m. The pick made in time domain (red curve, number 3, 4.8b) was nearly congruent with the tied position (green curve, number 3, 4.8b). Using an optimum velocity field, the posterior mean depth was found at the level of 254 m with ± 13 m credibility intervals, indicating that identifying that interface and picking good $T_0 - V_{int}$ prior pairs, that prediction along with the posterior credibility intervals is accurate. Note that in the above description, Units III and IV are not treated as separate units so as to keep the comparison consistent with the original interpretation from DSDP-258.

The base of black claystones / top glauconitic sandstones is identified as the black polarity lobe at ≈ 4268 ms TWT (green solid curve/red dashed curve, number 4, 4.8b) therefore the picked reflectivity both in time and depth is congruent. Nevertheless, the discrepancy between the modelled posterior mean and true interface was imprecise by 18 m (457 m real against 475 m predicted, Table in Fig. 4.8c), with the credibility intervals defined as ± 15 m. This mismatch arises from the incorrect velocity field used due to the presence of anisotropic shale sequence. More details about that phenomenon and possible solutions can be found in the following section 4.5.

Following the mismatch at the top glauconitic level, the top basalt interface is more than 40 m offset from the posterior mean and approximately 20 m from the -2σ value (congruent reflectivities in time/depth domains: blue solid curve/red dashed curve, number 5, depths mismatch in Fig.

4.8c). This represents the 6% of the modelled cumulative depths, however it is significant compared to the quality of the predictions for the shallowest interfaces.

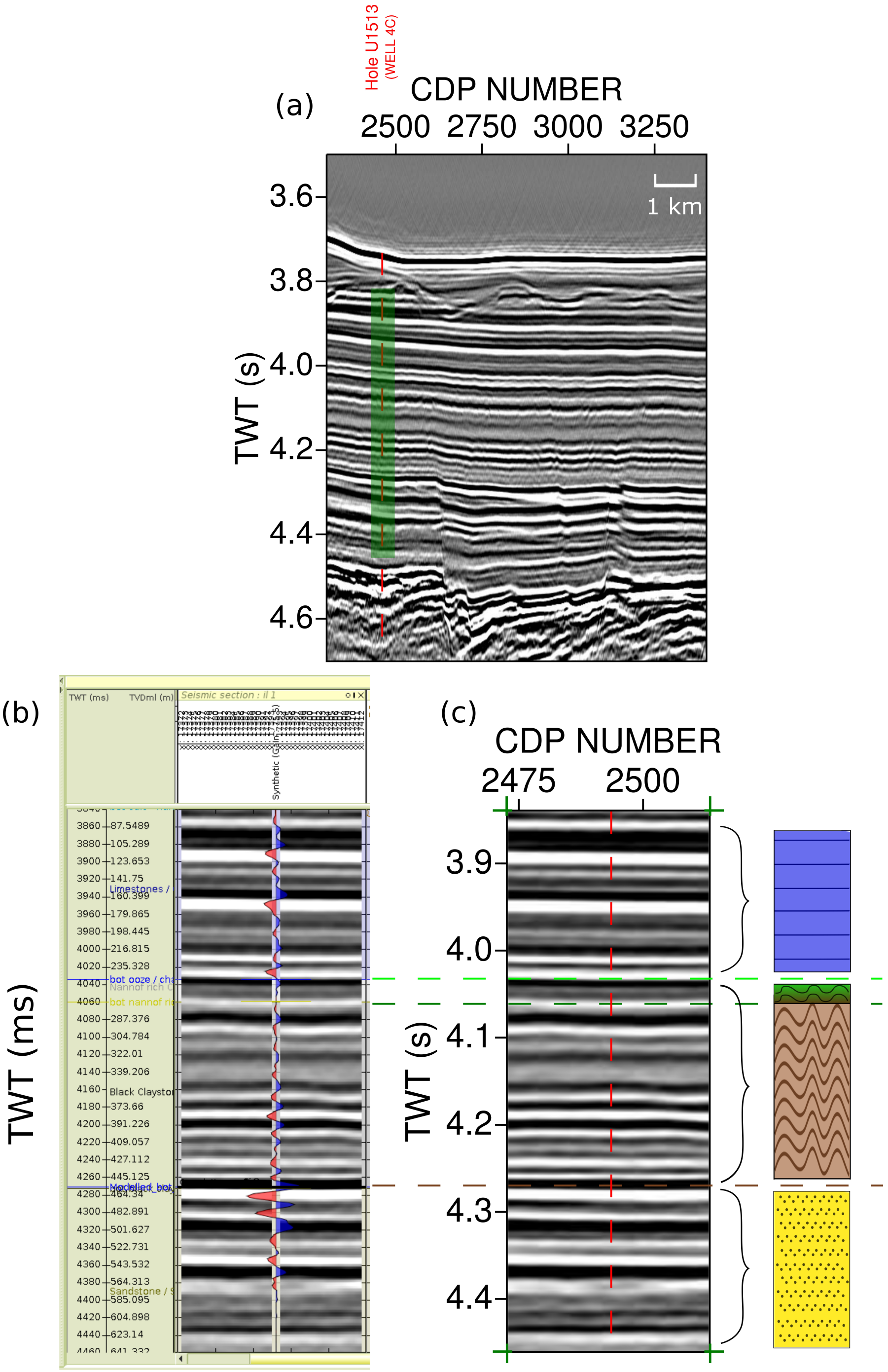

Figure 4.7: Time domain well - seismic tie based interpretation. (a) shows the anisotropic preSTM profile used for the well - seismic tie (section 4.3); (b) same as Fig. 4.6, but with gray scale color palette for direct comparison with the plotted seismic profiles; (c) is a zoomed version of the green region in (a) and is spatially/temporarily scaled with (b). Coloured dashed lines represent the geological boundaries (light green: limestones chalks/light gray-black claystones; dark green: light gray-black claystones/black claystones; brown: black claystones/sandstones. Lithological interpretation similar as Fig. 3.8b, with light gray-black claystones added for consistency with the reported description. In (a), (c), vertical red dashed lines show the CDP closest to well location.

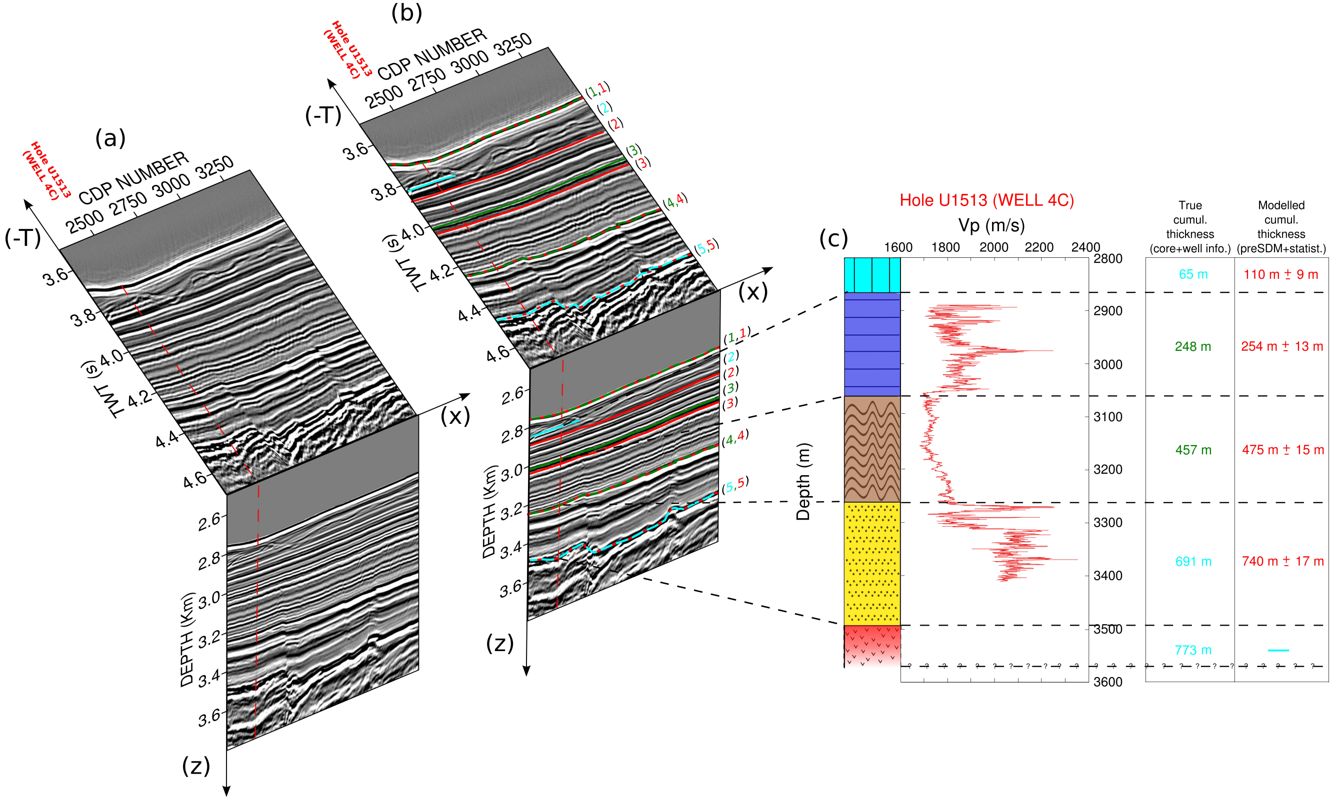

Figure 4.8: Updated interpretation in time/depth domains. (a) shows the uninterpreted preSTM (top surface) normal to the preSDM image (side surface). The preSTM image is the same profile used for well-seismic tie. Isotropic preSDM image, same as Fig. 3.8a, with a phase shift for consistency with the time profile; (b) is like (a) but with coloured lines interpretation. They are plotted in both domains at their respective horizons. Green lines indicate interpretation from well-tie information, red assumed interpretation used in Chapter 3, blue interpretation using core log information; (c) the sonic log as a function of depth from Hole U1513 (Well 4C/MBAS-4) is also shown (red dashed line in a, b), with the updated interpretation developed using all the available well and core log data. Interpretation is the same as in Fig. 3.8b, but due to well - seismic tie, the geological unit - reflectivity relation is established (black dashed lines). The table in (c) compares the true and the modelled cumulative depths for the lithological units (modelled depths same as in Fig. 3.8b). This clarifies that due to anisotropic effects related to black claystones sequence, the isotropic preSDM images in (a), (b) cannot be reliably used for depth estimation. Velocity information is unavailable for calcareous oozes and for the basaltic sequence (bottom of sonic log).

4.5 Anisotropic pre-stack depth migration

For the final stage of the analysis, the $V_{int.}$ velocity field will be rebuilt using additional information provided by the well log and implementing the sonic log velocities (in reality their low frequency representation) to determine the anisotropic parameters of the velocity model. Subsequently, an anisotropic preSDM migration will be performed, which will correct the observed depth errors associated with the claystone/shale layer.

Fig. 4.9a represents the isotropic preSDM image which was created based on the processing steps in Chapter 2 and Chapter 3 (Fig. 3.8a). To keep the comparison consistent with respect to previous chapters the phase is shown unchanged. The coloured lithological interpretation based on Davies et al., 1974 couldn't be used to assign reflectivities with geological boundaries as no wireline log was acquired. Therefore, the velocity model used for depth migration (Chapter 3) is not rigorously tied to the interpreted lithology. Nevertheless, based on true depth results from Hole U1513 the predictions of drilling targets were inside $\pm 2\sigma$ posterior credibility intervals until reaching the top glauconitic sandstones level where the true depth was offset by approximately 18 m from the posterior mean value. The isotropic preSDM CIG close to well location is shown in Fig. 4.9b. The gather, plotted without any outer/inner trace mute, looks acceptably flat until far offsets, for all drilling targets, indicating that preSDM was applied with an optimum velocity for imaging.

However, the results indicate two antithetical points. First, although there was no prior information to tie reflectivity with geological boundaries, the prior picked T_0 values were generally assigned correctly to their subsurface targets. Secondly, although the CIG appears practically flat, the velocity values used, overestimated the thickness of the black claystones. Typical of anisotropic conditions result from the presence of a shale sequence that causes vertical transverse anisotropy-VTI (Tsvankin et al., 2010).

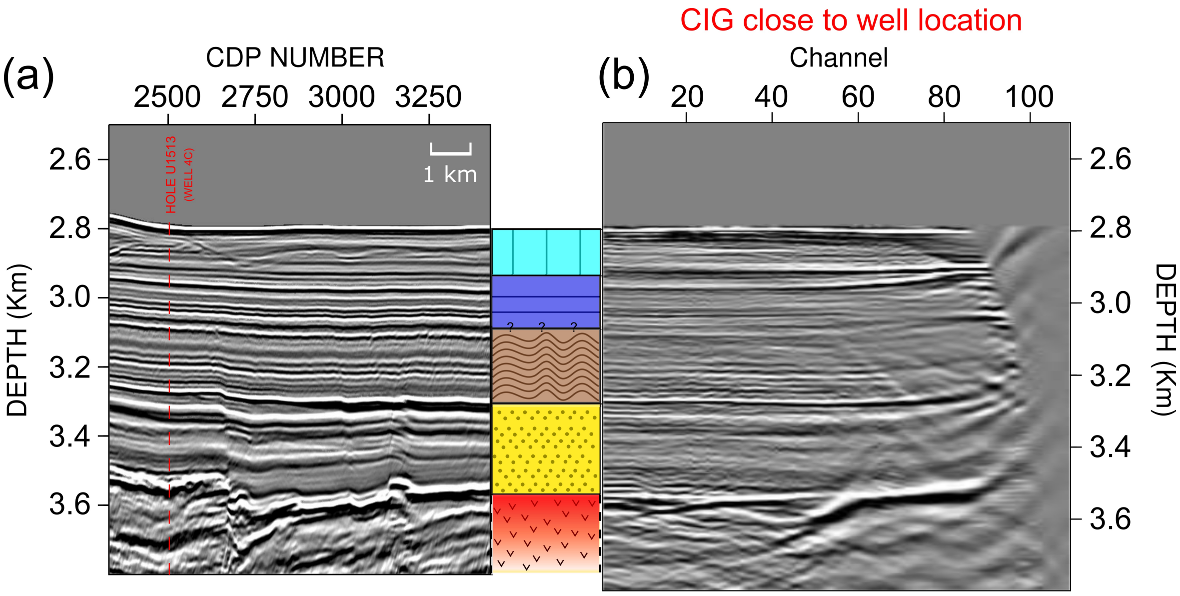

Figure 4.9: Initial interpretation of S310-07 profile. (a) the isotropic preSDM result is shown similar with Fig. 3.8a. The lithological interpretation based solely on Davies et al., 1974 description, is ambiguous in terms of assigning reflectivity to geological boundaries; (b) the unprocessed CIG close to well location (red dashed line in panel (a)) after using Kirchhoff isotropic preSDM. Note that the gather is considered acceptably flat for all depths until far offsets, indicating that the velocity field used for migration is considered optimum for imaging. Scale between (a) and (b) is slightly different to compensate for the depth difference between the well location (red dashed line) and the lithological panel at the right of (a). Both profile and CIG are shown with their original phase.

The depth discrepancy for bottom shales level which propagates to the deeper structures can be alleviated by performing anisotropic preSDM. For media which exhibit a Vertical Transverse Isotropy (VTI) such as shales, the process involves establishing Thomsen parameters (Thomsen, 1986), ϵ and δ, with their expressions given below

$$\begin{aligned}\epsilon &= \frac{V_h^2 - V_{p_0}^2}{2V_{p_0}^2} \approx \frac{V_h - V_{p_0}}{V_{p_0}}\\ \delta &= \frac{V_{nmo}^2 - V_{p_0}^2}{2V_{p_0}^2} \approx \frac{V_{nmo} - V_{p_0}}{V_{p_0}}.\end{aligned} \tag{4.3}$$

The parameters are incorporated during velocity model building using the η parameter (Alkhalifah and Tsvankin, 1995) which is compactly written in the expression

$$\eta = \frac{\epsilon - \delta}{1 + 2\delta} \approx \frac{V_h - V_{nmo}}{V_{nmo}} \tag{4.4}$$

where V_h is the horizontal velocity, V_{p_0} is the P wave average velocity in the vertical direction and V_{nmo} is the NMO velocity. Effectively η parameter represents the degree of deviation of a propagating wavefront from a perfect elliptical shape (anellipticity, Al-Chalabi, 2014).

The manual estimation of η parameter involves first the calculation of V_{nmo} in time domain by finding an optimum value. Afterwards, the V_{nmo} term is fixed and using a semblance spectrum a value for η can be estimated until the reflection event in the CMP gather looks acceptably flat for most of the available offsets. Although the η parameter can be expressed in terms of the vertical heterogeneity, δ (see equation 4.4), the latter cannot be retrieved using only surface seismic data. The measured velocity calculated during the velocity analysis stage represents only the horizontal component of the velocity vector expressed with the term V_{rms} (Al-Chalabi, 2014). As a result, the vertical heterogeneity, δ is only determined directly from VSP (Vertical Seismic Profile) data. However, δ parameter can be estimated using the ratio between the thickness of the subsurface layers from isotropic preSDM seismic data (H_{mig}) with respect to the true thickness measured from well logs (H_{well}) using the following equation

$$\delta = \frac{H_{mig} - H_{well}}{H_{well}}. \tag{4.5}$$

The calculation of δ in conjunction with η leads also to an estimation of ϵ value for each layer, also named as 'P wave anisotropy' term (Tsvankin et al., 2010).

In practice, the seismic data are migrated using an isotropic velocity model which is extracted from the low frequency representation of the $V_{instant.}$ from sonic log. In this way, the depth axis is scaled to force the seismic boundaries to match those observed from well logs depths. So, the depth targets in the migrated image are in accordance with the true depths but due to the lower $V_{int.}$ used for migration, the CIGs appear over-corrected at the mid-far offsets. Stacking the CIGs using this velocity model will result in a smeared image but with correct depth values.

As an example, Fig. 4.10 compares the subsurface image generated using isotropic preSDM, given the velocity information extracted from $V_{instant.}$ sonic log, with respect to the original preSDM image (Fig. 3.8a). The images are presented after a phase shift for consistency with the updated interpretation. Fig. 4.10a shows the original result, mirrored with respect to the depth axis, with the updated result shown in Fig. 4.10b. The green bullets represent the lithostratigraphic units, as deduced from the reflectivity-depth match (Figure 4.8), which show minimum or no resolvable depth differences. The green dashes depict the units which have resolvable depth discrepancies.

By comparing the two panels, it is evident the differential level of focusing, with Figure 4.10a showing acceptable focusing in most of the targets, contrary to Figure 4.10b where the focusing is less good. Figure 4.10b was migrated with the same depth sampling interval ($dz = 4$) and identical inner/outer trace mute with all the preSDM images presented in Chapter 3.

CIGs closest to well's location for both of the cases, are presented in Figs. 4.10c and 4.10d respectively. Fig. 4.10c is same as Fig. 4.9b but mirrored with respect to depth axis and phase shifted to match preSDM image in Fig. 4.8b. The overmigration effect in Figure 4.10d is clear at the mid-far offsets below ≈ 3.2 km which is the cause of the smeared preSDM profile in Fig. 4.10b. Similar to the top panels, green bullets represent units boundaries with no or negligible depth differences, green dashes boundaries with resolvable depth discrepancies.

However, by applying the correct vertical $V_{int.}$ field the depths to drilling targets are restored the observed, from the well/core logs, depths. This is directly shown in Figs. 4.10e, 4.10f, 4.10g. Fig. 4.10f is taken from the $RokDoc^{TM}$ analysis scaled in depth domain, therefore it represents a time to depth conversion. Fig. 4.10e is extracted from a region close to well location from Fig. 4.10a and is vertically scaled to match the scales of Fig. 4.10f. In a similar manner, Fig. 4.10g is the preSDM result extracted from the same data window from Fig. 4.10b. Although the poor focusing renders the comparison unfair in terms of vertical resolution, the major interfaces between units II - III (red dashed line) and IV - V (green dashed line) are apparent. The depth discrepancy is evident with the left panel overestimating the depth to the bottom claystones and the bottom sandstones (yellow lines). Note that due to poor CIGs quality, oversmoothing of $V_{instat.}$ sonic log or missing values, there is also an apparent small discrepancy between Figures 4.10f and 4.10g, more noticeably inside the sandstones unit (depth ≈ 3.3 Km), indicating that even with prior information some tests with different smoothed velocity fields must be performed in order to exactly map the reflectivity series with seismic.

The poorly focused image can be fully resolved by increasing the horizontal velocity V_h, applying anisotropic preSDM to flatten the convex mid - far offsets in CIGs and stacking the data. In Fig. 4.11, the progression of this update is depicted, showing the CIG gather closest to well location. Fig. 4.11a is the same CIG as in Fig. 4.9b which is isotropically migrated using the velocity field from Fig. 3.6a. The CIG shown in Fig. 4.11b is the same as in Fig. 4.10d after updating the V_{p_0} velocity. Finally 4.11c shows the anisotropic preSDM CIG gather after updating the V_h velocity, as inferred through a 4^{th} order NMO velocity model building. Note that the mid-far offsets for most of the depth levels appear nearly flat and can be considered equally flat with respect to their isotropic preSDM counterpart until the depth level of ≈ 3.6 km (Fig. 4.11a). This means that after applying a conservative outer trace mute similar to the data corrected with isotropic model, they will constructively stack and produce a well focused image. Concurrently, the lithostratigraphic units are repositioned in their correct depth level (green bullets on the left sides of Figs. 4.11a, 4.11b, 4.11c). Using the anisotropic Kirchhoff preSDM, the number of active traces athat can be used in the stack can be increased.

It is obvious that the level of focusing is a function of the number of effective traces stacked in every CIG (coloured bars in Fig.4.11). The anisotropic preSDM gather as shown in Fig. 4.11c has a maximum number of effective traces approximately equal with the original isotropic case (Fig. 4.11a) and larger than the Fig. 4.11b (72 against 68 and 50 active traces respectively). This means that the improvement in signal to noise ratio (S/N) due to stacking will be at a similar level of the isotropic case as shown in Chapter 3 using the same depth sampling interval ($dz = 4m$).

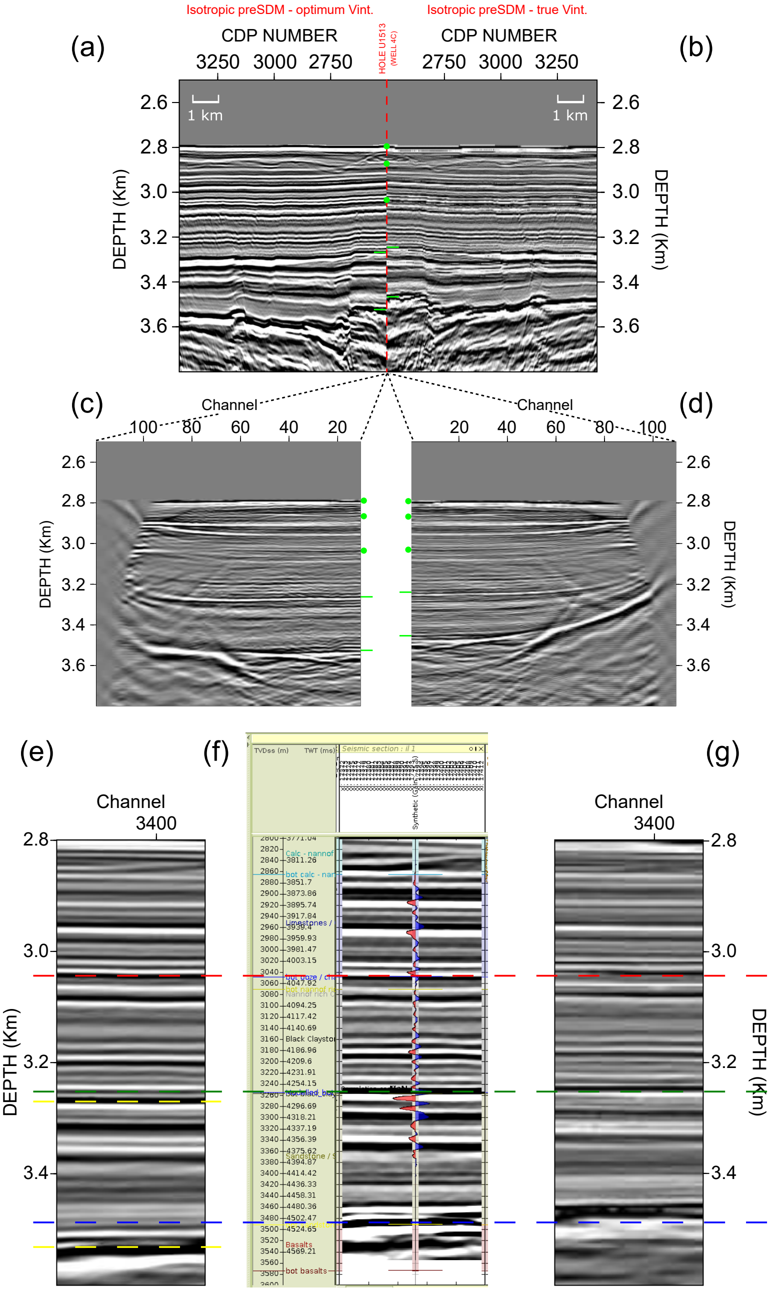

Figure 4.10: Using sonic log information for preSDM. (a), (b) show isotropic preSDM images generated using different velocity fields; (a) is similar to Fig. 4.19a, using $V_{int.}$ field optimum for imaging but with phase shift applied, whereas (b) is created using a smoothed version of sonic log. Green bullets show the major units interfaces with negligible or no depth differences, green dashes the interfaces with resolvable discrepancies. Note the poorly focused result in (b); (c), (d) show the CIG close to well location (red dashed line in a,b), juxtaposing the nearly flat CIG in (c) with the overmigrated CIG in (d) (green bullets, green dashes same as in (a), (b)); (e), (g) emphasize purely on the differences in retrieved depths after using the nearly correct velocity field (g), compared to the overestimated depths in (e). (e), (g) are compared with respect to the observed reflectivity in depth domain after time to depth conversion (f).

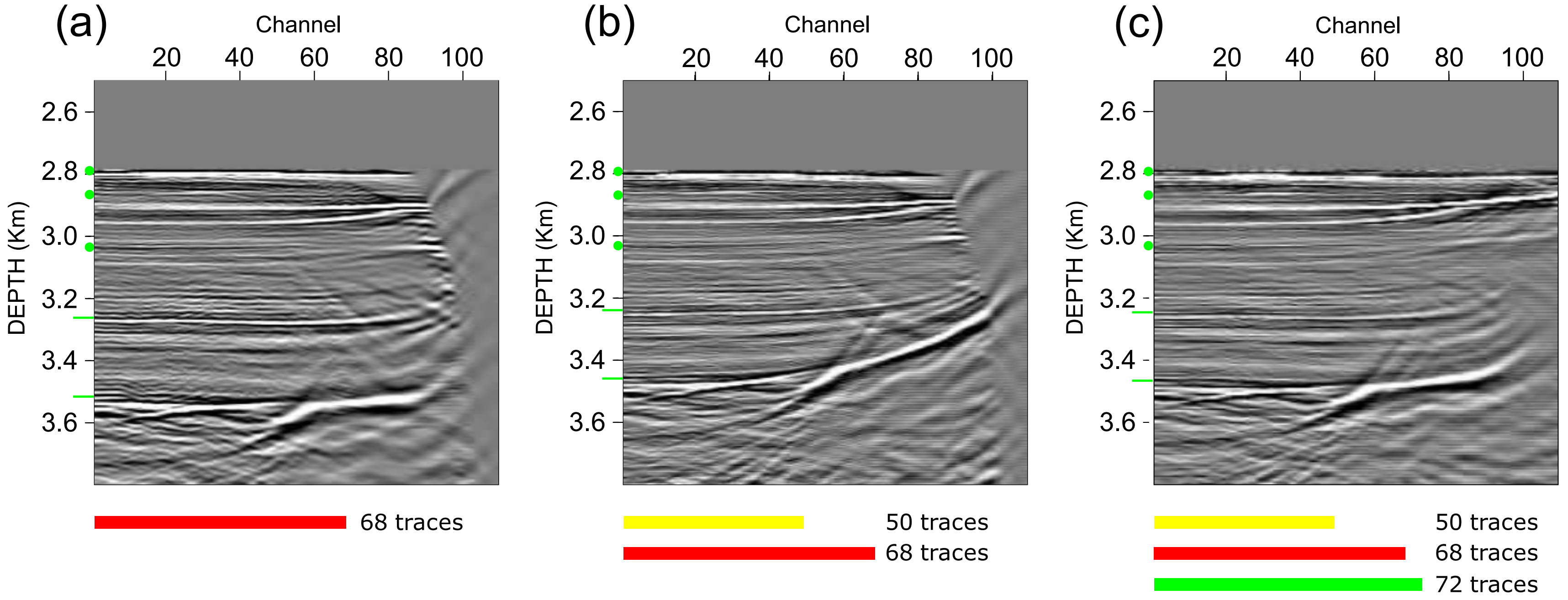

Figure 4.11: Anisotropic preSDM. (a) is same as Fig. 4.10c, an isotropic preSDM CIG closest to the well location; (b) is same as Fig. 4.10d, an isotropic preSDM CIG after editing the V_{p_0} field; (c) represents the anisotropic preSDM CIG closest to well location, after updating both the V_{p_0} and the V_h fields to compensate for the anisotropic propagation due to presence of shales sequence. Note how the reflection events appear equally flat with the isotropic case in (a), but their modelled depths are now in accordance with the observed from Hole U1513 depths. Green bullets/dashes on the left of each panel show the targets depths (similar as Figs. 4.10c, 4.10d). At the bottom of each panel, the maximum number of effective traces at the top glauconitic level is shown, as coloured scaled bars. The anisotropically migrated CIG can constructively stack up to 72 traces, nearly equal with the optimum isotropic CIG in (a) but more than the isotropic CIG in (b).

In Fig. 4.12, a comparison between the isotropic and the anisotropic images ($dz = 4m$) for the region close to well location is made, after updating the V_{p_0} and V_h fields and performing similar post-stack processing as in the isotropic preSDM case. Fig. 4.12a shows the two images orthogonal to each other intersected at the Hole U1513 position. The level of focusing in both images appear the same however, the depths to subsurface targets are correctly restored for the anisotropic preSDM image. The red nodes represent the spatial link for the lithological boundaries as interpreted in section 4.4. The most prominent differences are found in the top glauconitic sandstones level and the top basalt sequence (4^{th} and 5^{th} nodes respectively). The remaining boundaries are located approximately at the same depth level, taking into account the depth sampling interval.

The velocity fields used to develop the anisotropic result, V_{p_0} and V_h, are overlaid on the same anisotropic image (Figs. 4.12b, 4.12c). Fig. 4.12b represents the smooth version of the sonic log (Fig. 4.8c), with a notable velocity inversion at the black claystones sequence ($\approx$ 1800 m/s). In Fig. 4.12c, the horizontal velocity at the black claystones level is higher than the vertical velocity in order to flatten the convex mid - far offsets in CIGs ($\approx$ 2100 m/s). For the remaining units, the velocity values used are the same as in the V_{p_0} field. Note the V_h field as presented in Fig. 4.12c cannot be considered as the optimum representation of the 'true' field but depicts only its smoothed version. Due to time constraints and software limitations the field was built without any apparent lateral variations. Although the anisotropic image is focused, it is expected that by applying tomographic inversion in depth domain for both V_{p_0} and V_h fields parameters, the high frequency velocity perturbations along the profile will be retrieved and the subsurface image will become even better focused.

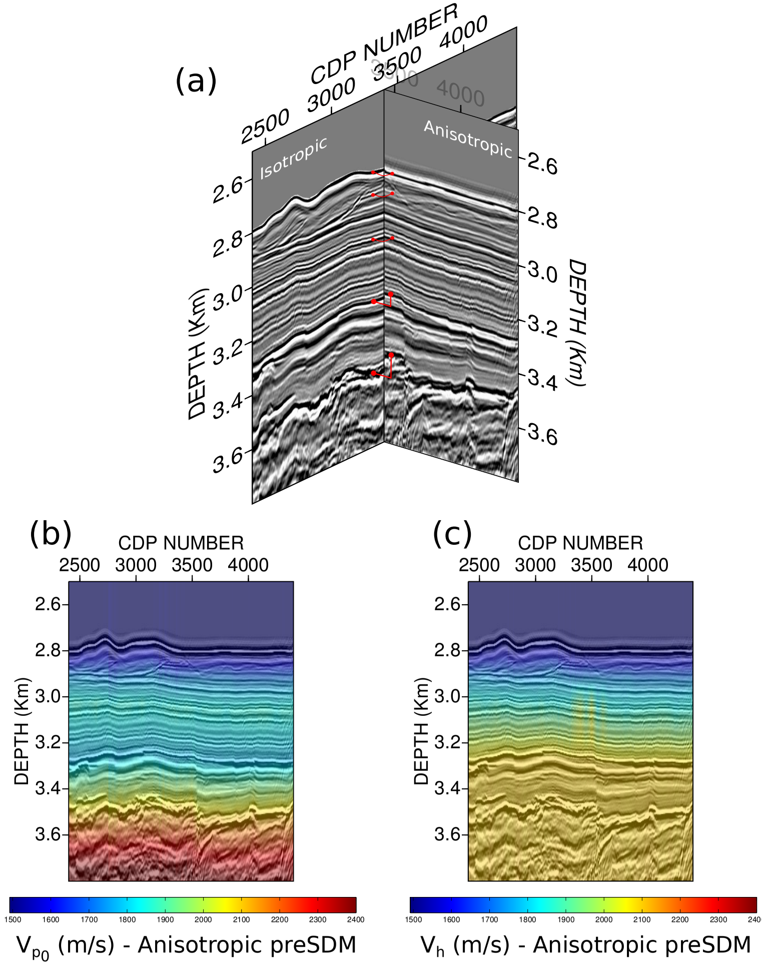

Figure 4.12: Anisotropic preSDM image. (a) shows a combination of isotropic and anisotropic images. The profiles are orthogonal to each other at the well location to emphasize the difference in the retrieved depths. The depths to drilling targets are restored while the focusing of the image features is preserved. Red nodes represent the link for every interpreted lithological boundary between the two images (section 4.4). Orthogonally linked nodes illustrate vertical depth differences, whereas curvedly link nodes represent negligible changes; (b) and (c) show the vertical and horizontal velocity fields used for anisotropic preSDM respectively. Note that in this case, the V_h field is considered as the smoothed version of the ϵ field.

4.6 Conclusion

In this chapter, the process of tying wireline log information from Hole U1513 to the seismic profile S310-07 is presented. The well-seismic tie allowed us to match the ‘true’ reflectivity as derived from sonic, density logs with the ‘modelled’ reflectivity from surface seismic data. Using the depths of the lithostratigraphic units as measured during the core logging along with their reflectivity function, the boundaries of interest were unambiguously matched. This information is the first step to better constrain the interpretation of MB, especially as more well-seismic ties will be performed from the remaining seismic profiles and drilled sites.

As part of the well-seismic tie, the low frequency representation of the $V_{instant.}$ field was implemented to perform anisotropic preSDM. The technique allowed to restore the depths of the drilling targets to their correct subsurface level and simultaneously generate a well focused image. However, due to the smooth V_{p_0} and V_h fields representation related to the vertical update velocity model building, the example should be considered purely as a test of the anisotropic preSDM and not as a conclusive result, especially in terms of focusing of the subsurface targets.

Chapter 5

Discussion

In previous chapters we described the processing steps and the Bayesian algorithm aiming to make predictions about the depths to drilling targets. Subsequently, using the true well log information from Hole U1513 we performed well-seismic tie and matched the reflectivity with the lithological boundaries. Finally, we restore the depths of key horizons in our preSDM image based on the true well information (V_{p_0}) and inferred V_h field using anisotropic preSDM. The result was optimum in terms of focusing and tying with borehole information.

In the following, we will discuss potential weaknesses and strengths of the approaches followed throughout the Thesis. Moreover, we will extend some of the ideas already described with the aim to develop strategies and suggest ways to improve the results.

5.1 Deghosting operators

We can utilize the extracted zero phase wavelet through the well-seismic tie process to eliminate the ghost effects in the post stack domain. In reality, the extracted wavelet incorporates the remnant source signature even, if there was already a de-signature operator applied, along with the ghost effects embedded in the stack data. Thus, in theory, the extracted wavelet can be inverted and applied post stack as a deghosting and designature filter.

The following multifigure example can be considered as an extension of the conversation concerning the ambiguity of deghosting operators (section 2.2.2). To keep the model consistent with the well-tie process, all the depicted profiles are generated using the same phase and time shift and band pass filter as mentioned in section 4.3. In Fig. 5.1, we compare the image results after applying different sets of deghosting operators. Fig. 5.1a represents the original segment close to well location. Fig. 5.1c is similar to Fig. 2.13e, whereas Fig. 5.1e shows the result after shaping the spectrum using two new filters with the following parameters:

- source's side filter: $A_{source} = -0.7$ centered at a frequency $f_{notch} = 94Hz$;
- receiver's side filter: $A_{rec.} = -0.05 - 0.08 - 0.1 - 0.15 - 0.1 - 0.08 - 0.05$ centered at frequency $f_{notch} = 74Hz$.

Finally, in 5.1g, the image is deghosted using the inverse of the extracted wavelet from the well-tie (4.5c).

For assessing the level of notch healing we also plot the relevant amplitude spectra for each trace ($f-x$ representation of the data) along with the usual stacked amplitude spectrum on the rightmost of the panels (Figs. 5.1b, 5.1d, 5.1f, 5.1h respectively). The manifestation of the non-trivial notches in the amplitude spectrum in 5.1b is undeniable. Due to variable sea surface conditions the two notches are merged in a frequency band between $70Hz - 100Hz$. Their expected notch positions, $75Hz$ for the receiver's notch and $107Hz$ for the source's notch, are effectively spread onto a wider frequency range making the amplitude shaping more demanding and uncertain.

Although the $f - x$ coloured panels are not normalized to each other, the nature of the ghost effect is visible and the improvement after applying the deghosting operators compensates for the spectral amplitude loss with varying degress of success. The differential level of healing is evident among the operators. Surprisingly, the worst operator appears to be the inverted wavelet extracted from the well - tie approach (Fig. 5.1h.) In a sense, this filter fails to fully heal the observed notch region manifested in the band between $70Hz - 100Hz$ and it misshapes the spectrum by boosting a narrow region between $80Hz - 90Hz$ with a simultaneous decrease of the mid frequency band $50Hz - 80Hz$. The image in Fig. 5.1g is blurred due to the poor content in mid frequencies rendering the result suboptimum.

The cause for the inaccurate operator is unclear. The extracted wavelet is a result from a well - tie approach of a reasonable quality and its inverse representation should theoretically be a good approximation of the amplitude content of the data. Still, if we consider the extracted wavelet window, we may be able to justify part of the phenomenon. As described in section 4.3 the approach was centered in a depth/time window where true data were missing. This window was chosen as it provided the recommended 500 ms window is needed for an unbiased tying process. To obtain this window it was required to map the measured density values to V_p and V_s values. The synthetically derived velocity data were subsequently used to generate impedance/reflectivity data which then were matched with the profile to extract a representative operator. The phase of the match between synthetic and best match location is nearly optimum but the amplitudes are not congruent (Fig. 4.6c). This indicates that the operator is successful of encoding the frequency content of the signal but fails to encode the relative amplitude level of these frequencies in it. With the inherent sensitivity of the deghosting process combined with the non-trivial nature of the ghosts effects in our data set, an incorrect scaling of the filter may lead to inferior results.

The two remaining operators produced good results with sharp images and nearly fully compensated amplitude spectra. Nevertheless, the inherent question of the validity of the operators persists. $f - x$ domain transform is the 1D Fourier transform of the signal and can be depicted either for every trace (Figs. 5.1b-5.1h) or with its stacked counterpart (rightmost panels in 5.1). Mathematically, the autocorrelation function is the inverse Fourier transform of the power spectrum of the signal which is again a measure of amplitude level of the data. It also indicates any repetition/reverberation present in the data. For pre-stack data an extra tool is the $f - k$ spectrum which measures the amplitude level of frequencies as a function of the angle. In the following, a number of extra criteria will be introduced that when combined with the processing tools mentioned previously can better assess the stability of the inverse filters.

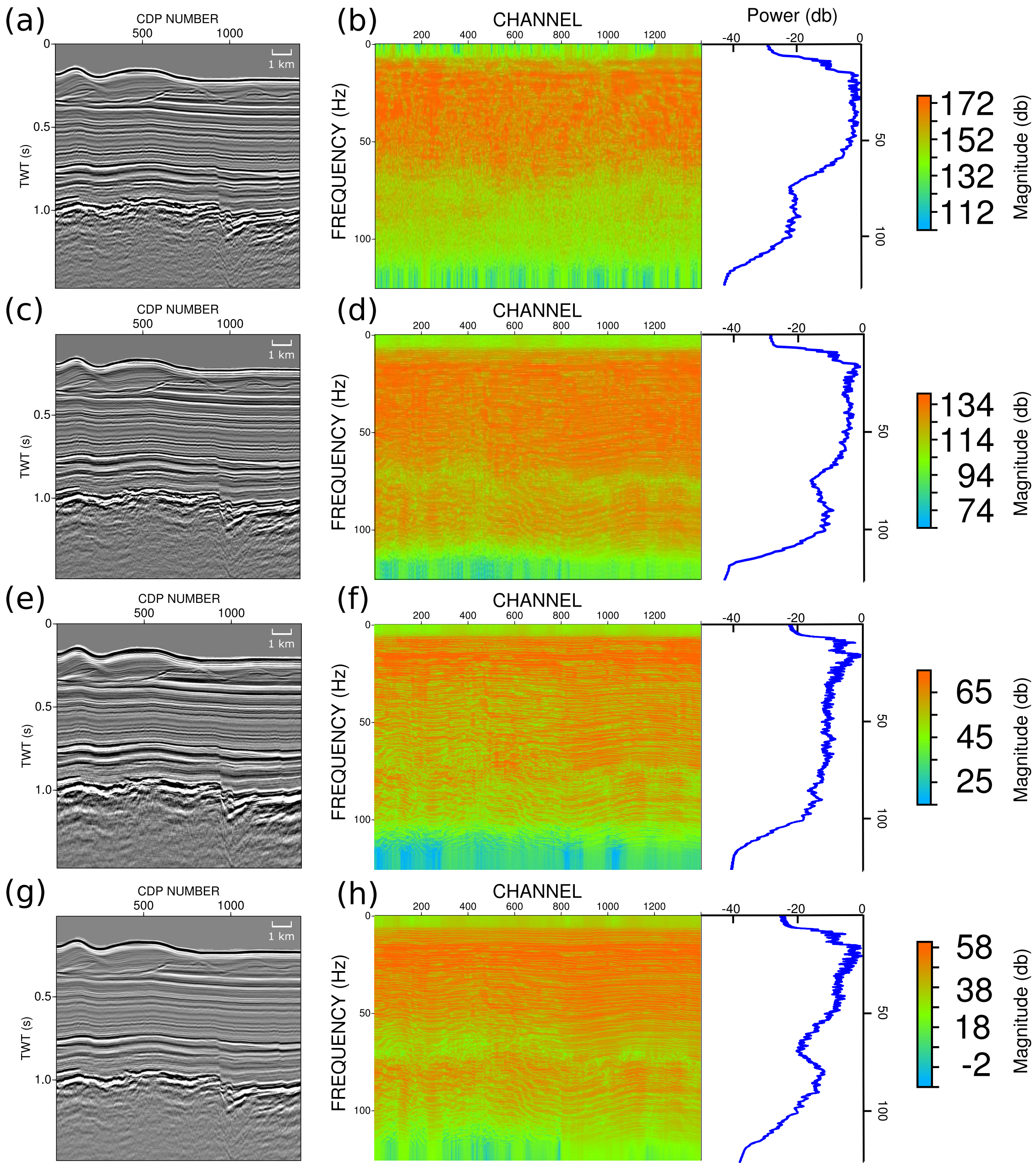

Figure 5.1: Effect of different deghosting filters. (a) represents the original preSTM image as used for well-seismic tie purposes without any ghost arrivals elimination; (b) $f-x$ spectrum of (a) with its stacked spectrum shown on the rightmost panel; (c) as (a) after applying deghosting filters similar to Fig. 2.13e; (d) $f-x$ spectrum of (c); (e) same as (a) after using the new set of deghosting filters (see text); (f) $f-x$ spectrum of (e); (g) as (a) after using the inverse of the extracted, from the seismic tie, wavelet; (h) $f-x$ spectrum of (g). The flattest spectrum is produced after applying the new sets of deghosting operators (f), whereas result in (d) shows a small remnant notch. Note the incomplete result after applying the inverse of the extracted wavelet from well-seismic tie (h).

5.2 Constrain the effectiveness of deghosting filters

Based on the results from Chapter 2, the deterministically derived inverse filters can be tailored to the post-stack observed notches and locally improve the resolution of the image. However, it is unclear if one operator outperforms another as the results are not easily quantifiable. To gain a better insight of the effectiveness of the filters, we have to locate the image components that are altered after applying the operators. Thus, we need to locate a visible ghost arrival in the image and subsequently track its relative suppression after applying different filters.

In order to locate the ghost component of the signal in our data set, we chose to pick the near offset trace for a number of shots close to well location and produce a near offset profile ($t-shotnumber$ domain). This domain can be considered as the pre-stack zero offset representation of the subsurface, but without the smearing effects that stacking process creates. Thus, it is relatively easier to locate the ghost arrivals which appear as opposite polarity events that arrive immediately after the primaries with a period approximately equal with the inverse of the notch frequency. We first need to locate a sharp, high impedance, seismic boundary such as the seabed or any clear subsurface target that can be tracked along the profile. In our data set, a very good candidate was found to be the top glauconitic sandstone level (Fig. 5.2). To facilitate the process of clarifying the ghost signal, we used a low-cut filter combined with a balance operator.

Fig. 5.2a shows the near offset profile in gray scale. The negative polarity event combined with the positive arrival directly below the sharp top glauconitic boundary (white and gray regions, red arrow) have all the characteristics of a ghost signal. Depending on the relative gain that we can apply to the data, this event can be more or less pronounced. Alternatively, the profile can be plotted in a different colour palette (Fig. 5.2b). Now the ghost signal is clearly manifested as a red-green-light blue zone located below the dark blue arrival. A zoom version of the signal (Fig. 5.2c), reveals some interesting characteristics of the ghost effect. Notably, the ghost arrivals (down-going wavefield) appear more oscillatory with different amplitude compared to the primary event (up-going wavefield). The ghost signal arrival times are related to the height of the water column above source/receivers, whereas its amplitude is associated more with the curvature of the rough sea-surface (Laws and Kragh, 2002). The result indicates that the notch has a spatial variability, an effect that is mapped onto the $f-x$ spectra and stacked amplitude spectra as a wide low power frequency band (Fig. 5.1b). In Fig. 5.2d.i, the zoom version of the red dashed rectangle from Fig. 5.2c is shown. A plot of the theoretical time responses of the primary and ghost arrivals overlaid on Fig. 5.2d.i is depicted in Fig. 5.2d.ii. In practice the spikes are band-limited as depicted in Fig. 5.2d.iii. Due to acquisition parameters and frequency content of the data the source/receiver ghosts are merged (red-green area in 5.2d.iii) but because of the scattering effects generated from rough sea surface conditions, the combined ghosts arrivals (source+receiver ghosts, light blue area in 5.2d.iii) appear reduced in amplitude and with lower frequency compared to the primary event.

Having located the ghost signal we are ready to compare the sets of deterministic filters as tested in Fig. 5.1 and apply them in the $t - shotnumber$ domain. Our main goal is to try to reduce the amplitude of these arrivals and output, where the event is optimally corrected, zero-phase arrivals with minimum side-lobe reverberations.

In Fig. 5.3 we show the results after applying the inverse operators. The base of comparison is Fig. 5.3a which is similar to Fig. 5.2b. Fig. 5.3b shows the resulted image after applying the deterministic filters as firstly described in section 2.2.1.4. Its spectrum (Fig. 5.1d), appears compensated but with a remnant notch at the receiver notch position, indicating that the ghost signal is partially suppressed. The result in Fig. 5.3c is probably optimal as it eliminated most of the ghost arrival energy especially at the rightmost region of the image (hanging wall-blue arrow). Note in particular, that the source's side deghosting filter was deliberately constructed to reshape a frequency band located in lower than the calculated, based on the source's depth, notch frequency. This indicates the non-trivial nature of the notches present in our data set. In the footwall region the compensation isn't complete but it is clear that the temporal resolution is improved (red arrow). The last Fig. 5.3d, was produced using the inverse of the wavelet extracted from the well-seismic tie approach. As a consequence of the remnant notch (Fig. 5.1h), the amplitude level of frequencies is uneven with poor mid frequency content and boosted low and high frequencies. The image appears with a low frequency shadow and, most importantly, the ghost signal is practically untouched. As described in section 5.1 the suboptimum ghost suppression shown in 5.3c could be possibly attributed to the incomplete modelling of the wavelet during the well-seismic tie matching process.

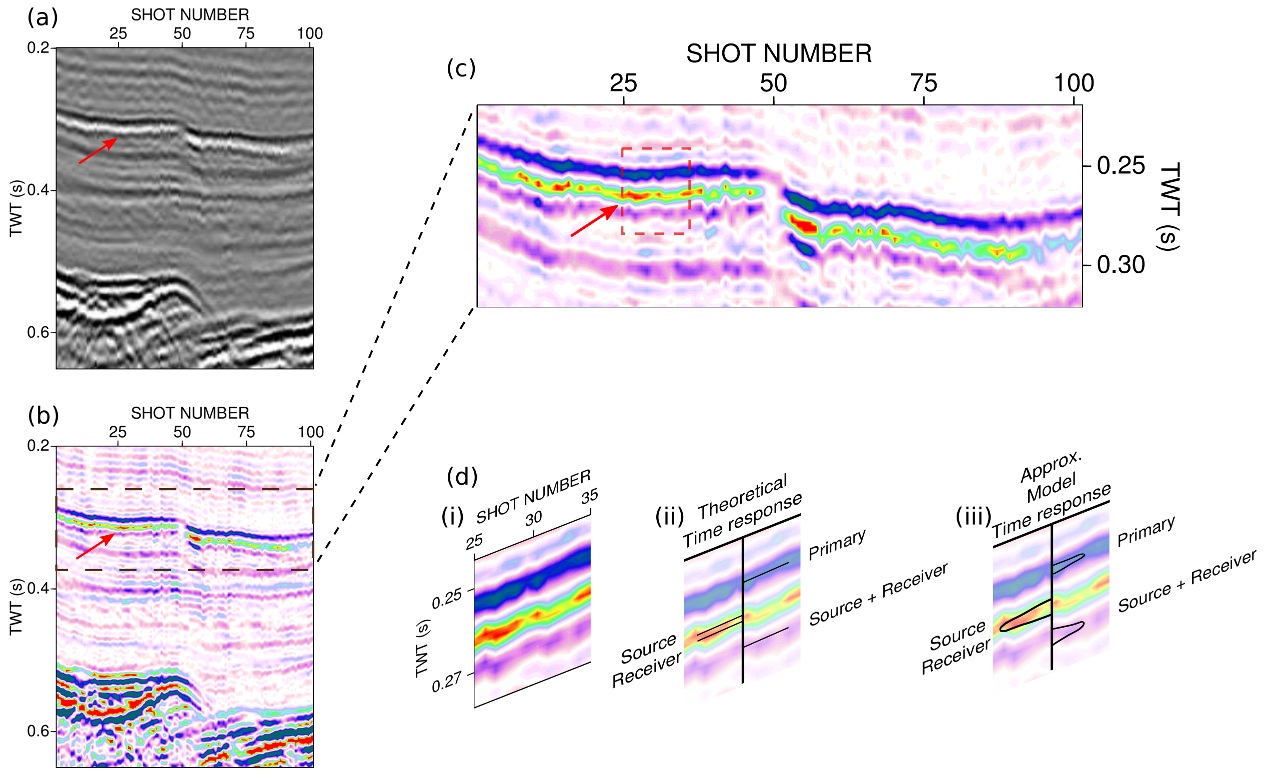

Figure 5.2: Visualising the ghost signal. (a) is created using 101 nearest traces from shot gathers and plotting them side by side ($t - shotnumber$ domain). Low cut filter and balance were applied to better clarify the structural features, with the image plotted in gray scale. The negative polarity event (white coloured region) along with the positive arrival (light gray coloured region) immediately after the positive polarity top glauconitic sandstone (dark coloured region) constitute the ghost signal (red arrow); (b) is same as in (a) but in different coloured palette. The ghost signal is more obvious (red arrow), manifested as red-green-light blue zone exactly after the dark blue top glauconitic event; (c) is the zoomed version of (b). Although subtle, the ghost signal appears more oscillatory than its primary counterpart as it incorporates the variable sea surface effects; Panel (i) in (d) shows the zoom of the red dashed rectangle from (c). In panel (ii) the theoretical time responses of the primary and ghost arrivals are overlaid on the signal. In panel (iii) an approximate model response is depicted. Due to acquisition parameters and frequency content of the data, the spikes are band-limited and the source/receiver ghost arrivals appear merged. However, the effects from rough sea surface conditions alter the ghost signal amplitude/frequency and arrival time.

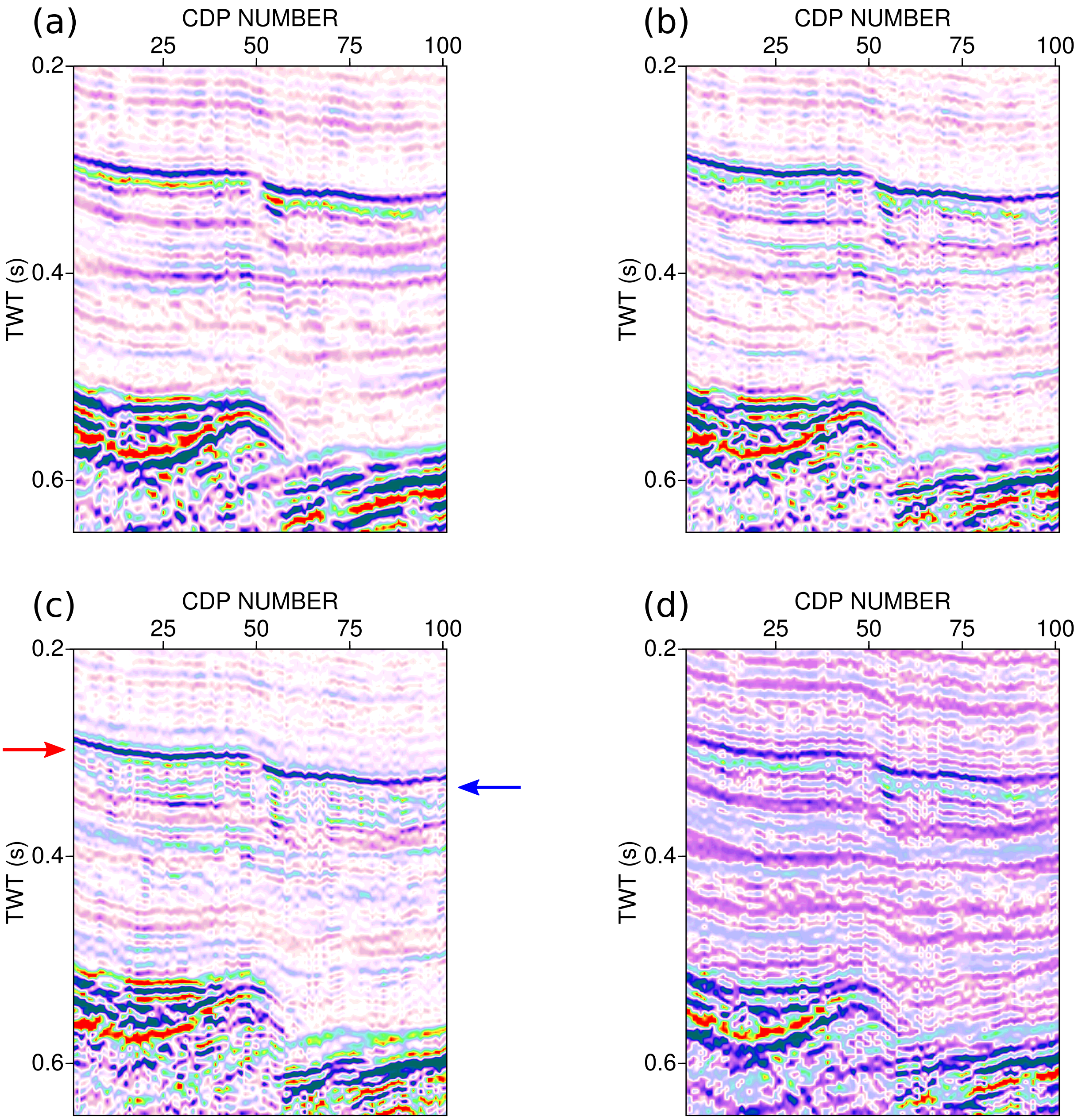

Figure 5.3: Effect of inverse filters on image. (a) is similar to Fig. 5.2b; (b) is the result after applying the two deghosting filters as shown in Fig. 2.13e (post stack spectrum in Fig. 5.1d). The ghost signal is only locally suppressed; (c) is the result after applying the operators as described in section 5.1. The ghost signal is successfully suppressed at the right part of the image (blue arrow) and locally suppressed on the left part of the image (red arrow); (d) is the result after applying the inverse wavelet extracted during the well-seismic tie process. Due to disproportionally shaping the spectrum, both low and high frequency reverberations dominate the image, while the ghosts signal remains untouched.

An alternative yet interesting criterion which can indicate both the level of high frequency noise and the boost of low frequencies is presented in Figure 5.4. The multiple field of the brute stack profile is shown following the filters application similar to Figs. 5.1, 5.3. The profile is generated using an $V_{nmo} = 1500$ m/s. Due to deep marine environment, the multiple events arrive in later times, overlaid on the primary signal which contain the lowest usable frequency band. Therefore, a relative increase of the amplitude level of these frequencies can become evident compared to the shallower subsurface targets. Simultaneously, any unwanted high frequency reverberations than can produce illusory reflectivity may also become apparent.

Fig. 5.4a is the ghosts included multiple field after time invariant bandpass filtering (corner frequencies 3, 8, 100, 120 Hz) and spherical divergence correction. The goal is to eliminate the white/dark regions immediately after the multiple sea bed arrival (red arrow). The zoomed version defined by the blue box is plotted for clarifying the result. Fig. 5.4b is the image after applying operators similar to Fig. 5.3b. Similar to the results from Figure 5.3b, the wavelet is compressed leading to an increase of the temporal resolution, however the ghost arrival isn't eliminated. Fig. 5.4c is generated using the filters used also in Fig. 5.3c. The result suppresses most of the ghost signal. It boosts the low frequency content, which is manifested by the filter induced low frequency shadow. Furthermore, no major reverberations are directly evident. Fig. 5.4d shows the application of the inverse operator from tying the data with the well. The result is in accordance with Fig. 5.3d and is considered suboptimum.

A test of the short period repetition of the signal is the autocorrelation function. To test the robustness of our filters the autocorrelation functions were calculated for all the panels shown in Figure 5.3. Figure 5.5a shows the autocorrelation function calculated from the near offset traces in 5.3a. The stacked autocorrelation trace is also shown overlaying the plot (green wavelet). Note that the autocorrelation function is symmetrical with respect to its maximum value, located always at zero lag ($\tau = 0$). The unwanted ghost signal is expressed through the negative polarity event (white polarity) combined with the light gray event in the 'sidelobes' of the zero-lag event (black polarity).

The target is to create a filter which reduces/eliminates the 'sidelobes' and avoid generating high frequency echoes. Figure 5.5b is the function after applying the filters used for Fig. 5.3b. To facilitate the comparison, the original stacked wavelet, from panel 5.5a, is overlaid as a red curve. Together they can be used to assess the compression of the wavelet, as the dark region gets sharper and the 'sidelobes' become less apparent. This compression does result in sharper image but the ghost effects aren't eliminated. Nevertheless, the filter does not generate significant high frequency noise.

Analogously, Fig. 5.5c plots the calculated autocorrelation function from Figure 5.3c. The wavelet is clearly compressed and the 'sidelobes' are significantly reduced. However, a closer look suggests that the compression is not uniform for all the traces but it varies spatially, with regions where the ghost is optimally suppressed and parts where the suppression is poorer. As the location of the notch in the frequency domain changes along the profile, a generic post-stack filter cannot fully compensate for the actual observed notches at every trace (an effect also depicted in Fig. 5.3c - blue/red arrows). Note that if this spatial variability is also present in all of the offsets, a complete pre-stack compensation requires the application of independent filters for every trace in the data set.

The filter does create some secondary reverberations that could induce high frequency events in our data set. Still, the amplitude of these events, based on the stacked trace is insignificant compared to the reduction of the ghost signal and the improvement in the temporal resolution of the data. Furthermore, taking into account the general smoothing of the result after applying preSTM (Asgedom et al., 2017), any potential reverberations will appear less pronounced post-stack. In the last Fig. 5.5d, the function plots the autocorrelation from Fig. 5.3d. The filter clearly distorts the wavelet and generates significant reverberations.

The optimum deghosting operators were used to generate the final version of profile S310-07. A summary of the increasing complexity of the processing in time domain is depicted in Fig. 5.6. Fig. 5.6a, same as Fig. 2.5a, plots the final isotropic preSTM result including the cosmetic post-stack processing steps, as described in (Chapter 2). Automatic gain control (AGC) with a time window of 500 ms was also applied as a comparison tool to clarify the structural features of the image. Most of the subsurface targets are focused, but the clarity of the events is compromised by the ghost signal which degrades the quality of the image. Fig. 5.6b shows the anisotropic preSTM image after applying all the post - processing steps previously described. The focusing is improved compared to the original isotropic result, mainly because more traces are used during the stacking procedure in every CDP gather. However, it is quite apparent that still the image can be improved in terms of temporal resolution. The last Fig. 5.6c displays the anisotropic image using the deghosting operators that best met all the available criteria. The difference in the image resolution is significant, especially in the sedimentary sequences associated with the black claystones and the glauconitic sandstones.

The operators cannot be considered perfect as some secondary reverberations are evident directly below the seabed, a phenomenon evaluated using the autocorrelation function (Fig. 5.5c). Nevertheless, it can be argued that the image's resolution is improved both in terms of high and low frequencies. The latter is an important consequence of the operators, as we are aiming to shape all the usable frequency band (flat spectrum in Fig. 5.1f). Red arrows in the panels indicate this dual effect in three different time/depth levels of the profile. The uppermost red arrow at 5.6c shows the improvement in the mid sedimentary sequence after applying the filters. The high frequency events are much sharper and clearly retrieved, as the signal is richer in mid to high frequencies. On the contrary, the middle and bottom arrows, show the critical aspect of boosting the low-mid frequency band. The arrow pointing at the glauconitic sandstones level highlights an interesting interbed thin layer, which becomes less resolvable on the hanging wall on the left of the fault at approximately CDP 2600. The illumination of this interbed target was achieved only after applying the inverse deghosting operators. In a similar manner, any remnant reflectivity below the basalts sequence is also clarified using the lowest available frequencies, a result that can lead to better sub-basalt imaging (bottom red arrow). Note that due to time constraints and project targets, further work on improving this part of the image was not pursued.

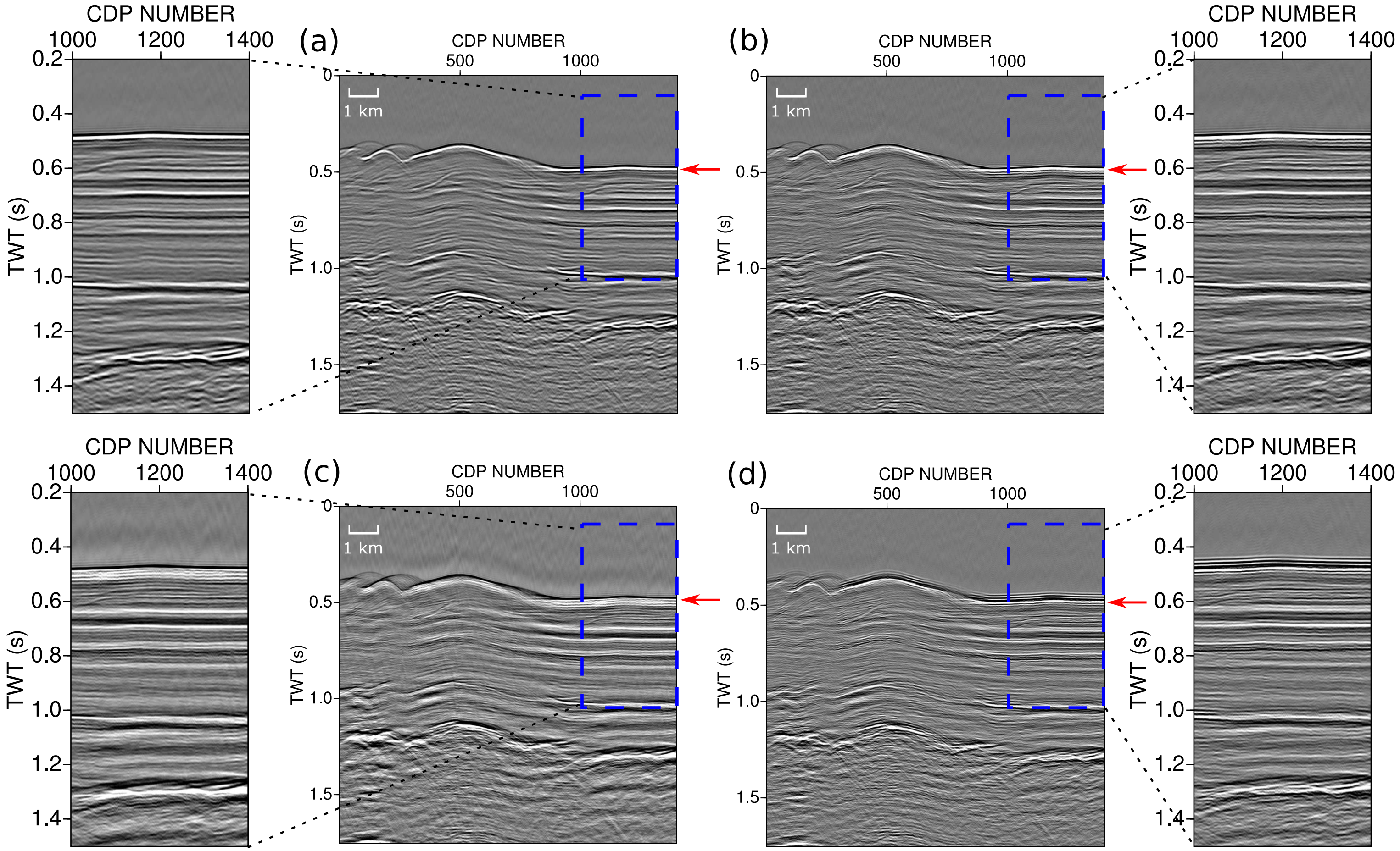

Figure 5.4: Multiple signal as deghosting criterion. (a) is the brute stack of the multiple field ($V_{nmo} = 1500$ m/s) after spherical divergence correction and time invariant bandpass filter. The target is to eliminate the white/light gray regions pointed by the red arrow, shown also in the zoomed version of blue dashed box for clarity; (b) shows the multiple signal after applying the same operators as in Fig. 5.3b. The filter compresses the wavelet but doesn't eliminate the ghost signal. No high frequency oscillations are directly visible; (c) and in its zoomed version, the filter optimally eliminates the ghost arrivals, with a relative increase in the low frequency signal. No major reverberations are evident; (d) shows the inverse filter similar as in Fig. 5.3d. Locally, some high frequency noise is evident but again the ghost elimination is not optimum.

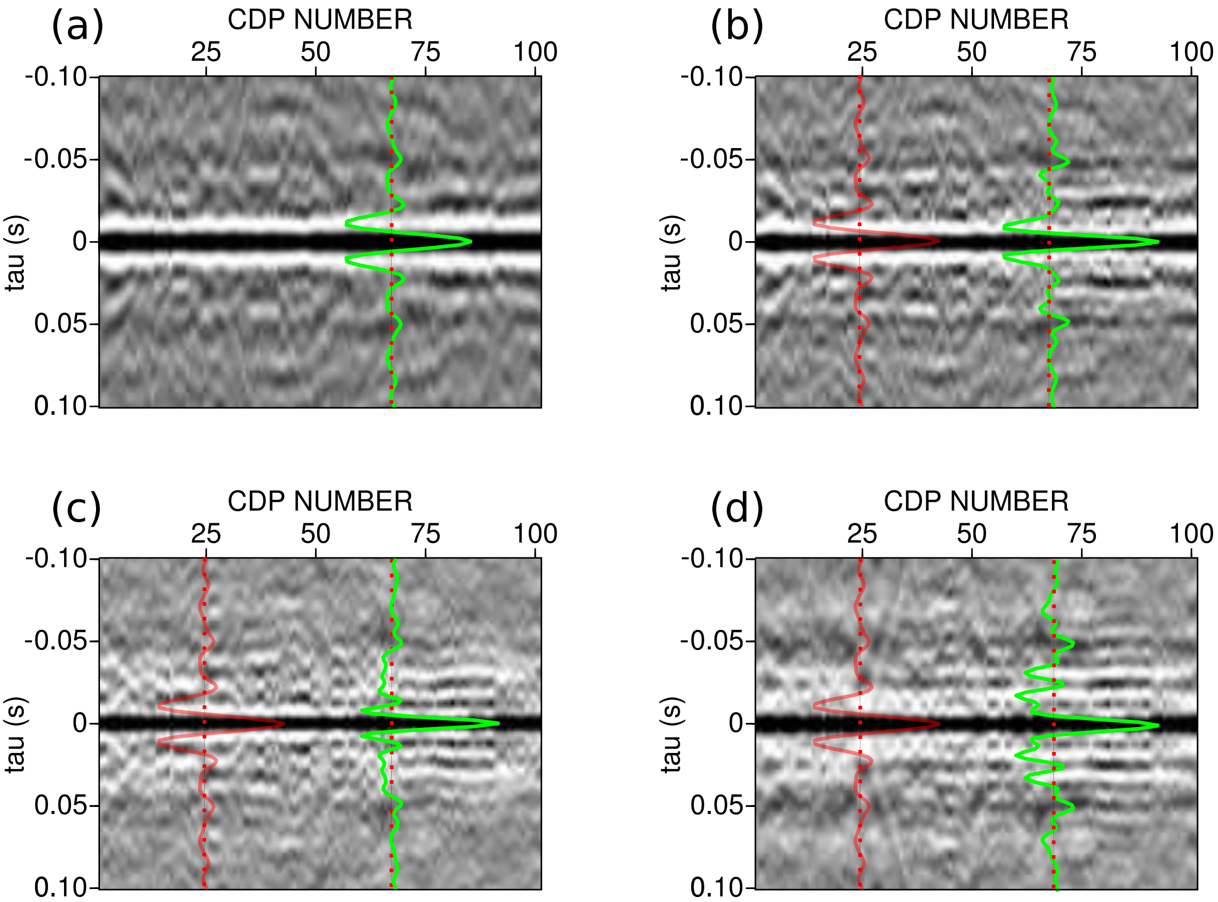

Figure 5.5: Autocorrelation functions of the near offset traces. (a) shows the autocorrelation function from the near trace profile, with its stacked representation superimposed (green color, red dashed line is the zero amplitude axis); (b) is same as (a) but after the application of the operators as in 5.1c, 5.1d. The wavelet is compressed compared to the original (red opaque waveform) and no secondary oscillations are generated but the ghost effect is still pronounced; (c) is extracted after applying the same filters as in 5.1e, 5.1f to the profile. The 'sidelobes' reduction is significant and some low amplitude reverberations are apparent; (d) is the resulted function after applying the filter as in 5.1g, 5.1h. The wavelet is distorted and secondary oscillations are visible.

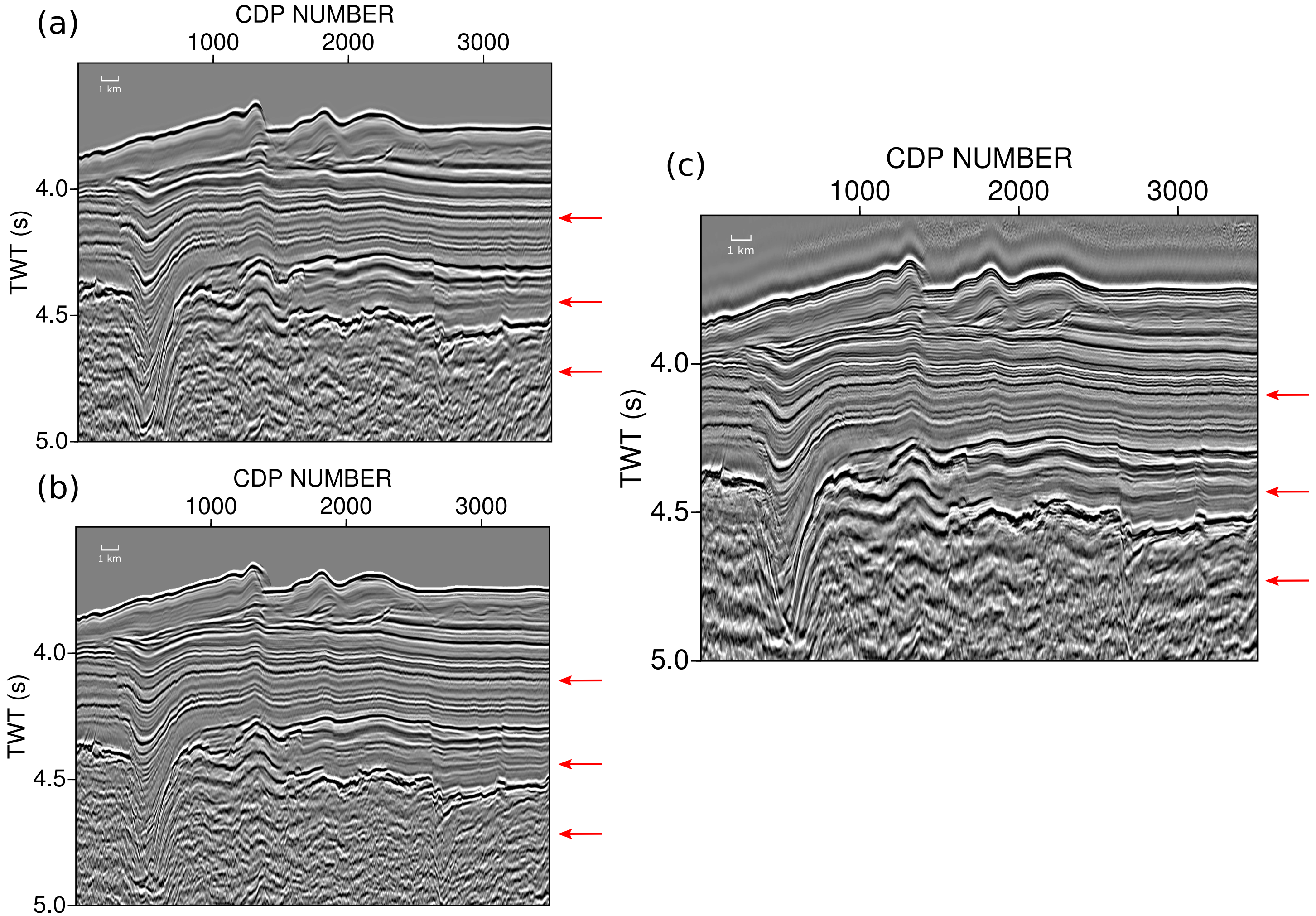

Figure 5.6: Synoptical view of preSTM imaging with deghosting operators. (a) is the final isotropic preSTM image without ghost compensation, similar with Fig. 2.5a; (b) is the final anisotropic preSTM image without ghost compensation. The image appears more focused compared to the isotropic result due to the increased number of active traces in a CMP gather for stacking; (c) shows the final image after post-stack processing and application of deterministic deghosting filters (no sea noise mute applied). In all images, red arrows indicate regions where the improvement is more obvious.

5.3 BRAINS algorithm and anisotropic parameters

The pre-drilling depth predictions as described in Chapter 3 and shown schematically in Figure 3.8b along with the true depths reported in Chapter 4, indicate a discrepancy between the posterior mean depth results and the true depths at the black shales/glauconitic sandstones interface. This observed mismatch can be attributed to two interlinked reasons. First, the top-bottom mapping of time domain signal to depth domain, favours an error accumulation which propagates from shallowest parts of the profile to deeper structures. As a result, assigning slightly incorrect $V_{int.}$ values in the shallowest sediments may not be directly translated into pronounced RMO in the preSDM image gathers, but their cumulative effect can propagate in deeper targets resulting in a mismatch between true/modelled mean depths.

Most importantly, the observed misfit can be directly attributed to the isotropic approximation of BRAINS and the migration algorithm originally used for imaging. As described in equations 3.6 - 3.8, the Gaussian process emulators do not include an explicit representation of epsilon (ϵ) and delta (δ) anisotropic parameters (Thomsen, 1986), therefore these terms are not statistically quantified as an output from the model. The uncertainty related with anisotropic conditions was integrated into the model discrepancy term which value is set accordingly to accommodate the mismatch in the predicted depths and observed data, partly driven by the exclusion of the Thomsen's ϵ and δ parameters. This approach was chosen in order to avoid narrow posterior variances which would indicate overconfident depths predictions for the drilling targets; predictions that couldn't be supported from the result extracted using an isotropic depth migration algorithm alone, without the confirmation from independent observations (well logs).

Although an over-simplification, this compensation of the anisotropic parameters through a unified discrepancy term can be considered as the optimum solution in our system. The lack of any wireline logs to provide independent information on seismic velocities does not permit the process of anisotropic velocity model building where the 'true' velocity values could be implemented to better constrain the prior information in our model and simultaneously be used as a starting point for higher order NMO correction (4^{th} order correction, η parameter). Secondly, due to the uncertain tie between the observed reflectivity in the final preSTM/preSDM images and the lithological boundaries (especially at the boundary between limestones to black shales), any scaling of the target horizons to match the observed depths (Davies et al., 1974) using an inferred δ parameter value is unwise due to the risk of assigning observed reflectivity to incorrect geological boundaries and hence depths. As a result, trying to infer the anisotropic parameters and provide their uncertainty estimations, without any well control, was a task prone to uncertainties that could compromise the predictions of velocities and depths for the horizons of interest.

However, there is an additional, more subtle reason that justifies our approach. It has been shown (Al-Chalabi, 2014), that the inclusion of a 4^{th} order term during NMO correction (estimation of η parameter) is associated with a large increase in the observed variance compared to the simpler 2^{nd} order hyperbolic approximation mainly due to the strong anti-correlated nature between V_{nmo} and η variables. This result indicates, that an anisotropic approach during the velocity analysis stage combined with anisotropic migration algorithms, although may result in better focusing of the final image and possibly better prior/posterior mean depth results, does not lead to a better uncertainty quantification of velocity values.

5.4 Well - seismic tie after notch compensation

The preSTM profile generated after applying the deghosting operators (section 5.1) was then used to perform a well-seismic tie. In theory, a complete notch compensation can lead to a better match of modelled with observed reflectivity, providing more robust seismic inversion results due to the compensation of low frequencies (Soubaras et al., 2012).

Figure 5.7 compares the wavelets extracted from the same well log information and preSTM profiles with and without ghosts respectively (Figure 5.7a, 5.7b). The PEP value with the best match location for the deghosted case is also plotted in Figure 5.7c. Both wavelets appear similar however the wavelet extracted from the deghosted profile shows a sharper main lobe with more pronounced secondary oscillations. The overall added noise in the data set renders the PEP value smaller than the original case (Figure 4.5). This effect can be attributed to the nature of the inverse filters which increase the temporal resolution but simultaneously add a high frequency noise component to the data set.

A more complete comparison of the two tied data sets is provided in Figure 5.8. The modelled traces, generated from the two wavelets plotted in Figure 5.7, are overlaid on top of the two preSTM profiles (left profile-result before application of deghosting filters, right profile-result after applying deghosting filters). The different in the level of increased bandwidth is evident especially in the shallow part of the profile (red curly bracket), where the modelled trace after deghosting the data shows an increase in the low frequency noise component. This low frequency effect is partially eliminated in deeper structures (green curly bracket) where the match is in accordance with the match from the original preSTM profile. In the region of the black claystones (green right curly bracket) the reflectivity, after the notch compensation, appears clearer and better resolved.

Overall, the comparison indicates the unstable nature of the operators which can lead to a better illumination for a number of targets, but in some regions can act as a hindrance for correctly interpreting the image.

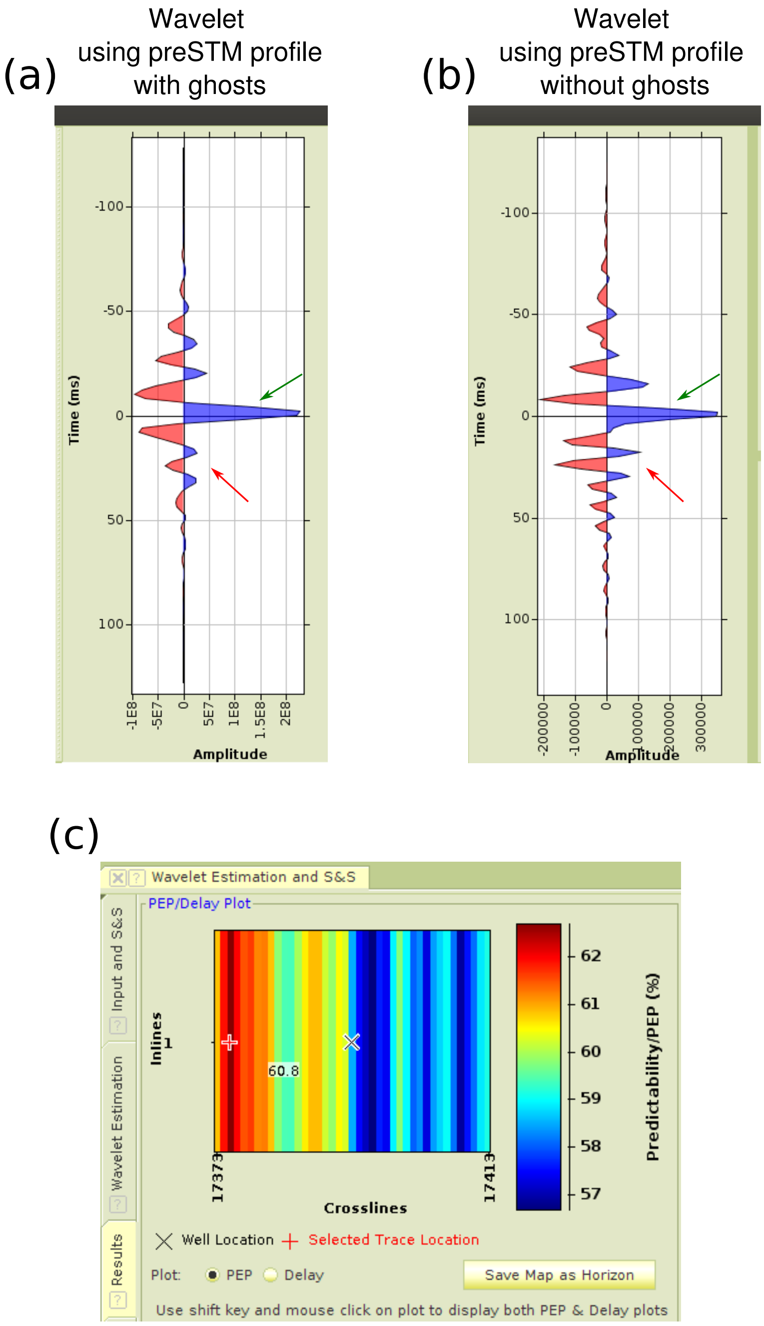

Use shift key and mouse click on plot to display both PEP & Delay plots

Figure 5.7: Comparison between extracted wavelets from data set with and without ghosts. (a) is the extracted wavelet as generated from the well-seismic tie procedure described in section 4.3; (b) the wavelet is extracted from the same process but using as an input the post-stack deghosted preSTM image. Although the wavelet appears sharper (green arrows) the inverse filters generated high frequency secondary oscillations (red arrows); (c) plots the PEP value from the well-tie procedure using the deghosted image.

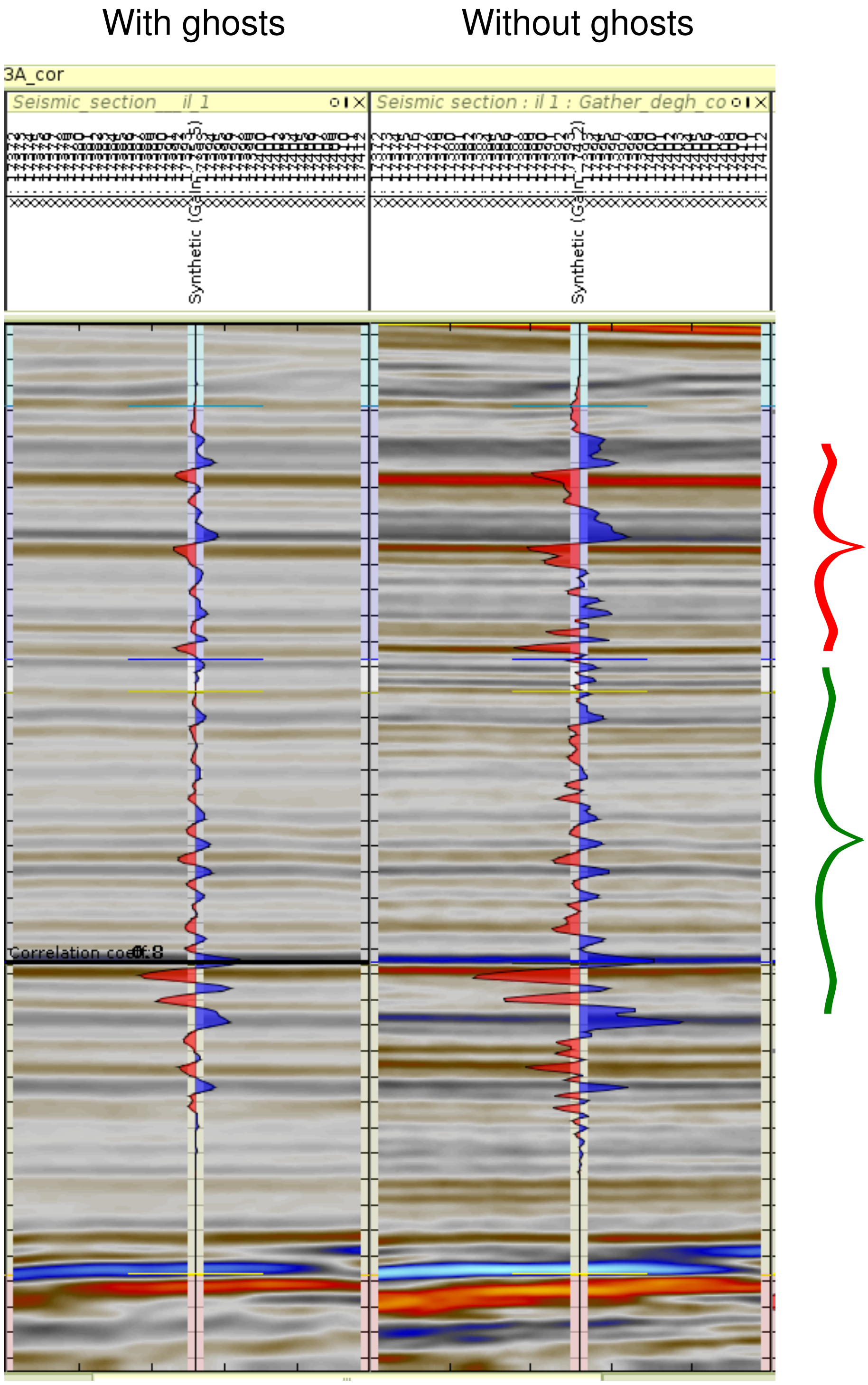

Figure 5.8: Modelled traces overlaid on preSTM profiles. The left panel shows the modelled trace overlaid on top of the preSTM profile with ghosts arrivals, same as in 4.6; Right panel shows the modelled trace on top of the preSTM profile after notch compensation. The wavelet appears to have a superimposed low frequency component, especially at the shallow sedimentary sequence (red curly bracket). For deeper structures, the match is comparable with the original tie (green curly bracket).

5.5 Conclusion

In this chapter we initially highlighted the most important aspects related to the effectiveness of the inverse operators. The results demonstrate the filter effects in different, yet interconnected domains. From the conversation and the relevant figures, it became apparent that a complete and fair comparison of the deghosting operators must incorporate both quantitative criteria (amplitude spectra, $f-x$, $f-k$ diagrams and autocorrelation functions) and interpretation oriented criteria. A clear ghost signal must be firstly located in the profile/gathers and its effect should be recognised in different domains. Subsequently, every filter has to be tested against the original image and domains in order to objectively confirm that a filter set outperforms one another.

Furthermore, a justification for merging the anisotropic parameters in a common term (model discrepancy term) was described. This alternative representation of the travel-time equation can potentially compensate not only for our incomplete knowledge of the values of anisotropic parameters during the pre-drilling evaluation stage, but also for the parameters' unreliable statistical quantification. However, I have to note that the results using the GP emulators must be considered as a first test of this approach and further investigation of the parameters' feasibility must be made in different profiles.

Finally, well-seismic tie procedure was tested for the deghosted preSTM profile given the filters from section 5.1. The results depict a less stable tie after applying the operators, with some parts of the profile showing a better illumination whereas others having a disproportional level of low frequency component.

In the next chapter Chapter 6, the main conclusions of the project will be recapitulated. Furthermore, potential implementations of the approaches described throughout this study will be proposed, aiming to deliver better results concerning imaging and depth predictions.

Chapter 6

Conclusions and future work

6.1 Conclusions

This study looked into the application of Bayesian statistics in seismic reflection velocity model building as a tool to make depth predictions for a number of drilling targets during the IODP expedition, leg 369. To optimize the results, a robust seismic reflection processing sequence was developed, focusing on maximising the resolution of the subsurface image by applying a set of deghosting operators combined with Kirchhoff preSTM/preSDM migration algorithms. With the synergy of high quality seismic data and carefully selected prior time-velocity picks, the statistical analysis provided very good predictions for depths to drilling targets. The predictions along with the processing strategy and the Gaussian models were published in Geophysical Journal International (Michelioudakis et al., 2018). The final deliverable of this research was the well to seismic tie processing conducted by merging the seismic line S310-07 with the well log information from Hole U1513. Using the results from this tie, an attempt was made to refine the Mentelle Basin interpretation. Furthermore, an initial application of anisotropic preSDM was performed, as a method to restore the depths of the subsurface targets to their true location and achieve optimally focused image.

The key findings of this Thesis are summarised in the following points:

1. **application of deghosting filters (pre-stack/post-stack)**: the application of deterministic deghosting filters in the pre-stack but particularly in the post-stack domains can improve the temporal resolution of the subsurface image, clarifying the targets of interest. By constructing filters to match the observed post-stack amplitude spectrum notches of a given data set, an optimum shaping of the spectrum can be achieved. Due to their 1D assumption, the filters are tailored primarily for deep marine environment data sets;

2. **deghosting filters for legacy seismic data**: for newly acquired data, the deghosting process is accomplished by acquisition based or processing based techniques (Tenghamn et al., 2007; Amundsen, 1993; Katibe, 1999) using sophisticated acquisition systems with accurate receiver depth information (Soubaras and Dowle, 2010). However, the deterministic deghosting filters can be particularly useful for a large number of legacy data sets where information about the streamer depth is unreliable and for legacy data acquired during rough sea conditions;

3. **caveats in the application of deterministic filters**: the deterministic filters are fast to model and their application is straightforward. Thus, a large number of different filters can be tested so as to achieve an optimum result. However, the rapid modelling of the operators in some cases has the cost of generating unwanted illusory reflectivity. As a result, a number of different criteria must be applied to every image so as to evaluate the operators' stability;

4. **importance of the criteria used to evaluate a deghosted result**: Due to the complicated nature of ghost arrivals, it is in some cases particularly demanding to evaluate if one deghosting filter produces better result compare to another. Using synergistically the criteria as stated in Chapter 4, the processor can evaluate the stability and most importantly the effectiveness of the deghosting operators applied.

5. **BRAINS algorithm results for the purposes of IODP, leg 369**: BRAINS algorithm provided constrained predictions for the depths of drilling targets at what was to become the Site IODP U1513. During the period of seismic processing and statistical analysis, no independent velocity information for MB targets or well-seismic tie was available. So it is expected that all the predictions would be inside the $\pm 2\sigma$ credibility intervals assuming isotropic media;

6. **BRAINS algorithm predictions as a tool to perform probabilistic imaging**: having information about the posterior mean and standard deviation of the $V_{int.}$ field, a set of randomly generated velocity fields was created and different sets of preSDM images were developed. The process can indicate the relative changes of the image features as mapped from changes in the velocity field, honouring the statistical information extracted from the algorithm. As a result, the probable 'image representations' of subsurface targets can be used as a tool that can identify the uncertainty in the depth to targets at proposal drill sites.

7. **well-seismic tie at Site U1513**: using the sonic and density logs information from Site U1513, a well-seismic tie was performed. Most of the subsurface targets were unambiguously matched with the observed reflectivity from profile S310-07, resulted in a tie with good

statistical results, taking into account that a segment of the log data was modelled. It is likely that the lithological boundaries would have been better identified if a complete sonic log data set was available;

8. **well seismic tie using deghosted data set**: a well-seismic tie using the deghosted preSTM image was also tested. The results indicated the partially unstable nature of the operators which illuminate the subsurface targets, but can add a noise component in the data set. In reality, with no reliable receiver depth information and rough sea surface conditions, it is in question whether similar type of filters can be applied without generating unwanted noise in a segment of the image. Depending on the quality of the data set, this suggests that different filters could be applied to illuminate different subsurface targets.

6.2 Future Work

The seismic processing routines and the statistical technique applied for the purposes of the project can be considered as the initial attempt to deliver probabilistic estimations for the depths to drilling targets. Due to time constraints and data quality, the full approach was tested solely on profile S310-07. Thus, the next step is to apply a similar seismic sequence and statistical analysis to more profiles, with the goal to test the strength of the algorithm in different environments. In the following, I summarise the aspects of this study that need further investigation.

6.2.1 Application of deterministic filters pre-stack

As mentioned previously, the modelled deterministic filters are tailored to match the observed post-stack amplitude spectrum. An initial attempt to apply the source side deghosting operator pre-stack was tested in Chapter 2. However, for the receiver's side ghost arrival, I used the Claritas in-built algorithm which is angle dependent (can be applied in shot or CMP domain) and can compensate for variable streamer depths. The potential drawback of the algorithm is related to situations where no reliable depth information is available or rough sea surface conditions are present. This effect manifests itself as an apparent remnant notch in the amplitude spectra of all the profiles applied (for example see Figures 2.6, 2.12).

Following a similar approach as developed in section 2.1.1.7, the receiver side inverse filter could be applied pre-stack, especially in deep marine environments profiles. Some initial tests of applying pre-stack both source and receiver's side operators, modelled post-stack, are encouraging and demonstrate that a stable notch compensation can be attained without generating illusory reflectivity. Therefore, attempts must be made to check the applicability of the filters in the pre-stack domain.

6.2.2 BRAINS and tomographic inversion

The predictions as published in Michelioudakis et al., 2018 were based on a posterior velocity field, with its prior analog being developed using the vertical update technique (Deregowski, 1990). For contemporary velocity model building studies, this approach is considered obsolete, but due to the relatively smooth subsurface structure and primarily due to software limitations (no available reflection tomographic inversion software) the technique was implemented to constrain the final depth results.

If the BRAINS algorithm can be effectively coupled to a layered based tomographic inversion routine, allowing more reliable predictions, the seismic sequence along with the statistical analysis can be outlined in the following:

- designatature - deghosting - denoise - demultiple and amplitude compensation of the shot gathers;
- initial layer based velocity model building (V_{rms}) for preSTM purposes using manual or automatic picking;
- using the initial velocity field as an input, apply tomographic inversion in depth domain until achieving optimum flat CIG gathers and developing a high frequency $V_{int.}$ field;
- depth to time conversion of the CIGs using a smooth version of the final $V_{int.}$ output from the tomographic inversion algorithm and inverse NMO the gathers;
- use of the un - NMO depth to time converted CIGs along with the final $V_{int.}$ field as prior information to BRAINS algorithm. Extract the posterior results for the variables of interest;
- perform new preSDM using the posterior mean $V_{int.}$ field to map differences from velocity field to image structures.
- use of the information from the posterior distribution to generate random $V_{int.}$ fields for probabilistic imaging.

The aforementioned flow is generic and can deliver probabilistic estimations for depths to drilling targets hosted in medium to high complexity environments.

6.2.3 BRAINS and anisotropic parameters

Incorporating the ϵ, δ anisotropic parameters in BRAINS algorithm involves assigning prior distributions in these parameters, a task that may render the algorithm more complete but not necessarily more robust. As explained in section 5.3, the full capacity of the parameters is only achieved for the case of having prior information concerning velocity values of the media from independent (well) information. In regions where information is poor or absent, the optimum approach is to tune the model discrepancy term (see Chapter 3) to relax the credibility intervals in a more realistic level. However, even were no independent information is available, the algorithm requires input from experts to define the target boundaries. In cases where reliable prior information is available a probabilistic analysis of the extra parameters can be indeed tested. However, I expect that the feasibility of this approach is of dubious benefit as a huge number of possible combinations between V_p and ϵ, δ (expressed as η term) have to be used for anisotropic preSDM. A more realistic approach may be to tailor the probabilistic estimation only to one critical subsurface target and generate sets of its most probable representations.

6.2.4 BRAINS and plotting tools

The current version of BRAINS algorithm does not produce plots that demonstrate the Implausibility measurement as depicted in Figures 3.4 and 3.5. Editing the algorithm to depict the outputs in a way that is more familiar in the geophysical community (plots similar to a semblance spectrum), can directly facilitate the processor to interpret the results from every step faster and more robustly.

6.2.5 Further tests on well - seismic tie

The results and the subsequent interpretation from well - seismic tie, as reported in Chapter 4 were based on modelling the middle part of the well log concerning the black shales sequence. This approach is not exhaustive as it is possible that some models may better represent the ρ - V_p - V_s relation. If true, better PEP values may be extracted and a more reliable well - seismic tie can be achieved. Furthermore, due to time constraints the tying process was solely tested on profile S310-07. During the IODP expedition, leg 369 (Hobbs et al., 2017), a total number of 4 sites where cored and well log information was acquired.

For the purposes of this study, most of the available Geoscience Australia 2D profiles were reprocessed in time domain using similar flows with those described in Chapter 2. Thus, depending on the quality of the well logs, well - seismic tie can be applied. The results will provide extra details for interpreting the MB area as the tied reflectivities will be reliably tracked across the basin.

6.3 Conclusion

This study investigated the application of Bayesian statistics as a tool to make depth predictions for a number of drilling targets associated with the IODP expedition, leg 369. To constrain the depth predictions, a seismic processing strategy was followed focused on improving the temporal resolution of the seismic data using deterministic deghosting filters. The filters were combined with Kirchhoff preSTM/preSDM migration algorithms to achieve well focused images in both time and depth domains. Using the processed seismic gathers as input along with carefully picked time-velocity values, the statistical algorithm provided good predictions for the targets of interest. Subsequently, well-seismic tie was performed by merging S310-07 profile with well information from Hole U1513. The result of the process aided to refine the Mentelle Basin interpretation. In order to restore the depths to drilling targets and account for the black claystones anisotropic conditions, the sonic log information was used as input to Kirchhoff anisotropic preSDM. The output image repositioned the targets to their observed depth level while preserving an optimum focusing.

Bibliography

Abrahamsen, P., Omre, H., and Lia, O. (1991). Stochastic models for seismic depth conversion of geological horizons. *SPE.* **23138**, 329-341. https://doi.org/10.2118/23138-MS.

Al-Chalabi, M. (1994). Seismic velocities - A critique. *First Break.* **12**(12), 589-596. doi: 10.3997/1365-2397.1994036.

Al-Chalabi, M. (1997). Parameter nonuniqueness in velocity versus depth functions. *Geophysics.* **62**(3), 970-979. doi: 10.1190/1.1444203.

Al-Chalabi, M. (2014). *Principles of Seismic Velocities and Time-to-Depth Conversion*, EAGE, 491 p.

Alkhalifah, T. and Tsvankin., I. (1995). Velocity analysis for transversely isotropic media. *Geophysics.* **60**(5), 1550-1566. doi: 10.1190/1.1443888.

Alkhalifah, T. (1997). Velocity analysis using nonhyperbolic moveout in transversely isotropic media. *Geophysics.* **62**(6), 1839-1854. doi: 10.1190/1.1444285.

Amundsen, L. (1993). Wavenumber-based filtering of marine point-source data *Geophysics.* **58**(9), 1335-1348. doi: 10.1190/1.1443516.

Amundsen, L., Pedersen, O., Osen, A., Robertsson, J.O.A. and Landrø, M. (2017). Broadband seismic over/under sources and their designature-deghosting. *Geophysics.* **82**(5), P61-P65. https://doi.org/10.1190/geo2016-0512.1

Amundsen, L., Reitan, A., Weglein, A.B. and Ursin B. (2016). On seismic deghosting using Green's theorem. *Geophysics.* **81**(4), V317-V325. https://doi.org/10.1190/geo2014-0296.1

Andrianakis, I., Vernon, I.R., McCreesh, N., McKinley, J.T., Oakley, J.E., Nsubuga, R.N., Goldstein, M. and White, R.G. (2015). Bayesian History Matching of Complex Infectious Disease Models Using Emulation: A Tutorial and a Case Study on HIV in Uganda. *PLOS*

Computational Biology. **11**(1), https://doi.org/10.1371/journal.pcbi.1003968.

Asgedom, E.G., Orji, O.C., Klüver, T., Tabti, H. and Söllner, S. (2017). Rough sea surface implications on receiver deghosting. *First Break.* **35**(4), 29-37. doi:10.3997/1365-2397.2017010.

Backus, G., E. (1962). Long-wave elastic anisotropy produced by horizontal layering. *Journal of Geophysical Research.* **67**(11), 4427-4440. doi:10.1029/JZ067i011p04427.

Bancroft, J.C. (2007). *A Practical Understanding of Pre- and Poststack Migrations: Prestack.* Society of Exploration Geophysicists, 482 p.

Bekara, M. and Van der Baan, M. (2010). High-amplitude noise detection by the expectation-maximization algorithm with application to swell-noise attenuation. *Geophysics.* **75**(3), V39-V49. doi:10.1190/1.3428749.

Beslier, M.O., Royer, J.Y., Girardeau, J., Hill, P.J., Boeuf, E., Buchanan, C., Chatin, F., Jacovetti, G., Moreau, A., Munschy, M., Partouche, C., Robert, U., and Thomas, S. (2004). Une large transition continent-ocean en pied de marge sud-ouest australienne: premiers resultats de la campagne MARGAU/MD110. *Bulletin Societe Geologique Francaise.* **175**(6), 629-641.

Bickel, S. H. (1990). Velocity-depth ambiguity of reflection traveltimes. *Geophysics.* **55**(3), 266-276. doi:10.1190/1.1442834.

Black, J. L. and Brzostowski M.A. (1994). Systematics of time - migration errors. *Geophysics.* **59**(9), 1419-1434. doi: 10.1190/1.1443699.

Borissova, I. (2002). Geological framework of the Naturaliste Plateau. *Geoscience Australia Record*.

Bower, R. G., Vernon, I., Goldstein, M., Benson, A.J., Lacey, C.G., Baugh, C.M., Cole, S. and Frenk, C.S. (2010). The parameter space of galaxy formation. *Monthly Notices of the Royal Astronomical Society.* **407**, 2017-2045. doi:10.1111/j.1365-2966.2010.16991.x.

Bradshaw, B.E., Rollet, N., Totterdell, J.M. and Borissova, I. (2003). A revised structural framework for frontier basins on the southern and southwestern Australian continental margin. *Geoscience Australia Record.* 2003/3.

Caiado, C.C.S. (2012a). Bayesian Methods Applied to Reflection Seismology.

Phd Thesis. University of Durham: U.K.

Caiado, C.C.S., Hobbs, R.W., Goldstein, M. (2012b). Bayesian Strategies to Assess Uncertainty in Velocity Models. *Bayesian Analysis.* **7**(1), 211–234. doi:10.1214/12-BA707.

Caiado, C.C.S., and Goldstein, M. (2015). Bayesian uncertainty analysis for complex physical systems modelled by computer simulators with applications to tipping points. *Communications in Nonlinear Science and Numerical Simulation.* **26**(1-3), 123-126. http://dx.doi.org/10.1016/j.cnsns.2015.02.006.

Canales, L. (1984). Random noise reduction. *SEG Technical Program, Expanded Abstracts.* 525-527. doi: 10.1190/1.1894168.

Chen, J., and Schuster, G.T. (1999). Resolution limits of migrated images. *Geophysics.* **64**(4), 1046-1053. doi:10.1190/1.1444612.

Chitu, D.A., Al-Ali, M.N. and Verschuur, D.J. (2008). Assessing estimated velocity-depth models: Finding error bars in tomographic inversion. *Geophysics.* **73**(5), VE223–VE233. doi: 10.1190/1.2951469.

Craig, P.S., Goldstein, M, Seheult, A.H. and Smith, J.A. (1997). Pressure matching for hydrocarbon reservoirs: a case study in the use of Bayes linear strategies for large computer experiments (with discussion). In: Gatsonis, C., Hodges, J.S., Kass, R.E., McCulloch, R.E., Rossi, P. and Singpurwalla, N.D., eds. *Case Studies in Bayesian Statistics.* **III**, 37-93. Springer-Verlag. doi: 10.1007/978-1-4612-2290-3-2.

Crawford, A.J., Direen, N.G., Coffin, M.F., Cohen, B., Paul, B. and Mitrovic, L. (2006). Extensive basaltic magmatism on the Naturaliste Plateau, offshore SW Australia. *Geochimica et Cosmochimica Acta.* **70**(18), A116. doi:10.1016/j.gca.2006.06.145.

Cumming, J.A. and. Goldstein, M. (2009). Bayes linear uncertainty analysis for oil reservoirs based on multiscale computer experiments. In: O' Hagan, A. and West, M., eds. *The Oxford Handbook of Applied Bayesian Analysis*, 241-270, Oxford, UK: Oxford University Press.

Davies, T. A., B. P. Luyendyk, et al. (1974) Shipboard site reports, site 258. Initial reports of the Deep Sea Drilling Project, Leg 26, in T. A. Davies, B. P. Luyendyk, et al., eds., Initial Reports of the Deep Sea Drilling Project, **26**, 359–414, U.S. Government Printing Office.

Deregowski, S. (1990). Common-offset migrations and velocity analysis. *First Break.* **8**(6), 225-234.

Direen, N.G., Borissova, I., Stagg, H.M.J., Colwell, J.B. and Symonds, P.A. (2007). Nature of the continent–ocean transition zone along the southern Australian continental margin: a comparison of the Naturaliste Plateau, SW Australia, and the central Great Australian Bight sectors. *Geological Society (London) Special Publication.* 282, 235-261. doi: 10.1144/SP282.12.

Direen, N.G., Stagg, H.M.J., Symonds, P.A. and Colwell, J.B. (2008). Architecture of volcanic rifted margins: new insights from the Exmouth-Gascoyne margin, Western Australia. *Australian Journal of Earth Sciences.* **55**(3), 325-347. doi:10.1080/08120090701769472.

Direen, N.G., Stagg, H.M.J., Symonds, P.A. and Colwell, J.B. (2011). Dominant symmetry of a conjugate southern Australian and East Antarctic magma-poor rifted margin segment. *Geochemistry Geophysics Geosystems.* **12**(2), doi:10.1029/2010GC003306.

Dix, C.H. (1955). Seismic Velocities from Surface Measurements. *Geophysics.* **20**(1), 68-86. doi: 10.1190/1.1438126.

Elboth, T., Qaisrani, H. and Hertweck, T. (2008). De-noising seismic data in the time-frequency domain. *73rd Annual International Meeting, SEG, Expanded Abstracts*, 2622–2626. https://doi.org/10.1190/1.3063887.

Elboth, T., Reif, B.A.P. and Andreassen, O. (2009). Flow and swell noise in marine seismic data. *Geophysics.* **74**(2), Q17-Q25. https://doi.org/10.1190/1.3078403.

Fokkema, J.T. and van den Berg, P.M. (1993). *Seismic Applications of Acoustic Reciprocity.* Elsevier, 350 p.

Ford, A.B. (1975). Volcanic rocks of Naturaliste Plateau, Eastern Indian Ocean, Site 264, DSDP Leg 28. In: D.E. Hayes, Frakes L.A., et al. (Editor). *Initial Reports of the Deep Sea Drilling Project*, 821-833.

Gardner, G. H. F., Gardner L.W. and Gregory A.R. (1974). Formation velocity and density - the diagnostic basics for stratigraphic traps. *Geophysics.* **39**(6), 770-780. doi:10.1190/1.1440465. Gibbons, A.D., Barckhausen, U., van den Bogaard, P., Hoernle, K., Werner, R., Whittaker, J.M., Müller, R.D. (2012). Constraining the Jurassic extent of Greater India: Tectonic evolution of the West Australian margin. *Geochemistry Geophysics Geosystems.* **13**(5), doi:10.1029/2011GC003919.

Goldstein, M. and Wooff, D. (2007). *Bayes Linear Statistics: Theory and Methods.* Chichester, John Wiley, 536 p.

Halpin, J.A., Crawford, A.J., Direen, N.G., Coffin, M.F., Forbes, C.J. and Borissova, I. (2008). Naturaliste Plateau, offshore Western Australia: a submarine window into Gondwana assembly and breakup. *Geology.* **36**(10), 807-810. doi: 10.1130/G25059A.1.

Hampson, D. (1986). Inverse velocity stacking for multiple elimination. *Journal of Canadian Society of Exploration Geophysicists.* **22**(1), 44-55.

Hawkins, K., Leggott, R., Williams, G. and Kat, H. (2001). Addressing anisotropy in 3-D prestack depth migration: A case study from the Southern North Sea. *The Leading Edge.* **20**(5), 528-543. doi: 10.1190/1.1438988.

Hilburn, G., He, Y., and Wang, B. (2017). Uncertainty in orthorhombic model building: Analysis, mitigation, and validation *The Leading Edge.* **36**(2), 133-139. doi: 10.1190/tle36020133.1.

Hobbs, R.W. (2002). Sub-basalt imaging using low frequencies. Sub-basalt imaging 9-11th April, 2002 Cambridge, UK. *Journal of Conference Abstracts.* **7**(2), 152-153.

Hobbs, R.W., Huber, B., and Bogus, K. (2017). Tectonic, paleoclimate, and paleoceanographic history of the Mentelle Basin and Naturaliste Plateau at southern high latitudes during the Cretaceous. *http://publications.iodp.org/scientific_prospectus/369,* doi:10.14379/iodp.sp.369.2016.

Hubral, P. (1977). Time migration - Some ray theoretical aspects. *Geophysical Prospecting.* **25**, 738–745. doi: 10.1111/j.1365-2478.1977.tb01200.x.

Jones, I.F. and Fruehn, J.K. (2003). Factors affecting frequency content in preSDM imaging. *The Leading Edge.* **22**(2), 128-134. doi:10.1190/1.1559039.

Jones, I.F., Surgue, M.J. and Hardy, P.B. (2007). Hybrid gridded tomography. *First Break*, **25**(4), 35-41. doi: 10.3997/1365-2397.2007013 .

Jones, I.F. (2010). *An Introduction to: Velocity Model Building.* EAGE Publications, The Netherlands, 295 p.

Jones, I.F. (2012). Tutorial: Incorporating near-surface velocity anomalies in pre-stack depth migration models. *First Break*, **30**(3), 47-58. doi : 10.3997/1365-2397.2011041.

Jones, I.F. (2014). Estimating subsurface parameter fields for seismic migration: Velocity model building, in Grechka, V. and Wapenaar, K. (eds.) *Encyclopedia of Exploration Geophysics.* Society of Exploration Geophysicists, pp. U1-1-U1-24.

doi: 10.1190/1.9781560803027.entry3.

Journel, A.G. and Huijbregts, C.H. (1978). *Mining Geostatistics.* Academic Press, London, 600 p.

Jongsma, D. and Petkovic, P. (1977). The structure of the Naturaliste Plateau and trough. *The APEA Journal.* **17**(1), 3-12.

Katibe, A. (1999). The footsteps of the receiver ghost in the f-k domain. *Geophysics.* **64**(5), 1618-1626. doi: 10.1190/1.1444666.

Kim, Y.C., and Krebs, J.R. (1993). Pitfalls in Velocity Analysis Using Common-Offset Time Migration. *SEG Technical Program Expanded Abstracts 1993.* 969-973. doi: 10.1190/1.1822670.

Kjartansson, E. (1979). Constant Q-wave propagation and attenuation. *Journal of Geophysical Research.* **84**(B9), 4737-4748. doi: 10.1029/JB084iB09p04737.

Ko, J. and Fox, D. (2009). GP-BayesFilters: Bayesian filtering using Gaussian process prediction and observation models. *Autonomous Robots.* **27**(1), 75-90. doi: 10.1007/s10514-009-9119-x.

Kosloff, D.D. and Sudman Y. (2002). Uncertainty in determining interval velocities from surface reflection seismic data. *Geophysics.* **67**(3), 952-963. doi: 10.1190/1.1484537.

Kragh, E., Robertsson, J., Laws, R., Amundsen, L. , Røsten, T., Davies, T., Zerouk, K., and Strudley, A. (2004). Rough sea deghosting using wave heights derived from low frequency pressure recordings-A case study. *65th Meeting, European Association of Geoscientists and Engineers,Expanded Abstracts. H024.*

Kuypers, M. M. M., Pancost, R. D., and Damste, J. S. S. (1999). A large and abrupt fall in atmospheric CO2 concentration during Cretaceous times. *Nature.* **399**, 342-345. doi:10.1038/20659.

Landa, E., Thore, P., Sorin, V., and Koren, Z. (1991). Interpretation of velocity estimates from coherency inversion. *Geophysics*. **56**(9), 1377-1383. doi: 10.1190/1.1443157.

Laws, R., and Kragh, E. (2002). Rough seas and time-lapse seismic. *Geophysical Prospecting*. **50**(2), 195-208. doi: 10.1046/j.1365-2478.2002.00311.x.

Letki, L.P., Ben-Hadj-Ali, H., and Desegaulx, P. (2013). Quantifying Uncertainty in Final

Seismic Depth Image Using Structural Uncertainty Analysis - Case Study Offshore Nigeria. *First EAGE West Africa Workshop 2013: Subsurface Challenges in West Africa*. doi: 10.3997/2214-4609.20131775.

Lewis, L., Caers, J. and Sava, P. (2015). Assessing seismic uncertainty via geostatistical velocity-model perturbation and image registration: An application to subsalt imaging. *The Leading Edge*. **34**(9), 1064-1066, 1068–1070. doi: 10.1190/tle34091064.1.

Lines, L. (1993). Ambiguity in analysis of velocity and depth. *Geophysics*. **58**(4), 596-597. doi: 10.1190/1.1443443.

MacKay, D. J. C. (1998). Introduction to Gaussian Processes. In C. M. Bishop (Ed.) *Neural networks and machine learning*. **168**, 133-166. Berlin: Springer-Verlag.

Maloney, D., Sargent, S., Direen, N. G., Hobbs, R. W. and Gröcke, D. R. (2011). Re-evaluation of the Mentelle Basin, a polyphase rifted margin basin, offshore southwest Australia: new insights from integrated regional seismic datasets. *Solid Earth*. **2**(2), 107-123. doi: 10.5194/se-2-107-2011.

Matheron, G. (1973). The Intrinsic Random Functions and Their Applications. *Advances in Applied Probability*. **5**(3), 439-468. doi: 10.2307/1425829.

Messud, J., Reinier, M., Prigent, H., Guillaume, P., Coléou, T. and Masclet, S. (2017). Extracting seismic uncertainties from tomographic velocity inversion and their use in reservoir risk analysis. *The Leading Edge* **36**(2), 127-132. doi: 10.1190/tle36020127.1.

Miao, X. and Cheadle, S. (1998). Noise attenuation with wavelet transforms. *SEG Technical Program Expanded Abstracts 1998*, 1072-1075. doi: 10.1190/1.1820071.

Michelioudakis, D.G., Hobbs, R.W., and Caiado, C.C.S. (2018). Uncertainty analysis of depth predictions from seismic reflection data using Bayesian statistics. *Geophysical Journal International* **213**(3), 2161-2176. doi:https://doi.org/10.1093/gji/ggy093.

Milkereit, B. and Spencer, C. (1989). Noise suppression and coherency enhancement of seismic data. *Statistical applications in the Earth Sciences*, edited by F. P. Agterberg and G. HF. Bonham-Carter, Geological Survey of Canada, **89**, 243-248.

Monk, D.J. (1993). Wave - equation multiple suppression using constrained gross - equalization. *Geophysical Prospecting*, **41**(6), 725-736. doi:10.1111/j.1365-2478.1993.tb00880.x.

Neidell, N.S., and Taner M.T. (1971). Semblance and other coherency measures for multichannel data. *Geophysics.* **36**(3), 482-497. doi:10.1190/1.1440186.

O'Hagan, A. (2006). Bayesian analysis of computer code outputs: A tutorial. *Reliability engineering and system safety.* **91**(10-11), 1290-1300 doi:10.1016/j.ress.2005.11.025.

Petkovic, P. (1975a). Naturaliste Plateau. In: J.J. Veevers (Editor), Deep sea drilling in Australasian waters. Macquarie Univ. North Ryde, N. S, W., Australia, 24-25.

Petkovic, P. (1975b). Origin of the Naturaliste Plateau. *Nature.* **253**(5486), 30-33. doi:10.1038/253030a0.

Powell, C.M., Roots, S.R. and Veevers, J.J. (1988). Pre-breakup continental extension in East Gondwanaland and the early opening of the eastern Indian Ocean. *Tectonophysics.* **155**(1-4), 261-283. doi:10.1016/0040-1951(88)90269-7.

Protasov, M., Kolyukhin D., Rostomyan, S., and Landa, E. (2017). Subsalt imaging in the presence of salt-body uncertainty. *The Leading Edge.* **36**(2), 146-150. doi:10.1190/tle36020146.1.

Pukelsheim, F. (1994). The Three Sigma Rule. *The American Statistician.* **48**(2), 88-91. doi:10.2307/2684253.

Rasmussen, C. E., and Williams, C. K. I. (2006). *Gaussian Processes for Machine Learning.* MIT Press, Cambridge, MA, 245 p.

Ripley, B.D. (1991). *Statistical Inference for Spatial Processes.* Cambridge University Press, 148 p.

Robinson, E. A., and Treitel, S. (1967). Principles of digital Wiener filtering. *Geophysical Prospecting.* **15**(3), 311-322. doi: 10.1111/j.1365-2478.1967.tb01793.x.

Royer, J.Y. and Coffin, M.F. (1992). Jurassic to Eocene plate tectonic reconstructions in the Kerguelen Plateau region. In: S.W. Wise Jr. and R. Schlich (Editors). *Proceedings of the Ocean Drilling Program, Scientific Results.* **120**, 917-928.

Sargent, C., Hobbs, R.W., Grocke, D.R. (2011). Improving the interpretability of air-gun seismic reflection data using deterministic filters: A case history from offshore Cape Leeuwin, southwest Australia. *Geophysics.* **76**(3), B113–B125. doi: 10.1190/1.3554396.

Schonewille, M., Vigner, A., and Ryder, A. (2008). Swell-noise attenuation using an iterative FX prediction filtering approach. *SEG Technical Program Expanded Abstracts 2008*, 2647-

2651. doi:10.1190/1.3063892.

Shen, X., Ahmed, I., Brenders, A., Dellinger, J., Etgen, J., and Michell, S. (2018).Full-waveform inversion: The next leap forward in subsalt imaging. *The Leading Edge.* **37**(1), 67b1–67b6. doi: 10.1190/tle37010067b1.1.

Sheriff, R.E. and Geldart, L.P. (1995). *Exploration Seismology.* U.S.: Cambridge University Press, 628 p.

Simm, R., White, R., and Uden, R. (2000). The anatomy of AVO crossplots. *The Leading Edge.* **19**(2), 150-155. doi: 10.1190/1.1438557.

Simm, R., and Bacon, M. (2014). *Seismic Amplitude: An Interpreter's Handbook.* Cambridge University Press, 270 p.

Simon, L., and Hale, D. (2012). Velocity analysis using weighted semblance. *Geophysics.* **77**(2), U15-U22. doi 10.1190/geo2011-0034.1.

Soubaras, R., Dowle, R. (2010). Variable-depth streamer - a broadband marine solution. *First Break*, **28**(12) 89-96.

Soubaras, R., Lafet, Y., and Whiting, P. (2010). Variable-depth streamer acquisition: broadband data for imaging, post and pre-stack inversion. *ASEG Extended Abstracts 2012: 22nd Geophysical Conference*, 1-4.

Stockwell, J.W. (1999). The CP/SU: Seismic Un(*x) package, *Computers and Geosciences*, **25**(4), 415-419.

Stockwell, J.W. (2011). Complete listing of CWP free program self - documentations, *CWP, Colorado School of Mines*, p.774.

Sullivan, M.F. and Cohen, J.K. (1987). Prestack Kirchhoff inversion of common-offset data. *Geophysics.* **52**(6) 745-754. doi:10.1190/1.1442341.

Taner, M. T., and Koehler, F. (1969). Velocity spectra - digital computer derivation and applications of velocity functions. *Geophysics.* **34**(6), 859–881. doi: 10.1190/1.1440058.

Tenghamn, S.T.L., Vaage, R.S. and Borresen C. (2007). A dual-sensor towed marine streamer: Its viable implementation and initial results *SEG Technical Program Expanded Abstracts 2007.* 989-993. doi: 10.1190/1.2792571.

Thorsos, E.I. (1988). The validity of the Kirchhoff approximation for rough surface scattering using a Gaussian roughness spectrum. *Journal of the Acoustical Society of America.* **83**(78) 78-92. doi: 10.1121/1.396188.

Tieman, H. J. (1994). Investigating the velocity-depth ambiguity of reflection traveltimes. *Geophysics.* **59**(11), 1763-1773. doi: 10.1190/1.1443563.

Thomsen, L. (1986). Weak elastic anisotropy. *Geophysics.* **51**(10), 1954-1699. doi: 10.1190/1.1442051.

Thore, P., Shtuka, A., Lecour, M., Ait-Ettajer, T., and Cognot, R. (2002). Structural uncertainties: Determination, management, and applications. *Geophysics.* **67**(3), 840-852. doi: 10.1190/1.1484528.

Tsvankin, I., Gaiser, J., Grechka, V., Van der Baan, M., and Thomsen, L. (2010). Seismic anisotropy in exploration and reservoir characterization: An overview. *Geophysics.* **75**(5), 75A15-75A29. doi: 10.1190/1.3481775.

Vernon, I., Goldstein, M., and Bower, R. G. (2010). Galaxy Formation: a Bayesian Uncertainty Analysis. *Bayesian Analysis.* **5**(4), 619-670.

Vernon, I. and Goldstein, M. (2010). A Bayes Linear Approach to Systems Biology. *MUCM Technical Report, 10/10*.

Verschuur D.J., Berkhout A.J., and Wapenaar C.P.A. (1992). Adaptive surface-related multiple elimination. *Geophysics.* **57**(9), 1166-1177. doi: 10.1190/1.1443330.

Walden, A., T., and White, R., E. (1998). Seismic wavelet estimation: a frequency domain solution to a geophysical noisy input-output problem *IEEE transactions on geoscience and remote sensing.* **36**(1), 287-297. doi: 10.1109/36.655337.

Wang, Y. (2002). A stable and efficient approach of inverse Q filtering. *Geophysics.* **67**(2), 657-663. doi: 10.1190/1.1468627.

Wang, Y. (2003). Multiple subtraction using an expanded multichannel matching filter. *Geophysics.* **68**(1), 346-354. doi: 10.1190/1.1543220.

Wang, Y. (2004). Stable Q analysis on vertical seismic profiling data. *Geophysics.* **79**(4), D217-D225. doi: 10.1190/geo2013-0273.1.

White, R.E. (1997). The accuracy of well ties: Practical procedures and examples. *SEG Annual Conference, Expanded Abstracts.* 816-819. doi: 10.1190/1.1886137.

White, R.E. (1998). Stretch and Squeeze - Just Keeping up Appearances? *60th EAGE Conference and Technical Exhibition, Leipzig, Germany, Extended Abstracts.* P138.

White, R.E. and Simm, R. (2003). Tutorial: good practice in well ties. *First Break.* **21**(10), 75-83.

White, R.E. and Simm, R. (2003). The Importance of Bandwidth in Seismic Cross Equalisation - Well Tie and Other Examples. *65th EAGE Conference & Exhibition, Stavanger, Norway, Extended Abstracts.* P071.

Williamson, D., and Vernon, I. (2013). Efficient uniform designs for multi-wave computer experiments. arXiv:1309.3520 [stat.ME].

Yilmaz, O. (2017). Circumventing velocity uncertainty in imaging complex structures. *The Leading Edge.* **37**(1), 14-18. doi:10.1190/tle37010014.1.

Ziolkowski, A. M. (1984). The Delft airgun experiment. *First Break.* **2**(6), 9-18. doi:10.3997/1365-2397.1984011.

Appendix A

Bayesian Statistics

Generally in statistics we can follow two main approaches: the frequentist and the Bayesian. For the frequentist, the parameters that govern a system are treated as unknown but fixed values. For the Bayesian approach, the model parameters are considered to be random and follow a prior distribution which is formulated before collecting the data.

For a given vector $\boldsymbol{m} = (m_1, m_2, m_3, ..., m_N)$ representing the parameters of the system and a set of observations $\boldsymbol{y} = (y_1, y_2, y_3, ..., y_M)$ the Bayes' theorem is written as

$$p(\boldsymbol{m}|\boldsymbol{y}) = \frac{p(\boldsymbol{y}|\boldsymbol{m})p(\boldsymbol{m})}{p(\boldsymbol{y})} \tag{A.1}$$

where $p(\boldsymbol{m}|\boldsymbol{y})$ represents the posterior distribution, the probability that the model parameters $\boldsymbol{m}$ are correct given the observation $\boldsymbol{y}$; $p(\boldsymbol{y}|\boldsymbol{m})$ is the likelihood function that represents the distribution of the data $\boldsymbol{y}$ for a fixed vector of the parameter space $\boldsymbol{m}$; $p(\boldsymbol{y}) = \int p(\boldsymbol{y}|\boldsymbol{m})p(\boldsymbol{m})d(\boldsymbol{m})$ representing the probability that data $\boldsymbol{y}$ have been observed; $p(\boldsymbol{m})$ is the prior distribution of the model parameters which incorporates our beliefs about the model before we make the observations $\boldsymbol{y}$.

From the posterior distribution $p(\boldsymbol{m}|\boldsymbol{y})$ we can calculate point estimates of the posterior mean value for each model parameter y by minimising a loss function $L(y, \hat{y})$, measuring the cost of selecting a value $\hat{y}$ for parameter y. Furthermore, credibility intervals, associated with the expected range of values of each model parameters y_i, can be estimated.

Appendix B

Bayesian Models and Gaussian Process in seismic reflection

In the following, we will briefly describe the 1D and 2D Gaussian Process emulators used. See Caiado et al., 2012 for a full description of the models.

B.1 1D emulator

Suppose a discretized subsurface model, with a finite number of interfaces b_i and a given array of source – receiver pairs, S_j and R_j, containing m pairs. All the pairs are symmetrically placed around a Common Mid Point (CMP), with x_j being the distance between S_j and R_j. As the medium is discretized, we can associate to every layer i, a two way travel time T_{0_i} with its time increment ΔT_{0_i}, a root–mean–square velocity V_{rms_i} with its increment ΔV_{rms_i} and a thickness Δz_i. Furthermore, let T_{ij} be the real time for a wave ray to propagate from seismic source S_j to detector R_j, by refracting at interfaces b_i to b_{i-1}, reflecting at b_i and refracting back to the receiver's position. In case of parallel boundaries and isotropic conditions, the real travel time T_{ij} is defined as

$$T_{ij} = \sqrt{T_{0_i}^2 + \left(\frac{x_j}{V_{rms_i}}\right)^2} + \epsilon_{ij} \tag{B.1}$$

where ϵ_{ij} counts for the modelling error due to propagating approximations and isotropic assumptions.

Now, the recorded travel time $T^{(r)}$ is a combination of the real travel time T_{ij} plus a set of recording errors e_{ij}, resulting in the equation

$$T_{ij}^{(r)} = \sqrt{T_{0_i}^2 + \left(\frac{x_j}{V_{rms_i}}\right)^2} + \epsilon_{ij} + e_{ij} \tag{B.2}$$

A generalization of equations (B.1) and (B.2), uses Gaussian Process techniques, works in function space instead of weight space and compensates for the lack of flexibility of the standard regression methods (Rasmussen & Williams, 2006).

For 1D case, we assume that a set of travel times, related to a certain interface in a CMP gather, is a sample of a continuous function with a hyperbolic trend. If a finite set of times in that curve follows a multivariate Gaussian distribution, we can think that every reflection hyperbola in a CMP gather is a Gaussian Process (GP) over offset x.

In a function form, the recorded travel-time curve, for a particular layer, $\mathcal{T}_i^{(r)}$ is a Gaussian Process

$$\mathcal{T}_i^{(r)}(x)|\Delta T_{0_{(1,\dots i)}}, \Delta V_{rms_{(1,\dots,i)}} \sim \mathcal{GP}(m_{t_i}(x), k_i(x, x')) \tag{B.3}$$

with mean and square exponential covariance functions

$$\begin{gathered} m_{t_i}(x) = (t_{0_i}^2 + x^2 \upsilon_{rms_i}^{-2})^{1/2} \\ k_i(x, x') = \sigma_{n_i} + \sigma_{s_i} exp\left(-\frac{(x - x')^2}{d_i}\right) \end{gathered} \tag{B.4}$$

where x and x' define two random points from the offset space in a single CMP, σ_{s_i} is a scale parameter, σ_{n_i} is a noise parameter and d_i is a length parameter. The last parameters are regarded as constants or can be set manually. The joint prior for both $\Delta T_{0_{(1,\dots i)}}$ and $\Delta V_{rms_{(1,\dots,i)}}$ is given by

$$\begin{pmatrix} \Delta T_{0_{(1,\dots i)}} \\ \Delta V_{rms_{(1,\dots,i)}} \end{pmatrix} \sim \mathcal{N}\left(\begin{pmatrix} \mu_{t_{0_i}} \\ \mu_{\upsilon_{(i)}} \end{pmatrix}, \Sigma_{(t_0, \upsilon_{rms_i})}\right) \tag{B.5}$$

and their prior distribution is written as

$$\pi(\upsilon_{rms}, t_0) = \prod_{i=1}^{n} \pi(\Delta t_{0_i}, \Delta_{\upsilon_{rms_i}}) \tag{B.6}$$

with $\pi(\Delta t_{0_i}, \Delta_{\upsilon_{rms_i}})$, the density of the joint prior in (B.5).

In a similar manner, we can express the likelihood function of the GP in (B.3) as

$$\pi(t_i^{(r)}(x)|\upsilon_{rms_i}, t_{0_i}) = \pi\left(t_i^{(r)}(x)|\Delta t_{0_{(1,\dots,i)}}, \Delta \upsilon_{rms_{(1,\dots,i)}}\right) \tag{B.7}$$

Finally, the posterior distribution is given as the combination of the prior distribution (B.6) and the likelihood (B.7), resulting in the following expression

$$\pi(\upsilon_{rms}, t_0|t^{(r)}) = \pi(\upsilon_{rms}, t_0)\int_x \frac{\pi\left(t_i^{(r)}(x)|\Delta t_{0_{(1,\dots,i)}}, \Delta\upsilon_{rms_{(1,\dots,i)}}\right)}{\pi(t^{(r)}(x))}dx \tag{B.8}$$

with $\pi(t^{(r)}(x))$, a normalizing constant that can be evaluated numerically.

B.2 2D emulator

For the 2D case, we expand the 1D Gaussian Process into a multi–gather representation by assuming that the variables ΔT_{0_i}, ΔV_{rms_i}, $V_{int._i}$ and Δz_i, for every geophysical boundary, follow a GP over the CMP positions (x_c) along a profile. As a result, for the recorded travel time $\mathcal{T}_i^{(r)}$ we have

$$\mathcal{T}_i^{(r)}(x, x_c)|\Delta T_{0_{(1,\dots i)}}(x_c), \Delta V_{rms_{(1,\dots,i)}}(x_c) \sim \mathcal{GP}\left(m_{t_i}(x, x_c), k_i(x, x', x_c)\right) \tag{B.9}$$

with mean and square exponential covariance functions

$$\begin{aligned} m_{t_i}(x, x_c) &= \left(t_{0_i}(x_c)^2 + x^2\upsilon_{rms_i}(x_c)^{-2}\right)^{1/2} \\ k_i(x, x', x_c) &= \sigma_{n_i}(x_c) + \sigma_{s_i}(x_c)exp\left(-\frac{(x-x')^2}{d_i(x_c)}\right) \end{aligned} \tag{B.10}$$

In a similar manner, as ΔV_{rms_i} and ΔT_{0_i} follow a GP, they take the following form

$$\Delta V_{rms_i}(x_c) \sim \mathcal{GP}\left(m_\upsilon(x_c), \sigma_{nv_i} + \sigma_{sv_i}exp\left(\frac{(x_c - x_c')^2}{d_{\upsilon_i}}\right)\right) \tag{B.11}$$

$$\Delta T_{0_i}(x_c) \sim \mathcal{GP}\left(m_{t_0}(x_c), \sigma_{nt_i} + \sigma_{st_i}exp\left(\frac{(x_c - x_c')^2}{d_{t_i}}\right)\right) \tag{B.12}$$

with $m_\upsilon(x_c)$, $m_{t_0}(x_c)$ polynomial functions, x_c, x_c' two different CMP locations along the profile and σ_{nv_i}, σ_{sv_i}, d_{υ_i}, σ_{nt_i}, σ_{st_i}, d_{t_i} noise, scale and length parameters for $\Delta V_{rms_i}(x_c)$ and $\Delta T_{0_i}(x_c)$ respectively. The multi-gather case model, compensates for lateral variations in the velocity field. Analogous expressions can link the recorded travel time $\mathcal{T}_i^{(r)}(x, x_c)$ with $V_{int_{(i)}}(x_c)$ and $\Delta z_i(x_c)$ allowing probabilistic estimations for all variables of interest in seismic reflection processing.

Appendix C

Bayes Linear

In order to update the Gaussian Process emulators as described in Chapter 3 and Appendix B, we follow the statistical approach of Bayes linear analysis (for a full description of Bayes linear see Goldstein and Wooff, 2007). The approach can be considered as an alternative method of specifying and analysing the uncertainties of the system explored and it is based on assigning prior distributions solely for means and variances/covariances, which greatly simplifies the uncertainty estimation for large systems (Caiado and Goldstein, 2015). For a given model $f(x)$, the technique uses the following update equations (C.1) for the adjusted mean, $E_D(f(x))$ and adjusted covariance, $Var_D(f(x)$, respectively:

$$\begin{aligned} E_D(f(x)) &= E(f(x)) + Cov(f(x), D)Var(D)^{-1}(D - E(D)) \\ Var_D(f(x)) &= Var(f(x)) - Cov(f(x), D)Var(D)^{-1}Cov(D, f(x)) \end{aligned} \tag{C.1}$$

with x a vector of inputs, $E(f(x)), Var(f(x))$ the prior mean and variance of the model, D the vector of output values of model $f(x)$, evaluated at a number of points from the vector x, $E(D), Var(D)$ the mean and variance of D vector and $Cov(f(x), D))$ the covariance of the model $f(x)$ with the vector of evaluated points D.

Appendix D

Extra Tables

Table D.1: Time domain processing sequence for seismic line S310-17.

S310-17
Reformat and geometry import - CDP spacing = 6.25 m - Nominal CDP fold = 108 (**Flows 1 & 2**)
Instrument delay correction = 100 ms, Source-Receiver datuming (**Flows 1 & 2**)
Minimum phase low cut Butterworth filter 4 Hz, 18 db/octave (**Flows 1 & 2**)
Modelled designature inverse filter (shot gathers) (**Flows 1 & 2**)
Swell noise attenuation (FK domain) (**Flows 1 & 2**)
Deterministic inverse filter for source's notch compensation (shot gathers) derived from post-stack amplitude spectrum (**Flow 2**)
Receiver's notch compensation in $f - x$ domain (shot gathers) (**Flow 2**)
Linear noise elimination (FK domain) (**Flow 2**)
CMP Sorting and 2^{nd} order Velocity analysis (every 312.5 m / 50 CMPs) (**Flows 1 & 2**)
Straight ray isotropic Kirchhoff Pre Stack Time Migration (PreSTM) (**Flows 1 & 2**)
Spherical Divergence Correction (**Flows 1 & 2**)
Outer Trace Mute and Stack (**Flows 1 & 2**)
Deterministic inverse filters for source's & receiver's notch compensation derived from observed average notches as appeared in the post-stack amplitude spectrum (**Flow 1**)
Time variant zero phase Butterworth filter (**Flows 1 & 2**): 10-20-100-125 at seabed (sb), 8-15-100-120 at sb + 0.6 s, 5-10-85-110 at sb + 0.9 s, 3-8-50-75 at sb + 1.2 s
Frequency - distance (f-x) deconvolution for random noise attenuation (**Flows 1 & 2**)
Phase Inverse Q compensation = 200 (**Flows 1 & 2**)
Cosmetic sea noise mute (**Flows 1 & 2**)

Table D.2: Time domain processing sequence for seismic line S310-01.

S310-01
Reformat and geometry import - CDP spacing = 6.25 m - Nominal CDP fold = 108 (**Flows 1 & 2**)
Instrument delay correction = 100 ms, Source-Receiver datuming (**Flows 1 & 2**)
Minimum phase low cut Butterworth filter 4 Hz, 18 db/octave
Modelled designature inverse filter (shot gathers) (**Flows 1 & 2**)
Swell noise attenuation (FK domain) (**Flows 1 & 2**)
Deterministic inverse filter for source's notch compensation (shot gathers)
derived from post-stack amplitude spectrum (**Flow 2**)
Receiver's notch compensation in $f - x$ domain (shot gathers) (**Flows 2**)
Linear noise elimination (FK domain) (**Flow 2**)
CMP Sorting and 2^{nd} order Velocity analysis (every 312.5 m / 50 CMPs) (**Flows 1 & 2**)
Straight ray isotropic Kirchhoff Pre Stack Time Migration (PreSTM) (**Flows 1 & 2**)
Spherical Divergence Correction (**Flows 1 & 2**)
Outer Trace Mute and Stack (**Flows 1 & 2**)
Deterministic inverse filters for source's & receiver's notch compensation
derived from observed average notches as appeared in the post-stack amplitude spectrum (**Flow 1**)
Time variant zero phase Butterworth filter (**Flows 1 & 2**):
10-20-100-125 at seabed (sb),
8-15-100-120 at sb + 0.6 s,
5-10-85-110 at sb + 0.9 s,
3-8-50-75 at sb + 1.2 s
Frequency - distance (f-x) deconvolution for random noise attenuation (**Flows 1 & 2**)
Phase Inverse Q compensation = 200 (**Flows 1 & 2**)
Cosmetic sea noise mute (**Flows 1 & 2**)

Table D.3: Inverse deghosting filters for seismic profiles.

S310-07
$A_{source} = -0.05, -0.1, -0.15, -0.3, -0.15, -0.1, -0.05$ ($dt = 0.5$ ms, $f_{center} = 105$ Hz)
$A_{rec.} = -0.05, -0.1, -0.15, -0.18, -0.15, -0.1, -0.05$ ($dt = 0.5$ ms, $f_{center} = 74$ Hz)
S310-01
$A_{source} = -0.7$ ($dt = 0.5$ ms, $f_{center} = 94$ Hz)
$A_{rec.} = -0.05, -0.08, -0.1, -0.2, -0.1, -0.08, -0.05$ ($dt = 0.5$ ms, $f_{center} = 64$ Hz)
S310-17
$A_{source} = -0.7$ ($dt = 0.5$ ms, $f_{center} = 94$ Hz)
$A_{rec.} = -0.05, -0.08, -0.1, -0.2, -0.1, -0.08, -0.05$ ($dt = 0.5$ ms, $f_{center} = 64$ Hz)
S310-05
$A_{source} = -0.7$ ($dt = 0.5$ ms, $f_{center} = 94$ Hz)
$A_{rec.} = -0.05, -0.08, -0.1, -0.15, -0.1, -0.08, -0.05$ ($dt = 0.5$ ms, $f_{center} = 91$ Hz)

Appendix E

Time domain processing of line S310-17

E.1 Comparison of deghosting filters results

In Fig. E.1 we present the results of preSTM image (E.1a) along with its post-stack deghosted equivalent (E.1b). As the streamer was positioned deeper compared to acquisition of line S310-07 (Nominal streamer depth = 12 m, Table 2.1) the receiver's inverse filter was altered to match the post-stack average spectrum. Note the complex shallow environment including faulted zones and channel features. Note also that some of the faults possibly incise the seabed (blue arrow in Figs. E.1c, E.1d). These features render the velocity model building/imaging more complex than line S310-07 where the seabed was relatively flat so did not include any significant lateral velocity changes. After post-stack deghosting (Figs. E.1b, E.1d, E.1f), the resolution is improved through the whole profile. A notable difference is the possible intra-layer event retrieved in the middle level of the sedimentary sequence after ghost compensation (red arrow in Fig. E.1f compared to Fig. E.1e).

Contrary to profile S310-07, where the intra/sub basalt reflectivity is poor, profile S310-17 does show possible reflection events below the top basalts sequence (bright faulted horizon after 6.0s TWT, red dashed box in Figs. E.1a, E.1b). Although out of the scope of this project, an attempt was made to extrapolate the velocity model at these regions solely for time domain imaging. Locally some of the events appear continuous but confidence in their interpretation as primary reflectivity from actual geological interfaces is low, due to possible presence of internal multiple events generated from top basalts sequence which could superimpose deeper primary events.

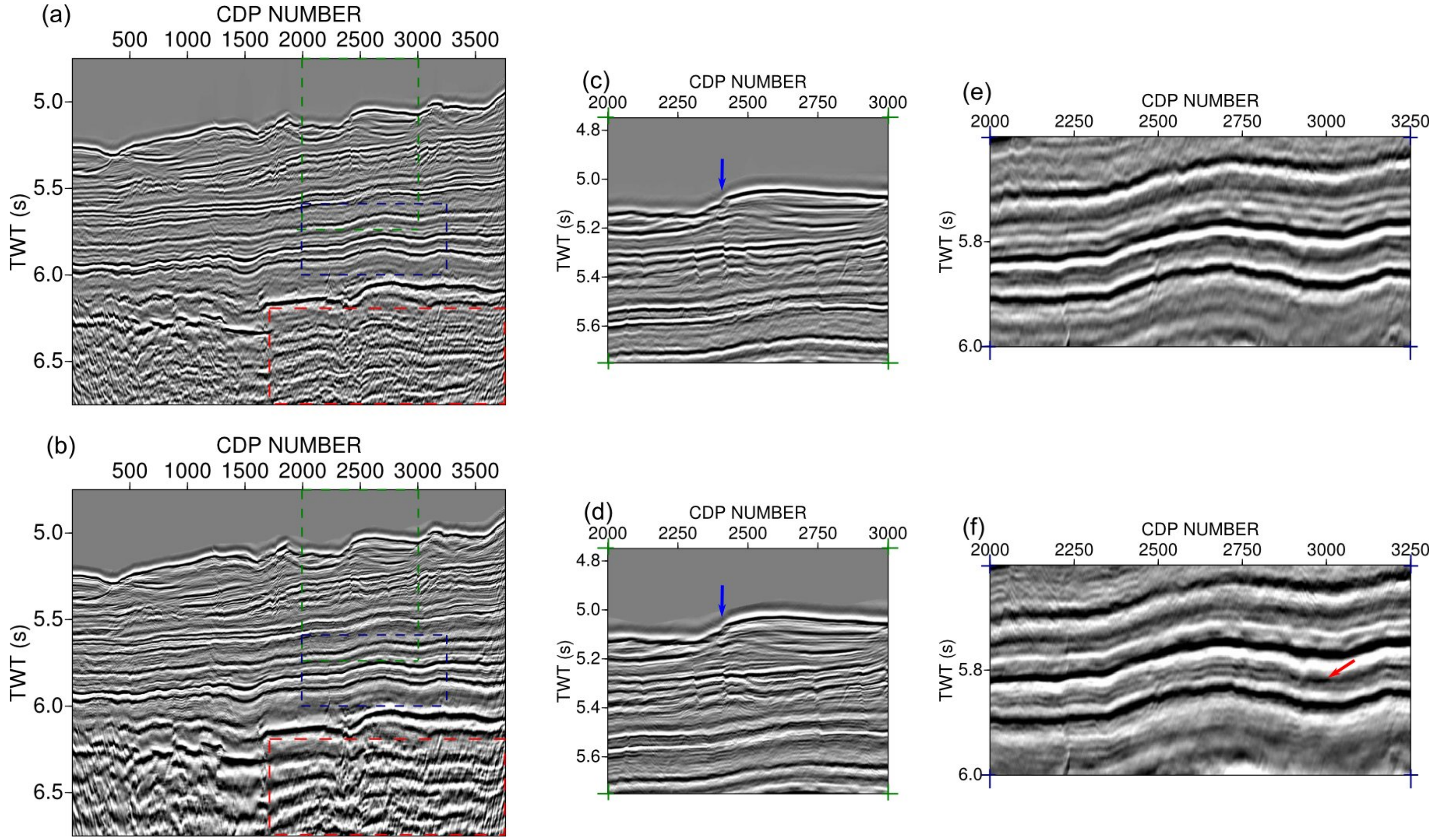

Figure E.1: Comparison of seismic profiles before and after post-stack deghosting. (a) preSTM result including ghost arrivals; (b) Same as (a) but with deghosting in the post-stack domain; (c) Zoomed version of the complex shallow channel system from profile (a). The window is defined by the green dashed box in (a); (d) Same version as in (c) taken from profile (b); (e) Zoomed version of the lower sedimentary sequence in (a). The window is defined by the blue dashed box in (a); (f) Same version as in (e) taken from profile (b). Note the better delineation of the channel features in (d) and the possible intra-layer event retrieved after the deghosting process in (f) (red arrow). Faults possibly reaching seabed (blue arrows in c ,d) and potential intra/sub basalts targets may be evident (red dashed boxes in a, b).

Similarly to Fig. E.1 a comparison between post-stack and pre-stack deghosting flow is depicted in Fig. E.2. The results in all panels indicate the robustness of the pre-stack deghosting approach with a good delineation of the whole image (Figs. E.2b, E.2d, E.2f). However, the post-stack filters have a richer low frequency content manifested by the more pronounced intra/sub basalt arrivals.

A meticulous inspection of the results after ghost compensation must be made, in order to reassure that the retrieved events are part of the original signal and not an artefact generating purely by the deghosting process. The possible pitfalls caused by using an incorrect deterministic filter is presented in Figure E.3. Figs. E.3a and E.3c show some zoomed versions of two different locations from the S310 - 17 profile (E.1a), deghosted using a deliberately incorrect inverse filter that misshapes the receiver's notch. The obvious artefacts, compared to results in Figs. E.3b and E.3d, are manifested as high frequency stripes which follow the local dip of the reflection events or as an echo of the true reflectivity of the signal (blue and red arrows in Figs. E.3a, E.3c). The frequency of the echo is close to the pick frequency of the inverse filter which was chosen to be the receiver's notch. In case of an analogously incorrect compensation of the source's notch, the resulted image will have two groups of superimposed reverberations with harmonics similar to the picked frequencies of the inverse filters.

A simple approach to address this issue could be to use a bandpass filter which excludes the reverberations period, but this could discard a considerably large frequency window and compromise the resolution of high frequency, shallow events. Hence, testing a set of different inverse operators is the only realistic solution for stable deghosting.

Normally the illusory reflectors are easily identifiable as in this example, especially if the applied inverse filter follows the flat surface approximation which generates even more pronounced artefacts. However, in all applications of post-stack deterministic filters, sideswipe events could generate high frequency artefacts as the ghost notch of the noise deviates from the expected notch (Sargent et al., 2011).

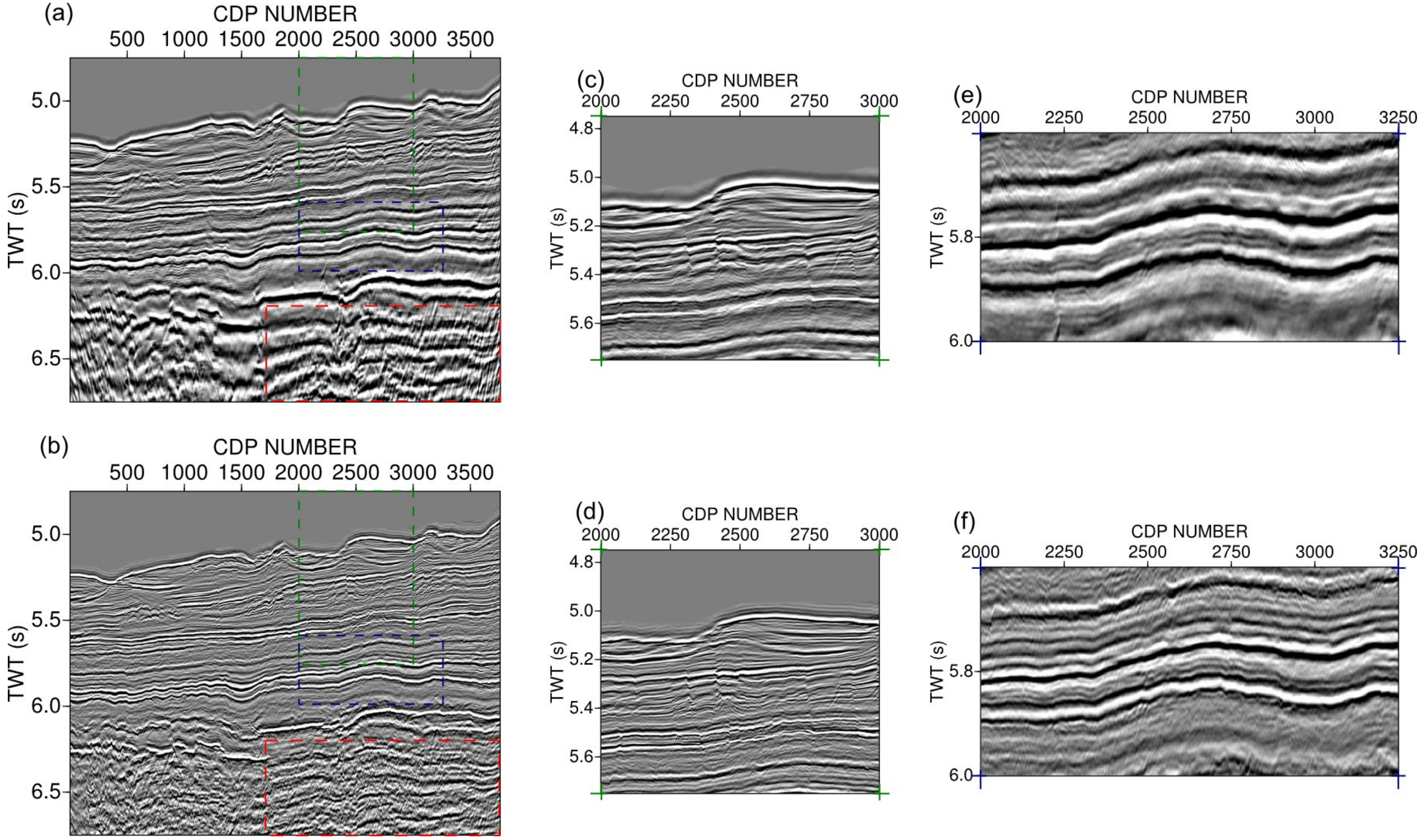

Figure E.2: Comparison of seismic profiles after pre-stack / post-stack deghosting. (a) preSTM result after post-stack deghosting; (b) Same as (a) but with amplitude shaping in the pre-stack domain; (c) Zoomed version of the complex shallow channel system from profile (a). The window is defined by the green dashes in (a); (d) Same version as in (c) taken from profile (b); (e) Zoomed version of the lower sedimentary sequence (a). The window is defined by the blue dashes in (a); (f) Same version as in (e) taken from profile (b). The images are comparable with differences located mainly at the sub-basalt region were the post-stack spectrum generates richer low frequency data.

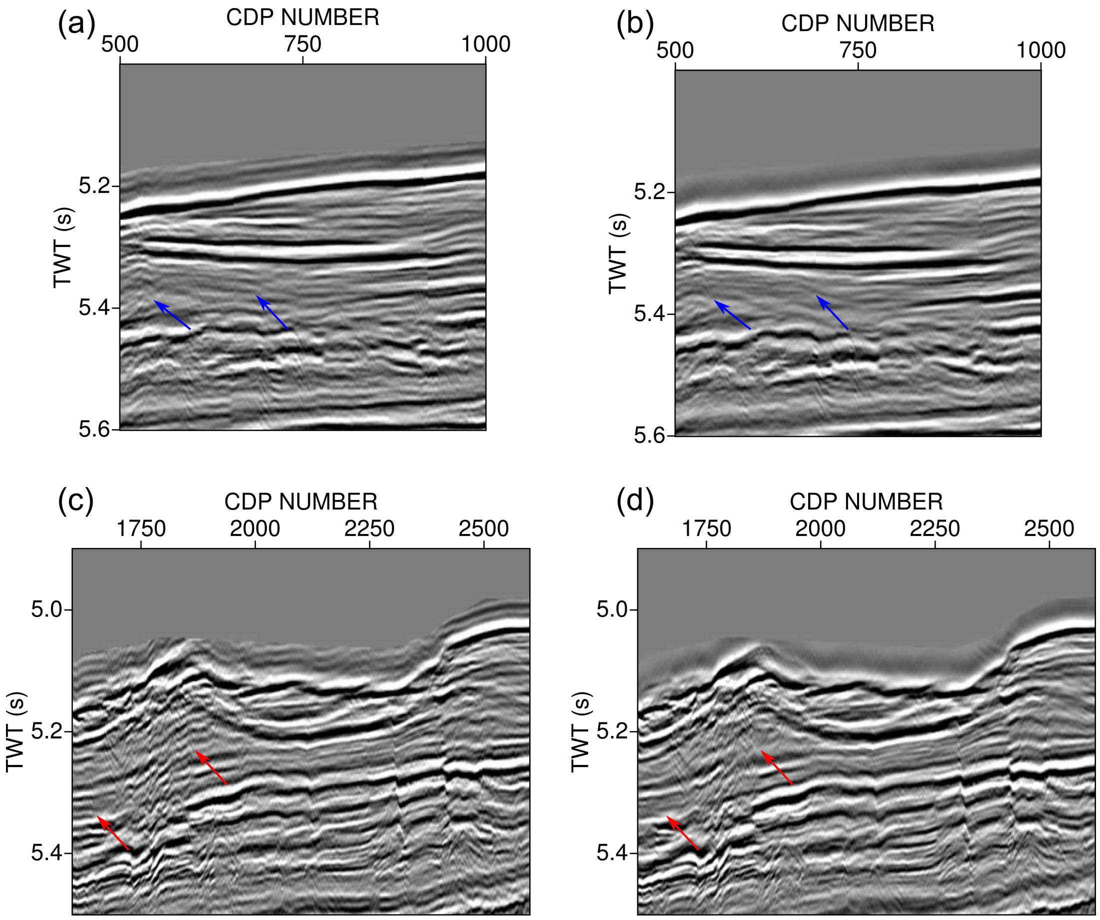

Figure E.3: Effects of applying an incorrect deghosting operator in a post-stack image. (a) and (c) show zoomed versions of two areas from Figs. E.1a, after application of an incorrect receiver's deghosting filter; Contrary to (b), (d) which are compensated with a stable inverse filter, (a) and (c) contain a superimposed high frequency noise with frequency similar to the picked frequency of the applied filter. The illusory reflectivity is induced artificially, as it wasn't originally evident in the preSTM profile with ghost arrivals.

E.2 Effect of velocity model building interval in imaging

In contemporary seismic processing flows for industrial projects, the velocity model building stage is aided by automatic pickers, where the algorithm tracks events in the semblance space at a fine CMP interval, to ensure that lateral changes are efficiently mapped in the velocity field. As this was not directly possible in our project, the manual velocity model building interval (spacing where the $T_0 - V_{rms}$ picks are made) was chosen to be equal to 50 CMP gathers or approximately 312.5 m apart (Table 2.2). This spacing is sufficient enough to image, after preSTM, most of the faulted regions in all the profiles processed and produced well focused and continuous events. Also, the spacing was kept unaltered in all the profiles to make a fair comparison between image features across the different regions of the Mentelle Basin and between different lines passing over the same proposed site.

However, particularly for profile S310-17, the deghosted preSTM images appear well focused in the mid to lower sedimentary sequence (events approximately after 5.5 s TWT), but the shallowest sedimentary sequence, is locally poorly imaged, mainly due to the presence of faults. Severe faulting causes high frequency oscillations in the velocity field, events which are not efficiently modelled with the chosen velocity model building interval (Table D.1).

As an illustration, in Figure E.4 we present zoomed versions of some shallow events from the profile (Figs. E.4a, E.4c, E.4e), that are inefficiently imaged and need extra refinement of the velocity field to be mapped successfully. Note here, that due to time domain migration limitations and possibly due to 2D migration approximation, some of the complex features evident in this profile can only be fully imaged with a combination of pre-stack depth migration algorithm (2D or 3D) along with tomographic inversion update scheme for velocity model building. Nevertheless, the incomplete focusing of most of the features is attributed primarily to the inefficient modelling of high frequency velocity events.

To address this problem a finer sampling interval of 20 CMP gathers spacing (approximately 125 m) was also tested to better refine the shallowest part of the velocity field, with the results presented in Figs. E.4b, E.4d and E.4f respectively. Note the better focusing of the seabed, continuation of some events and sharper fault images after using the refined field with preSTM (red arrows). Although still locally unfocused, it is expected that the image could be improved by using an even finer velocity model building spacing.

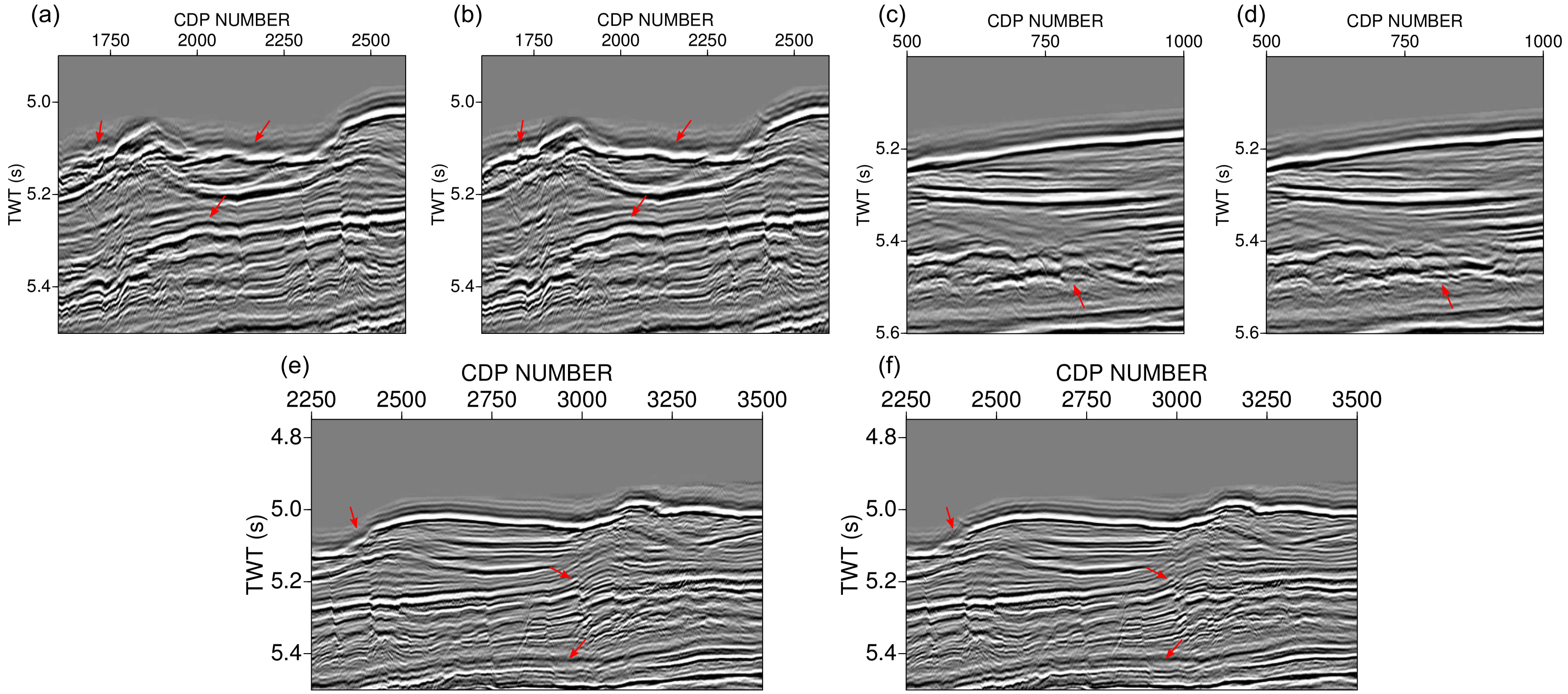

Figure E.4: Effect of velocity analysis interval in imaging. Deghosted preSTM images in (a), (c) and (e) are produced using a velocity model which was picked with spacing of 50 CMP gathers or 312.5 m; (b), (d) and (f) are produced using a velocity field picked every 20 CMP gathers or 125 m. In all panels, red arrows show some of the differences in focusing of shallow events which lead to better delineation of the seabed and faulted structures.

Similarly to the processing sequence of lines S310-07 and S310-01, an anisotropic preSTM algorithm was used to show the potential improvement of the final result after taking advantage of more traces in an image gather. Figure E.5 presents the anisotropic result before (Fig. E.5a) and after (Fig. E.5b) the notch compensation. The events appear sharper with better continuity of horizons due to improved stacking power. The zoomed panels depict the region defined by the green dashed rectangle for clarification of the result. The retrieved reflectivity is evident after shaping the spectrum.

In Fig. E.5c we present the amplitude spectra extracted from the preSTM results, for all the possible processing roots followed for this line (brown, green, blue curves for isotropic case, orange, yellow, red for anisotropic case). Note the notches positions and how every processing flow shaped the spectrum differently. The post-stack deterministic filters, applied either in isotropic or in anisotropic case (green and yellow curves respectively), improved the frequency content of the image. In a similar manner, both the pre-stack roots (blue and red curves respectively), further improved frequency the content with a small remnant notch close to the receiver's notch ≈ 62 Hz, most likely caused by the incomplete receiver depth information. In this example, the flattest result was extracted using the post-stack deterministic inverse filters combined with a anisotropic preSTM algorithm.

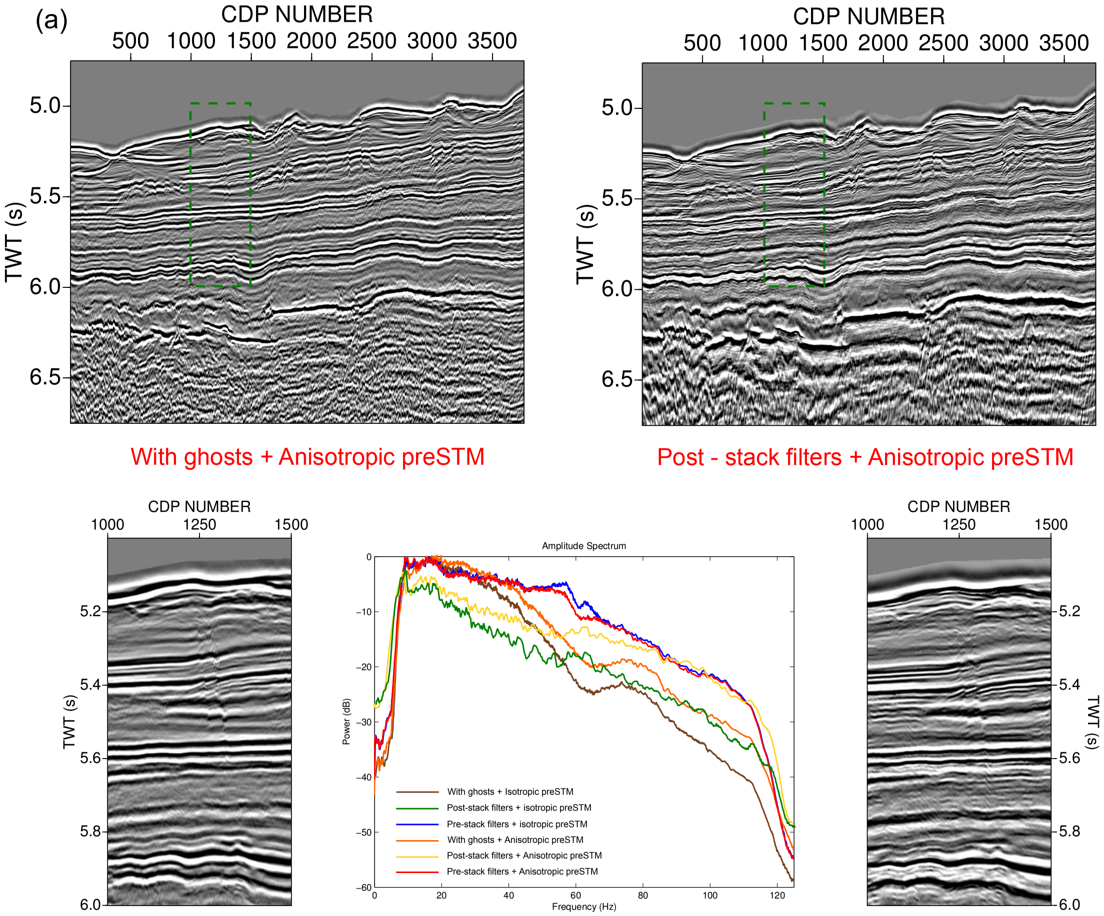

Figure E.5: Anisotropic preSTM and notch compensation. (a). Anisotropic preSTM including ghost arrivals; (b) Anisotropic preSTM with notch compensation post-stack. The result can be considered optimum for a time domain representation of the subsurface, with the extra frequency content delineating the shallow channels features and the anisotropic algorithm providing extra focusing to the events; (c) Comparative diagram showing amplitude spectra extracted from the profiles for all combinations of isotropic/anisotropic migration and pre/post stack deghosting. Note the difference in notch compensation between different migrations and particularly the results between isotropic/anisotropic pre-stack curves. In this case, the best result can be considered the anisotropic post-stack deghosting processing path. The two zoomed panels represent the area defined by the green dashed rectangle. Differences are apparent both in shallow and in deeper targets.

Appendix F

Modelling velocities from density log

The $\rho - V_p$ mapping shown in Fig. 4.2, used a linear regression model to express the relationship between observed ρ, V_p values. The linear equation modelled the incomplete velocity information at the black claystones level which was subsequently used for the well-seismic tie procedure. Although out of the scope of the project, this trend can be considered as the mean trend from a set of linear models. Using *Matlab* regression analysis tools, the uncertainty of the slope and intercept can be also calculated. From the parameters uncertainties and mean values, random Gaussian realizations of linear trends are generated leading to different V_p logs. Fig. F.1 shows an example of that process. Using the observed $\rho - V_p$ values at the black claystone level (green-red dashed boxes in Fig. F.1a, Fig. F.1b respectively), we produce the crossplot in Fig. F.1b. From the uncertainty of the slope/intercept, a number of different linear trends that pass from the data (example of linear trends is given in F.1c) is produced. The trends are subsequently used to map the same ρ values to different V_p logs as shown in Fig. F.1d. Note however, that only a small number of the trends correctly matches the observed V_p values at the top and bottom of the black claystone sequence. In order to perform a robust probabilistic uncertainty estimation of the modelled velocity values, one should condition the models with respect to the observed information, where all the models start and end at (or close) to the observed points. This suggests that a non-linear regression model, like a Gaussian Process, could be implemented to better model the missing values.

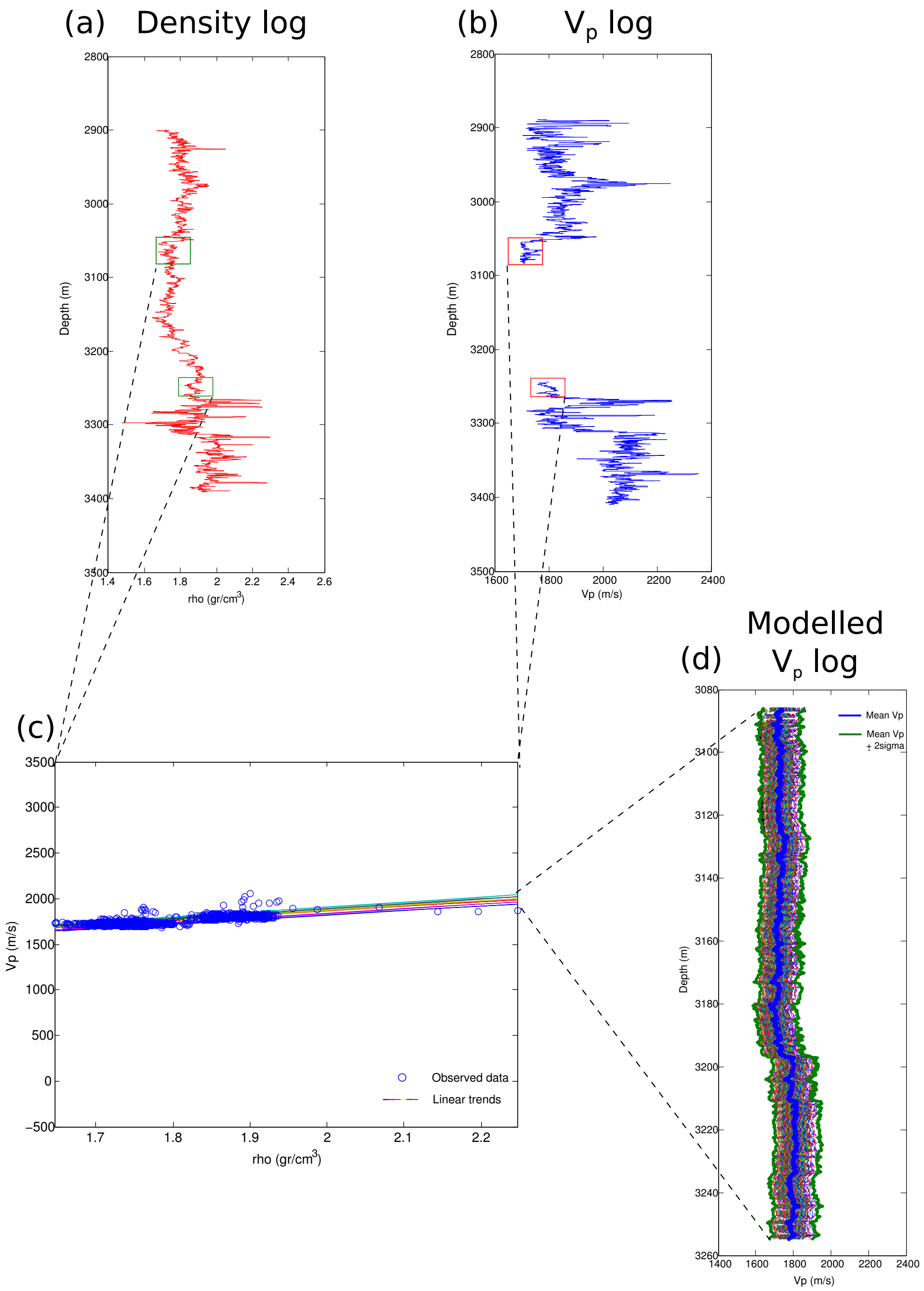

Figure F.1: Random V_p values using probabilistic linear trends. (a) The ρ log as shown in Fig. 4.1; (b) V_p log shown in Fig. 4.1; (c) Using the observed $\rho - V_p$ information at the black claystones level (green, red boxes in (a), (b) respectively), a $V_p - \rho$ crossplot is generated (blue circles). As the data are contaminated by noise, the slope and intercept are non-unique. Their uncertainty can be calculated and from their distribution characteristics random linear trends are generated (lines with different colours in (c)); (d) Different trends map ρ values into different V_p logs (mean V_p trend in blue, $\pm 2\sigma$ in green). However, a small number of the trends actually matches the observed values at top/bottom of black claystones sequence, indicating that a non-linear regression approach must be used for robust uncertainty estimation of modelled velocity values.